Synoptic-scale and mesoscale controls for tornadogenesis on cold fronts

Matthew Richard Clark

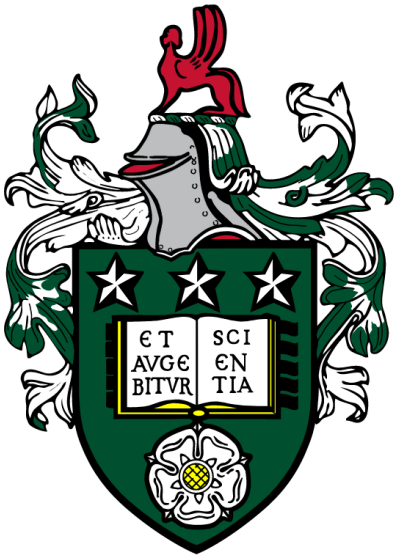

Submitted in accordance with the requirements for the degree of Doctor of Philosophy

The University of Leeds

School of Earth and Environment

August 2021

Declaration of Authorship

The candidate confirms that the work submitted is his own, except where work which has formed part of jointly authored publications has been included. The contribution of the candidate and the other authors to this work has been explicitly indicated below. The candidate confirms the appropriate credit has been given within the thesis where reference has been made to the work of others.

Chapters based on work from jointly authored publications:

Chapter 2: A generalised measure of tornado risk and identification of synoptic types.

Clark, M.R. and Parker, D.J. (2020) Synoptic-scale and mesoscale controls for tornadogenesis on cold fronts: A generalised measure of tornado risk and identification of synoptic types. *Quarterly Journal of the Royal Meteorological Society*, 146, 4195–4225.

Work directly attributable to M. R. Clark: Scoping and design of the research question and methodology. Analysis of data including writing of python scripts. Presentation of data. Writing of manuscript. Revision of manuscript.

Work attributable to author D. J. Parker: Supporting discussion, review of manuscript, discussions at the revision stage and various suggestions at the revision stage.

Chapter 3: Shear-zone vortex-genesis in a developing frontal wave.

Clark, M.R., Parker, D.J. and Hanley, K.E. (2021) Synoptic-scale and mesoscale controls for tornadogenesis on cold fronts: Shear-zone vortex-genesis in a developing frontal wave. *Quarterly Journal of the Royal Meteorological Society*. https://doi.org/10.1002/qj.4164

Work directly attributable to M. R. Clark: Scoping and design of the research question and methodology. Analysis of data including writing of python scripts. Presentation of data. Writing of manuscript. Revision of manuscript.

Work attributable to author D. J. Parker: Supporting discussion, review of manuscript, discussions at the revision stage and various suggestions at the revision stage.

Work attributable to author K. E. Hanley: Setting up and running of the 1.5 km and 300 m grid-length models. Provision of the model output files to M. R. Clark. Contribution of required model setup details for the Methodology section.

Chapters based on work from sole-authored publications:

Chapter 4: A tornadic cold front in amplifying north-westerly flow.

Prepared for submission to *Quarterly Journal of the Royal Meteorological Society*.

Acknowledgements

First and foremost, I would like to thank my supervisor, Professor Doug Parker, for his enthusiasm, interest, expertise, guidance, and encouragement throughout the period of study. I will always remember and be grateful for the many hours that Doug has dedicated to discussing various aspects of the work (in email and in person), and for his reviews of earlier drafts of the various chapters, all of which have improved the content and clarity of presentation and helped to guide the direction of the research. I feel honoured to have had the opportunity to undertake this study under Doug's excellent guidance and supervision.

I would also like to thank my co-supervisors, Professor Chris Collier, Dr Kirsty Hanley, and Dr Kalli Furtado, for their time and expertise in support of this study, in particular to Kalli for guidance on the use of ERAi and model data, and to Kirsty for running the various models at the Met Office and providing the output files for analysis.

Secondly, I would like to thank the Met Office, my employer throughout the course of this study, for sponsoring the study and for allowing me the time to pursue the research as part of my existing job. I am particularly grateful to my managers, past and present: Mike Molyneux, Malcolm Kitchen, Dave Jones, Oak Wells, Katie Norman, and Claire Bartholomew, for recognising the value of the research and for providing useful guidance throughout, including reviews of the material in various chapters of the thesis prior to submission as papers for external peer review.

Thirdly, I would like to thank the Tornado and Storm Research Organisation (TORRO) for provision of the UK and Ireland tornado data over the period of study; in particular, to Terence Meaden for granting permission for use of the data, and Paul Brown for extracting and providing the relevant data in electronic form. Without TORRO's work and the resulting UK and Ireland tornado database, this study would not have been possible. I would like to pay tribute, in particular, to several studies of Professor G. Terence Meaden and the late Professor Derek Elsom, which drew attention to the presence of frontal waves in some tornado outbreaks in the 1970s and 1980s; these studies have helped to motivate the current work.

I would like to thank Dan Suri and Matthew Lehnert, of the Met Office, for their comments on the proposed forecasting methodologies, and for conducting ad-hoc operational trials of the tornado probability metric for a selection of cases in the winters of 2019-20 and 2020-21.

I would like to thank the reviewers of chapters submitted and/or accepted as papers for external publication (at the time of writing, Chapters 2 and 3), for their detailed and helpful comments, which have led to improvements in the content and clarity of presentation; and to Ed Pavelin, of the Met Office, for his review of Chapter 1.

Finally, I would like to thank my friends and family for their support throughout; in particular, to my family for hosting me on various trips to Yorkshire when working at the University of Leeds, and for their encouragement and interest over the several years of this study and in the years prior to that.

Abstract

This thesis addresses the origins, dynamics and forecasting of tornadoes in narrow cold-frontal rainbands (NCFRs). A review of current understanding is undertaken, which is set in context by comparison with the situation for tornadoes in supercell thunderstorms.

Environments of 114 tornadic and non-tornadic NCFRs in the UK and Ireland are explored using ECMWF reanalysis data. A generalised measure of tornado probability is obtained using the distribution of points within the parameter space defined by the two environmental parameters exhibiting the best discrimination between event classes.

Synoptic situations commonly associated with tornadic NCFRs are identified and conceptual models are developed for each. Two distinct types are defined. Firstly, those associated with developing secondary cyclones (i.e., frontal waves), which account for over half of all tornadic cases. Secondly, those associated with upper-level jet streaks cutting across the front within amplifying large-scale flow patterns, at the rear flank of a longwave trough (so-called 'north-westerly flow' events), which account for just over one-quarter of all tornadic cases.

For one example of each type, further analysis is undertaken using convection-permitting models and observations. Physical links are found across a wide range of spatiotemporal scales in both events. In the frontal wave case, changes in the relative magnitudes of vertical vorticity and horizontal strain at the front favoured meso-γ- to miso-scale vortex-genesis, likely by release of horizontal shearing instability, just down-front of the wave centre in the early stages of secondary cyclogenesis. In the north-westerly flow case, although the front was generally weaker, interaction of an upper-level jet streak and tropopause fold with the surface front's transverse circulation initiated a sequence of events that culminated in locally tornado-favourable conditions at the surface front, near the left exit of the cross-cutting jet.

Finally, results are reviewed and compared with existing cyclone paradigms and conceptual models of cold fronts, and directions for further study are outlined.

Table of Contents

List of Tables

List of Figures

List of abbreviations

AGL	Above Ground Level
AMS	American Meteorological Society
ASXX	Met Office Surface Analysis
CAPE	Convective Available Potential Energy
CP14	Clark and Parker (2014)
CP20	Clark and Parker (2020); i.e., Chapter 2 of this thesis.
DAM	Decametre
ECMWF	European Centre for Medium-range Weather Forecasting
ERAi	ECMWF Interim Re-Analysis
FNFM	Front-Normal Forward Motion
HSI	Horizontal Shearing Instability
HT	High-Tornadic
LEWP	Line-Echo Wave Pattern
MCS	Mesoscale Convective System
MSLP	Mean Sea-Level Pressure
nT	non-Tornadic
NCFR	Narrow Cold-Frontal Rainband
p[NCFR]	Probability of an NCFR
p[TN]	Probability of tornado(es) (conditional on the presence of an NCFR)
PV	Potential Vorticity
PVU	Potential Vorticity Unit (1×10^{-6} m^2 s^{-1} K kg^{-1})
PSPC	Sum of radial convergence and cyclonic azimuthal shear (positive only)
QLCS	Quasi-Linear Convective System
RH	Relative Humidity
SRTM	Shuttle Radar Topography Mission
T	Tornadic
TORRO	TORnado and storm Research Organisation
UK	United Kingdom

UKV	1.5 km grid-length version of the Met Office's Unified Model
US	United States
UTC	Coordinated Universal Time

Chapter 1: Introduction

1.1 Overview

This thesis addresses the origins, dynamics and forecasting of cold-frontal tornadoes in the UK. A tornado is a rapidly rotating column of air extending vertically between the surface and the base of a cumuliform cloud (AMS, 2021), typically associated with a funnel cloud extending below the base of the cloud, and a debris cloud near the ground surface. The rotating wind field comprising a tornado generally ranges from a few tens of metres to perhaps 1 km in diameter, with lifetimes typically ranging from a few seconds to a few tens of minutes. Tornadoes are capable of catastrophic damage, owing to the exceptionally high wind speeds within their circulations (often > 30 m s^{-1}, and occasionally > 75 m s^{-1}); even tornadoes of relatively modest intensity are capable of substantial property damage and constitute a risk to life. Owing to their small scales and short lifetimes, tornadoes pose a formidable forecasting challenge. Great advances have been made in the US in the second half of the 20th century, where tornado warnings are now issued routinely. Even here, however, warning lead times are typically short (15 minutes or less) and false alarm rates remain high. Many of the US's tornadoes are spawned by supercell thunderstorms i.e., thunderstorms possessing a deep, rotating updraft; consequently, current forecasting and warning techniques have been designed with this type of tornado in mind (though interest in non-supercell tornadoes is also growing at the time of writing).

Case studies and existing climatologies show that, whilst tornadic supercell thunderstorms do occur in the UK, many of the UK's tornadoes occur in non-supercell storms, including slow-moving showers developing at zones of horizontal convergence, and precipitation systems exhibiting linear morphologies in radar rainfall imagery, such as narrow cold-frontal rainbands (NCFRs). Non-supercell tornadoes in general, and NCFR tornadoes in particular, require a somewhat different approach to forecasting because the environments in which they form, and the physical mechanisms leading to tornado-genesis, likely differ in at least some respects from those in supercells. If forecasting techniques are to be developed for UK tornadoes, they must therefore be applicable to these events, in addition to tornadic supercell thunderstorms. Sound forecasting techniques require a solid underlying knowledge of the typical environments of tornadic storms, and the physical mechanisms associated with vortex- and tornado-genesis, both of which are comparatively lacking in the case of NCFRs. Accordingly,

this thesis focusses on tornadoes in NCFRs, with the aim of improving this underlying knowledge and providing new tools for the forecasting of these events in the UK and elsewhere.

1.2 History of tornado research in the UK and the development of a tornado climatology

It has long been recognised that parts of northwest Europe, including the UK, have a high frequency of tornadoes when compared to many other parts of the globe (Peltier, 1840; Wegener, 1917). Early studies of tornadoes in the UK (pre-1950) generally document individual cases, and they naturally tend to focus on tornadoes that were exceptionally intense or long-lived for the region. These studies generally comprise detailed descriptions of the damage, but also occasionally contain information about the meteorological conditions at the time of the event. For example, Symons (1900) described the aftermath of a tornado that carved a 20-mile-long path of damage through Wiltshire on 1 October 1899. Using available surface observations, he showed that the tornado occurred at the northeast (i.e., forward) flank of a depression that moved slowly northeast across England. Billett (1914) documented exceptionally severe damage in south Wales after the tornado of 27 October 1913, which was later assigned a rating of T7 on the International Tornado Intensity (T) Scale (Meaden, 1976; Meaden *et al*., 2007). Billett (1914) showed that this and other tornadoes on the same day were located along a single, south-to-north orientated path over 200 miles in length. Lamb (1957) documented the damage produced by the intense, long-track tornadoes of 21 May 1950 in the southeast Midlands, showing the tornadoes to have occurred near the centre of a mesoscale area of low pressure that moved northeast with the parent thunderstorm.

The systematic study of tornadoes in the UK, leading to the eventual development of climatologies, began with the studies of Lamb (1957) and Lacy (1968). Lamb (1957) listed 54 destructive tornadoes that occurred between 1868 and 1950, as reported in issues of the *Quarterly Journal of the Royal Meteorological Society*, *Weather* and *Meteorological Magazine* (see his Appendix I). These events revealed an annual maximum in tornado frequency in the late summer and autumn months, with October having the largest number of events (22.2% of the total). Lacy's (1968) study,

whilst covering a period of only four years (1963 – 1966), was important in demonstrating that the frequency of tornadoes in the UK was considerably higher than previously estimated, with a total of 78 tornadoes occurring on 36 days during this period alone. These events were discovered by searching for reports of weather-related structural damage in press cuttings. The higher frequency of tornadoes, relative to earlier estimates, was attributed to inclusion of weaker events that were less likely to have been included in historical listings or to have appeared in the scientific literature. The issue of underreporting, especially of weaker tornadoes, was therefore highlighted for the first time in the UK. Lacy (1968) found, contrary to initial expectations, that most tornadoes and tornado days (60 and 20, respectively) occurred in winter. Furthermore, whilst it was apparently uncommon for more than one tornado to occur on any single day in summer, outbreaks of 12 or more tornadoes on a single day occurred in winter. Most tornadoes developed in showery conditions, in a variety of different synoptic situations. However, the largest outbreaks were associated with cold frontal passages.

In 1974, the Tornado Research Organisation (later renamed the Tornado and Storm Research Organisation; TORRO) was founded by Prof. G. Terence Meaden. TORRO's principal aim was to catalogue historical and recent reports of tornadoes and other severe weather phenomena, in order to obtain more detailed estimates of the frequency and spatial distribution of tornadoes and damaging convective storms in the UK (Elsom *et al*., 2001). Numerous historical reports of tornadoes came to light following extensive searches of press cuttings by Terence Meaden and Michael Rowe (Meaden, 2016; Brown and Meaden, 2016). These reports were collated and archived, and thus the TORRO tornado database was born. The TORRO database remains the only long-term, systematic record of tornadoes in the UK and Ireland, and its creation and subsequent expansion permitted the development of more detailed UK and Ireland tornado climatologies (Meaden, 1976; Elsom and Meaden, 1984; Meaden, 1985; Elsom, 1985a).

In their 1960–1982 climatology, Elsom and Meaden (1984) noted that tornadoes in the UK occurred in a large range of synoptic types, but that medium and large outbreaks (defined as 10 – 19 and ≥20 tornadoes, respectively) almost always occurred along well-marked fronts or troughs associated with rapidly deepening or very deep

depressions (in agreement with Lacy's (1968) observations). The monthly distribution of tornadoes showed a reasonably well-defined annual cycle, with a late autumn and early winter maximum (highest frequencies in the months of November to January, inclusive) and a spring minimum. Subsequent climatologies (Reynolds, 1999; Kirk, 2007; Kirk, 2014; Mulder and Schultz, 2015; Clark and Smart, 2016) show similar results, though the timing of the annual peak in tornado frequency varies according to the period of study (Mulder and Schultz, 2015), from late summer or early autumn to late autumn or early winter. These differences likely relate to the irregular occurrence of the larger tornado outbreaks in the autumn and winter, which tend to occur in clusters separated by long periods with no events. The largest outbreaks have the potential to skew climatologies substantially; for example, the total number of tornadoes in the outbreak of 23 November 1981 (104) considerably exceeds the next highest *annual* total in the TORRO database (Rowe and Meaden, 1985).

Recent climatologies have adopted gridding and spatial averaging techniques to provide an estimate of the areal frequency of tornadoes, and its spatial variability, across the UK. For example, Kirk *at al*. (2016), identified maxima in tornado frequency along the south coasts of England and East Anglia. Conversely, Mulder and Schultz (2015) identified maxima in the Welsh Marches and west Midlands. The differences likely relate to differing periods of analysis, gridding methodologies, and uncertainties associated with the calculation of frequencies in coastal regions. Mulder and Schultz (2015) further analysed the morphology (i.e., radar-observed organisational structure) of the parent storms of tornadoes, by comparing archived composite radar imagery with tornado report times and locations. 42% of tornadoes were found to be associated with cellular convection (i.e., relatively discrete rainfall cores, likely associated with individual convective cells), with the remainder associated with quasi-linear convective systems (QLCSs; defined as radar echoes with length of at least 10 times width, and generally comprising an amalgam of several or many individual convective cells). A subset of these QLCSs occurred along frontal boundaries, suggesting that they were narrow cold-frontal rainbands (NCFRs; Houze *et al*., 1976), also sometimes known as 'line convection' (e.g., James and Browning, 1979). Although generally considered a subset of QLCSs, NCFRs differ from non-frontal QLCSs in several important ways, as discussed in Section 1.6. Clark (2013), in an analysis of cool season QLCSs over the

UK between 2003 and 2011, the large majority of which were NCFRs, found that 28% of events produced at least one tornado.

1.3 Development of severe storms meteorology

Whilst the UK experiences a high frequency of tornadoes per unit area in comparison to many other countries, most of the UK's tornadoes are relatively weak (intensities ≤T3 on the International Tornado Intensity Scale (e.g., Kirk, 2014). Strong tornadoes (≥T4 or ≥F2) are rare, whilst violent tornadoes (≥T8 or ≥F4) very seldom occur; only two UK tornadoes in the TORRO database are estimated to have reached T8 intensity, with the most recent of these, at the time of writing, having occurred on 14 December 1810 i.e., over 200 years ago. In the US, whilst most tornadoes are similarly weak (e.g., Kelly *et al*., 1978), strong to violent tornadoes occur in substantial numbers every year. Furthermore, large outbreaks of tornadoes occur more-or-less every year, sometimes affecting several States. Other hazards associated with deep, moist convection, including large hail and damaging outflow winds, similarly pose a much larger socio-economic threat in the US than in the UK (and many other countries). This is especially so in the Great Plains region, where the incidence of strong-to-violent tornadoes is at a maximum. Consequently, since 1950, much research into severe thunderstorms and related hazards, including tornadoes, has taken place in the US, with a particular focus on the supercell thunderstorms of the Great Plains region. The advent of new and improved observations techniques, such as Doppler and dual polarisation weather radars, together with major advances in computing capability for numerical simulations of the atmosphere, have led to great advances in the understanding of supercell thunderstorms and related hazards in the second half of the 20th century and beginning of the 21st. Collectively, this research provides a self-consistent body of knowledge that is used operationally in forecasting and nowcasting of supercell thunderstorms and associated tornadoes in the US. A brief overview of this research is provided in the following sections, which is then compared with the current state of understanding for non-supercell tornadoes.

A key concept in the forecasting of convective storms and related hazards is the 'ingredients-based' methodology (e.g., McNulty, 1978; Johns and Doswell, 1992;

Doswell *et al*., 1996); in order for deep, moist convection to occur, there must be sufficient moisture, conditional instability, and a source of lift (Doswell, 1987). Each ingredient is necessary, but not sufficient, for the formation of deep, moist convection and all three must be present for it to occur. Organised convection (i.e., upscale growth of individual convective cells into clusters with a well-defined overall structure, or the development of rotating cells that have longer lifetimes than ordinary cells) additionally requires strong vertical wind shear (e.g., Moller *et al*., 1994). These concepts lead to a forecasting approach in which the likelihood, severity and mode (i.e., organisational structure) of storms may be anticipated by analysis of forecast values of relevant *environmental* parameters. For example, Convective Available Potential Energy (CAPE) is used to describe the amount of buoyant energy of an air parcel lifted from a specified level (usually the surface), which depends strongly on the initial temperature and moisture content of the parcel, and the environmental temperature profile (i.e., the measure incorporates both the moisture and stability ingredients for deep, moist convection). Lift is generally provided by mesoscale boundaries such as fronts, convergence zones and drylines. Although large-scale dynamic forcing for ascent is also a source of lift, it is typically too slow to be important in triggering convection, though the integrated effect of large-scale dynamic lift over a sustained period of time (~hours) is often important in priming the atmosphere for convection (for example, by increasing mid-level lapse rates and thereby contributing positively to the instability; e.g., Doswell, 1987).

The likelihood and mode of convection may be assessed by analysis of the presence or otherwise of each ingredient, looking for regions where all ingredients are likely to be present; for example, organised convection may be expected to occur where sufficient instability, moisture, a source of lift and strong vertical wind shear coincide. An advantage of this approach is that convection-resolving models are not required to anticipate the likely severity and mode of convection (indeed, at the time these concepts were developed, convection-permitting models did not exist in operational meteorology); this is because environmental parameter values tend to vary rather slowly in time and space and so may be estimated using models with relatively coarse resolution (such as global operational numerical models). Anticipation of the mode of convection is relevant because, to a greater or lesser degree, the type and likelihood of occurrence of convective hazards depends upon the storm mode.

1.4 Tornadoes and tornado-genesis in supercell storms

Globally, it is thought that most strong tornadoes, and virtually all violent tornadoes, are associated with supercell thunderstorms. The defining characteristic of a supercell is its persistent (lifetimes at least on the order of tens of minutes), deep (extending through at least one-third to one-half of the storm's depth), rotating updraft (e.g., Moller *et al*., 1994). Supercell thunderstorms, whilst comparatively rare, are also responsible for a disproportionate fraction of other convection-related severe weather, including large hail and damaging non-tornadic (i.e., rectilinear, or 'straight-line') wind gusts. Research efforts have accordingly focussed on this type of storm. Although the term 'supercell' was introduced in a study of a severe thunderstorm in the UK (the 'Wokingham storm' of 9 July 1959; Browning and Ludlam, 1962), the vast majority of subsequent research into these storms has been conducted in the US; observational studies have elucidated the key structural features of supercells (e.g., Fujita, 1965; Browning, 1965; Brown *et al*., 1975; Lemon and Doswell, 1979), clarified the environmental conditions supportive of their development (e.g., Moller et al., 1994), described the synoptic-scale and mesoscale situations in which the required environmental parameters are often brought together[1], and revealed a range of morphological attributes, leading to the discovery of a spectrum of supercell types (e.g., Bluestein and Parks, 1983; Moller et al., 1994). Furthermore, idealised modelling studies have provided insights into the dynamics of supercells, showing the physical mechanism by which these storms acquire vertical vorticity (e.g., Weisman and Klemp, 1984; Weisman and Rotunno, 2000), and leading to the replacement of the early kinematic or morphological definitions of a supercell with a dynamical one.

As with other types of organised convection, vertical shear of the horizontal wind was identified as a key ingredient for supercell storms, with supercells tending to form only in environments in which the bulk vector wind difference over the 0 – 6 km layer is greater than about 30 – 40 knots (provided sufficient CAPE and a source of lift are also present). Early modelling studies (e.g., Weisman and Klemp, 1984; Klemp, 1987) showed that in such conditions, storms acquire vertical vorticity by tilting, on the flanks of the updraft, of the horizontal vorticity associated with the vertical wind shear.

[1] In parallel, studies have elucidated the typical environments and synoptic- and meso-scale settings of other storm types, such as the back-building multicell clusters that pose an elevated threat of flash flooding (e.g., Doswell *et al*., 1996).

This process results in a counter-rotating vortex pair flanking the updraft (Figure 1.1(a)). Storm splitting then occurs as new updrafts continually redevelop on the outer flanks nearest to the vortices, due to associated perturbation vertical pressure gradients (Figure 1.1(b)). Where the hodograph is relatively straight, the resulting mirror image storms diverge as they propagate to the left and right of the mean deep-layer vertical wind shear vector in the convective layer (Figure 1.2, top). However, in environments in which the hodograph exhibits clockwise curvature (Figure 1.2, bottom) the cyclonic vortex becomes dominant, with the vertical velocity and vertical vorticity maxima becoming collocated (i.e., a rotating updraft – the mesocyclone), leading to a strong and often long-lived right-split storm that propagates to the right of the mean vertical wind shear vector in the convective layer (e.g., Rotunno and Klemp, 1982; Figure 1.3). These 'right-moving' supercell storms are responsible for many of the convective severe weather reports in the US, particularly large hail and tornadoes (e.g., Smith *et al*., 2012). A measure of the potential for such right-moving supercells is provided by another environmental parameter, the storm-relative helicity, which is typically analysed over the 0 – 3 km above ground level (AGL) layer and which may be visualised as twice the area swept out by the storm-relative wind vectors over the layer of interest, when plotted on a hodograph. Large storm-relative helicity is generally associated with wind profiles that exhibit both strong increases in wind speed and large veering of the wind direction with height.

More recently, research attention in the US has focussed on the analysis of differences between tornadic and non-tornadic supercells, including identification of environmental parameters that have skill in discriminating between the two types (e.g., Davies-Jones *et al*., 1990; Markowski *et al*., 2002; Markowski and Richardson, 2009). Although the tornado-genesis process within supercells is still not fully understood, recent modelling studies have shown that downdrafts are important in amplifying the near-ground vertical vorticity (Figure 1.4(a)). Furthermore, studies using proximity soundings have shown that the 0 – 1 km AGL storm-relative helicity, bulk vertical wind shear, and the low-level relative humidity are potentially useful environmental parameters for discriminating between tornadic and non-tornadic supercells, with tornadic supercells tending to occur in environments with larger values of these parameters. Environmental parameters (particularly bulk vertical wind shear, storm-relative helicity and CAPE) are now analysed routinely in the US to identify

environments supportive of supercell storms in general, and to estimate the risk of tornadoes where supercells are expected to develop. In recent years, ultra-high-resolution model simulations (grid spacing < 100 m) have been used to explore the tornado-genesis process in more detail (e.g., Betten *et al*., 2017; Coffer *et al*., 2017). Large field campaigns have provided observations of unprecedented detail for a small number of events (Wurman *et al*., 2012). An overarching aim is to improve the lead time of warnings, and to reduce the false alarm rate, by improving the ability to identify those cells most likely to produce tornadoes.

The collective outcome of the above research is a relatively complete and well-established understanding of the dynamics of supercell thunderstorms, and well-established forecasting methodologies for supercells and related hazards. Consequently, it is possible to anticipate the risk of supercells and associated hazards several days in advance. As the lead time to the event decreases, the output of convection-permitting models may be used to refine the forecasts, focussing in on areas and time periods at particularly high risk. In the nowcasting timeframe (0 – 6 hours ahead of the event), observations are used to monitor individual storms. Radar signatures associated with rotating storms (such as hook echoes in reflectivity fields, velocity couplets in radial wind fields, and differential reflectivity columns and debris signatures in polarimetric fields) are routinely monitored, with automated detection algorithms employed to identify those signatures most likely to be associated with tornadoes and other hazards. In several countries, storm-scale warnings are based upon these observations.

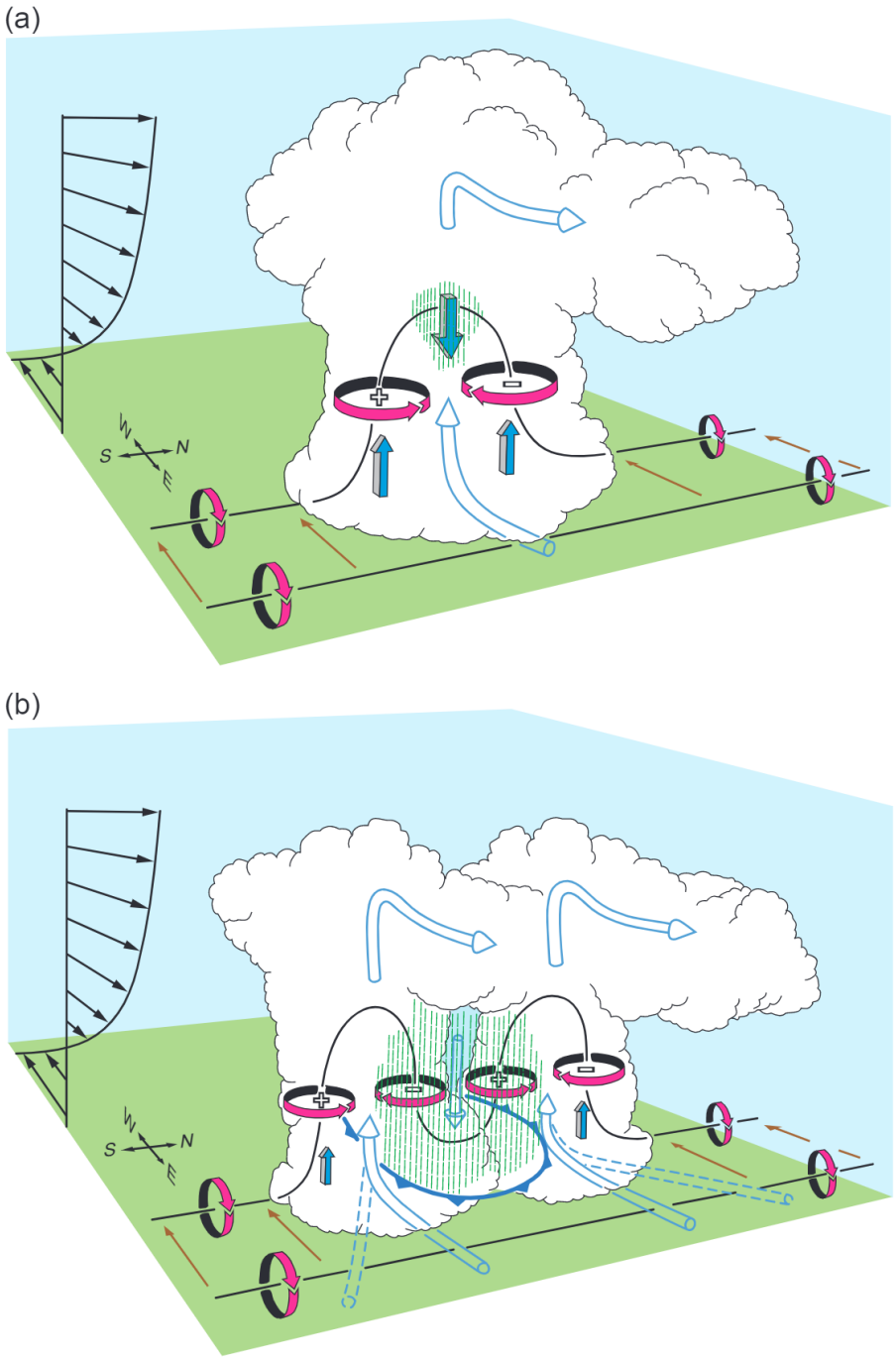

Figure 1.1: The splitting of cells and the subsequent development of rotation through vortex line tilting in the case of a straight hodograph. (a) In the early stage a vortex pair forms through tilting of the horizontal vorticity associated with the mean shear, creating vertical perturbation pressure gradient forces (blue shaded arrows) on the flanks. (b) As rainy downdrafts form and the cell splits, vortex lines are tilted downward, and the original updraft-centred vortex pair is transformed into two vortex pairs. The updraft of the rightward (facing downshear) moving member propagates toward the positive vorticity on the right flank, and thus a correlation between updraft and positive vorticity develops. In (a) and (b), the transparent blue arrows indicate storm-relative trajectories. In (b), the dashed transparent blue arrows indicate storm-relative trajectories after storm splitting. Figure and caption reprinted with permission from Markowski and Richardson (2010) (their Figure 8.35, p. 235; originally adapted from Klemp, 1987).

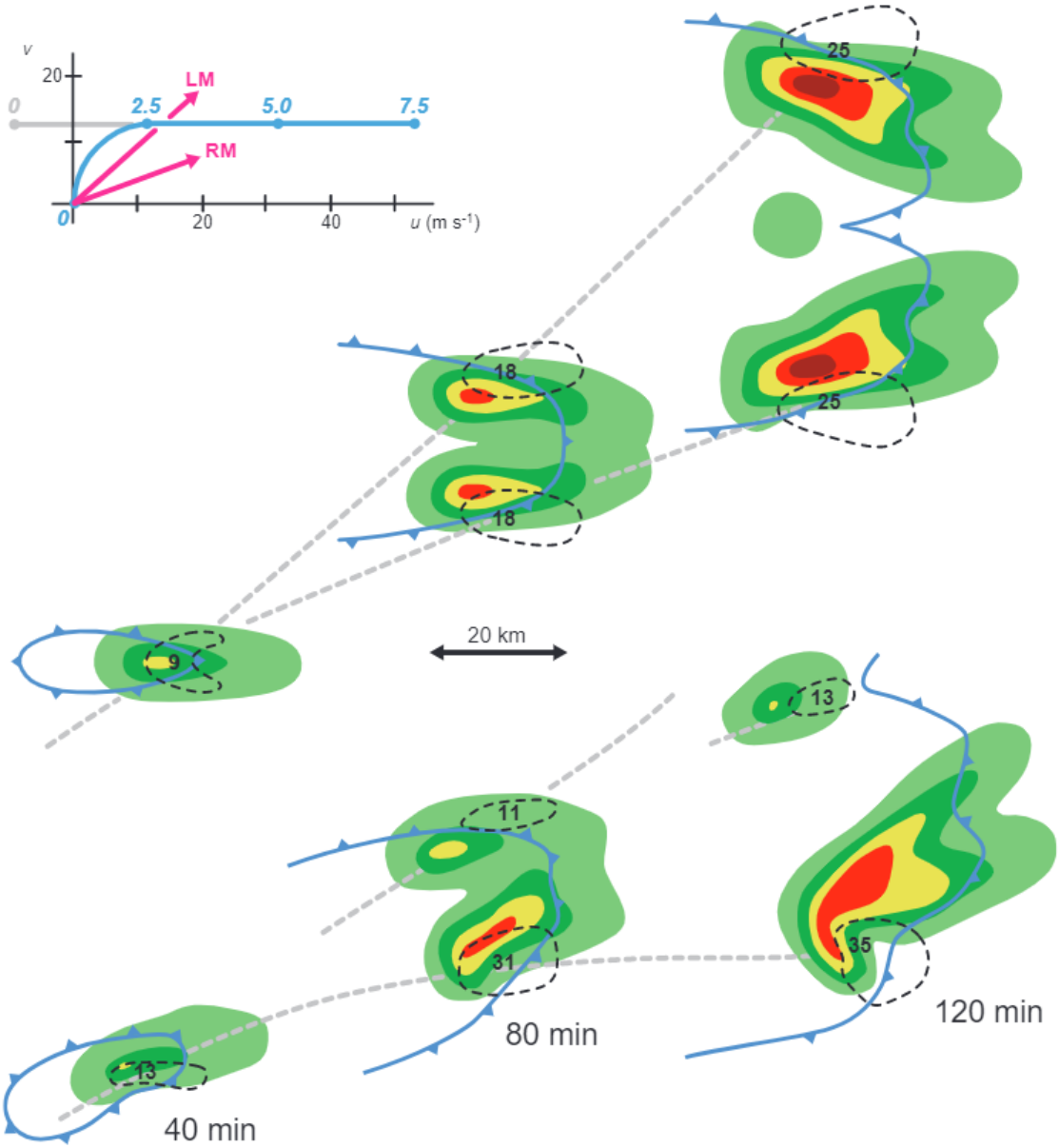

Figure 1.2: Plan views of cloud-model-produced, low-level rainwater fields for two simulations using, respectively, a straight hodograph (grey in lowest 2.5 km, blue above; numerals along the hodograph indicate altitude in km) and one with low-level clockwise hodograph curvature (blue). The straight hodograph produces storms with mirror-image symmetry, whereas the curved hodograph enhances the right-moving storm. The left- and right-moving storm motions are indicated on the hodographs with magenta arrows and are labelled 'LM' and 'RM', respectively. The dashed black contours enclose the regions of significant midlevel updraft, and the numerals indicate the location and magnitude of the maximum vertical velocity (m s^{-1}). Gust fronts are also shown. The gray dashed lines indicate storm motions. Figure and caption reprinted with permission from Markowski and Richardson (2010) (their Figure 8.41, p. 240; originally adapted from Klemp, 1987).

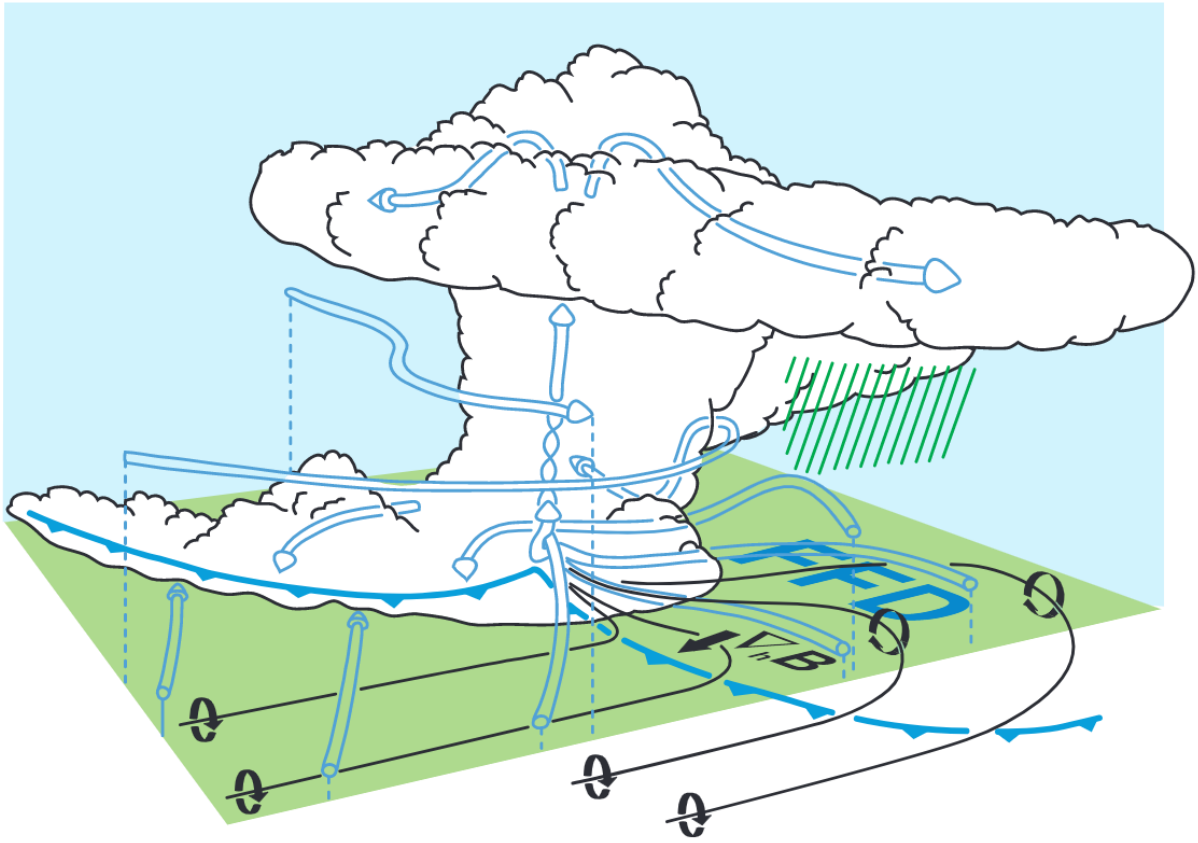

Figure 1.3: Schematic of a supercell thunderstorm in westerly mean shear, viewed from the southeast, at a stage when low-level rotation is intensifying. The cylindrical arrows depict the storm-relative winds. The black lines are vortex lines, with the sense of rotation indicated by the circular arrows. The blue barbed line marks the gust front. The orientation of the horizontal buoyancy gradient, $\nabla_h B$, is also indicated. Figure and caption reprinted with permission from Markowski and Richardson (2010) (their Figure 8.34, p. 232; originally adapted from Klemp, 1987).

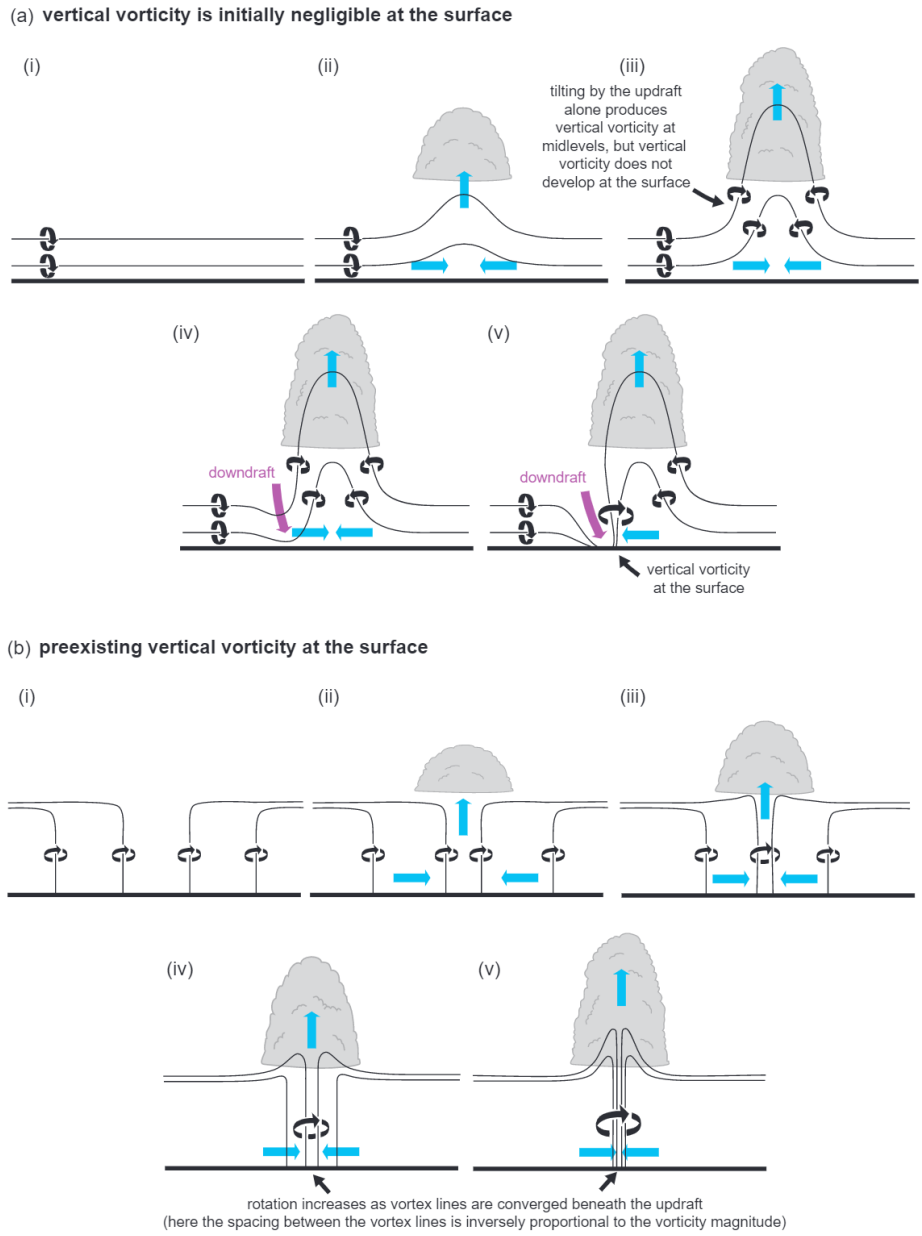

Figure 1.4: (a) Simple vortex line demonstration of why a downdraft is needed in order for significant vertical vorticity to develop at the ground beneath a thunderstorm in the absence of pre-existing vertical vorticity at the surface. There is assumed to be no baroclinic vorticity generation; thus, the vortex lines are assumed to be frozen in the fluid. This is obviously an oversimplification, for there must be baroclinicity at least somewhere or else a buoyant updraft could not exist in the first place (rainy downdrafts and their associated baroclinicity, even if it is just a result of hydrometeor loading, are also a virtual certainty at least somewhere in the vicinity of a thunderstorm updraft). Nonetheless, the basic conclusion reached from considering only a purely barotropic redistribution is not changed; if tilting of vortex lines is accomplished by only an updraft, significant vertical vorticity cannot arise at the ground because air is rising away from the ground as it is tilted. On the other hand, if a downdraft is involved, a positive contribution to the vertical vorticity tendency can arise from tilting even as air is sinking toward the ground. (b) Simple vortex line demonstration of how a tornado can arise from convergence alone, in the absence of a downdraft, when pre-existing vertical vorticity is present at the ground. Figure and caption reprinted with permission from Markowski and Richardson (2010) (their Figure 10.3, p. 277).

1.5 Tornadoes and tornado-genesis in non-supercell storms

In comparison to the body of understanding of supercells and associated tornadoes, understanding of non-supercell tornadoes and tornado environments remains limited, owing to the lesser research focus on these events. Consequently, recent gains in forecasting and warning capability for supercells are not reflected by similar gains in non-supercell events. In addition to the perceived lower risk posed by non-supercell tornadoes (especially in the regions where the most research has been conducted to date), this relative lack of research focus may be due to the wide variety of storm morphologies and synoptic- to meso-scale environments (and, by inference, variety of physical processes) that can support non-supercell tornado-genesis (e.g., Forbes and Wakimoto, 1983; Wakimoto and Wilson, 1989; Roberts and Wilson, 1995; Lee and Wilhelmson, 1999).

In recent years, interest in non-supercell storms and tornadoes has increased. This is partly due to an increasing recognition that the storm environments of the US Great Plains may not be typical of other countries, or even other regions within the US. There has been increasing focus, for example, on so-called high-shear, low-CAPE events (e.g., Davis and Parker, 2014; Sherburn and Parker, 2014; 2019; Wade and Parker, 2021) and QLCSs (e.g., Trapp *et al*., 2005), both of which contribute substantially to the tornado totals in south-eastern US states. Another motivating factor is that non-supercell tornadoes may occur in regions and at times of day and year where and when the public is less aware of the hazard; for this reason, vulnerability to the hazard may be heightened. Furthermore, parent vortices of non-supercell tornadoes are typically more difficult to observe, using remote sensing techniques, than those of supercell tornadoes (e.g., Davis and Parker, 2014), and so these events tend to impact negatively on warning verification statistics.

Non-supercell tornadoes may be split into two types, based on the predominant morphology of the parent storm (cellular versus linear). In the following sections, an overview is presented of the typical situations in which non-supercell tornadoes occur, partitioned by the dominant morphology of the parent storm.

1.5.1 Cellular convection

Non-supercell tornadoes in cellular convection tend to occur where substantial vertical vorticity exists within the boundary layer prior to the development of convection. Such 'pre-existing' vertical vorticity is usually found along boundaries such as sea breeze fronts, drylines or topographically induced convergence zones. Convection forms preferentially over these boundaries because they also provide a source of lift. As an updraft develops above the boundary, the pre-existing vertical vorticity may be stretched to tornadic intensities by the horizontal convergence and vertical stretching beneath the updraft (Wakimoto and Wilson, 1989; Figure 1.4(b); *cf.* the tilting mechanism in Figure 1.4(a)). Tornadoes of this kind, sometimes colloquially referred to as 'landspouts' in the US, are difficult to observe by radar because they generally do not occur within a broader and deeper region of rotation within the storm. Furthermore, tornadoes occur early in the lifecycle of the associated convective cell, often even before downdrafts and precipitation have reached the ground. In an analysis of the synoptic situations associated with tornadoes in the UK, Clark and Smart (2016) found that tornadoes that were likely to fall into this type (i.e., those associated with discrete cells in weak flow situations, where convection was generally orchestrated by slow-moving boundaries) were usually very weak, the overwhelming majority being rated as T0 or T1 on the International Tornado Intensity Scale. Therefore, whilst sometimes visually impressive, these tornadoes generally pose a lesser risk to property and life than those in supercells and QLCSs.

1.5.2 Quasi-linear convective systems

Another important class of storms in which non-supercell tornadoes occur is mesoscale convective systems (MCSs) that exhibit predominantly linear structure, often called quasi-linear convective systems (QLCSs). In such systems, the updrafts and associated intense rainfall cores are predominantly organised in a line, usually with a merged downdraft area and contiguous gust front at the leading edge of the system. Triggering of new updrafts occurs along much or all of the gust front, whilst decaying cells move rearward, often resulting in a wider region of 'stratiform' rainfall at the trailing edge of the system (e.g., Houze *et al*., 1989; Figure 1.5). Although no universal criteria exist, a horizontal extent of $\geq$ 100 km in one horizontal direction is often taken as the minimum size criterion for classification as a QLCS (for example, in climatological studies of

these systems), consistent with the definition of MCSs. However, in the UK, many QLCSs have a maximum horizontal extent < 100 km; these smaller systems are also capable of producing severe weather (e.g., Earl *et al*., 2017), suggesting that such a definition may not be entirely useful. Although QLCSs are responsible only for a small minority of tornadoes in the Great Plains of the US, regional variations within the US are substantial, such that QLCSs are a more common source of tornadoes in some other areas (e.g., Smith *et al*., 2012). For example, Trapp *et al*. (2005) showed that over 50% of tornado days were associated with QLCSs in certain US States, even though only 18% of tornadoes were associated with QLCSs over the country as a whole. Similarly, there is evidence to suggest that QLCS tornadoes comprise a substantial fraction of tornadoes in some other countries. For example, in the UK, current estimates suggest that approximately 40 – 50% of tornadoes are associated with storms exhibiting linear morphologies (Mulder and Schultz, 2015; Clark and Smart, 2016).

Observational and modelling studies show that long-lived and damaging QLCSs (i.e., those producing tornadoes and severe, non-tornadic wind gusts) generally occur in environments with large vertical wind shear and large CAPE (e.g., Johns, 1993; Weisman, 1993; Trapp and Weisman, 2003; Weisman and Trapp, 2003). Some studies also note the possibility of long-lived QLCSs in lower-CAPE environments, especially where the wind field or the dynamic forcing are particularly strong (Johns, 1993; Burke and Schultz, 2004). Systems occurring in low-CAPE, strongly forced environments in the cool season appear to be an important facet of the UK convection climatology (e.g., Browning and Reynolds, 1994; Browning and Golding, 1995; Clark, 2011; Clark, 2013). Rotunno *et al*. (1988) showed that an optimal condition may exist in which horizontal vorticity associated with the ambient environmental vertical wind shear is balanced with that associated with density gradients along the leading edge of the QLCS, thereby resulting in vertically erect, deep updrafts. The applicability of this model (often referred to as the Rotunno–Klemp–Weisman, or RKW, model) beyond the high-CAPE, high-shear environments typical of the observed and simulated QLCSs in the US is unknown.

QLCS tornadoes and other instances of localised, intense wind damage are usually associated with small vortices along the leading edge of the system (e.g., Funk *et al*., 1999; Trapp and Weisman, 2003; Weisman and Trapp, 2003; Wakimoto *et al*.,

2006; Atkins *et al*., 2004; Atkins and St. Laurent, 2009a,b; Smart and Browning, 2009), variously called leading-line vortices, mesovortices, misovortices or misocyclones. These vortices are structurally distinct from a supercell's mesocyclone, in that the vortex is generally relatively shallow (occupying less than one-half to one-third of the depth of the storm) and often somewhat smaller in diameter (typically 1 – 4 km). They also tend to be less persistent than a supercell's mesocyclone and may develop very rapidly (in as little as the interval between radar scans, which is typically ~5 minutes). Radar detection of QLCS vortices is therefore comparatively difficult and, even where achieved, tends to provide little advance warning of tornadoes and a high false-alarm rate (since the large majority of QLCS vortices are non-tornadic). Trapp *et al*. (1999) found warning lead times averaging 25 minutes for the descending vortex signatures typical of supercell mesocyclones, compared to 5 minutes for the non-descending vortex signatures typical of other types of storm in general, and QLCSs in particular.

The genesis mechanism of QLCS leading-line vortices is not universally agreed upon and likely varies from event to event, but studies show tilting of horizontal vorticity to be an important mechanism, with subsequent stretching of the resulting vertical vorticity by storm updrafts. The tilting may be associated, variously, with embedded updraft maxima (Atkins and St. Laurent, 2009b) or downdraft maxima (Trapp and Weisman, 2003) along and near the leading edge of the system, and the horizontal vorticity may arise from either the ambient environmental vertical wind shear (e.g., Weisman and Davis, 1998), the presence of a rear-inflow jet some distance above ground level, or solenoidal effects at the leading edge of the cold pool (e.g., Trapp and Weisman, 2003). These details may vary with the lifecycle stage of the system as well as between individual cases. In all cases, tilting results in cyclonic–anticyclonic vortex couplets (Figure 1.6), with the cyclonic vortices tending to dominate over time due to stretching of planetary vorticity (Trapp and Weisman, 2003). In Figure 1.6, the vertical vorticity pattern depicted arises through tilting of the solenoidal horizontal vorticity (i.e., that associated with density differences at the leading edge of the cold pool), which Trapp and Weisman (2003) suggested to be dominant in the developing stage of QLCS evolution. In the mature stage, vertical shear beneath (and associated with) the rear-inflow jet (as depicted by the shear vector in the figure) was suggested to be the dominant contribution to the horizontal vorticity and, since this is of opposite sign to the solenoidal horizontal vorticity, tilting by downdrafts in the mature stage of system

evolution results in vortex couplets of opposite sign to those shown in the figure. Modelling studies suggest that strong, and therefore potentially damaging, mesovortices generally form only when the vertical wind shear is strong, especially in low levels (0 – 2.5 km AGL) (Trapp and Weisman, 2003; Atkins and St. Laurent, 2009a), and where the translational velocities of the vortices is large (as in fast-moving systems, or near the apex and rear-inflow jet of a bow echo, as described below).

In QLCSs a line-transverse circulation exists which, in non-frontal systems, is driven by buoyancy differences between updrafts, which tend to tilt rearward over the developing cold pool with time, and the cold pool itself. A mid-level low pressure area is generated, causing air to accelerate into the system from the rear. Weisman (1993) showed that this rear inflow tends to be strong, and penetrates close to the leading convective line before descending (a condition often associated with damaging winds and system longevity), in QLCSs forming in environments of large CAPE ($\geq$2000 J kg^{-1}) and large low- to mid-level wind shear ($\geq$20 m s^{-1} bulk wind difference over the lowest 2.5 – 5.0 km AGL). In some cases, the rear-to-front part of this flow (i.e., the rear inflow) is also augmented by the presence of counter-rotating, mesoscale vortices at mid-levels near the line ends (so called ‘book-end’ or ‘line-end’ vortices; e.g., Weisman and Davis, 1998). These vortices act to focus the rear inflow near the centre of the system, resulting in the development of bow echoes (Fujita, 1978; Przybylinski, 1995).

The rear inflow is particularly important in maintaining the system, by maintaining and enhancing convergence, and therefore lifting and triggering of new updrafts, at the leading edge of the system (Weisman, 1993). The rear inflow can also be associated with relatively widespread wind damage where it descends to the surface. In some cases, the damaging winds are long-lived and may extend for hundreds of kilometres along the track of the system; such cases are called ‘derechoes’ (Johns and Hirt, 1987). In bow echoes, leading line vortices producing tornadoes and other instances of localised wind damage have been found to occur preferentially near the apex or on the northern flank of the bow (e.g., Wakimoto, 1983; Przybylinski, 1988; Przybylinski and Schmocker, 1993; Przybylinski, 1995; Wakimoto *et al*., 2006); furthermore, the vortices often distort the leading edge of the system, leading to smaller-scale embedded bowing structures (e.g., Figure 1.7), which may constitute preferred regions for subsequent vortex-genesis.

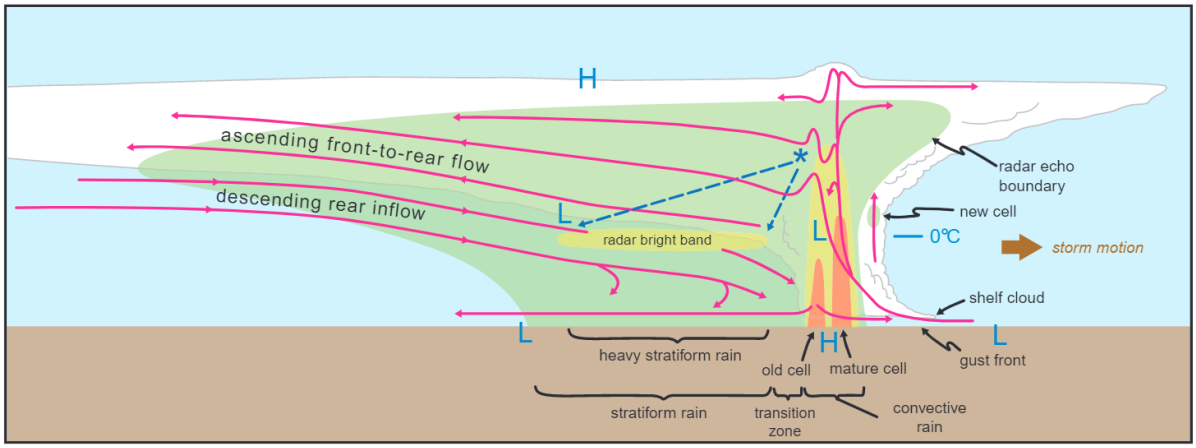

Figure 1.5: Conceptual model of a squall line with trailing stratiform area viewed in a vertical cross-section orientated perpendicular to the convective line. The green shading indicates the region of precipitation-sized hydrometeors, i.e., where radar echo is present. The yellow and orange shading indicates more intense radar echoes. Pressure minima and maxima are also indicated, as is the height of the melting level, which is located just above the height at which a radar bright band is observed. The asterisk and dashed blue arrows depict the possible trajectories of ice crystals, originating in the leading updrafts and drifting rearward through the mesoscale region of slantwise ascent, wherein growth by vapour deposition, and size sorting due to differing fall velocities, occurs (the steeper arrow depicting the trajectory of a relatively large crystal). Figure and caption reprinted with permission from Markowski and Richardson (2010) (their Figure 9.7, p. 250; originally adapted from Houze *et al*., 1989).

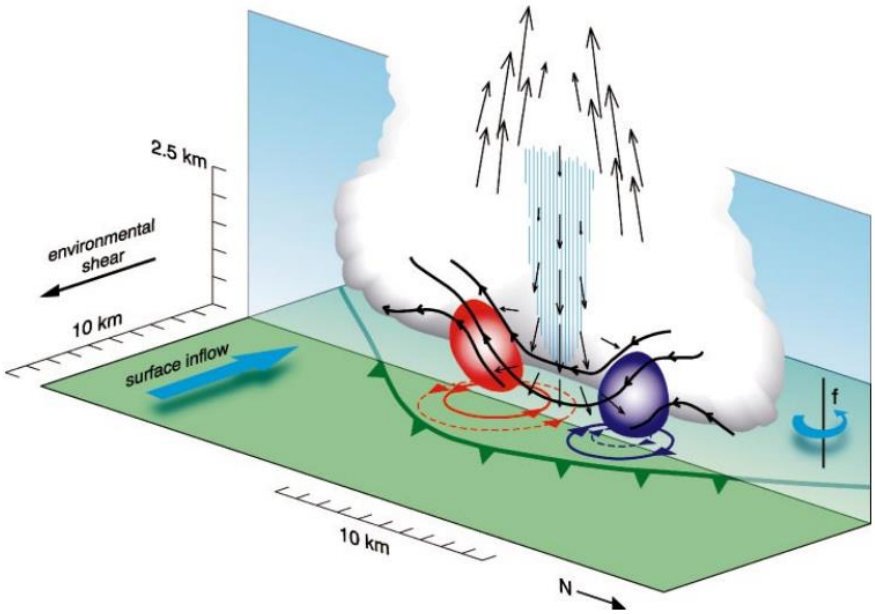

Figure 1.6: Schematic showing a proposed mechanism for low-level mesovortexgenesis within a QLCS. The green barbed line indicates the gust front, vectors are of air motion in the vertical plane, blue hatching depicts rain core, bold black lines are vortex lines in the vertical plane, and red (purple) areas indicate positive (negative) vertical vorticity in the vertical plane. Vortex lines are tilted vertically by the downdraft, resulting in a surface vortex couplet (red is cyclonic

vortex; purple is anticyclonic vortex). The future state of the vortex couplet, which results in part from the stretching of planetary vorticity (*f*), is shown by the dashed red and purple circles. Schematic represents early-QLCS-stage vortexgenesis. During the mature QLCS stage, relevant vortex lines would have opposite orientation; hence, resultant vortex couplet orientation would be reversed. From Trapp, R.J. and Weisman, M.L. (2003) Low-level mesovortices within squall lines and bow echoes. Part II: Their genesis and implications. *Mon. Wea. Rev.*, 131, 2804–2823. © American Meteorological Society. Used with permission.

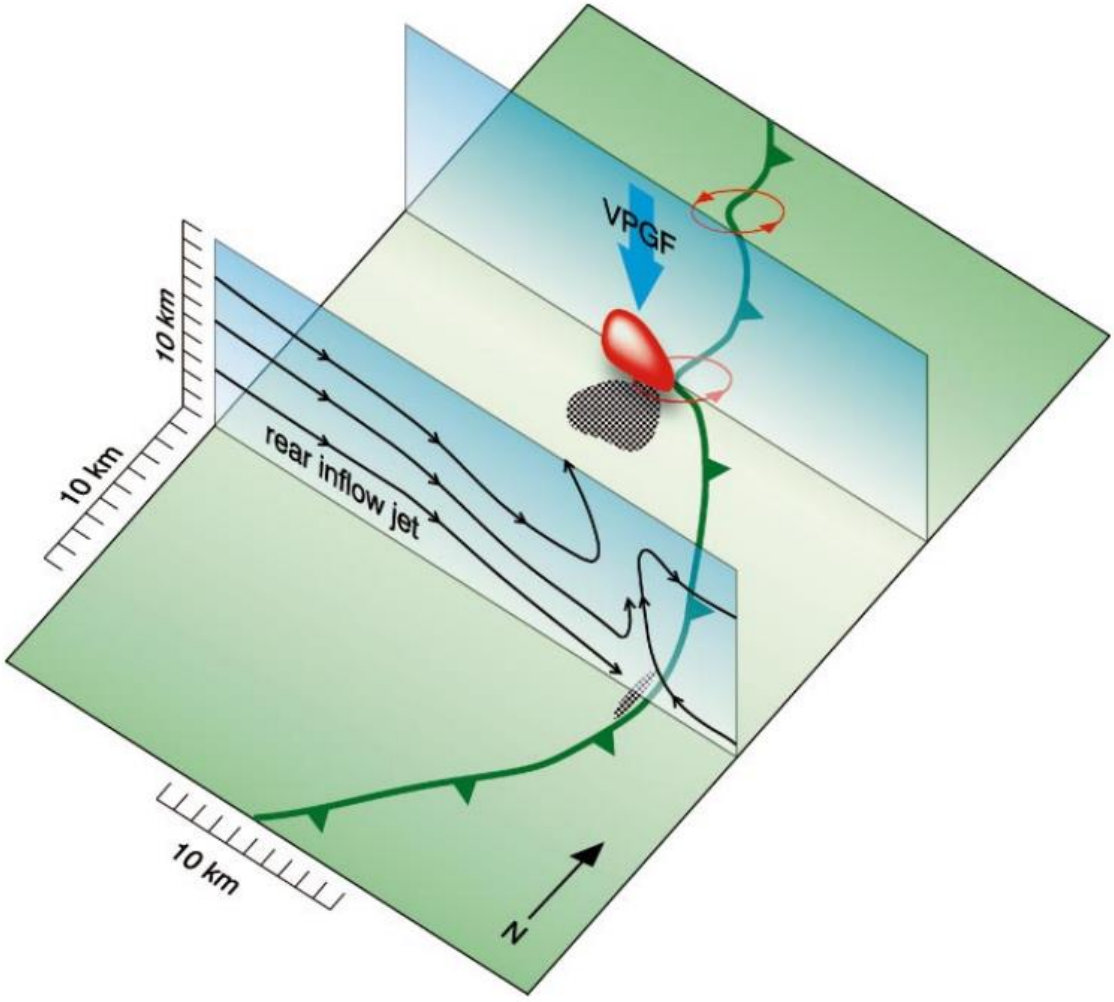

Figure 1.7: Schematic showing proposed effect of low-level mesovortices on QLCS structure and also their role in the production of damaging surface winds. The green barbed line indicates gust front and red circles denote low-level mesovortices. The red area in the vertical plane shows vertical extent and tilt of positive vertical vorticity and the corresponding mesovortex. The implication is an associated downward-directed vertical pressure-gradient force (bold blue arrow) that acts to locally eliminate or "fracture" the updraft above the mesovortex location. Black stippling on the south-southwest flank of this mesovortex shows the area of instantaneous damaging "straight line" winds driven by the vortex circulation. A lesser area, or a narrow strip of such winds, is indicated well southeast of the vortex, at the apex of the primary bowing segment. These winds are due to a rear-inflow jet that descends to the ground, represented by the black streamlines in the other vertical plane. From Trapp, R.J. and Weisman, M.L. (2003) Low-level mesovortices within squall lines and bow echoes. Part II: Their genesis and implications. *Mon. Wea. Rev.*, 131, 2804–2823. © American Meteorological Society. Used with permission.

1.6 Narrow cold frontal rainbands (NCFRs)

Kinematically and morphologically, NCFRs resemble QLCSs in non-frontal environments, and so they are often considered to be a subset of QLCSs, as mentioned in Section 1.2. For example, NCFRs often meet the QLCS size, duration and intensity criteria of Trapp *et al*. (2005), in that they comprise a persistent line of updrafts (and associated strong rainfall cores) exceeding 100 km in the along-front direction. However, the environments in which NCFRs form are markedly different to the high-CAPE, high-shear environments typical of the non-frontal QLCSs studied to date. NCFR updrafts are forced primarily by strong horizontal convergence in the boundary layer, as opposed to buoyant instability (e.g., Browning and Harrold, 1970; Matejka *et al*., 1980; Hobbs and Persson, 1982); pre-frontal environments tend to be close to moist-neutral, or only slightly unstable (e.g., Parsons, 1992; Clark, 2009). Furthermore, these systems tend to be considerably shallower than their larger-instability counterparts, with updrafts typically only 1 – 3 km deep in the UK (James *et al.*, 1978; James and Browning, 1979). Although shallow, updrafts often reach intensities of 8 – 10 m s^{-1} as low as 1 – 1.5 km AGL (e.g., Browning, 1971; Parsons, 1992), and may reach 20 m s^{-1} in extreme cases (Carbone, 1982; Rutledge, 1989). Large rainfall rates occur due to the lifting, within these updrafts, of warm, moist air that has been advected poleward within the warm conveyor belt flow of the associated extra-tropical cyclone. NCFRs frequently exhibit ‘core–gap’ morphology (i.e., precipitation cores separated by gaps with lesser, or zero, precipitation rates), with individual precipitation cores usually orientated slightly clockwise of the larger-scale frontal boundary (e.g., Hobbs and Biswas, 1979; Matejka *et al*., 1980; Hobbs and Persson, 1982; Locatelli *et al*., 1995; Wakimoto and Bosart, 2000; Jorgensen *et al*., 2003). Mechanisms proposed to explain this structure include wavelike disturbances above the surface front (Kawashima, 2007), trapped gravity waves (Brown *et al*., 1999) and horizontal shearing instability (HSI) (Carbone, 1982, 1983; Smart and Browning, 2009).

In addition to these structural differences, there are important dynamical differences between NCFRs and other types of QLCS. In particular, the thermally direct transverse circulation at a cold front, of which the leading updrafts associated with the NCFR may be considered the rising branch (Browning, 1990), is an ageostrophic response to geostrophic frontogenesis (e.g., Sawyer, 1956; Eliassen, 1962; Hoskins and

Bretherton, 1972). NCFRs form where the near-surface cold front collapses to a narrow cross-frontal scale (typical shear zone widths of order 1 – 2 km; e.g., see Figure 4(a) of Browning and Harrold, 1970), under the influence of the frontogenesis (Hoskins and Bretherton, 1972; Koch and Kocin, 1991). The transverse circulation in non-frontal QLCSs in high-CAPE environments, on the other hand, results from internal buoyancy and pressure perturbations and associated accelerations, as described in the preceding section. Substantial (>100 J kg^{-1}) pre-frontal CAPE is apparent in a minority of NCFRs (e.g., Geerts and Hobbs, 1995; Clark, 2013), suggesting that a spectrum of QLCS types may exist, from the NCFRs associated with strong frontogenesis in statically stable or very weakly unstable environments, to those in which frontogenesis and buoyancy both play a role, to those in which formation and maintenance is entirely dependent on large buoyant instability in relatively horizontally homogenous pre-convective environments (i.e., the non-frontal QLCSs described in the preceding section).

The archetypal cross-sectional structure of the classical, rearward-sloping cold front with line convection (also known as an 'ana' front; Sansom (1951)) was described by Browning (1990) (also see Figure 1.8(c)). In spite of the aforementioned dynamical differences, it strongly resembles the cross-sectional structure of a squall line as described by Houze *et al*. (1989) (*cf*. Figure 1.5). In the archetypal case strong updrafts at the leading edge of the system, which are associated with the line convection, transition to a region of gentler, rearward-sloping, slantwise ascent above the sloping frontal surface aloft. The slantwise ascent region is associated with a broader band of lighter precipitation reaching the surface behind the surface front. A rear-to-front flow exists within the cold air beneath the slantwise ascent region, with the two flows separated by a shallow zone of strong vertical wind shear coincident with the sloping frontal surface aloft. Ahead of the NCFR, a low-level jet is typically located at ~850 – 900 hPa (Browning and Pardoe, 1973; Kotroni and Lagouvardos, 1994). In the ground-relative frame of reference, winds within the low-level jet flow approximately parallel to the front, but in the front-relative frame of reference there is a rearward component of flow, with some of the air being extruded rearwards within the region of slantwise ascent aloft. This low-level jet forms part of the cyclone's warm conveyor belt flow (Harrold, 1973).

Although NCFRs are generally associated with rearward-sloping fronts conforming to the conceptual model of Browning (1990), there is considerable evidence to suggest that they also occur in some fronts exhibiting predominantly forward-relative flow (i.e., the 'kata' fronts of Sansom (1951); Figure 1.8(a)), including the split fronts of Browning and Monk (1982). Browning (1999) later noted the possibility of a spectrum of frontal types from pure ana to pure kata (Figure 1.8). It appears that an NCFR is possible over much of this spectrum of frontal types, wherever forward-relative flow locally undercuts rearward-relative flow (even in cases where the mid- to upper-level flow is more generally forward-relative; e.g., Figure 1.8(b)). In this thesis, we provide further evidence for this spectrum of frontal types, and of the occurrence of NCFRs in association with fronts exhibiting split or hybrid cross-sectional structures, in addition to classical rearward-sloping structures.

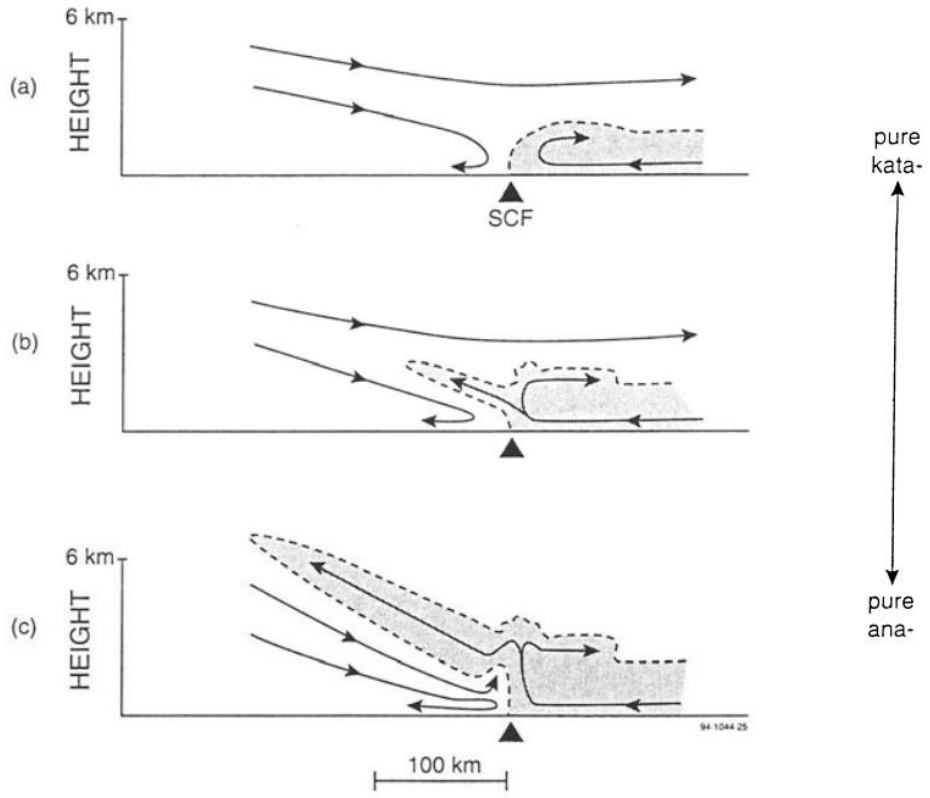

Figure 1.8: Schematic cross-sectional representations of the spectrum of cold-front types, ranging from a pure kata-cold front to a pure ana-cold front. Arrows show transverse flow relative to the front. Stippled shading bounded by dashed contour represents boundary-layer or extruded boundary-layer air. From Browning K.A. (1999) Mesoscale Aspects of Extratropical Cyclones: An Observational Perspective. In: Shapiro M.A., Grønås S. (eds) The Life Cycles of Extratropical Cyclones. American Meteorological Society, Boston, MA. © American Meteorological Society. Used with permission.

1.7 Tornadoes in NCFRs

1.7.1 NCFRs as a source of tornadoes

Over a nine-year study period ending 2012, Mulder and Schultz (2015) found that 42% of UK tornadoes were associated with storms exhibiting linear morphologies, of which NCFRs are a subset. Clark and Smart (2016) found that 34.1% of tornadoes over the period 2003–2012 were associated with NCFRs specifically. When the weakest tornadoes are excluded (those rated T0 or T1 on the International Tornado Intensity Scale), this fraction rises to ~50%. Therefore, NCFRs are the single largest source of T2 and stronger tornadoes in the UK (i.e., those capable of substantial property damage). Furthermore, NCFRs have been responsible for most, if not all, of the larger outbreaks of tornadoes in the UK since at least 1970 (Meaden, 1976, 1978, 1983; Elsom, 1983, 1985b; Turner *et al.*, 1986), including the largest outbreak on record (Meaden and Rowe, 1985; Apsley *et al*., 2016). The occurrence of a cluster of especially large outbreaks in the late 1970s and early 1980s prompted a number of case studies of these events, which showed that tornado outbreaks tended to be associated with fast moving fronts exhibiting large cross-frontal wind veer (e.g., Meaden, 1983; Elsom, 1985b; Turner *et al*., 1986; Pledgley, 1996). In some studies, it was also noted that frontal waves or rapidly developing secondary depressions were present, with tornadoes tending to occur close to the centre of the developing wave (e.g., Buller, 1980; Elsom, 1983a; Elsom, 1983b; Turner *et al*., 1986; Pike, 1993).

1.7.2 Candidate vortex- and tornado-genesis mechanisms in NCFRs

Doppler radar studies provide evidence that NCFR tornadoes are often associated with misocyclones forming along a zone of strong relative vertical vorticity, sometimes called a ‘vortex sheet’, coincident with the NCFR (Carbone, 1982, 1983; Clark and Parker, 2014). Horizontal shearing instability (HSI), in which the initially rather uniform vortex sheet breaks down (or ‘rolls up’) into discrete vertical vorticity maxima separated by braid regions with lesser vortical vorticity (e.g., Buban and Ziegler, 2016) is often suggested to be the vortex-genesis mechanism (e.g., Carbone, 1983; Smart and Browning, 2009), though this is not universally agreed upon (e.g., Mulder, 2015; Apsley *et al*., 2016). As mentioned in Section 1.5, a different mechanism, involving tilting of ambient horizontal vorticity, has been found to explain vortex-genesis along

the leading edge of QLCSs in high-CAPE, high-shear environments in the US (e.g., Trapp and Weisman, 2003; Weisman and Trapp 2003; Atkins and St. Laurent, 2009b) and this is also a plausible mechanism for vortex-genesis in NCFRs; QLCS leading-line vortices appear at least kinematically similar to NCFR misocyclones, having similar size, depth and duration characteristics. Furthermore, NCFRs tend to form in environments with large low-level (0 – 1 km and 0 – 3 km AGL) vertical wind shear (Clark, 2013), suggesting large horizontal vorticity upon which tilting may operate. However, modelling studies have yet to demonstrate, conclusively, the presence of the tilting mechanism in NCFRs. In summary, the exact mechanisms responsible for vortex-genesis within NCFRs, and the variability or otherwise of vortex-genesis mechanisms from case to case, remain largely unresolved problems.

1.7.3 Environmental influences on tornado probability in NCFRs

In contrast to tornadic and non-tornadic supercell thunderstorms, relatively little is known about the differences in environmental conditions between tornadic and non-tornadic NCFRs. Gatzen (2011) analysed the environments of cold-season NCFRs in Germany over a 10-year period ending in 2009, and found that most of the 120 detected events occurred at the cyclonically sheared flank of strong mid-level jet streaks where severe weather, including tornadoes and strong 'straight line' wind gusts, was also most likely to occur. Clark (2013) analysed environmental parameters for cool-season QLCSs in the UK over the period 2003 – 2011, 87% of which occurred in association with frontal systems. Several parameters exhibited statistically significant differences between tornadic and non-tornadic events, including the pre-frontal CAPE, cross-frontal veering of the 10 m AGL wind, cross-frontal temperature difference and the forward speed of the front in the direction normal to its length (hereafter front-normal forward motion; FNFM). Furthermore, tornadic events tended to occur underneath the core, cyclonic-shear flank, or left-exit region, of a mid-level jet, broadly in agreement with the results of Gatzen (2011). Interestingly, and contrary to the environments of tornadic versus non-tornadic supercells, pre-frontal low-level vertical wind shear apparently showed little skill in discriminating between tornadic and non-tornadic NCFRs (Gatzen, 2011; Clark, 2013); strong shear (> ~10 m s^{-1} 0 – 1 km bulk wind difference) was present in almost all cases. Apsley *et al.* (2016) conducted a reanalysis and modelling study of the exceptional NCFR tornado outbreak of 23 November 1981, showing that

tornadoes occurred along a limited subsection of the front, bounded to the north by the line of zero CAPE, and to the south by reducing vertical vorticity along the frontal boundary. Therefore, tornadoes appeared to occur where sufficient vertical vorticity and sufficient CAPE overlapped. In an analysis of nine tornado outbreaks associated with QLCSs over the UK, most of which were associated with cold fronts, Buckingham and Schultz (2020) showed that the events may be classified into two types, based on differences in the typical orientation of the front over the UK, the configuration of the upper-level trough, and the location of the parent cyclone; type 1 events exhibited meridionally orientated fronts, confluent troughs and cyclones situated to the north of the UK, whilst type 2 events were associated with zonally orientated fronts, diffluent troughs and cyclones situated to the northeast of the UK.

One issue with existing results is that, although statistically significant differences exist, the distribution of environmental parameter values for tornadic and non-tornadic events tend to show large overlap, suggesting that analysis of single parameter values, in isolation, may be of limited use for estimating tornado risk in any given NCFR. Furthermore, the physical relevance to candidate vortex- and tornado-genesis mechanisms of the various identified parameters was not explored in depth by Clark (2013), though it was suggested that the cross-frontal wind veer may be a proxy for the magnitude of vertical vorticity at the leading edge of the line—a potentially relevant factor if HSI is invoked as the vortex-genesis mechanism, since the intensity of vortices is known to be proportional to the initial vertical vorticity of the vortex strip (e.g., Buban and Ziegler, 2016). The idea that cross-frontal wind veer is a useful proxy for the vertical vorticity is supported by Clark and Parker (2014), who showed that the large cross-frontal wind veer typical of tornadic NCFRs (optimally near 90°) corresponded to larger vertical vorticity at the frontal boundary, assessed using time-composited surface observations mapped onto a 5 km grid. Clark and Parker (2014) further showed that tornadic events exhibited comparatively little reduction in wind speed across the front, and that tornadoes occurred after a period of increasing vertical vorticity. These increases occurred over a period of several hours, which is short relative to the overall lifetime of the synoptic front; it was postulated that increases in the vertical vorticity may destabilize a shear zone in which the release of HSI was formerly supressed by the horizontal strain, consistent with previous theoretical work on the stability of vortex strips in the presence of strain (e.g., Dritschel *et al*., 1991; Bishop

and Thorpe, 1994). Release of HSI is one possible explanation for the transition of an initially relatively two-dimensional NCFR (i.e., approximately uniform in the along-front direction) to one exhibiting a distinct line-echo wave pattern (LEWP; Nolen, 1959), owing to the development of a string of vortices along the vorticity strip at the surface front i.e., vortex sheet roll-up (Figures 1.9 and 1.10). The characteristic wave-like pattern is produced by local distortion of the NCFR by the flow in the vicinity of each vortex (e.g., Smart and Browning, 2009).

Since the near-surface pre-frontal wind vector is often approximately aligned with the front (e.g., Browning *et al*., 1998; Clark and Parker, 2014), cross-frontal wind veer near 90°, as found by Clark and Parker (2014) in tornadic NCFRs, suggests post-frontal winds with a large front-normal component, directed towards the warm air (i.e., rear-to-front flow, with respect to the direction of advance of the NCFR). The FNFM was found by Clark and Parker (2014) to be strongly positively correlated with this front-normal flow component on the cold side of the front, and so these results are consistent with Clark's (2013) finding that tornadic fronts exhibited larger FNFM. The relevance of the magnitude of the front-normal component of post-frontal flow to the vortex- and tornado-genesis mechanisms remains unclear, though it could suggest the presence of a strong system-scale rear-inflow jet, a feature that has been documented in other intense NCFRs (e.g., Browning *et al*., 1997). Various authors have suggested that strong rear-inflow may be dynamically important in that it transports dry air, sometimes of high potential vorticity, from the post-frontal environment into the front-transverse circulation; where this dry air undercuts precipitation falling from the slantwise ascent region above the sloping frontal boundary aloft, cooling by evaporation or sublimation may be enhanced, leading to increases in the cross-frontal temperature gradient and a strengthening of the front-transverse flow (e.g., Koch and Kocin, 1991; Browning and Reynolds, 1994; Browning and Golding, 1995).

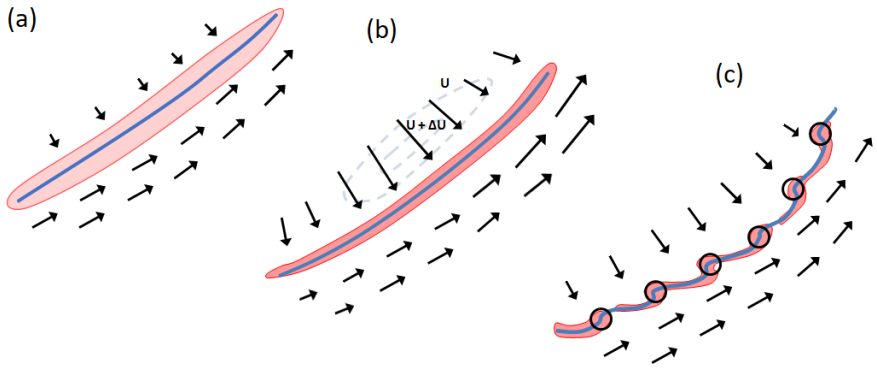

Figure 1.9: Schematic illustrating the release of HSI in a vertical vorticity strip at a surface cold front, following Clark and Parker (2014), and anticipating some of the results of the current study. (a) A vertical vorticity strip at a trailing cold front, in which the release of HSI is largely supressed by the horizontal strain (strain > 0.25 x vorticity; Dritschel *et al*., 1991); (b) The vorticity strip narrows further, under the influence of enhanced cross-frontal confluence associated, for example, with an increase in the front-normal component of flow behind the front (as depicted here by the light grey dashed contours), or intensification of a strain field in which the axis of dilatation is orientated approximately along the front. Although the vertical vorticity increases within the narrowing strip, the release of HSI is still prevented at this stage, due to corresponding increases in the horizontal strain (in particular, the cross-frontal confluence). This allows an intense and very narrow (~1 – 4 km width) vertical vorticity strip to develop; (c) A subsequent reduction in the horizontal strain allows release of HSI within the now-intense vortex strip, resulting in the rapid development of a string of cyclonic vortices (black circles) along the front (i.e., vortex sheet roll up).

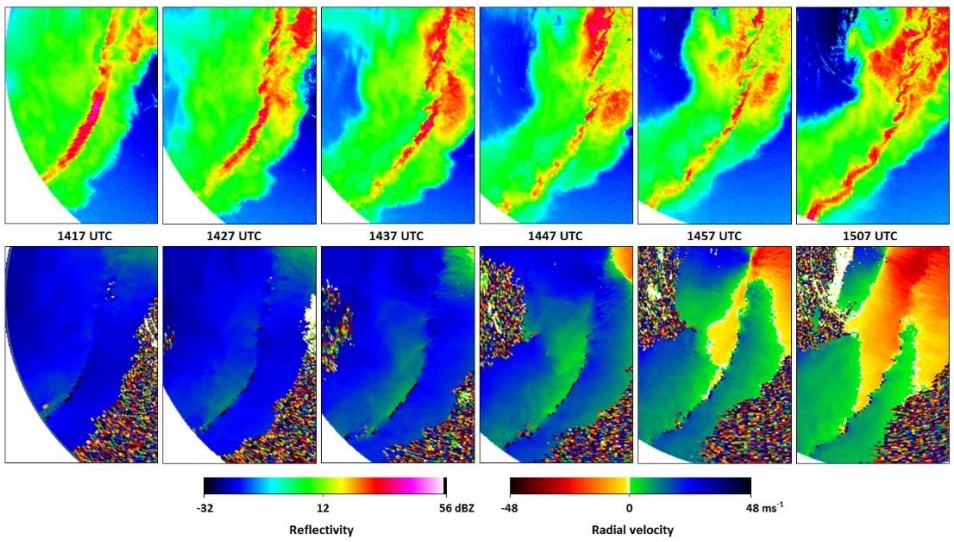

Figure 1.10: Transition of an initially relatively two-dimensional vertical vorticity sheet at an NCFR (left) to one exhibiting marked wave-like structures (right), likely due to the release of HSI, as observed by the Ingham (Lincolnshire) Doppler radar on 25 January 2014. Top row: radar reflectivity factor (dB*Z*). Bottom row: radial velocity (positive values indicate a component of flow towards the radar). Each panel has width 71 km, and the domain moves with the NCFR over the period shown. The radar location is near the top, right-hand corner of the panels at 1457 and 1507 UTC. This NCFR produced several tornadoes and numerous instances of localized, non-tornadic wind damage as it moved southeast over England.

1.8 Open questions in the literature concerning NCFR tornadoes

In the above discussion, the current state of knowledge about tornadoes from NCFRs has been outlined, and this has been set in context by comparison with the situation for tornadoes associated with supercell thunderstorms. It is apparent that understanding of NCFR tornado environments, leading-line vortex-genesis mechanisms, and tornado-genesis mechanisms lags behind that of supercells. Gaps in our current understanding, which hinder attempts to forecast tornado risk in NCFRs, may be summarised as follows:

- **Large-scale environments supportive of tornadic NCFRs**. Other than the fact that tornadoes occur in association with NCFRs which, by definition, occur along frontal systems associated with extratropical cyclones (specifically, cold fronts and occlusions), we know little about the kinds of large-scale environments typically associated with tornadoes and tornado outbreaks. No conceptual models exist of the synoptic- and meso-scale settings of tornadic cold fronts. It is not clear how tornadic events relate to existing models of frontal type, or cyclone paradigms and lifecycle models, or whether the situations associated with tornadoes are even synoptically evident (as compared to those not associated with tornadoes). Increased understanding in these areas would allow for improved operational recognition of the large-scale setups conducive to tornadic NCFRs.

- **Environmental parameters**. Unlike for supercells, it is still not clear whether there exist certain environmental parameters that can reliably distinguish between tornadic and non-tornadic NCFRs, though existing studies have identified several candidate parameters with promising results. The concept of environmental parameters is more difficult to apply to NCFRs than to supercells, since the pre- and post-frontal environments typically differ markedly (compared to the relatively homogeneous environments in which supercells often form, at least on the mesoscale). How should environmental parameters be defined? For example, is analysis of the pre- or post-frontal environment more relevant? In spite of these difficulties and open questions, existing studies

suggest that the concept of environmental parameters is likely to be useful in the case of NCFRs. Identification of environmental parameters that have skill in distinguishing between tornadic and non-tornadic NCFRs would improve operational recognition of tornado-favourable environments, could allow for more quantitative measures of tornado risk, and could pave the way for construction of global climatologies of NCFR tornado-favourable environments, and analysis of possible future changes in these environments using climate models.

- **Vortex- and tornado-genesis mechanisms**. No universal agreement exists as to the most likely vortex-genesis mechanisms within NCFRs. Candidate mechanisms include HSI, vertical vorticity stretching (as for other types of non-supercell tornadoes e.g., Wakimoto and Wilson, 1989; Figure 1.4(b)), and tilting of ambient horizontal vorticity (Figure 1.6). Little is known about the substructure of NCFR vortices and how, where and when tornadoes form within these vortices. Related to this issue, little is known about the differences (for example as observed by radar) between tornadic and non-tornadic NCFR vortices (or even damaging and non-damaging NCFR vortices, more generally). Improved understanding in these areas would facilitate operational recognition of potential tornado parent vortices in NCFRs, using Doppler radar data, and the distinction between tornadic and non-tornadic vortices, both of which would be useful for nowcasting during NCFR events.

1.9 Aims of the current work

The above knowledge gaps and open questions motivate the current work. The aim of this thesis is to further the understanding of NCFR tornado environments by analysis of a large set of tornadic and non-tornadic NCFRs. It is anticipated that the results will provide a methodology for the forecasting of NCFR tornado risk, and a framework for improved operational recognition of tornado-favourable environments. This is particularly important considering that NCFRs are the single largest source of damaging tornadoes in the UK, and given that tools and techniques developed for supercell

tornadoes are unlikely to yield satisfactory results for NCFR tornadoes. In detail the thesis will provide the following:

- A list of environmental variables that have skill in discriminating between tornadic and non-tornadic events, isolating those that have the best skill for discriminating between event types. This approach is analogous to the studies that sought to find statistically significant differences in near-storm environmental parameters (e.g., 0 – 1 km storm-relative helicity, boundary layer relative humidity) between tornadic and non-tornadic supercells. This builds on the work of Clark and Parker (2014) but uses a much larger sample of tornadic and non-tornadic NCFRs, in order to provide increased confidence in the generality of the results. A measure of tornado probability will be derived, depending on the combined value of the two parameters found to yield the best discrimination between tornadic and non-tornadic events. Questions to be addressed include: *Do the results of Clark and Parker (2014) hold true for a larger set of cases? Are there any other attributes of tornadic NCFRs that set them apart from non-tornadic NCFRs (in a statistically significant sense)?*

- Conceptual models describing the synoptic- and meso-scale situations commonly associated with tornadic NCFRs in the UK and Ireland, showing how the timing and location of tornadoes relates to the large-scale flow pattern and its evolution in each situation. This should facilitate improved operational recognition of the environments favourable for tornadoes, especially when used in conjunction with the tornado probability metric described above. Questions to be addressed include: *Are the synoptic and mesoscale situations in which tornadic fronts occur distinct from non-tornadic fronts? Can these be recognised ahead of time? Does the location relative to the parent cyclone, the developmental stage of the parent cyclone, or the type of parent cyclone have any bearing on tornado risk? Are frontal waves important, as suggested by some existing case studies?*

- For one case belonging to each of the two situations found to be most commonly associated with tornadic NCFRs, high-resolution model simulations and observations will be used to explore the processes culminating in tornado-genesis along the front, and to provide insights into the vortex-genesis mechanisms. The analysis will focus on links across spatiotemporal scales, demonstrating how the smaller-scale processes are orchestrated by various features of the larger-scale flow field. The physical relevance of the identified environmental parameters will be investigated. Whilst the 1.5 km grid-length models (and even the nested 300 m grid-length model) are insufficient for a complete investigation of the vortex- and tornado-genesis processes, the case studies will provide some additional insights into the likely vortex-genesis mechanisms within NCFRs, in addition to improving understanding of the meso-γ-scale and miso-scale structure of the NCFR near to developing miso-vortices and the typical sub-structure of the miso-vortices themselves. Questions to be addressed include: *Does miso-cyclogenesis occur along preferred sections of a front, and if so, how is the spatiotemporal distribution of the resulting vortices orchestrated by the larger scale (i.e., synoptic- and meso-scale) situation? What is the typical structure and evolution of misocyclones and does this tell us anything about likely tornado-genesis mechanisms?*

Collectively, the results will allow forecasters to recognise situations potentially favourable for NCFR tornadoes, potentially up to several days ahead of an event, in the same way as is already possible for supercells and supercell tornado environments. In the arena of nowcasting, results should improve operational recognition of the signatures typically associated with developing miso-scale vortices in tornadic NCFRs, where tornado risk is maximised. Finally, insights provided by the high-resolution model simulations will help to guide the direction of future research into vortex-genesis and tornado-genesis mechanisms in NCFRs.

1.10 Strategy employed and novel aspects of the work

Firstly, a large set of NCFR events is identified, by manual inspection of surface analysis charts and archived composite radar imagery over the UK and Ireland (the latter are available at 30-minute intervals from late-2003). Simple thresholds for NCFR longevity, intensity and along-front length are used, following the methodology of Trapp et al. (2005) and Clark (2013). A manual approach is adopted for this task owing to the difficulties associated with automated detection of NCFRs which may, for example, be embedded in wide frontal rainbands, be intermittent in time and space, and be difficult to detect at larger range from the radar owing to their typical small width and shallow depth. Events are classified as tornadic and non-tornadic by analysis of the TORRO tornado database; where one or more tornadoes can be attributed unambiguously to one of the identified NCFRs, that NCFR is classed as tornadic. A high-tornadic class, comprising NCFRs that produced ≥7 tornadoes, is also defined. The end result is a set of 114 events (18 high-tornadic, 26 tornadic, and 70 non-tornadic), which is much larger than any previously analysed set of NCFR cases in the UK.

Secondly, statistically significant differences are sought between the environments of high-tornadic, tornadic and non-tornadic events, using ECMWF interim (hereafter ERAi) reanalyses, which use a 0.75° grid. 22 environmental parameters are analysed, selected on the basis of previous studies (e.g., Gatzen, 2011; Clark, 2013) and considering the candidate vortex-genesis mechanisms in QLCSs, generally. A novel ‘bulk measures’ approach, involving analysis of parameter values at specified points in the air masses on either side of each front, is developed for this purpose. A composite parameter describing NCFR tornado risk is developed using parameters showing the best ability to differentiate between tornadic and non-tornadic events, and the spatiotemporal variation of this parameter is investigated in individual cases, demonstrating an ability to pinpoint regions (along the front) and time periods of maximum tornado risk. This constitutes a potentially significant advance for the forecasting of tornado risk in NCFRs, since no other tools exist to pinpoint particular regions and time periods of tornado risk in any given front (with the possible exception of the results of Apsley et al. (2016), which are however limited to a single case, so the generality or otherwise of the results remains unknown). An analysis of exceptions (i.e., tornadic cases in which the composite parameter value was relatively low) is also

conducted, to provide insights into the limitations of this parameter as a forecasting tool and possible tornado-genesis failure modes.

Tornadic NCFRs are then split into identifiable sub-types, based on inspection of surface analysis charts and the ERAi fields for each tornadic NCFR; the typical setup and evolution in each is described by construction of composite analyses from the ERAi data, at various analysis times relative to the reported times of tornadoes. The aim of this part of the work is to identify synoptic- and meso-α-scale features in the vicinity of the NCFR which could be used to aid operational recognition of situations with high tornado risk (e.g., by recognition of similar patterns within forecast fields from global numerical weather models). This forms the basis of the larger-scale aspects of the conceptual models developed for each type of tornadic NCFR, as described below, which may be used in conjunction with the composite parameter described in the previous paragraph.

Finally, a detailed, multiscale analysis of one example of each identified tornadic NCFR type is conducted. The aim is to identify links between the different scales, demonstrating how the identified larger-scale features orchestrate smaller-scale processes relevant to tornado-genesis (and, therefore, how they ultimately dictate the timing and location of tornadoes), and to provide insights into the likely vortex-genesis mechanisms. These studies draw mainly on analysis of output of high-resolution, convection-permitting numerical weather models (1.5 km grid length), but also refer to the ERAi data, surface analysis charts, and surface and radar observations. For one case, a nested simulation with 300 m grid spacing in the inner domain is run, to provide more detailed insights into the structure and evolution of miso-scale vortices which, as suggested by comparison with radar data and the reported location of tornadoes, constitute potential tornado parent vortices. Detailed conceptual models are constructed for each type, based on both the large-scale analysis described in the previous paragraph, and the results of the in-depth case studies.

1.11 Structure of the thesis

The remainder of the thesis is structured as follows. In Chapter 2, the sample of tornadic and non-tornadic NCFRs is defined and environmental parameters are assessed and

compared for tornadic and non-tornadic events. The large-scale patterns most often associated with tornadic NCFRs are identified and outlined using ERAi reanalysis data and surface analyses. In Chapter 3, a detailed study of one case belonging to the frontal wave tornadic NCFR sub-type is described, using a set of high-resolution simulations, including the nested 300 m grid-length model. A conceptual model for tornadic NCFRs in frontal waves is developed, and the small-scale structure of the NCFR near to miso-scale vortices is described using the model output and observations. In Chapter 4, a detailed study of one case belonging to the north-westerly flow type of tornadic NCFR is performed, using output from a model with grid spacing of 1.5 km and available observations, including those from a Doppler radar. A summary of the results, including a critical discussion of the methodology, further interpretation and discussion of the results, and suggested directions for future work, are presented in Chapter 5.

Chapters 2, 3, and 4 constitute three papers prepared for and/or published in the *Quarterly Journal of the Royal Meteorological Society*; at the time of writing, the first and second papers (Chapters 2 and 3) are published, and the third paper (Chapter 4) is prepared but not yet submitted for peer review. Chapters 2, 3 and 4, as shown in this thesis, may differ from the versions accepted or potentially accepted for publication in the *Quarterly Journal of the Royal Meteorological Society*.

References

AMS. 2021. *Glossary of Meteorology*. Available online: https://glossary.ametsoc.org/wiki/Tornado [viewed 13 July 2021].

Apsley M, Mulder KJ, Schultz DM. 2016. Reexamining the United Kingdom's greatest tornado outbreak: forecasting the limited extent of tornadoes along a cold front. *Wea. Forecasting* **31**: 853–875.

Atkins NT, Arnott JM, Przybylinski RW, Wolf RA, Ketcham BD. 2004. Vortex structure and evolution within bow echoes. Part I: Single-Doppler and damage analysis of the 29 June 1998 derecho. *Mon. Wea. Rev*. **132**: 2224–2242.

Atkins NT, St. Laurent M. 2009a. Bow echo mesovortices. Part I: Processes that influence their damaging potential. *Mon. Wea. Rev.* **137**: 1497–1513.

Atkins NT, St. Laurent M. 2009b. Bow echo mesovortices. Part II: Their genesis. *Mon. Wea. Rev.* **137**: 1514–1532.

Betten DP, Biggerstaff MI, Wicker LJ. 2017. A trajectory mapping technique for the visualization and analysis of three-dimensional flow in supercell storms. *J. Atmos. and Oceanic Tech.* **34**: 33–49.

Billett H. 1914. The South Wales tornado of October 27, 1913. With a note on remarkable pressure oscillations observed on August 14, 1914. *Geophysical Memoirs* **11**. HMSO, London, UK.

Bishop CH, Thorpe AJ. 1994. Frontal wave stability during moist deformation frontogenesis. Part II: The suppression of nonlinear wave development. *J. Atmos. Sci*. **51**: 874–888.

Bluestein HB, Parks CR. 1983. A synoptic and photographic climatology of low-precipitation severe thunderstorms in the southern Plains. *Mon. Wea. Rev.* **111**: 2034–2046.

Brown PR, Meaden GT. 2016. Historical tornadoes in the British Isles. *Extreme Weather. Forty years of the Tornado and Storm Research Organisation (TORRO),* R. K. Doe, Ed., Wiley Blackwell, Chichester, UK, 17–30.

Brown RA, Burgess DW, Carter JK, Lemon LR, Sirmans D. 1975. NSSL dual-Doppler radar measurements in tornadic storms: a preview. *Bull. Amer. Meteor. Soc.* **56**: 524–526.

Brown MJ, Locatelli JD, Stoelinga MT, Hobbs PV. 1999. Numerical modelling of precipitation cores on cold fronts. *J. Atmos. Sci*. **56**: 1175–1196.

Browning KA. 1965. Some inferences about the updraft within a severe local storm. *J. Atmos. Sci*. **22**: 669–677.

Browning KA. 1971. Radar measurements of air motion near fronts. *Weather* **26**: 320–340.

Browning KA. 1990. Organization of clouds and precipitation in extratropical cyclones. In *Extratropical Cyclones, Erik Palmen Memorial Volume,* C. W. Newton and E. O. Holopainen, Eds., Amer. Meteor. Soc., 129–153.

Browning KA. 1999. Mesoscale aspects of extratropical cyclones: An observational perspective. In *The Life Cycles and Extratropical Cyclones,* M. A. Shapiro *et al*., Eds., Amer. Meteor. Soc., Boston, MA., 265–283.

Browning KA, Golding BW. 1995. Mesoscale aspects of a dry intrusion within a vigorous cyclone. *Q. J. Roy. Meteor. Soc.* **121**: 463–493.

Browning KA, Harrold TW. 1970. Air motion and precipitation growth at a cold front. *Q. J. Roy. Meteor. Soc.* **96**: 369–389.

Browning KA, Jerrett D, Nash J, Oakley T, Roberts NM. 1998. Cold frontal structure derived from radar wind profilers. *Meteor. Appl.* **5**: 67–74.

Browning KA, Ludlam FH. 1962. Airflow in convective storms. *Q. J. Roy. Meteor. Soc.* **88**: 117–135.

Browning KA, Monk GA. 1982. A simple model for the synoptic analysis of cold fronts. *Q. J. Roy. Meteor. Soc.* **108**: 435–452.

Browning KA, Pardoe CW. 1973. Structure of low-level jet streams ahead of mid-latitude cold fronts. *Q. J. Roy. Meteor. Soc.* **99**: 619–638.

Browning KA, Reynolds R. 1994. Diagnostic study of a narrow cold-frontal rainband and severe winds associated with a stratospheric intrusion. *Q. J. Roy. Meteor. Soc.* **120**: 235–257.

Buban MS, Ziegler CL. 2016. The formation of small-scale atmospheric vortices via horizontal shearing instability. *J. Atmos. Sci.* **73**: 2061–2084.

Buckingham TJ, Schultz DM. 2020. Synoptic-scale environments and precipitation morphologies of tornado outbreaks from quasi-linear convective systems in the United Kingdom. *Wea. Forecasting* **35**: 1733–1759.

Buller PSJ. 1980. Tornado damage in Maidenhead, 9 December 1979. *J. Meteor. (UK)* **5**: 201–206.

Burke PC, Schultz DM. 2004. A 4-yr climatology of cold-season bow echoes over the continental United States. *Wea. Forecasting* **19**: 1061–1074.

Carbone RE. 1982. A severe frontal rainband. Part I. Stormwide hydrodynamic structure. *J. Atmos. Sci.* **39**: 258–279.

Carbone RE. 1983. A severe frontal rainband. Part II. Tornado parent vortex circulation. *J. Atmos. Sci.* **40**: 2639–2654.

Clark MR. 2009. The southern England tornadoes of 30 December 2006: Case study of a tornadic storm in a low CAPE, high shear environment. *Atmos. Res.* **93**: 50–65.

Clark MR. 2013. A provisional climatology of cool-season convective lines in the UK. *Atmos. Res.* **123**: 180–196.

Clark M, Smart D. 2016. Supercell and non-supercell tornadoes in the United Kingdom and Ireland. *Extreme Weather. Forty years of the Tornado and Storm Research Organisation (TORRO),* R. K. Doe, Ed., Wiley Blackwell, Chichester, UK, 31–59.

Coffer BE, Parker MD, Dahl JML, Wicker LJ, Clark AJ. 2017. Volatility of tornadogenesis: an ensemble of simulated nontornadic and tornadic supercells in VORTEX2 environments. *Mon. Wea. Rev.* **145**: 4605–4625.

Davies-Jones RP, Burgess DW, Foster M. 1990. Test of helicity as a tornado forecast parameter. *Preprints, 16th Conference on Severe Local Storms, Kananaskis Park, AB, Canada.* American Meteorological Society, 588–592.

Davis JM, Parker MD. Radar climatology of tornadic and nontornadic vortices in high-shear, low-CAPE environments in the mid-Atlantic and southeastern United States. *Wea. Forecasting* **29**: 828–853.

Doswell CA III. 1987. The distinction between large-scale and mesoscale contribution to severe convection: A case study example. *Wea. Forecasting* **2**: 3–16.

Doswell CA III, Brooks HE, Maddox RA. 1996. Flash flood forecasting: an ingredients-based methodology. *Wea. Forecasting* **11**: 560–581.

Dritschel DG, Haynes PH, Juckes MN, Shepherd TG. 1991. The stability of a two-dimensional vorticity filament under uniform strain. *J. Fluid. Mech.* **230**: 647–665.

Earl N, Dorling S, Starks M, Finch R. 2017. Subsynoptic-scale features associated with extreme surface gusts in UK extratropical cyclone events. *Geophysical Research Letters* **44**: 3932–3940.

Eliassen A. 1962. On the vertical circulation in frontal zones. *Geofys. Publ. Oslo* **24**: 147–160.

Elsom DM. 1983a. Tornado at Eynsham, Oxfordshire, on 13 January 1983: Problems of interpretation. *J. Meteor. (UK)* **8**: 305–311.

Elsom DM. 1983b. Tornado at Bicester, Oxfordshire, on 21 September 1982. *J. Meteor. (UK)* **8**: 141–148.

Elsom DM. 1985a. Tornadoes in Britain: where, when and how often. *J. Meteor. (UK)* **10**: 203–211.

Elsom DM. 1985b. Tornadoes formed in association with a cold front: the example of the outbreak of 21 tornadoes on 8 February 1984. *J. Meteor. (UK)* **10**: 4–15.

Elsom DM, Meaden GT. 1984. Spatial and temporal distributions of tornadoes in the United Kingdom 1960-1982. *Weather* **39**: 317–323.

Elsom DM, Meaden GT, Reynolds DJ, Rowe MW, Webb, JDC. 2001. Advances in tornado and storm research in the United Kingdom and Europe: the role of the Tornado and Storm Research Organisation. *Atmos. Res.* **56**: 19–29.

Forbes GS, Wakimoto RM. 1983. A concentrated outbreak of tornadoes, downbursts and microbursts, and implications regarding vortex classification. *Mon. Wea. Rev.* **111**: 220–235.

Fujita T. 1965. Formation and steering mechanisms of tornado cyclones and associated hook echoes. *Mon. Wea. Rev.* **93**: 67–78.

Fujita TT. 1978. Manual of downburst identification for project NIMROD. SMRP Research Paper 156, University of Chicago.

Funk TW, Darmofal KE, Kirkpatrick JD, DeWald VL, Przybylinski RW, Schmocker GK, Lin Y. 1999. Storm reflectivity and mesocyclone evolution associated with the 15 April 1994 squall line over Kentucky and southern Indiana. *Wea. Forecasting* **14**: 976–993.

Gatzen C. 2011. A 10-year climatology of cold-season narrow cold-frontal rainbands in Germany. *Atmos. Res.* **100**: 366–370.

Geerts B, Hobbs PV. 1995. A squall-like narrow cold-frontal rainband diagnosed by combined thermodynamic and cloud microphysical retrieval. *Atmos. Res.* **39**: 287–311.

Harrold TW. 1973. Mechanisms influencing the distribution of precipitation within baroclinic disturbances. *Q. J. Roy. Meteor. Soc*. **99**: 232–251.

Hobbs PV, Biswas KR. 1979. The cellular structure of narrow cold-frontal rainbands. *Q. J. Roy. Meteor. Soc*. **105**: 723–727.

Hobbs PV, Persson P. 1982. The mesoscale and microscale structure and organization of clouds and precipitation in midlatitude cyclones. Part V: The substructure of narrow cold-frontal rainbands. *J. Atmos. Sci*. **39**: 280–295.

Hoskins BJ, Bretherton FP. 1972. Atmospheric frontogenesis models: mathematical formulation and solution. *J. Atmos. Sci.* **29**: 11–37.

Houze RA Jr, Biggerstaff MI, Rutledge SA, Smull BF. 1989. Interpretation of Doppler weather radar displays of midlatitude mesoscale convective systems. *Bulletin of the American Meteorological Society* **70**: 608–619.

Houze RA, Hobbs PJ Jr., Biswas KR, Davis WM. 1976. Mesoscale rainbands in extratropical cyclones. *Mon. Wea. Rev*. **104**: 868–878.

James PK, Browning KA. 1979. Mesoscale structure of line convection at surface cold fronts. *Q. J. Roy. Meteor. Soc*. **105**: 371–382.

James PK, Browning KA, Gunawardana R, Edwards JA. 1978. A case of line convection observed by radar using a high resolution colour display. *Weather* **33**: 212–214.

Johns RH. 1993. Meteorological conditions associated with bow echo development in convective storms. *Wea. Forecasting* **8**: 294–299.

Johns RH, Doswell CA III. 1992. Severe local storms forecasting. *Wea. Forecasting* **7**: 588–612.

Johns RH, Hirt WD. 1987. Derechos: widespread convectively induced windstorms. *Wea. Forecasting* **2**: 32–49.

Jorgensen DP, Pu X, Persson POG, Tao W. 2003. Variations associated with cores and gaps of a Pacific narrow cold frontal rainband. *Mon. Wea. Rev.* **131**: 2705–2729.

Kawashima M. 2007. Numerical study of precipitation core-gap structure along cold fronts. *J. Atmos. Sci.* **64**: 2355–2377.

Kelly DL, Schaefer JT, McNulty RP, Doswell CA III. 1978. An augmented tornado climatology. *Mon. Wea. Rev.* **106**: 1172–1183.

Kirk P. 2007. UK tornado climatology, 1980–2004. *Int. J. Meteorol. (UK)* **32**: 158–172.

Kirk PJ. 2014. An updated tornado climatology for the UK: 1981–2010. *Weather* **69**: 171–175.

Kirk P, Prosser T, Smart D. 2016. Tornadoes in the United Kingdom and Ireland: frequency and spatial distribution. *Extreme Weather. Forty years of the Tornado and Storm Research Organisation (TORRO),* R. K. Doe, Ed., Wiley Blackwell, Chichester, UK, 61–76.

Klemp JB. 1987. Dynamics of tornadic thunderstorms. *Ann. Rev. Fluid Mech*. **19**: 369–402.

Koch SE, Kocin PJ. 1991. Frontal contraction processes leading to the formation of an intense narrow rainband. *Meteorology and Atmospheric Physics* **46**: 123–154.

Kotroni V, Lagouvardos K. 1994. Dynamic structure and evolution of the prefrontal boundary layer: Three case studies of FRONTS 87. *Atmos. Res.* **35**: 55–70.

Lacy RE. Tornadoes in Britain during 1963–6. *Weather* **23**: 116–124.

Lamb HH. 1957. Tornadoes of May 21, 1950. *Geophysical Memoirs* **99**. HMSO, London, UK.

Lee BD, Wilhelmson RB. 1999. The numerical simulation of nonsupercell tornadogenesis. Part III: Parameter tests investigating the role of CAPE, vortex sheet strength, and boundary layer vertical shear. *J. Atmos. Sci.* **57**: 2246–2261.

Lemon LR, Doswell CA III. 1979. Severe thunderstorm evolution and mesocyclone structure as related to tornadogenesis. *Mon. Wea. Rev.* **107**: 1184–1197.

Locatelli JD, Martin JE, Hobbs PV. 1995. Development and propagation of precipitation cores on cold fronts. *Atmos. Res.* **38**: 177–206.

Matejka TJ, Houze RA Jr., Hobbs PV. 1980. Microphysics and dynamics of clouds associated with mesoscale rainbands in extratropical cyclones. *Q. J. R. Meteor. Soc.* **106**: 29–56.

Markowski PM, Richardson YP. 2009. Tornadogenesis: our current understanding, forecasting considerations, and questions to guide future research. *Atmos. Res.* **93**: 3–10.

Markowski P, Richardson Y. 2010. *Mesoscale Meteorology in Midlatitudes*. Chichester, UK: Wiley Blackwell.

Markowski PM, Rasmussen EN, Straka JM. 2002. Direct surface thermodynamic observations within the rear-flank downdrafts of nontornadic and tornadic supercells. *Mon. Wea. Rev.* **130**: 1692–1721.

McNulty RP. 1978. On upper tropospheric kinematics and severe weather occurrence. *Mon. Wea. Rev.* **106**: 662–672.

Meaden GT. 1976. Tornadoes in Britain: their intensities and distribution in space and time. *J. Meteor. (UK)* **1**: 242–251.

Meaden GT. 1978. Tornadoes in eastern England on 3 January 1978. *J. Meteor. (UK)* **3**: 225–229.

Meaden GT. 1983. Tornadoes and severe squalls of 21 September 1982. *J. Meteor. (UK)* **8**: 148–151.

Meaden GT. 1985. *A study of tornadoes in Britain with assessments of the general tornado risk potential and the specific risk potential at particular regional sites.* Health and Safety Executive, H.M. Nuclear Installations Inspectorate, and Tornado and Storm Research Organisation, Oxford, UK.

Meaden GT. 2016. Researching extreme weather in the United Kingdom and Ireland: The History of the Tornado and Storm Research Organisation, 1974 – 2014. *Extreme Weather. Forty years of the Tornado and Storm Research Organisation (TORRO),* R. K. Doe, Ed., Wiley Blackwell, Chichester, UK, 1–16.

Meaden GT, Kochev S, Kolendowicz L, Kosa-Kiss A, Marcinoniene I, Sioutas M, Tooming H, Tyrrell J. 2007. Comparing the theoretical versions of the Beaufort scale, the T-Scale and the Fujita scale. *Atmos. Res.* **83**: 446–449.

Meaden GT, Rowe MW. 1985. The great tornado outbreak of 23 November 1981 in which North Wales, central and eastern England had 105 known tornadoes in about five hours. *J. Meteor. (UK)* **10**: 295–300.

Moller AR, Doswell CA III, Foster MP, Woodall GR. 1994. The operational recognition of supercell thunderstorm environments and storm structures. *Wea. Forecasting* **9**: 327–347.

Mulder KJ, Schultz DM. 2015. Climatology, storm morphologies, and environments of tornadoes in the British Isles: 1980–2012. *Mon. Wea. Rev.* **143**: 2224–2240.

Nolen RH. 1959. A radar pattern associated with tornadoes. *Bull. Amer. Meteor. Soc.* **40**: 277–279.

Parsons DB. 1992. An explanation for intense frontal updrafts and narrow cold-frontal rainbands. *J. Atmos. Sci.* **49**: 1810–1825.

Peltier JCA. 1840. *Météorologie: Observations et Recherches Expérimentales sur les Causes qui Concourent à la Formation des Trombes (Meteorology: Observations and Experimental Research on the Causes that Contribute to the Formation of Tornadoes*). H. Cousin, 444 pp.

Pike WS. 1993. The relationship between 'triple point' frontal passages and tornadoes over the southern United Kingdom and Ireland, including a historical synoptic reconstruction of the multiple outbreak on 19th October 1870. *J. Meteor. (UK)* **18**: 77–84.

Pledgley DE. 1996. A remarkable winter cold front hailstorm, 22 February 1995. *Weather* **51**: 330–341.

Przybylinski RW. 1988. Radar signatures associated with the 10 March 1986 tornado outbreak over central Indiana. Preprints, *15th Conference on Severe Local Storms*. Kananaskis Park, AB, Canada, American Meteorological Society, 52–57.

Przybylinski RW. 1995. The bow echo: observations, numerical simulations, and severe weather detection methods. *Wea. Forecasting* **10**, 203–218.

Przybylinski RW, Schmocker G. 1993. The evolution of a widespread convective windstorm event over central and eastern Missouri. Preprints, *13th Conference on Weather Analysis and Forecasting*. Vienna, VA, American Meteorological Society, 461–465.

Reynolds DJ. 1999. A revised U.K. tornado climatology, 1960-1989. *J. Meteor. (UK)* **24**: 290–321.

Roberts RD, Wilson JW. 1995. The genesis of three nonsupercell tornadoes observed with dual-Doppler radar. *Mon. Wea. Rev.* **123**: 3408–3436.

Rotunno R, Klemp JB. 1982. The influence of the shear-induced pressure gradient on thunderstorm motion. *Mon. Wea. Rev.* **110**: 136–151.

Rotunno R, Klemp JB, Weisman ML. 1988. A theory for strong, long-lived squall lines. *J. Atmos. Sci.* **45**: 463–485.

Rowe MW, Meaden GT. 1985. Britain's greatest tornado outbreak. *Weather* **40**: 230–235.

Rutledge SA. 1989. A severe frontal rainband. Part IV: Precipitation mechanisms, diabatic processes and rainband maintenance. *J. Atmos. Sci.* **46**: 3570–3594.

Sansom HW. 1951. A study of cold fronts over the British Isles. *Q. J. Roy. Meteor. Soc*. **77**: 96–120.

Sawyer JS. 1956. The vertical circulation at meteorological fronts and its relation to frontogenesis. *Proc. R. Soc. London Ser. A* **234**: 346–362.

Sherburn KD, Parker MD. 2014. Climatology and ingredients of significant severe convection in high-shear, low-CAPE environments. *Wea. Forecasting* **29**: 854–877.

Sherburn KD, Parker MD. 2019. The development of severe vortices within simulated high-shear, low-CAPE convection. *Mon. Wea. Rev.* **147**: 2189–2216.

Smart DJ, Browning KA. 2009. Morphology and evolution of cold-frontal misocyclones. *Q. J. Roy. Meteor. Soc*. **135**: 381–393.

Smith BT, Thompson RL, Grams JS, Broyles C, Brooks HE. 2012. Convective modes for significant severe thunderstorms in the contiguous United States. Part 1: Storm classification and climatology. *Wea. Forecasting* **27**: 1114–1135.

Symons GJ. 1900. The Wiltshire whirlwind of October 1, 1899. *Q. J. Roy. Meteor. Soc.* **26**: 261–272.

Trapp RJ, Mitchell ED, Tipton GA, Effertz DW, Watson AI, Andra DL Jr., Magsig MA. 1999. Descending and nondescending tornadic vortices signatures detected by WSR-88Ds. *Wea. Forecasting* **14**: 625–639.

Trapp RJ, Tessendorf SA, Godfrey ES, Brooks HE. 2005. Tornadoes from squall lines and bow echoes. Part I: Climatological distribution. *Wea. Forecasting* **20**: 23–34.

Trapp RJ, Weisman ML. 2003. Low-level mesovortices within squall lines and bow echoes. Part II: Their genesis and implications. *Mon. Wea. Rev.* **131**: 2804–2823.

Turner S, Elsom DM, Meaden GT. 1986. An outbreak of 31 tornadoes associated with a cold front in southern England on 20 October 1981. *J. Meteor. (UK)* **11**: 37–50.

Wade AR, Parker MD. 2021. Dynamics of simulated high-shear, low-CAPE supercells. *J. Atmos. Sci.* **78**: 1389–1410.

Wakimoto RM. 1983. The West Bend Wisconsin storm of 4 April 1981. A problem in operational meteorology. *Mon. Wea. Rev.* **111**: 181–189.

Wakimoto RM, Bosart BL. 2000. Airborne radar observations of a cold front during FASTEX. *Mon. Wea. Rev.* **128**: 2447–2470.

Wakimoto RM, Wilson JW. 1989. Non-supercell tornadoes. *Mon. Wea. Rev.* **117**: 1113–1140.

Wakimoto RM, Murphey HV, Davis CA, Atkins NT. 2006. High winds generated by bow echoes. Part II: The relationship between the mesovortices and damaging straight-line winds. *Mon. Wea. Rev.* **134**: 2813–2829.

Wegener A. 1917. *Wind- und Wasserhosen in Europa*. Friedrich Vieweg & Sohn, Braunschweig, 301 pp.

Weisman ML. 1993. The genesis of severe, long-lived bow echoes. *J. Atmos. Sci.* **50**: 645–670.

Weisman ML, Davis CA. 1998. Mechanisms for the generation of mesoscale vortices within quasi-linear convective systems. *J. Atmos. Sci.* **55**: 2603–2622.

Weisman ML, Klemp JB. 1984. The structure and classification of numerically simulated convective storms in directionally varying wind shears. *Mon. Wea. Rev.* **112**: 2479–2498.

Weisman ML, Rotunno R. 2000. The use of vertical wind shear versus helicity in interpreting supercell dynamics. *J. Atmos. Sci.* **57**: 1452–1472.

Weisman ML, Trapp RJ. 2003. Low-level mesovortices within squall lines and bow echoes. Part I: Overview and dependence on environmental shear. *Mon. Wea. Rev.* **131**: 2779–2803.

Wurman J, Dowell D, Richardson Y, Markowski P, Rasmussen E, Burgess D, Wicker L, Bluestein HB. 2012. The Second Verification of the Origins of Rotation in Tornadoes Experiment: VORTEX2. *Bull. Amer. Meteor. Soc.* **93**: 1147–1170.

Chapter 2: A generalised measure of tornado risk and identification of synoptic types

Matthew R. Clark[1,2,3] and Douglas J. Parker[2]

[1]Met Office, FitzRoy Road, Exeter, Devon, EX1 3PB, UK; matthew.clark@metoffice.gov.uk

[2]University of Leeds, Leeds, UK

[3]Tornado and Storm Research Organisation (TORRO), Oxford, UK

A version of this Chapter is published in the *Quarterly Journal of the Royal Meteorological Society*: https://doi.org/10.1002/qj.3898

Abstract

Environments of tornadic and non-tornadic narrow cold frontal rainbands (NCFRs) are investigated using ERA-Interim reanalyses for a sample of 114 events over the UK and Ireland (44 tornadic). The results offer a practical tool for prediction of the likelihood of tornadoes in these potentially high-impact events. Of 22 analysed parameters, a bulk measure of shear vorticity, and the front-normal wind component on the cold side of the front, yield the best discrimination between event classes, showing significantly larger values in tornadic events. A generalised measure of tornado probability, *p*[TN], is obtained using the distribution of points within the two-dimensional parameter space defined by these parameters. Synoptic situations commonly associated with tornadic NCFRs are identified and conceptual models describing the large-scale evolution are developed. Most events are associated with developing secondary cyclones (i.e., frontal waves) along trailing cold fronts (≥54.5%), generally within west to south-westerly large scale flow. Another significant class of event corresponds to situations where a strong mid- to upper-level jet streak cuts across the front within an amplifying large-scale flow pattern (upstream ridge building and downstream trough extension), generally within north-westerly flow (27.3%). In frontal waves, tornadoes occurred relatively early in the wave's development and just down-front of the wave centre, where rapid increases in *p*[TN] occurred as the wave amplified. In north-westerly flow cases, tornadoes occurred along a well-defined NCFR bulge close to where the mid- to upper-level jet streak and an associated positive PV anomaly intersected the front. Analysis of a high-tornadic subset of tornadic events (NCFRs producing ≥7 tornadoes) revealed an even stronger association with frontal waves (72.2% of cases), suggesting that the highest-impact events are usually associated with secondary cyclogenesis. The possible relevance of identified environmental parameters to candidate vortex-genesis and tornadogenesis mechanisms within NCFRs and quasi-linear convective systems is discussed.

***Keywords*:** tornado, front, narrow cold frontal rainband, NCFR, frontal wave, secondary cyclogenesis, reanalysis.

2.1. Introduction

Narrow cold frontal rainbands (NCFRs) are an important source of tornadoes in the UK. Mulder and Schultz (2015) found that 42% of tornadoes occurred in storms exhibiting linear morphologies in radar imagery over the period 2004 – 2012, of which NCFRs are a major subset. Clark and Smart (2016) found that 34.1% of tornadoes over the period 2003 – 2012 were associated with NCFRs specifically; this percentage increases to 48.8% when the weakest tornadoes (T0 or T1 on the International Tornado Intensity (T) Scale; Meaden, 1976a) are excluded. Furthermore, NCFRs have been responsible for many of the larger outbreaks of tornadoes in the UK (Meaden, 1976b, 1978, 1979, 1983; Elsom, 1983, 1985; Meaden and Rowe, 1985; Turner *et al.*, 1986; Apsley *et al.*, 2016). In spite of these facts, only a minority of NCFRs actually produce tornadoes. For example, of 90 NCFRs identified during the cool seasons of 2003 – 2010, Clark (2013) found that only 28% produced one or more tornadoes. This raises questions about how tornadic NCFRs and their environments differ from non-tornadic ones. Furthermore, questions exist about the timing of tornadogenesis, given that the tornadic phase of an NCFR tends to be short compared to its total lifetime.

Environmental parameters traditionally employed to forecast tornado risk in supercell thunderstorms and quasi-linear convective systems (QLCSs) show little skill in NCFR situations. Pre-frontal CAPE is usually small compared to that in typical severe thunderstorm environments. Whilst statistically significant CAPE differences have been found between tornadic and non-tornadic NCFR environments (e.g., Clark, 2013), absolute differences are correspondingly small. Similarly, bulk measures of vertical wind shear cannot discriminate between tornadic and non-tornadic NCFRs, in part because strong low-level vertical wind shear is almost always present in NCFR environments, tornadic or otherwise (Gatzen, 2011; Clark, 2013). The consequent difficulty in forecasting tornado risk is compounded by the lack of conceptual models of synoptic or mesoscale situations favouring tornadogenesis in NCFRs. These issues mean that, until now, it has not been feasible to issue forecasts of NCFR tornado risk for individual cases, even in a generalised sense (e.g., area-averaged tornado probabilities).

Analysis of the near-surface wind field has been shown to offer potential as an alternative method of predicting NCFR tornadoes. Clark and Parker (2014) (hereafter CP14) found that tornadic NCFRs usually exhibited large vertical vorticity at the

surface front and a large front-normal component of flow in the cold air. Furthermore, tornadoes tended to occur immediately after, or during the latter stages of, a period of increasing vertical vorticity, leading the authors to postulate that vortex-genesis and associated tornadogenesis occurred as a result of the release of horizontal shearing instability (HSI). Only a small sample of cases was investigated, however, leaving some doubt about the generality of the results.

In a reanalysis of the NCFR of 23 November 1981, which produced the largest tornado outbreak on record in the UK, Apsley *et al.* (2016) similarly noted the importance of vertical vorticity along the frontal boundary. They found that tornadoes occurred only where large absolute vertical vorticity coincided with positive CAPE in the immediate pre-frontal environment. As in the CP14 tornadic cases, the wind field exhibited a near-90° veer across the front, and post-frontal winds were orientated approximately normal to the NCFR. The role of temporal changes in parameters was not analysed for this case, however.

In this study, ERA-Interim data are used to examine the environments of a set of 114 fronts exhibiting NCFRs[2] over the UK and Ireland (44 tornadic). The ERA-Interim dataset contains analyses at 6-hourly intervals from January 1979 to August 2019, with a horizontal resolution of 0.75° (~80 km) and 60 vertical levels (Dee *et al*., 2011). The purpose is two-fold. Firstly, the aim is to identify diagnostics that have skill in discriminating between tornadic and non-tornadic NCFRs, including testing whether the results of CP14 hold true for a much larger set of cases. Secondly, the aim is to clarify how values of these parameters, and therefore tornado risk, relate to the synoptic- and mesoscale setting of the front, identifying specific synoptic situations in which tornadic events tend to occur. This builds on work undertaken by Gatzen (2011) and CP14; for example, Gatzen (2011) showed that severe NCFRs tend to occur at the cyclonic shear flank of strong mid-level jets, suggesting that dynamic forcing is important and that the synoptic- to meso-scale situations supportive of such events may be operationally recognisable.

[2] A small number of the events were associated with occlusions, and so narrow frontal rainband (NFR) is a more accurate term for the analysed events than narrow *cold* frontal rainband (NCFR). However, we use the latter to ensure consistency with existing nomenclature.

The remainder of the paper is structured as follows. The methodology is described in Section 2.2. Results are presented in Section 2.3. Discussion follows in Section 2.4 and the key messages of the paper are summarised in Section 2.5.

2.2. Method

2.2.1 Selection of cases

NCFRs were identified using archived composite radar imagery and surface analysis charts over the period 2004 – 2014, using a modified version of the methodology of Trapp *et al*. (2005). This requires a quasi-linear radar echo of length at least 100 km, length at least ten times width, and peak rainfall rates >4 mm h^{-1}. Events meeting these criteria for ≥2 hours and showing at least some evidence of an NCFR for ≥5 hours (of any intensity or horizontal extent for the longer period) were included for analysis, in order to ensure a high probability of each analysed NCFR being present at one or more reanalysis times. Association with a surface front was sought by comparison with the surface analysis charts, so that non-frontal QLCSs could be excluded. The TORRO tornado database (www.torro.org.uk) was used to classify each event as tornadic or non-tornadic. Tornadic NCFRs were defined as those to which at least one tornado could be unambiguously attributed, based on comparison of the position of the NCFR in archived radar imagery with the location and timing of tornadoes as recorded in the TORRO database. NCFRs producing ≥7 tornadoes were assigned to a separate class (high-tornadic) in order to investigate whether differences exist between NCFRs producing larger outbreaks of tornadoes and those producing smaller numbers. In order to increase the sample size of high-tornadic events, the TORRO tornado database was further scrutinised to identify other instances of ≥7 tornadoes within a single 24-hour period between 1979 and 2003 (i.e., events that occurred within the period covered by the ERA-Interim dataset, but prior to archival of the composite radar imagery). Non-frontal tornado outbreaks were identified and excluded by comparison of the reported locations, dates and times of tornadoes with archived Met Office surface analysis charts; any outbreak that could not be attributed unambiguously to a frontal passage was excluded. Since these older events occurred prior to the archival of UK composite radar imagery, it was assumed that an NCFR was present in all identified cases of frontal tornado

outbreaks. In some cases, this is confirmed by radar imagery published after the event (e.g., Elsom, 1983). In others, surface analyses showed a sharp wind-shift across the front and a narrow and sharp trough collocated with the front and the line of wind-shift, features that are generally associated with NCFRs (e.g., James and Browning, 1979). Observations of these features were therefore taken to imply the presence of an NCFR in the absence of radar data. Following this procedure, nine additional high-tornadic NCFR events were identified, giving a total of 18 such events in the 1979 – 2014 period.

2.2.2 Definition of on-front analysis points and a natural coordinate system

In the following analysis, a natural coordinate system (x', y') is adopted in which x' is everywhere tangential to the local front and y' is everywhere normal to the local front (see inset panel in Figure 2.1(a)). Positive x' points towards lower geopotential height in the along-front direction, and positive y' points towards the cold air. The x' and y' wind components are given the notation u' and v', respectively. The term 'up-front' will be taken as the direction pointing along the front towards lower geopotential heights (i.e., the positive x' direction), and 'down-front' as the direction pointing towards higher geopotential heights (i.e., the negative x' direction).

For each NCFR, analysis points were defined at regular intervals along the associated front, as depicted in Met Office surface analysis (ASXX) charts. Fronts displayed in ASXX charts are identified manually, through inspection of model data in conjunction with observations such as satellite imagery. The analyses therefore represent the best available estimate of surface frontal positions. Analysis points were defined such that the distance between adjacent points was always ≤150 km near the UK. For convenience, points were generally defined where the front crossed either a whole degree of latitude or longitude (whichever represented the shortest distance between points, given the orientation and latitude of the front). This methodology ensured that the separation of points was large enough for each to be located within a separate ERA-Interim grid box, but small enough for along-front variability on scales of a few hundred kilometres and larger (i.e., meso-α to synoptic scales) to be adequately resolved (Figure 2.1(a)). The first analysis point was defined as the location along the front closest to the parent low pressure centre, with subsequent points defined further down-front. The final analysis point was defined as the trailing end of the front as

shown in the analysis chart, or the point at which the front extended out of the analysis domain, if applicable. Where fronts exhibited large curvature, the spacing between analysis points was reduced in order to capture the shape of the front adequately. For practical reasons, the along-front spacing was increased to ~250 km along the trailing portion of cold fronts at a large distance (> ~ 1500 km) from the UK, if the front extended to such distances. Where a frontal wave existed that was sufficiently developed for an associated warm-front–cold-front pair to be analysed, the first analysis point was taken to be the apex of the frontal wave (i.e., the meeting point of the warm-front–cold-front pair).

In order to evaluate temporal trends, analysis points were similarly defined using ASXX charts over the period beginning 12 hours prior to the first radar detection of the NCFR and ending when the NCFR and associated front had entirely cleared the UK and Ireland. For NCFRs decaying in-situ, points were defined up to 12 hours after the time of cessation of the NCFR. Using this method, 8212 analysis points were defined at 270 analysis times, for 114 separate NCFR events (comprising 105 NCFRs with duration ≥5 hours in the 2004-2014 climatology period, and the nine additional high-tornadic events identified over the period 1979–2003). This equates to a mean number of analysis times per event of 2.4, and a mean number of on-front points per event, per analysis time, of 30.4.

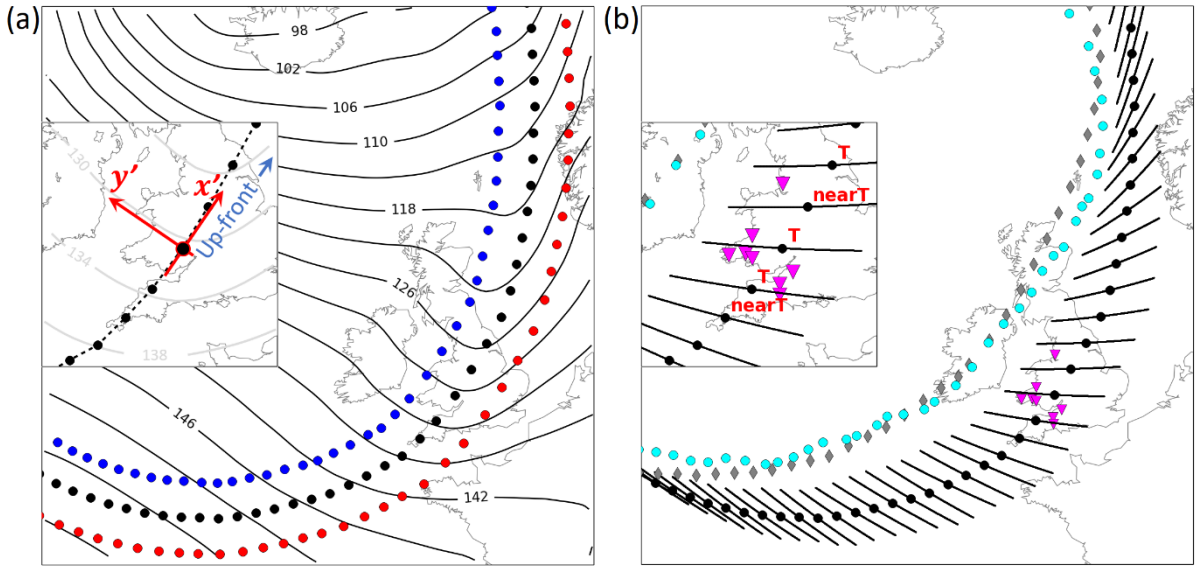

Figure 2.1: (a) On-front, warm air and cold air analysis points (black, red and blue dots, respectively) at 0000 UTC 28 December 2004, overlaid on 850 hPa geopotential height (black contours at 4 DAM intervals). Inset panel illustrates the natural coordinate system used to evaluate cross-front and along-front components. (b) ±3 hour analysis point trajectories (black lines), derived frontal positions at previous analysis time (cyan dots) and on-front analysis points at previous analysis time (grey diamonds), where the previous analysis time is 1800 UTC 27 December 2004. Inset panel gives an expanded view of the tornadic part of the front over the UK. Tornado report locations are shown by magenta inverted triangles, with tornado classification of adjacent analysis points annotated ('T' and 'nearT' for tornadic and near-tornadic points, respectively).

2.2.3 Definition of cold- and warm-air analysis points and calculation of derived parameters

For each identified event and analysis time, parameter fields were obtained from the European Centre for Medium-Range Weather Forecast's ERA-Interim reanalysis dataset. Parameters selected for analysis fall into four classes:

- Those known to be relevant to the vortex-genesis and tornadogenesis process in QLCSs, as shown by modelling studies (e.g., Trapp and Weisman, 2003)
- Those for which significant differences have been found between tornadic and non-tornadic NCFR environments (e.g., Clark, 2013; CP14)
- Those known to influence the kinematic stability of shear zones (e.g., vertical vorticity and horizontal strain, and their along- and cross-frontal components,

which may relate to the potential for the development of HSI; e.g., Dritschel *et al*., 1991).

- Those relating to frontal processes, such as the two-dimensional frontogenesis function

In order to evaluate cross-frontal differences in parameter values, where applicable, a 'bulk measures' approach was adopted. Values were analysed at points located on the warm and cold sides of the front, each at a front-normal distance of 150 km from the corresponding on-front analysis point (red and blue markers in Figure 2.1(a), respectively). The local orientation of the front was calculated from the latitude and longitude differences between neighbouring on-front points. Parameter values were obtained for the cold and warm air points by taking the value at the nearest reanalysis grid point.

Bulk measures of cross-frontal shear vorticity (i.e., $-\partial u'/\partial y'$), along-front vorticity ($\partial v'/\partial x'$), cross-front confluence ($-\partial v'/\partial y'$), and along-front dilatation ($\partial u'/\partial x'$) were calculated by evaluating finite differences in the front-normal and front-parallel flow components between corresponding cold and warm air analysis points. The cross-frontal measures (as indicated by the subscript 'XF') were defined as:

$$Bulk\ confluence = -D_{XF} = \frac{-\Delta v'}{\Delta y'} = \frac{(v'_{warm} - v'_{cold})}{300km} \qquad (1)$$

$$Bulk\ shear\ vorticity = \xi_{XF} = \frac{-\Delta u'}{\Delta y'} = \frac{(u'_{warm} - u'_{cold})}{300km} \qquad (2)$$

The above quantities were calculated using the full, geostrophic, and ageostrophic winds, so that geostrophic and ageostrophic contributions could be evaluated separately and compared. The geostrophic wind was calculated from the 850 hPa geopotential height field, and the ageostrophic wind was obtained by subtracting the geostrophic component from the total wind field. Along-front bulk gradients (as indicated by the subscript 'AF') were calculated by analysing, on each side of the front, the mean of the gradient between the given point and the adjacent points up-front and down-front, and then by taking the mean of the resulting gradients on the warm and cold sides of the front. For example, in the case of along-front dilatation:

$$Dilatation_{AF} = 0.5\left(\frac{\Delta u'_{warm}}{\Delta x'_{warm}} + \frac{\Delta u'_{cold}}{\Delta x'_{cold}}\right) \qquad (3)$$

Along-front bulk gradients were calculated only where the horizontal separation between adjacent points on each side of the front was >50 km (the spacing being variable where the front exhibited curvature) and were not calculated at the first and last analysis points along the front at each analysis time.

Additional parameters extracted or computed include the bulk cross-front temperature difference (temperature at the warm analysis point minus that at the cold analysis point), total frontogenesis (calculated at the *on-front* analysis point, following Markowski and Richardson (2010), p.124), cross-frontal wind veer, ratio of the wind speeds on each side of the front (i.e., wind speed at the cold point divided by that at the warm point), front-normal, forward-directed flow at the cold air point (hereafter $-v'_{cold}$), and various measures relating to the static stability and vertical wind shear analysed at the warm air points (Table 2.1). Parameter values were then compared for high-tornadic, tornadic and non-tornadic points, and the t-test was used to assess the statistical significance of differences between event classes.

2.2.4 Assumptions, limitations and interpretation of the 'bulk measures' approach

The bulk measures approach assumes that parameter values are relatively uniform within the cold and warm air masses, and that gradients are constrained to a narrow zone at the front (i.e., the frontal shear zone), where the width of this zone is much less than the reanalysis grid spacing. Under these assumptions, and for a given, uniform shear zone width, the magnitude of cross-front gradients within the shear zone will be dependent only on the difference in the relevant parameter values between the warm and cold air masses. An alternative, but equivalent, interpretation is that the bulk values represent a measure of the potential magnitude of the given parameter that would be realised given collapse of the frontal shear zone to some specified, uniform, narrow width, assuming the initial width of the shear zone to be less than the 300 km separation of cold and warm air points. Since the dataset analysed here consists of NCFR-bearing fronts, collapse to small cross-frontal scales (e.g., Hoskins and Bretherton, 1972; Koch and Kocin, 1991) can be assumed for most, if not all, cases. The bulk measures have the advantage of being insensitive to the substantial small-scale variability in parameter values typically observed along and within the frontal shear zone itself. Furthermore, they avoid errors arising from uncertainties in frontal position, which could be substantial if gradients were computed at the on-front analysis points. The above

assumptions were tested by recalculating various bulk parameters using a range of separation distances between the warm and cold air points (not shown). Parameters of most interest in the following analysis (notably, $-v'_{cold}$ and shear vorticity) were found to be relatively insensitive to the choice of separation distance.

2.2.5 Calculation of analysis-point trajectories

In order to evaluate 850 hPa parameter values in a Lagrangian frame of reference, front-following analysis points were defined by computation of 'pseudo trajectories' for each on-front point, using the observed 850 hPa *u'* and *v'* wind components at each analysis time. A parcel was assumed to move along-front with the mean *u'* on the cold and warm sides of the front, whilst the front-normal forward motion was assumed to approximate to $-v'_{cold}$ (the latter parameters are strongly positively correlated in the analysed sample). Back trajectories were terminated at *t* - 6 hours (i.e., the previous analysis time), where *t* is the current analysis time. The minimum distance between the terminus of the back trajectory at *t* - 6 h and any on-front point at the previous analysis time was then calculated. If this distance was <100 km, the corresponding on-front point at the last analysis time was taken to be the closest on-front point to the terminus of the back trajectory. Where the minimum distance was >100 km, no corresponding point was defined, and parameter trends were not calculated. Figure 2.1(b) shows an example of *t* - 6 h trajectory end points computed using this method (cyan dots) and illustrates how they compare to the actual position of the front at the previous analysis time (grey diamonds). In general, positions calculated using the back-trajectories agreed closely with the analysed frontal position at the previous analysis time; the average distance between back trajectory terminus and closest on-front point in the preceding analysis was 75 km, and 80% of back trajectory termini were located within 100 km of an on-front point. Performance tended to be poorer where the front exhibited large curvature and close to the apex of frontal waves, situations in which larger spatiotemporal variations in the wind field might reasonably be expected.

2.2.6 Classification of analysis points as non-tornadic, tornadic and high-tornadic

On-front points were categorised firstly according to whether they were associated with a high-tornadic, tornadic or non-tornadic NCFR, and then, in tornadic and high-tornadic cases, based on their proximity to tornadoes. An on-front point was classified as

tornadic if the point, or any part of a trajectory extending from the point over a period of ±3 hours from analysis time (computed in the same way as the 6-hour back trajectories described above), lay within 50 km of a tornado report (Figure 2.1(b)). A point was classified as near-tornadic if it, or any part of its trajectory, lay between 50 and 100 km from the nearest tornado report. Points at greater distances from a tornado report were classified as 'non-tornadic (of tornadic)' (nT(ofT)). All points in non-tornadic events were classified as 'non-tornadic' (nT). For the purposes of comparing tornadic and non-tornadic parameter values, nT(ofT) points were excluded from the sample, because parameter values at these points cannot be considered independent of the values at neighbouring tornadic or near-tornadic points.

For nT points, two additional filters were applied. The first was to remove on-front points not situated over the UK and Ireland. This was necessary because tornadoes are unlikely to be reported over sea, so the true tornado classification of non-land points must be considered unknown. For the remaining nT points, proximity of the NCFR was assessed using composite radar rainfall imagery. Although events were selected in the first place on the basis that they exhibited an NCFR, it was not uncommon for an NCFR to affect only part of the UK and Ireland, due either to its limited along-front extent or to genesis or dissipation over the region. Points with no NCFR were removed in order to avoid the undesirable comparison of non-NCFR-bearing, non-tornadic points with tornadic points (given that the presence of an NCFR is assumed to be a pre-requisite for tornadoes). An NCFR was deemed present at the given analysis point if one was evident in the radar imagery at any time within ±3 hours from analysis time, and within a radius of approximately 100 km from the analysis point or its trajectory. This filtering, and the prior definition of non-tornadic, tornadic and high-tornadic event types, resulted in three classes of analysis point, for which the distributions of the various parameter values were compared:

- *Non-tornadic*: all analysis points along NCFR-bearing, non-tornadic fronts over the UK and Ireland
- *Tornadic*: near-tornadic and tornadic analysis points in tornadic NCFRs (irrespective of location, but in practice always over or adjacent to the UK and Ireland, since only UK and Ireland tornadoes in the TORRO tornado database were considered)

- *High-tornadic*: as for tornadic, but in high-tornadic events

Inspection of the analysis point trajectories and the tornado classes for each tornadic case revealed two limitations of the methodology that necessitated manual removal of a number of tornadic and near-tornadic analysis points. Firstly, where the front exhibited large curvature and the tornadoes occurred before the analysis time in question, convergence of back-trajectories sometimes resulted in an unrealistically large along-front extent of tornadic and near-tornadic points at analysis time, compared to the along-front extent of reported tornadoes. In order to address this issue, tornadic and near-tornadic points were removed where trajectories were orientated at an angle of less than 45° to the front, if another tornadic point (or its trajectory) lay closer to the reported tornadoes. 12.4% of tornadic and high-tornadic points were removed for this reason. Secondly, tornadic and near-tornadic points were excluded where the difference between the analysis time and the nearest tornado time was >3 hours and the minimum distance between the back trajectory terminus and an on-front analysis point in the preceding analysis was >100 km. This was undertaken in order to reduce the impact of potential misclassification of points as tornadic- or near-tornadic where a trajectory deviated substantially from the observed movement of the front (e.g., where there were substantial differences between front-normal forward motion and $-v'_{cold}$). 10.9% of tornadic and high-tornadic points were removed for this reason.

Following this filtering, the final number of analysis points was 375 for non-tornadic, 100 for tornadic, and 102 for high-tornadic classes. The total number of separate events in each class was 70 for non-tornadic, 26 for tornadic, and 18 for high-tornadic. In agreement with previous studies (e.g., Clark, 2013), the frequency of events shows a strong seasonal cycle, with a maximum in the autumn and early winter (86% of events occurring between October and January, with no events in June or July). 85.1% of events were associated with cold fronts, 7.0% associated with occluding cold fronts (where an NCFR was present along sections of both the cold front and the occlusion, as shown in ASXX charts) and 7.9% were associated with occlusions (see Table S1 in Appendix A). The mean number of points per individual analysis time was 2.82 for non-tornadic, 2.27 for tornadic, and 3.00 for high-tornadic. Comparison of results using the filtered and unfiltered tornadic and high-tornadic datasets (not shown) revealed

stronger differences between event classes when using the filtered dataset; however, the results were qualitatively unaffected by the filtering.

2.2.7. Generation of composite analyses on a rotated, translated grid

To complement the analysis of parameter values at individual on-front points, composite analyses were generated for high-tornadic, tornadic and non-tornadic NCFRs over a domain spanning approximately 27° latitude and 50° longitude. In tornadic and high-tornadic cases, the origin of the domain was set to the tornado or mean tornado report latitude and longitude. In non-tornadic cases, the origin was set to the mean latitude and longitude of on-front analysis points over the UK and Ireland. The origin was then translated so that it always lay at 51.5N, 2.0W, and the domain rotated such that the orientation of the front, α, was equal to the mean orientation at the origin for each event class.

Composite analyses were generated by calculating the mean parameter fields in the translated, rotated domains for all events in each NCFR category. The composites include all analysis times for which at least part of the front lay over the UK or Ireland; therefore, for some events, more than one analysis time is included. A maximum of three analysis times was allowed for each event, so as not to give undue weighting to any single event. Given the large spread in shear vorticity amongst the non-tornadic cases, two vorticity sub-classes were defined, separated by a threshold shear vorticity of 4.0×10^{-5} s^{-1}. The aim of this partitioning was to determine whether cases with high and low vorticity were associated with distinctly different synoptic situations. This methodology resulted in compositing of 31 analysis times from 18 high-tornadic events, 35 analysis times from 26 tornadic events, 64 analysis times from 43 high-vorticity non-tornadic events, and 81 analysis times from 53 low-vorticity non-tornadic events[3].

[3] The total number of events implied by these figures (140) is higher than the actual total (114) because some non-tornadic events contributed to both high- and low-vorticity classes at different analysis times.

Table 2.1: Median values of all analysed parameters, for each event class. *p* values are derived using the Student's t-test. *p* values indicating differences significant at the 99% level are highlighted by bold type. Figures in square brackets indicate the sample size for each event class.

Parameter	*Median nT [375]*	*Median all-T [202]*	*Median T [100]*	*Median HT [102]*	*p value nT – all-T*	*p value nT – T*	*p value nT – HT*	*p value T – HT*
t – 6 h back trajectory terminus: distance to nearest on-front point at previous analysis time (km)	58.7	59.4	54.2	68.7	0.1788	0.3144	0.2590	0.9665
Angle of front, α (degrees clockwise from north–south with cold air to the west)	32.3	23.3	19.0	27.6	**<0.0001**	**0.0001**	**0.0034**	0.2969
Bulk confluence (–*dv*'/*dy*') (s^{-1} x 10^{-5})	0.75	1.87	1.95	1.86	**<0.0001**	**<0.0001**	**<0.0001**	0.5738
Bulk confluence trend (s^{-1} x 10^{-5} / 6 hours)	-0.27	0.20	-0.08	0.68	**0.0013**	0.6229	**<0.0001**	**0.0079**
Shear vorticity (–*du*'/*dy*') (s^{-1} x 10^{-5})	2.90	5.08	4.35	5.76	**<0.0001**	**0.0001**	**<0.0001**	**0.0014**
Shear vorticity trend (s^{-1} x 10^{-5} / 6 hours)	0.06	1.67	1.41	1.97	**<0.0001**	**<0.0001**	**0.0002**	0.3705
Bulk cross-front temperature difference (K)	4.05	4.18	3.15	5.20	0.4353	**<0.0001**	**<0.0001**	**<0.0001**
Cross-front temperature difference trend (K / 6 hours)	-0.17	-0.56	-0.53	-0.59	0.3699	0.5481	0.3966	0.8716

Front-normal forward motion (m s^{-1})	10.5	16.4	15.8	17.6	**<0.0001**	**<0.0001**	**<0.0001**	**<0.0001**
$-v'_{cold}$ (i.e., cold-air front-normal flow) (m s^{-1})	11.7	19.3	17.1	21.2	**<0.0001**	**<0.0001**	**<0.0001**	**<0.0001**
$-v'_{cold}$ trend (m s^{-1} / 6 hours)	-0.24	1.15	0.5	2.14	**<0.0001**	**0.0014**	**<0.0001**	0.0128
Front-relative $-v'_{cold}$ (forward relative flow positive) (m s^{-1})	1.27	2.19	0.98	3.64	0.3616	0.1322	**0.0013**	**0.0034**
Along-front dilatation (mean of *du*'/*dx*' at warm and cold air points) (s^{-1} x 10^{-5})	0.40	-0.51	-0.49	-0.51	**<0.0001**	**<0.0001**	**<0.0001**	0.5093
Total frontogenesis (K m^{-1} s^{-1} x 10^{-10})	3.93	7.18	4.37	10.56	**<0.0001**	0.9408	**<0.0001**	**<0.0001**
Total frontogenesis trend (K m^{-1} s^{-1} x 10^{-10} / 6 hours)	0.22	0.61	0.48	1.38	0.4587	0.8237	0.3299	0.6050
Cross-front wind veer (degrees)	17.5	38.6	37.7	40.7	**<0.0001**	**<0.0001**	**<0.0001**	0.0935
Wind speed ratio (post-front / pre-front)	0.76	0.87	0.89	0.82	**<0.0001**	**<0.0001**	**<0.0001**	0.2600
Overall mean wind speed (m s^{-1})	21.9	23.7	21.9	25.7	**<0.0001**	0.3352	**<0.0001**	**0.0006**
Angle between mean wind (analysed at the cold and warm air points) and front (degrees)	33.6	53.5	50.5	56.5	**<0.0001**	**<0.0001**	**<0.0001**	0.0260

Surface to 850 hPa lapse rate (K km^{-1}) at warm air point	5.48	5.48	6.26	4.70	0.1300	**<0.0001**	**<0.0001**	**<0.0001**
Surface to 850 hPa saturated static stability, N_S^2, at warm air point (s^{-1} x 10^4)	0.67	0.70	0.30	1.13	0.7118	**<0.0001**	**<0.0001**	**<0.0001**
Bulk vertical *u*' shear 975 – 850 hPa (m s^{-1} difference between top and bottom of layer) at warm air point	3.85	2.91	2.29	3.71	0.0572	0.0403	0.3601	0.3574
Bulk vertical –*v*' shear 975 – 850 hPa (m s^{-1} difference between top and bottom of layer) at warm air point	8.35	9.75	8.59	11.37	**<0.0001**	0.5913	**<0.0001**	**<0.0001**

2.3. Results

Results are presented as follows. The distribution of parameter values in tornadic and non-tornadic events is described in Section 2.3.1, and the generalised measure of tornado risk is defined in Section 2.3.2. Along-front variability, ageostrophic contributions to key parameters, and composite fields are explored in Sections 2.3.3 to 2.3.5, from which we infer the association of many tornadic events with frontal waves. This association is explored further in Section 2.3.6 by inspection of surface analysis charts. Conceptual models for frontal wave and non-frontal wave events are developed in Sections 2.3.7 and 2.3.8, respectively.

2.3.1 Parameter value distributions for non-tornadic, tornadic and high-tornadic event classes

Significant differences (i.e., $p < 0.01$) were found between high-tornadic, tornadic and non-tornadic classes for many of the analysed parameters (Table 2.1). The results for shear vorticity, wind speed ratio, and cross-front wind veer are in agreement with those of CP14, in that significantly larger values of each parameter occur in tornadic events. The fact that significant differences exist between tornadic and high-tornadic events suggests that it should be possible to distinguish between NCFR environments supporting only isolated tornadoes and those more likely to support larger outbreaks, in addition to being able to distinguish between tornadic and non-tornadic NCFR environments.

Figure 2.2 shows the distribution of values, by class, for parameters exhibiting statistically significant differences ($p < 0.01$) between all three event classes, and in which the median values conform to the pattern:

high-tornadic > tornadic > non-tornadic

These parameters are shear vorticity, front-normal forward motion and $-v'_{cold}$. Since front-normal forward motion and $-v'_{cold}$ are strongly positively correlated (r^2 = 0.5435), these reduce to two parameters: shear vorticity and $-v'_{cold}$. Bulk confluence is also considered further since, although median values were slightly lower in high-tornadic events than in tornadic events, differences between tornadic and non-tornadic events were amongst the largest of any analysed parameter when expressed as a percentage of the interquartile range.

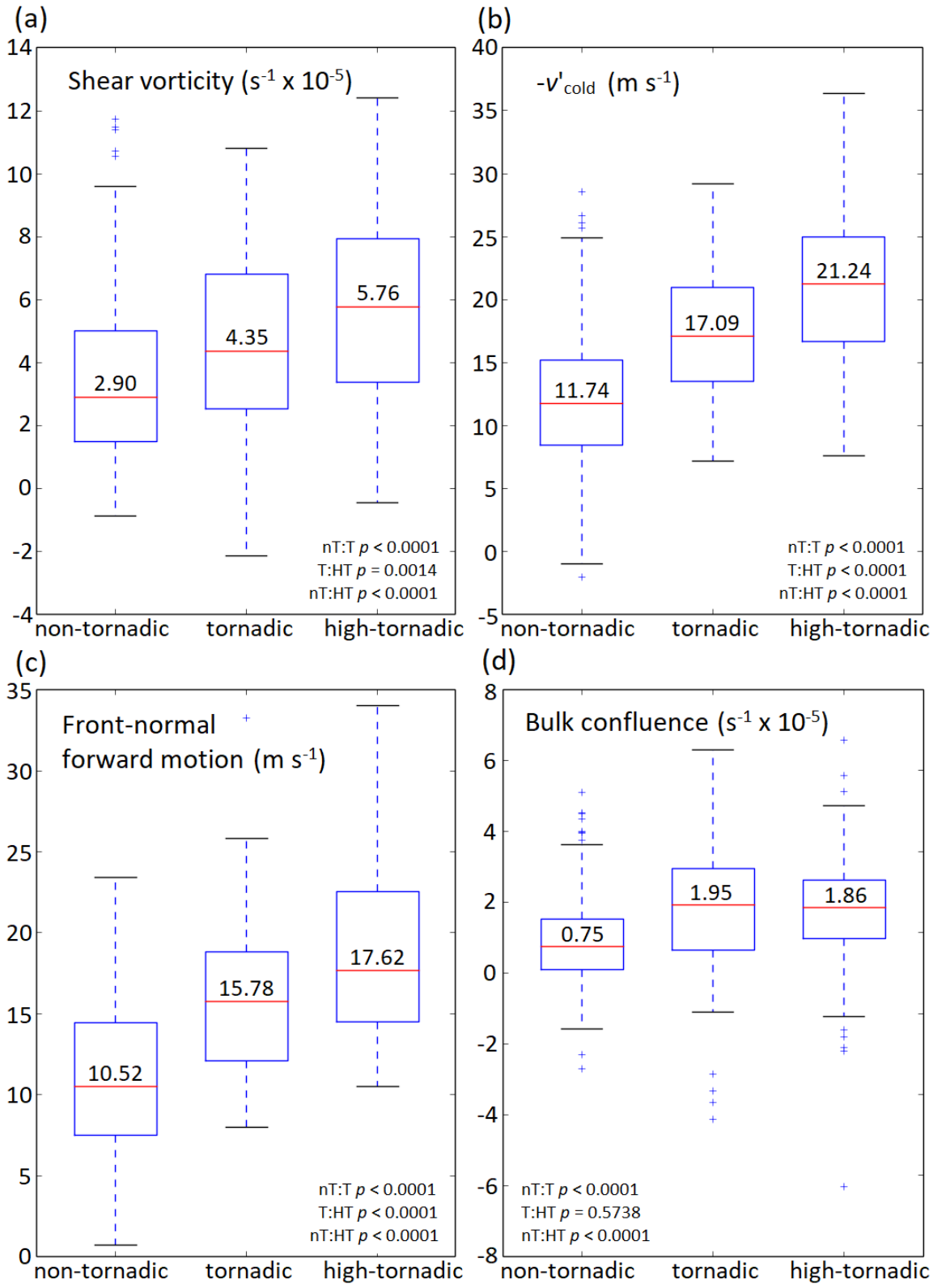

Figure 2.2: Box and whisker plots for selected parameters. (a) Shear vorticity (s^{-1} x 10^{-5}); (b) $-v'_{cold}$ (s^{-1} x 10^{-5}); (c) Front-normal forward motion (m s^{-1}); (d) Bulk confluence (s^{-1} x 10^{-5}). Red bar and text within each box denote the median value in each case. The upper and lower edges of the box denote the upper and lower quartile values, and the whiskers extend 1.5 interquartile ranges beyond the upper and lower quartiles.

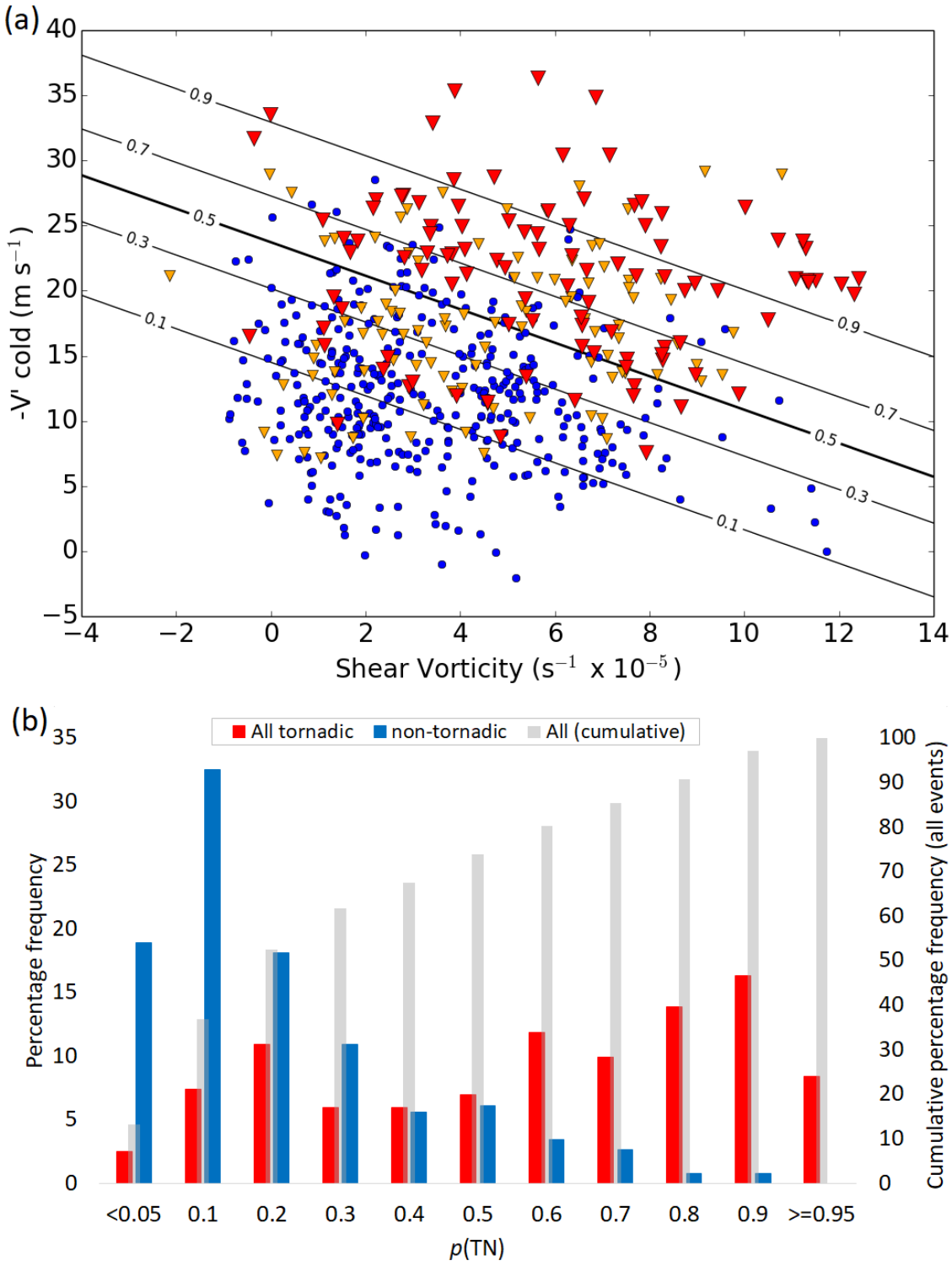

Figure 2.3: (a) Scatterplot of shear vorticity versus $-v'_{cold}$ for high-tornadic, tornadic and non-tornadic analysis points (red inverted triangles, orange inverted triangles, and blue dots, respectively). Black contours denote the probability of a point being tornadic or high-tornadic across the two-dimensional parameter space, *p*[TN], calculated using linear discriminant analysis. (b) Histogram showing the percentage frequency of all-tornadic (i.e., tornadic plus high-tornadic) and non-tornadic events as a function of *p*[TN]. The cumulative frequency of all events, as a function of *p*[TN], is shown by the grey bars. Values on the x-axis show the bin midpoints, except for the lowest and highest bins.

2.3.2. Combining shear vorticity and $-v'_{cold}$ into a single parameter to describe NCFR tornado risk

The distribution of points within the two-dimensional parameter space defined by shear vorticity and $-v'_{cold}$ is shown in Figure 2.3(a). The probability of a point being tornadic (hereafter *p*[TN]) was calculated using linear discriminant analysis. This probability is shown by the black contours in Figure 2.3(a) (see Appendix B for empirical formulae describing the relationship between *p*[TN], shear vorticity and $-v'_{cold}$). A useful partition exists between high and low *p*[TN] environments across the parameter space, as indicated by the relatively close spacing of the probability isolines.

The frequency distribution of *p*[TN] shows that events with small shear vorticity and $-v'_{cold}$ are considerably more common than those with large values of both parameters (Figure 2.3(b)). For example, ~50% of points have *p*[TN] < 0.25, whereas only ~10% of points have *p*[TN] > 0.75. This is consistent with the result that only a minority of NCFRs (33.3% over the 2004 – 2014 period) produced one or more tornadoes. In the following sections, we show that analysis points with large shear vorticity and $-v'_{cold}$ (and therefore large *p*[TN]) tend to occur in specific synoptic situations and in well-defined locations relative to synoptic and mesoscale features along the front, such as frontal waves. We further show that these synoptic situations and along-front locations differ from those typically associated with small shear vorticity and $-v'_{cold}$.

Notwithstanding the above results, Figure 2.3 shows that a minority of tornadic NCFRs occur in low *p*[TN] environments. This is illustrated in the bimodal distribution of *p*[TN] for tornadic points in Figure 2.3(b), with a secondary maximum in percentage frequencies at *p*[TN] < 0.25. These low *p*[TN] tornadic cases, which represent exceptions to the rules developed in the remainder of this section, are analysed in Appendix C.

2.3.3 Parameter values as a function of distance along front

Along-front variability was assessed by plotting parameter values as a function of normalised along-front distance (Figure 2.4). In tornadic cases, the origin was taken to be the analysis point located closest to the tornado (or to the mean position of tornadoes in cases with more than one tornado). In non-tornadic cases, the origin was taken to be

the mean of analysis points located over the UK and Ireland. Points were grouped into normalised distance bins of width 100 km in order to ensure an adequate sample size. Distance bins with sample sizes <20 were not plotted[4].

Several of the parameters exhibiting significant differences between event classes in Table 2.1 show localised maxima near the UK in tornadic and high-tornadic classes (i.e., at normalised along-front distances near zero; Figure 2.4(a)-(c)). For example, $-v'_{cold}$ is maximised at distances of 200 km and 100 km in tornadic and high-tornadic classes, respectively, with strong decreases down front (i.e., smaller $-v'_{cold}$ in the trailing section of fronts (Figure 2.4(a)). Shear vorticity is maximised in tornadic and high-tornadic cases at the analysis point located furthest up-front (i.e., nearest to the apex of the frontal wave, where present (Figure 2.4(d))). Statistically significant differences between event classes are generally restricted to those parts of the front located close to the UK and Ireland, with smaller differences at large along-front distances (i.e., towards the trailing end of fronts). The distance range over which differences are significant (for example, in the case of $-v'_{cold}$, -200 to 700 km in tornadic events and -200 to 1200 km in high-tornadic events) is on the order of the typical scale of a secondary cyclone (i.e., ~1000 km).

In contrast to other parameters, along-front dilatation and α exhibit down-front increases in median values in all event classes. Whilst the median dilatation near the UK is negative in tornadic and high-tornadic cases, it is positive in non-tornadic cases (Figure 2.4(e)). Down-front increases in α are symptomatic of the substantial curvature exhibited by many fronts with, on average, nearly zonal orientation at the trailing ends of fronts and more meridional orientation close to the parent cyclone centre or frontal wave apex in all event classes (Figure 2.4(f)).

[4] A threshold of 10 was used for along-front dilatation, since this parameter was calculated at fewer analysis points owing to the requirement for a minimum along-front spacing of warm-air and cold-air analysis points of 50 km, as described in Section 2.2.3.

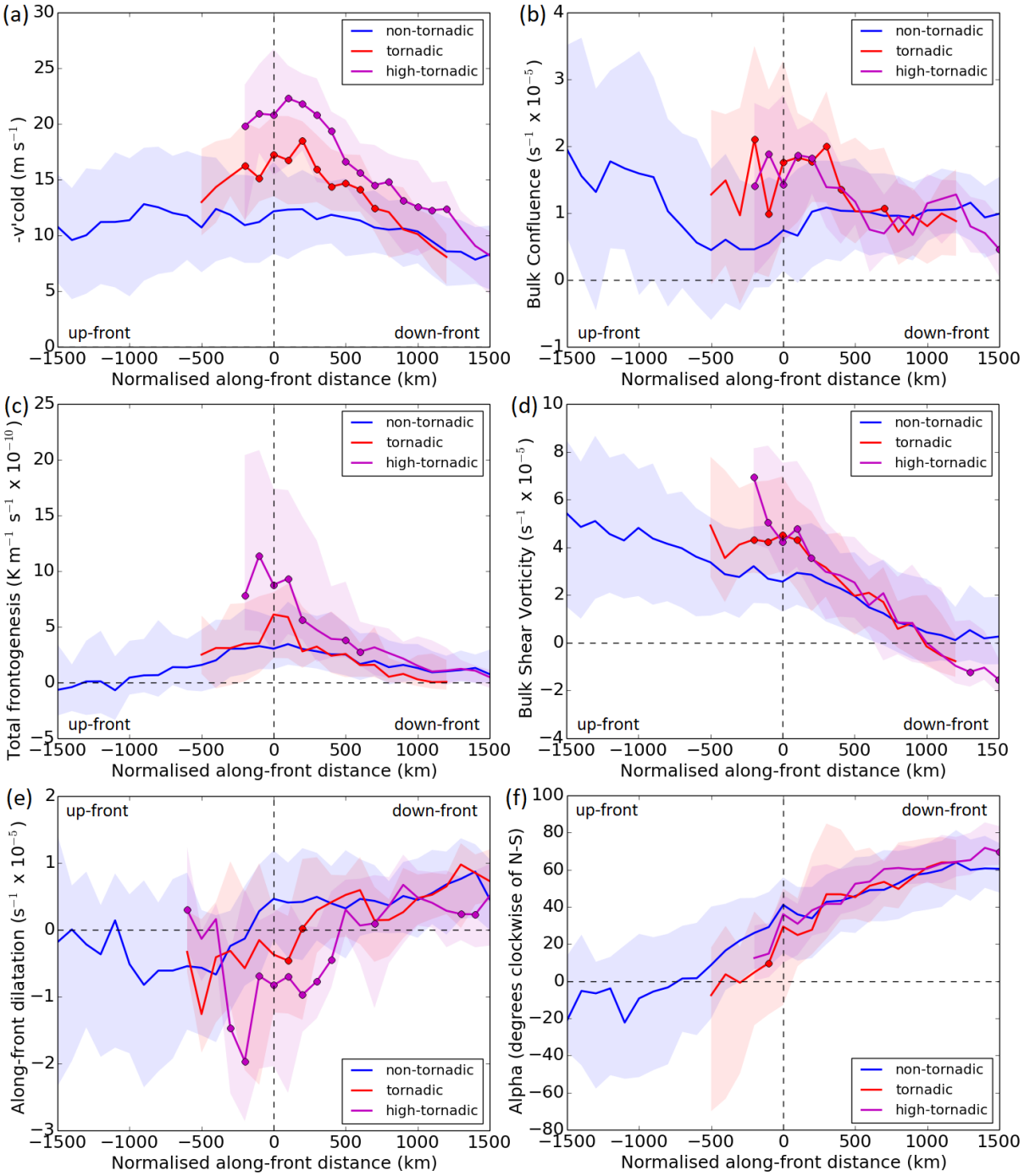

Figure 2.4: Median parameter values (bold, coloured lines) and interquartile range (shading) as a function of normalised along-front distance, where the origin is defined as the mean along-front distance of tornado reports (tornadic and high-tornadic cases), or analysis points located over the UK and Ireland (non-tornadic cases). Negative (positive) distances indicate locations up-front (down-front) of the origin. Markers are plotted at the median value where the distributions are significantly different (at the 95% level) between the non-tornadic and tornadic classes (red dots), and non-tornadic and high-tornadic classes (magenta dots). (a) $-v'_{cold}$; (b) Bulk confluence; (c) Total frontogenesis; (d) Shear vorticity; (e) Along-front dilatation; (f) Angle of front (α) (degrees clockwise of a north–south orientated front with cold air to the west).

2.3.4 Geostrophic and ageostrophic contributions to shear vorticity and confluence

Figure 2.5 shows the mean contributions of geostrophic, ageostrophic and total flows to the shear vorticity and bulk cross-frontal confluence for each event class, analysed at the 850 hPa level. Ageostrophic contributions to shear vorticity are small in all event classes, being only a few percent of the total. This suggests that the front-parallel winds are largely in geostrophic balance, in agreement with previous studies (e.g., Browning and Pardoe, 1973). In contrast, whilst in non-tornadic cases ageostrophic contributions to the bulk confluence are negligible (being only 6% of the geostrophic bulk confluence), they are positive and substantial in tornadic and high-tornadic cases (30% and 37% of the total bulk confluence, respectively). The large ageostrophic contribution is suggestive of the presence of a strong front-transverse circulation; in particular, ageostrophic confluence would be expected to occur near the leading edge of the near-ground, forward-directed branch of the circulation (e.g., Markowski and Richardson (2010), p.124). This is consistent with the observed larger frontogenesis near to the mean tornado location in tornadic and (particularly) high-tornadic cases (Figure 2.4(c)), since the ageostrophic circulation is the atmosphere's response to the geostrophic frontogenesis.

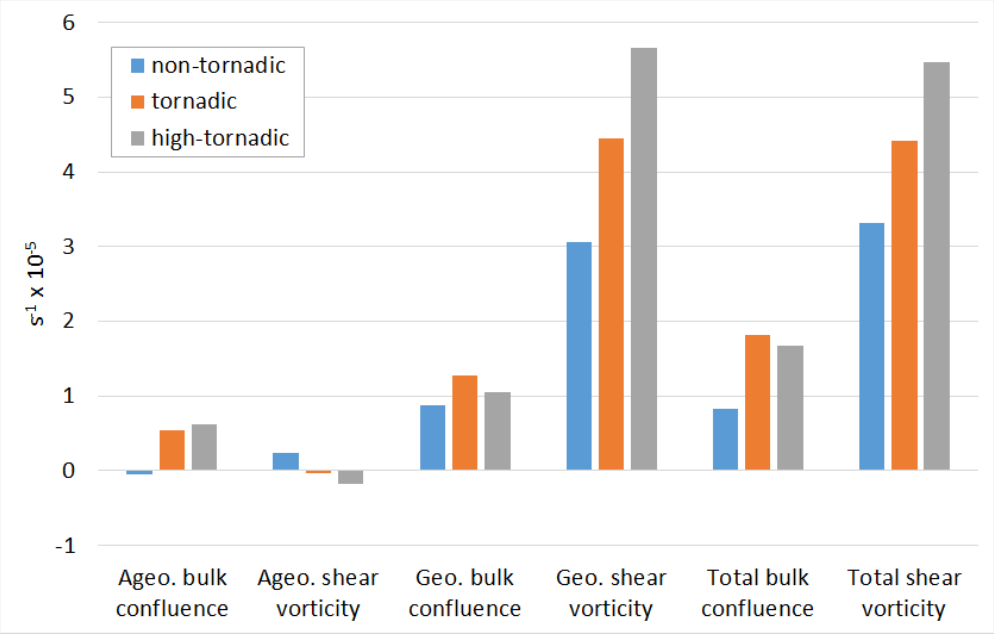

Figure 2.5: Mean ageostrophic (left) and geostrophic (centre) contributions to the total bulk confluence and total shear vorticity (right) for each event class.

2.3.5 Composite fields

Composite fields show that all event classes are associated with synoptic patterns exhibiting generally westerly flow near the UK. At 925 hPa, the strongest winds are situated within an elongated zone on the immediate warm side of the front in all classes, which likely represents the mean position of the pre-frontal low-level jet (Figure 2.6). However, substantial differences exist in the structure of the frontal trough and in the strength and orientation of the post-frontal wind and pressure fields between classes. Non-tornadic (low vorticity) events exhibit a comparatively weak 925 hPa trough, with a relatively small veer in the geostrophic flow across the trough axis (Figure 2.6(a)). Non-tornadic (high vorticity) events exhibit a much sharper trough, but post-frontal wind speeds are markedly weaker than in other event classes (Figure 2.6(b)).

Tornadic and high-tornadic events exhibit strong pressure gradients and geostrophic wind speeds on both sides of the front, with a well-marked frontal trough, as shown by the large difference in the orientation of the 925 hPa geopotential height contours across the trough axis (Figure 2.6(c)-(d)). Near the UK and Ireland, post-frontal winds are orientated approximately normal to the front (i.e., west-north-westerly flow). The inequality in wind speeds between warm and cold sides of the front is much smaller than in the non-tornadic (high vorticity) events, such that these events conform closely to CP14's type A pressure and wind fields (which were likewise found to be conducive to tornadoes). The strong front-normal component of flow on the cold side of the front suggests typically fast-moving fronts. This strong flow extends many hundreds of kilometres to the rear of the front, and is therefore seen to be a characteristic of the large-scale flow field, rather than a local feature confined to the immediate post-frontal region. Compared to tornadic events, high-tornadic events exhibit slightly stronger winds and a slightly sharper frontal trough, but in general terms the fields appear similar (*cf.* Figures 2.6(c) and (d)), suggesting that the environment of high-tornadic events is essentially a stronger variant of that associated with tornadic events (as opposed to being a different type of environment entirely).

In non-tornadic (low vorticity) events (Figure 2.6(a)), the strongest 300 hPa flow is on the down-wind side of the upper-level trough axis (i.e., the upper-level trough is slightly confluent). Conversely, in high-tornadic events, the strongest flow is located on the upwind side of the trough and close to the trough axis, such that the upper level

trough is slightly diffluent (Figure 2.6(d)). In tornadic and high-tornadic events, the 300 hPa jet exit is located close to the origin (and therefore to the mean position of tornado reports), with the strongest wind speeds on the immediate cold side of the front. The jet axis crosses the surface front near the origin. In contrast, in non-tornadic events of both classes, the origin lies on the anticyclonic shear (i.e., equatorward) side of the 300 hPa jet axis, and the jet axis crosses the surface front over the North Sea, several hundred kilometres up-front of the origin. In non-tornadic (high vorticity) cases, the upper-level jet is almost parallel to the front near to the origin.

Composite fields further show that a well-defined 500 hPa PV maximum is situated on the immediate cold side of the front in all event classes (as shown by the shading in Figure 2.7). In non-tornadic events of both vorticity classes, the PV maximum is relatively weak and located slightly further rearward of the surface front, when compared to tornadic and high-tornadic event classes. The greater intensity and closer proximity of the PV maximum in tornadic event classes suggests greater dynamic forcing for ascent near the origin. This is confirmed by analysis of the magnitude of the vorticity advection term in the quasi-geostrophic height tendency equation (analysed at 500 hPa) and Q vectors (Sanders and Hoskins, 1990) calculated using the 700 – 300 hPa layer-mean wind and temperature fields (shown by bold, red–blue contours and arrows, respectively, in Figure 2.7). Composites for all event classes exhibit forcing couplets close to the UK and Ireland, comprising forcing for height falls and Q-vector convergence immediately to the rear of front, and forcing for height rises and Q-vector divergence further rearward of the front. However, the forcing couplets are considerably stronger in tornadic and high-tornadic events than they are in non-tornadic events of both classes, with the strongest couplets in high-tornadic events. In the high-tornadic events, the maximum forcing for height rises corresponds closely to a region of slight anticyclonic curvature in the 925 hPa geopotential height contours over and just southeast of Ireland (*c.f.* Figures 2.6(d) and 2.7(d)). This correspondence suggests localised large height rises (and associated additional veering of the geostrophic wind in the region between the centre of height rises and the trough axis) may contribute to the overall sharpness of the frontal trough and the magnitude of shear vorticity near to the mean tornado location.

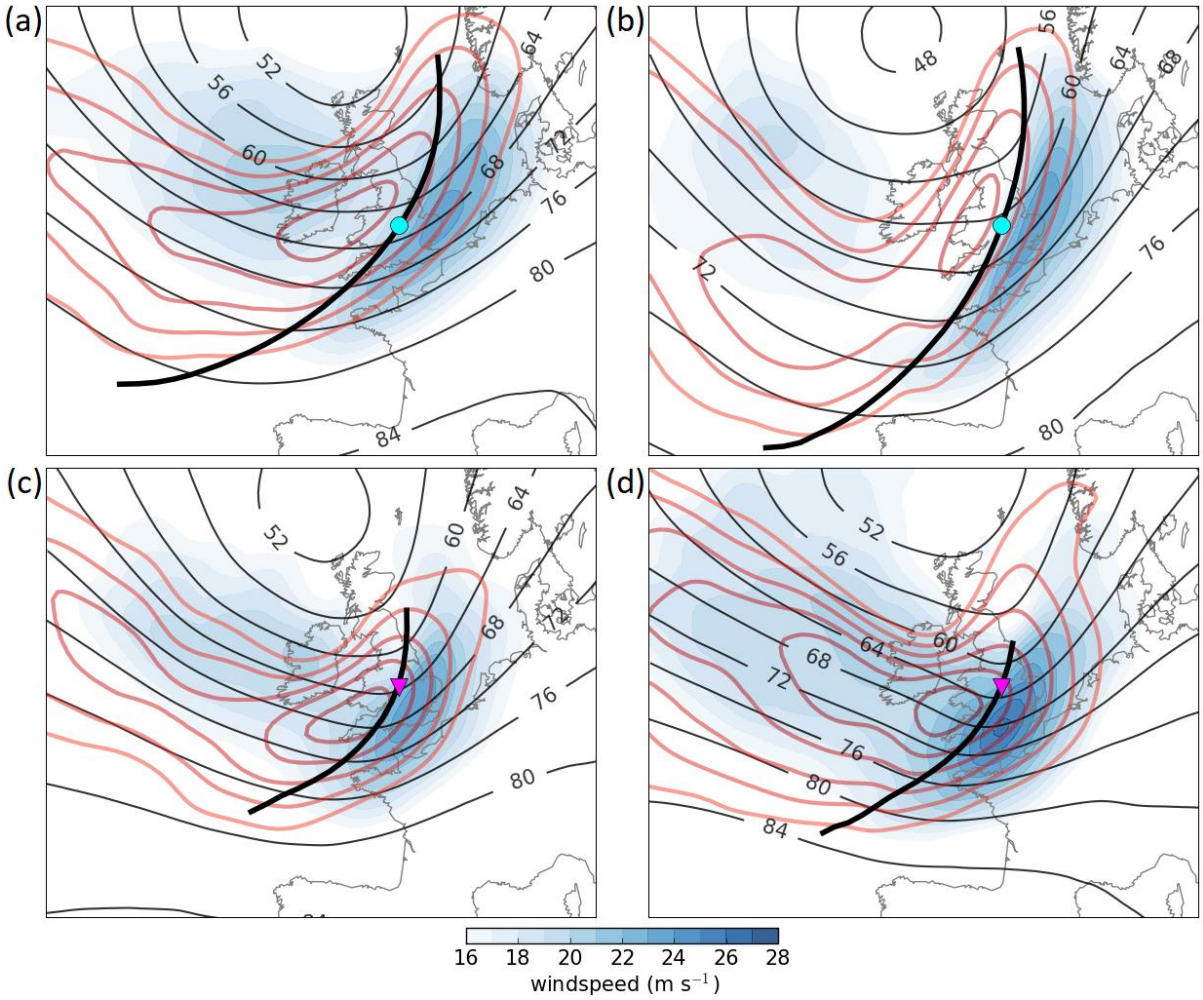

Figure 2.6: Composite plots on translated, rotated grids for all event classes: (a) low-vorticity non-tornadic; (b) high-vorticity non-tornadic; (c) tornadic; (d) high-tornadic. 925 hPa geopotential height (black contours; contour interval 4 DAM), 925 hPa wind speed (grey shading, as per the colour scale) and 300 hPa wind speed (bold, pink contours; contour interval 5 m s^{-1} starting at 30 m s^{-1}). Bold black line indicates the mean position of the surface front for each event class, plotted only where ≥67% of events contribute an analysis point at the corresponding normalised along-front distance (where the origin is set to the mean along-front distance of tornado reports (magenta inverted triangle) or UK land analysis points (cyan circle)).

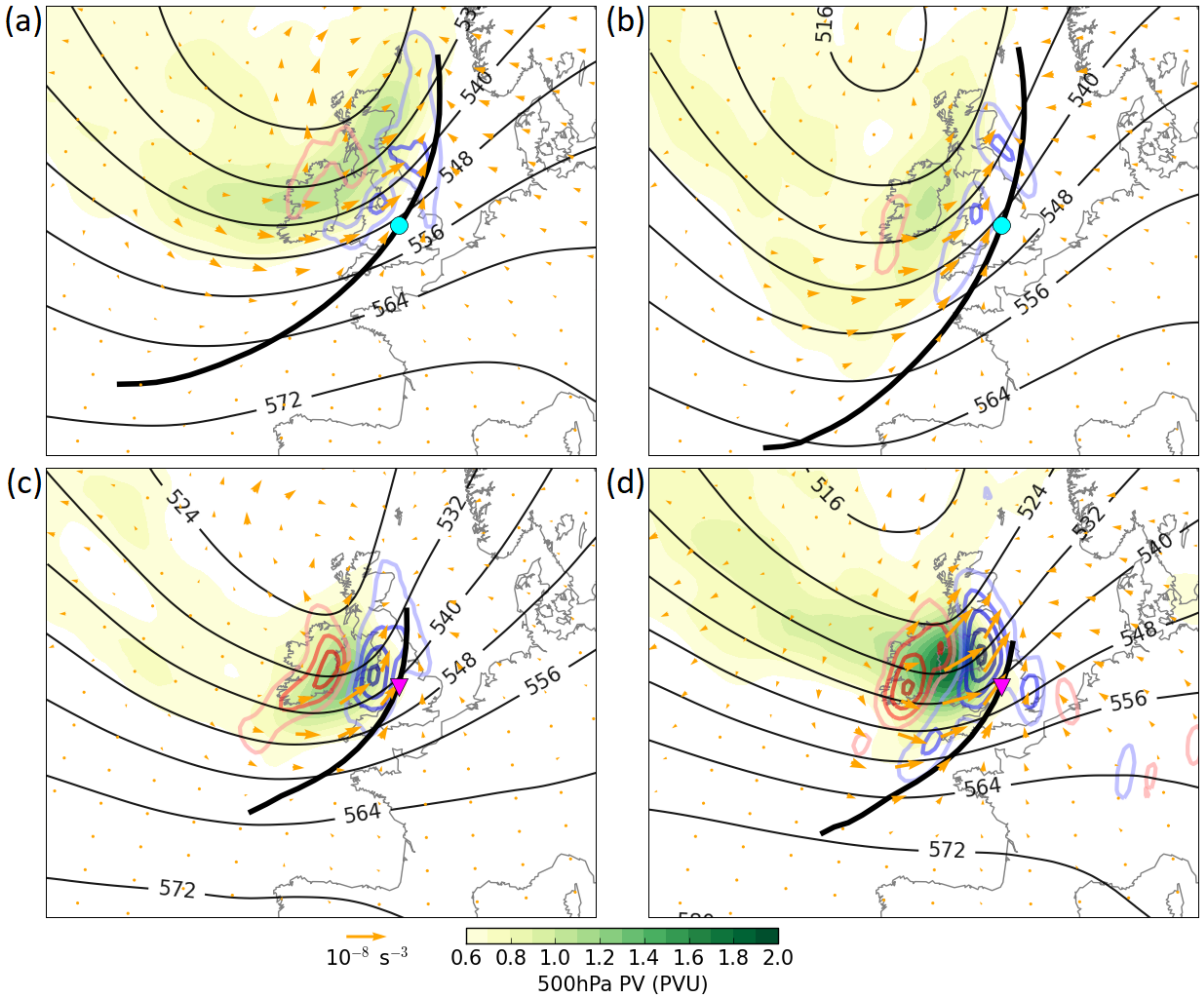

Figure 2.7: Composite plots on translated, rotated grids for all event classes: (a) low-vorticity non-tornadic; (b) high-vorticity non-tornadic; (c) tornadic; (d) high-tornadic. 500 hPa geopotential height (black contours; contour interval 8 DAM), 500 hPa PV (yellow-green shading, as per the colour scale), vorticity advection term of the quasi-geostrophic height tendency equation calculated at 500 hPa (red and blue contours indicating forcing for pressure rises and falls, respectively; contour interval 0.5 x 10^{-12} s^{-3} with the zero contour supressed) and Q vectors calculated using the mean temperature and wind fields over the 300 – 700 hPa layer (orange arrows). Composite frontal positions are shown by bold black lines, as described for Figure 2.6.

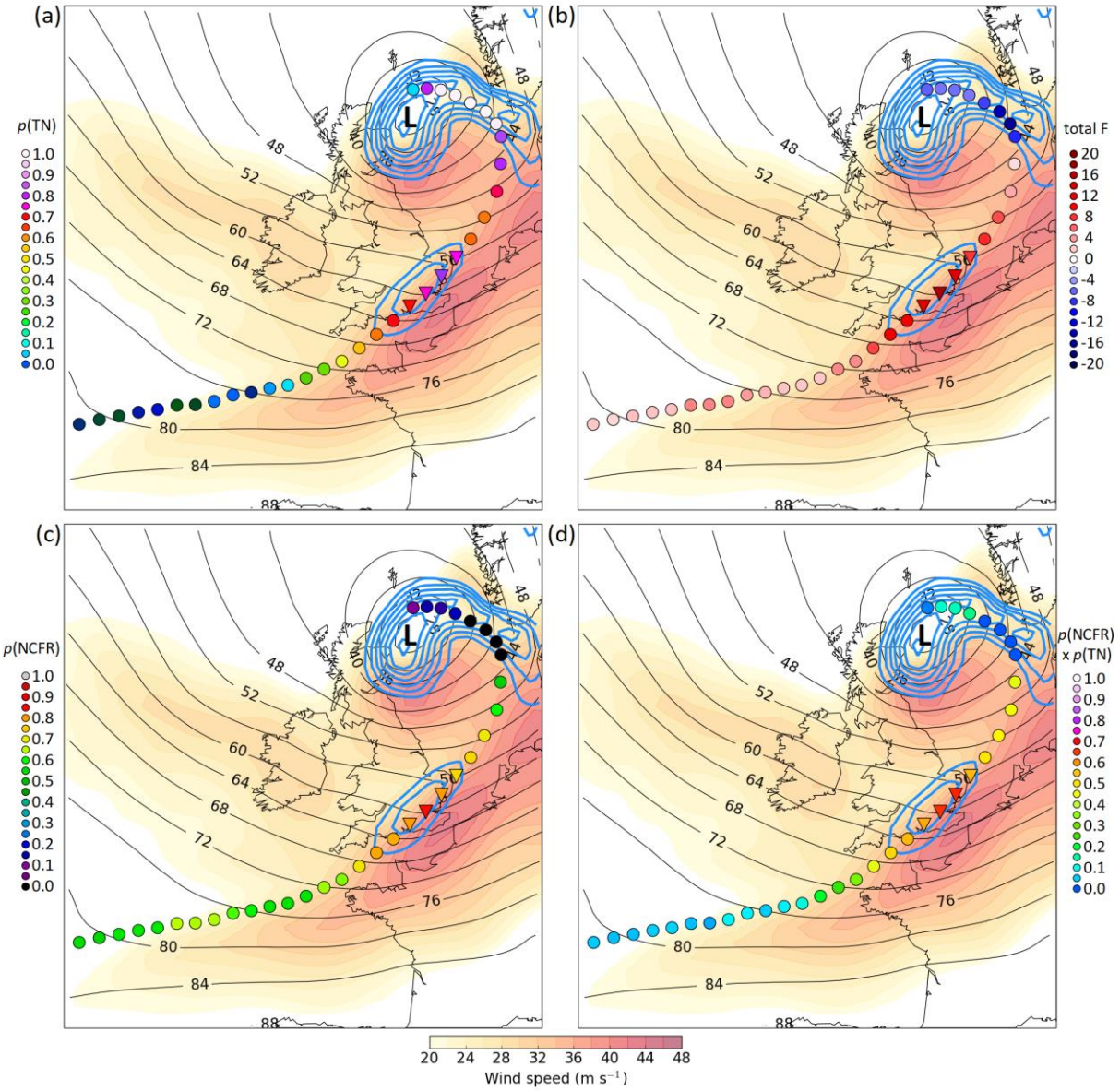

Figure 2.8: ERA-Interim fields at 1200 UTC 3 January 2012; 925 hPa geopotential height (thin black contours at 4 DAM intervals), 850 hPa wind speed (red shading; contour interval 2 m s^{-1} starting at 20 m s^{-1}) and 850 hPa relative vertical vorticity (blue contours at intervals of 0.5 x 10^{-4} s^{-1}, starting at 1 x 10^{-4} s^{-1}). 'L' denotes the centre of the surface cyclone. Coloured circles (triangles for tornadic and near-tornadic analysis points) show along-front point values of selected parameters, according to the colour scale at the side of each panel: (a) *p*[TN]; (b) Total frontogenesis (K m^{-1} s^{-1} x 10^{-10}); (c) *p*[NCFR], as based on the value of total frontogenesis (see Appendix C for details); (d) *p*[NCFR]-weighted *p*[TN].

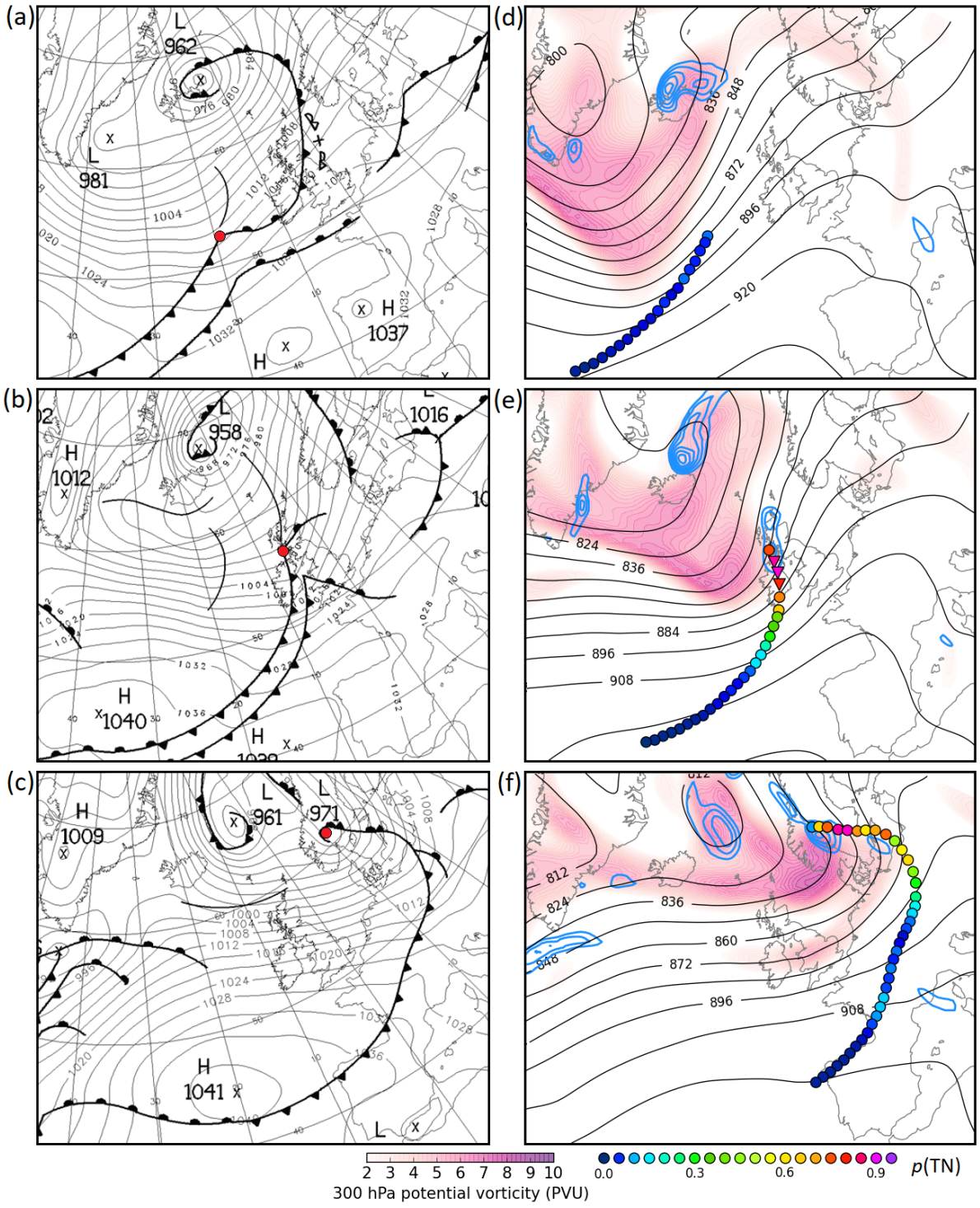

Figure 2.9: (a)-(c): Sequence of Met Office surface analysis charts showing mean sea level pressure (contour interval 4 hPa) and frontal positions. (a) 0000 UTC 1 January; (b) 1200 UTC 1 January; (c) 0600 UTC 2 January 2005. Red circles denote centre of the frontal wave at each analysis time. (d)-(f) ERA-Interim 300 hPa geopotential height (contour interval 12 DAM), 300 hPa PV (purple shading, as per the colour scale) and 850 hPa vertical vorticity (blue contours; contour interval 0.5 x 10^{-4} s^{-1}, starting at 1 x 10^{-4} s^{-1}). (d) 0000 UTC 1 January; (e) 1200 UTC 1 January; (f) 0600 UTC 2 January 2005. Circles (triangles for tornadic and near-tornadic points) in panels (d)-(f) are on-front analysis points; colour shading indicates the magnitude of *p*[TN] at each point (as per colour scale at bottom, right of the figure).

2.3.6 Association of tornadic NCFRs with frontal waves

Surface analysis charts were further inspected in order to quantify the association of tornadic and high-tornadic events with frontal waves, defined here as either a distinct warm-front–cold-front pair, or an inflection point (suggestive of a diminutive frontal wave; Hewson, 2009). Frontal waves meeting this definition were found near the UK and Ireland in 42.3% of tornadic and 72.2% of high-tornadic cases (i.e., 54.5% of events producing any number of tornadoes). Inspection of reanalysis fields at the 925 and 850 hPa levels further revealed the presence of a local maximum in relative vertical vorticity near to the reported location of tornadoes in 60.0% of tornadic and high-tornadic cases without a warm-front–cold-front pair or inflection point, suggesting the possible presence of incipient or diminutive frontal waves (Hewson, 2009). An example of the latter occurred on 3 January 2012 (Figure 2.8); a local maximum in 850 hPa relative vertical vorticity is evident over southeast England at 1200 UTC, where at least one tornado occurred. Radar and surface data indicated the presence of a shallow frontal wave over the area (e.g., Figures 14 and 15 of CP14), which was evidently too weak to have been included in the ASXX charts. These results suggest that up to 77.3% of tornadic and high-tornadic events may have been associated with a frontal wave of one kind or another. Frontal waves were also present in a minority of non-tornadic NCFRs; these events, and factors distinguishing between tornadic and non-tornadic waves, are discussed in Appendix D.

2.3.7 A conceptual model for tornadic NCFRs associated with frontal waves

As a frontal wave amplifies, the along-front distribution of key parameters undergoes a characteristic temporal evolution. The typical evolution is illustrated well by the high-tornadic case of 1 January 2005 (Figure 2.9). A frontal wave developed along a trailing cold front to the southwest of the UK early on 1 January 2005. The wave amplified rapidly as it crossed the UK between 0600 and 1800 UTC, before maturing into a relatively deep cyclone of 971 hPa over Norway by 0600 UTC 2 January 2005 (Figure 2.9(a)-(c)). ERA-Interim fields show a potent PV maximum approaching the trailing front from the cold air side, coming into close proximity with it and inducing the wave development just before the front reached Ireland (Figure 2.9(d)-(f)).

At the outset of wave development, shear vorticity and $-v'_{cold}$ are small everywhere along the front (Figure 2.10). However, as the wave develops, values of

both parameters increase rapidly near to the wave's centre. A maximum in shear vorticity develops at the wave centre (Figure 2.10(b)), whilst a maximum in $-v'_{cold}$ develops several hundred kilometres down-front of the wave centre, where the front begins to bulge forwards (Figure 2.10(c)). *p*[TN], based on a combination of these two parameters, therefore increases very rapidly in the early stages of wave development, with a well-defined maximum developing just down-front of the wave centre (Figure 2.10(a)). In the analysed case, the largest value of *p*[TN] at 0600 UTC is 0.38, increasing to 0.88 by 1200 UTC and reaching a peak of 0.98 at 1800 UTC, by which time the front had moved out of the UK and into the North Sea. The tornadoes (star-shaped markers in Figure 2.10) occurred in the region of rapidly increasing *p*[TN].

The Lagrangian evolution may be evaluated using a front-following point passing through the region with tornado reports (Figure 2.11; the trajectory of this point is constructed using the methodology described in Section 2.2.5). Tornadoes occurred near the end of the period of rapidly increasing *p*[TN] and close to the time of maximum *line-relative* $-v'_{cold}$. The associated acceleration of this part of the front may be inferred from the position of on-front analysis points in Figure 2.10, the front having travelled a greater distance during the 1200 – 1800 UTC 1 January period than during the preceding 6-hour period.

High values of *p*[TN] persist for ~6 to 12 hours after the known tornadic phase of the cold front (e.g., over southern Norway and northern Denmark in Figure 2.10(a)). Whilst it is possible that further tornadoes occurred after frontal passage over the UK, the lack of reports over northeast England and southeast Scotland suggests that the tornadic phase ended before the front crossed into the North Sea. The evolution of total frontogenesis provides a possible explanation for the cessation of tornadoes in spite of continuing high *p*[TN]; after peaking near the wave centre early in the wave's development, frontogenesis begins to decrease, eventually becoming negative in the high *p*[TN] region, just down-front of the wave centre (e.g., over Scandinavia in Figure 2.10(d)). Of the eight tornadic and high-tornadic cases falling most obviously into the frontal wave type, as described for the 1 January 2005 case, seven exhibited a similar transition from frontogenesis to frontolysis in the high *p*[TN] region as the wave matured, with seven exhibiting an associated transition from positive to negative bulk confluence in the same region. This evolution is consistent with frontal fracture in the

Shapiro-Keyser cyclone lifecycle model (Shapiro and Keyser, 1990), and likely explains the oft-observed dissipation of the NCFR just down-front of the wave centre as the wave begins to mature. Whilst the NCFR tends to persist longer along the trailing part of the front, where frontogenesis generally remains positive, *p*[TN] is generally low in this region. Transition from frontogenetic to frontolytic flow in the otherwise tornado-favourable region just down-front of the wave centre may therefore signify the end of the period favourable for tornadoes in cases following the frontal wave conceptual model.

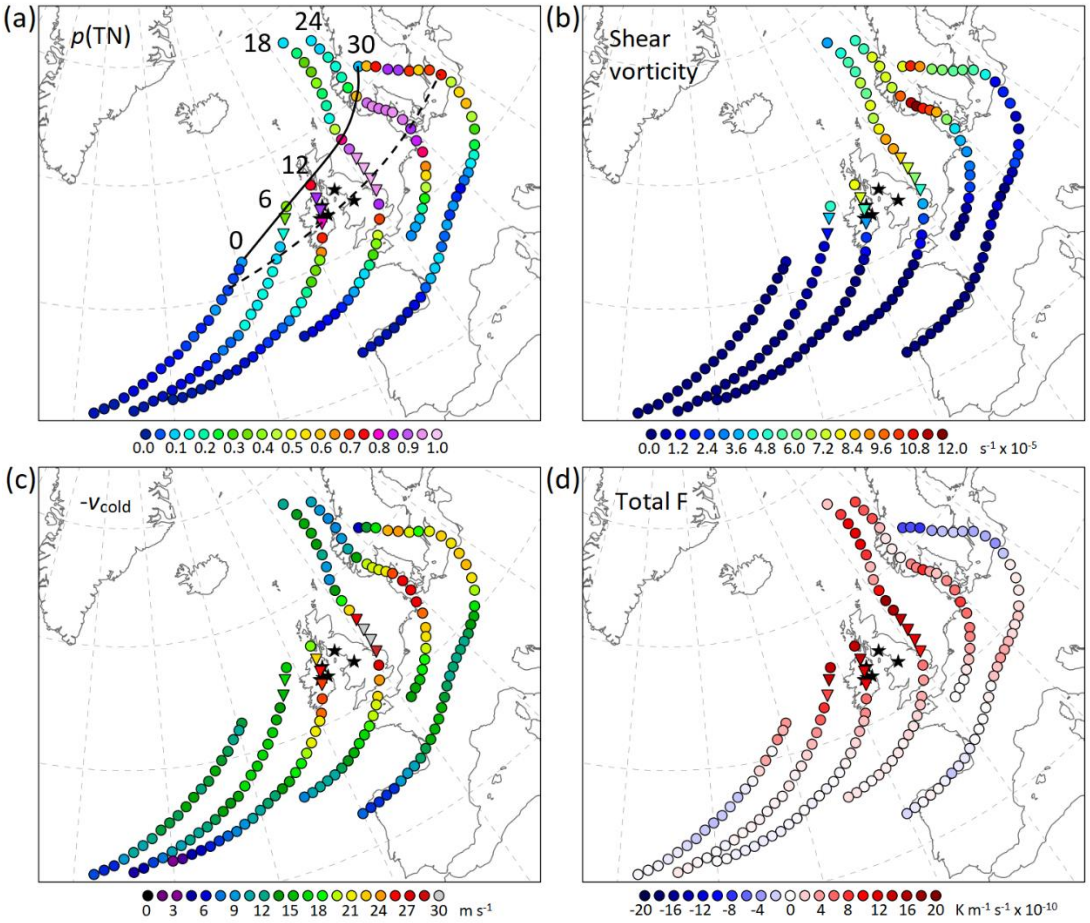

Figure 2.10: Evolution of selected parameter values for the high-tornadic case of 1 January 2005. (a) *p*[TN]; (b) Shear vorticity; (c) $-v'_{cold}$; (d) Total frontogenesis. On-front analysis points are shown by coloured circles (inverted triangles for tornadic and near-tornadic points), with colour shading indicating the magnitude of the corresponding parameter (as per colour scale below each panel). Black star symbols are tornado reports. Solid and dashed black lines in panel (a) denote, respectively, the track of the frontal wave centre and the track of a Lagrangian analysis point passing through the region of tornado reports. Figures in panel (a) denote the analysis time in hours after 0000 UTC 1 January 2005.

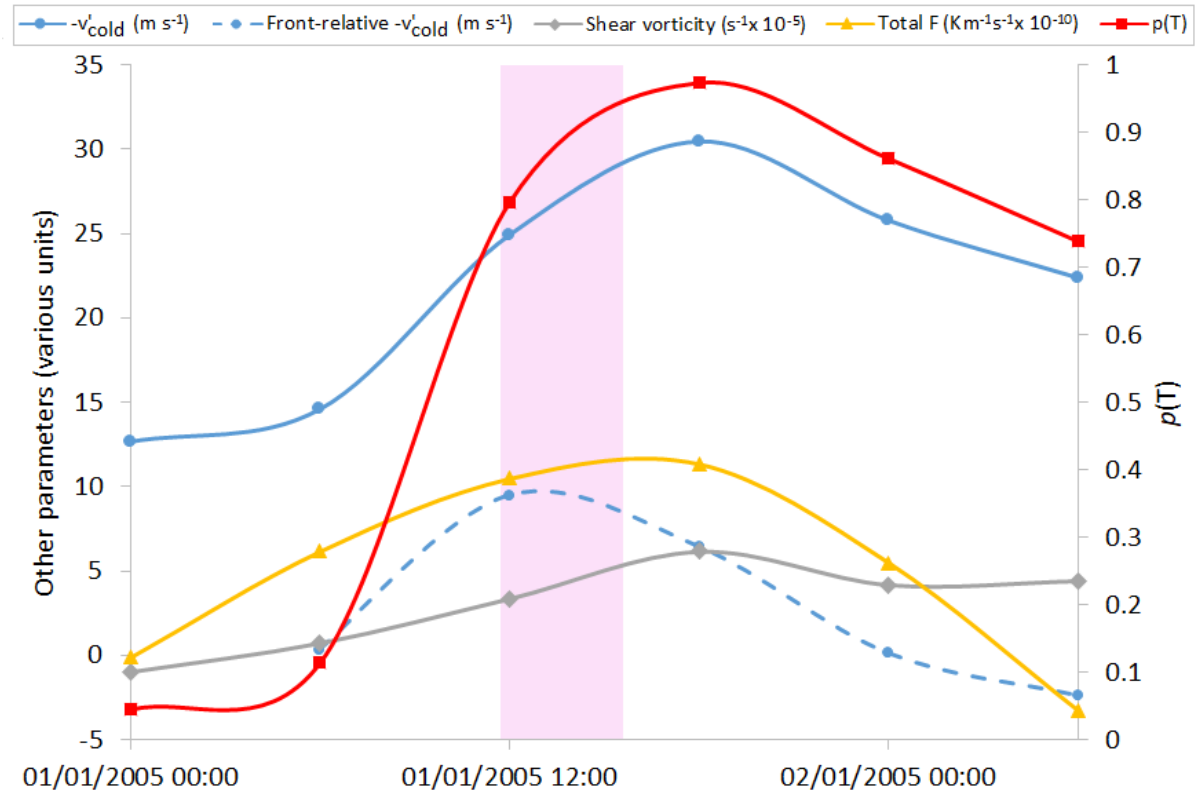

Figure 2.11: Time series of selected parameter values for a Lagrangian point passing though the region of tornado reports on 1 January 2005 (the trajectory of this point is shown by the dashed line in Figure 2.10(a)). Magenta shading denotes the tornadic phase of the event.

2.3.8 A conceptual model for tornadic NCFRs not associated with frontal waves

Further analysis of the ASXX charts and ERA-Interim fields for tornadic and high-tornadic events without a frontal wave shows that many of these events occur within a synoptic regime characterised by large-scale amplification, with ridge building upstream of the UK and trough extension immediately downstream. 75.0% of non-wave cases exhibited strong curvature of the front near to the location of the tornadoes (convex on the warm side). The along-front distribution of shear vorticity and $-v'_{cold}$ along this 'frontal bulge' is similar to that found along the meso-α-scale bulge down-front of the secondary cyclone in frontal wave cases, with tornadoes occurring close to the associated *p*[TN] maximum in both types of event.

ERA-Interim wind fields show that frontal bulges in non-wave cases are associated with a discrete and often intensifying wind maximum between 925 and 300 hPa. Winds are orientated at a large angle to the front and point towards the warm air. At upper-levels, the wind maximum comprises a well-defined jet streak embedded

within the broader jet stream. The centre of the jet streak is typically located on the immediate cold side of the surface front, but strong flow also extends over the surface front. In 70.0% of cases without frontal waves or inflections (i.e., 31.8% of all tornadic and high-tornadic events), the tornadoes occurred underneath, or on the immediate cyclonic shear side of this jet streak (in agreement with the results of Gatzen (2011) and Clark (2013)).

60.0% of the non-frontal-wave tornadic and high-tornadic events (27.3% of all tornadic and high-tornadic events) were associated with northerly or north-westerly flow regimes, usually with low pressure areas moving rapidly southeast across the North Sea and a strong, amplifying ridge to the west and southwest of the UK (accordingly, these cases will be referred to as 'north-westerly flow' events). Differences between this and the frontal wave scenario are illustrated by comparing composite fields for events fitting this north-westerly flow type most obviously (8 February 1984, 28 January 2004, 24 November 2005, 29 August 2010, 12 September 2012, 20 November 2013 and 25 January 2014) with those for events fitting the frontal wave conceptual model most obviously (20 October 1981, 21 September 1982, 4 April 2004, 4 October 2004, 1 January 2005, 30 December 2006, 24 September 2007 and 17 October 2011) (Figure 2.12). At the analysis time closest to the tornado reports (i.e., t + 0 hours; Figure 2.12(c)), the mean tornado location is under the forward, left (i.e., cyclonic shear) flank of the jet streak and near the centre of the well-defined bulge in the surface cold front. An intense PV maximum is located at the cyclonic shear (i.e., northeast) flank of the jet streak, centred immediately behind the tornadic part of the front.

Further insight is provided by analysis of the evolution of composite fields over the period beginning 12 hours before and ending six hours after tornado occurrence (Figure 12(a)-(d)). Initially, the PV maximum is located to the rear of the front (Figure 2.12(a)). Over time, it gradually approaches the front, with the leading edge of PV > 1.0 PVU overtaking the surface front close to the time of tornadogenesis (Figure 2.12(c)). The lower- and upper-level flow veers substantially over the same period, especially in the post-frontal region. The jet streak intensifies between t - 12 and t + 0 h, with core speeds at 300 hPa increasing from ~50 to ~60 m s^{-1}. Caution is required in the interpretation of apparent changes in intensity given that the position of features relative

to the origin is likely to vary more the further the analysis time is from that at which the origin is fixed (i.e., t + 0), as a consequence of the variable trajectories of these features (Ayrault et al., 1995). However, in this case, inspection of fields for individual events shows intensification of the jet over the period t - 18 to t + 0 h in four of the seven cases, with subsequent weakening of the jet in the six hours following tornadogenesis in six of the seven cases. The substantial veering and slight strengthening of the 925 hPa flow field near the front over the t - 18 to t + 0 h period, associated with the large-scale amplification, results in increases in $-v'_{cold}$ near the bulging section of front during the pre-tornadic period and an acceleration of the front (increasing front-normal forward motion).

By way of comparison, composite fields for frontal wave events over the period t – 12 to t + 6 h are shown in Figure 2.12(e)-(h). The 925 hPa geopotential height field strongly resembles that in the composites for all tornadic and high-tornadic events (*cf.* Figure 2.6(c)-(d)), again demonstrating the predominance of the frontal wave scenario. Relative to the north-westerly flow cases, the PV maximum at t + 0 is slightly weaker and located slightly further rearward of the surface front. However, in common with north-westerly flow cases, the PV maximum intensifies in the ~12 hours prior to tornadogenesis (*cf.* Figures 2.12(e) and (g)).) The mean position of the secondary cyclone's centre is marked by a local maximum in low-level relative vertical vorticity and, on its poleward flank, a local weakness in the 925 hPa geopotential height gradient, centred at t + 0 h over northern England, and therefore just up-front of the mean tornado location. The 300 hPa jet is slightly weaker than in the north-westerly flow composite (~50 m s^{-1} near the jet core) and orientated at a shallower angle to the front. The front exhibits a bulge that is less amplified, but of longer wavelength, than that in north-westerly flow cases. The small amplification of the bulge at t + 0 h likely reflects the fact that tornadoes tend to occur at a relatively early stage in the development of the frontal wave.

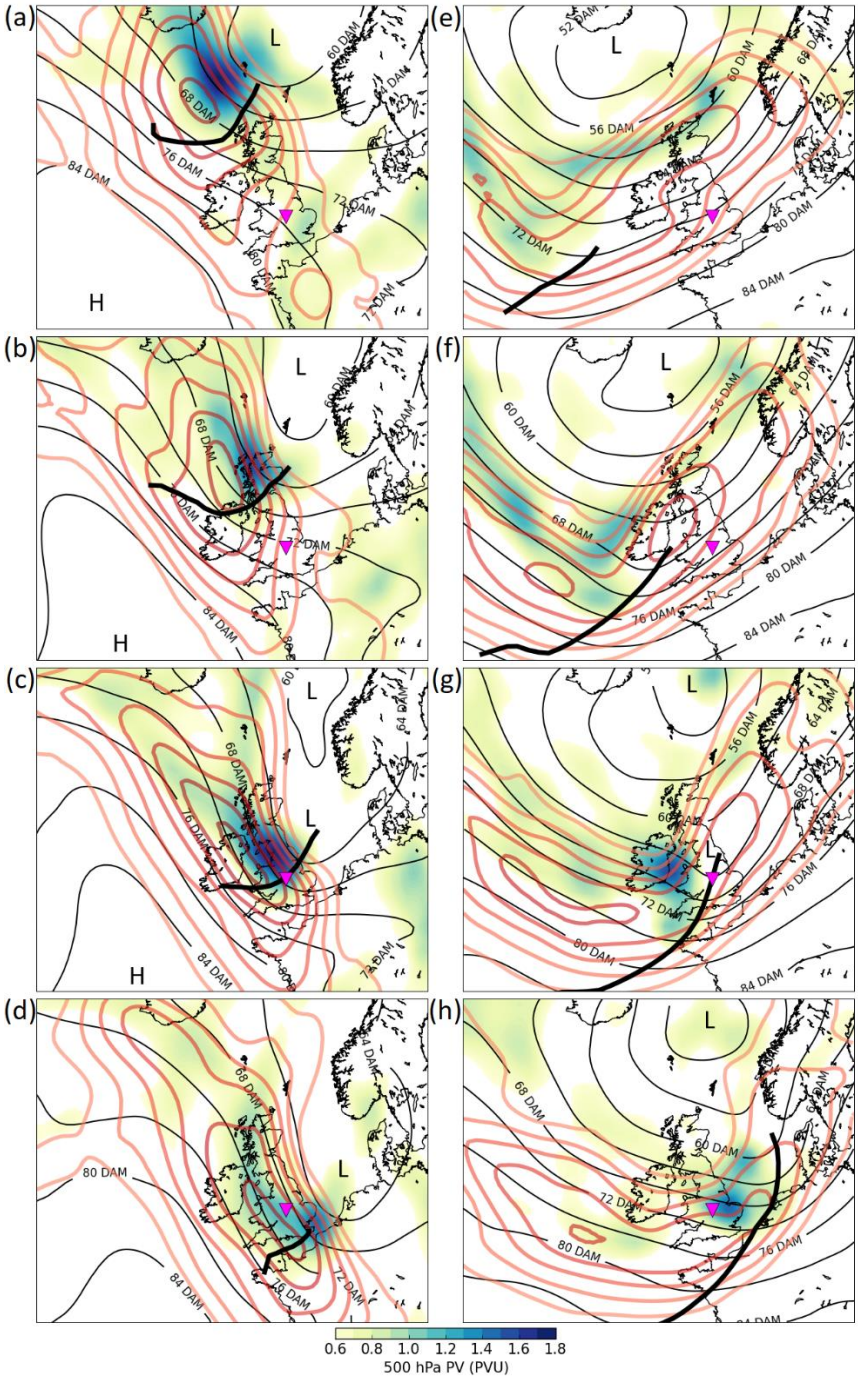

Figure 2.12: Composite fields on rotated, translated grids for seven north-westerly flow cases (panels (a)-(d)) and eight frontal wave cases (panels (e)-(h)) over the period t – 12 hours (top row) to t + 6 hours (bottom row), where t + 0 hours is the analysis time closest to the mean tornado report time. Bold black lines show mean frontal positions at each analysis time, plotted only where ≥67% of events contribute an analysis point at the given normalised along-front distance, where zero is taken to be the mean along-front distance of tornado reports in each event. Thin black contours show 925 hPa geopotential height (contour interval 4 DAM), bold, pink-red contours 300 hPa wind speed (5 m s^{-1} contour interval starting at 30 m s^{-1}) and green-blue shading 500 hPa PV (as per the colour scale). Rotation and translation of the domain are as described in Figure 2.6, whereby the mean tornado report location is set to 51.5°N 2.0°W (magenta inverted triangle in each panel).

2.4. Discussion

In this section, results are discussed in light of existing literature on cold fronts, frontal waves, and NCFRs. Firstly, we explore the origins of large shear vorticity and $-v'_{cold}$ in frontal waves with the aid of a simple model. Secondly, we explore the variability of static stability amongst the identified event classes. Thirdly, we consider how the results relate to candidate vortex-genesis mechanisms in NCFRs and QLCSs.

2.4.1 Exploring the origins of large shear vorticity and $-v'_{cold}$ in frontal waves

In this section we use a simple model to illustrate how large values of shear vorticity and $-v'_{cold}$ come to arise within a frontal wave. In the model, the geostrophic flow is split into three components: that associated with the synoptic-scale, background pressure field, that associated with the frontal trough's pressure field, where the front bears the characteristic S-shaped inflection associated with the early stages of wave development, and that associated with the secondary cyclone's pressure field. The morphology of the frontal trough, secondary cyclone, and their associated geostrophic flow fields, are described in Appendix E.

i) Shear vorticity

In the simple model, the background flow field is assumed to be uniform on the scale of the frontal wave and trough. Furthermore, the along-front component of flow associated with the frontal trough is assumed to be in geostrophic balance (as confirmed by Figure 2.5 for the set of cases analysed herein). Under these conditions, and in the absence of a secondary cyclone, large shear vorticity at the front is symptomatic of a deep frontal trough. This is because the geostrophic flow associated with the trough is of equal magnitude, but opposite sign, at given distance from the trough axis on each side of the trough (i.e., large $-du'/dy'$ across the trough axis; see Appendix E). For a fixed trough width, the magnitude of the opposing along-front flow on each side of the trough increases with increasing trough depth. However, where a secondary cyclone is present, the associated cyclonic anomaly flow field also contributes to the bulk shear vorticity, especially where the radius of curvature of the anomaly flow field is small relative to the distance across which the bulk measures are calculated, and where the anomaly flow field is strong. Given superposition of a cyclonic anomaly flow field on that associated with a frontal trough of uniform depth in the along-front direction, bulk shear vorticity

will therefore be maximised near the centre of the frontal wave (Figure 2.13(a)), and will increase as the magnitude of the anomaly cyclonic wind field increases in an intensifying wave.

Although various mechanisms may contribute to the development of a frontal trough (e.g., Schultz, 2005), the feature is usually attributed to the anomalous warmth of the atmospheric column within the frontal zone, relative to that within the air masses on either side of the front (e.g., Godson, 1951). Since latent heating contributes substantially to the column-integrated warm anomaly in the frontal zone, a deep frontal trough (and therefore large geostrophic shear vorticity) may be symptomatic of large latent heating rates in strong updrafts comprising the ascending branch of a strong front-transverse ageostrophic circulation. The association of strong front-transverse circulations with frontogenesis implies that deep troughs are associated with intensifying fronts in strongly frontogenetic environments. These ideas are supported by the strong positive correlation between total frontogenesis and shear vorticity in the set of tornadic and near-tornadic analysis points in the current sample of fronts; a linear fit between $\log_e$(total frontogenesis) and shear vorticity yields an r^2 value of 0.4788 (not shown). Since the frontogenesis also tends to be maximised near to the wave centre early in the evolution of the secondary cyclone (e.g., Figure 2.10(d)), this suggests the trough is likely to be deepest (and therefore its contribution to the shear vorticity greatest) near the frontal wave centre at these early development stages. This aspect is not represented in Figure 2.13 since the trough is depicted as being of uniform depth across the domain.

In summary, the above considerations suggest that large bulk shear vorticity is symptomatic of fronts with deep troughs that are undergoing strong frontogenesis, especially where embedded within cyclonic anomaly flow fields associated with secondary cyclones. This explains why it tends to be maximised along the front near to the centre of actively developing secondary cyclones.

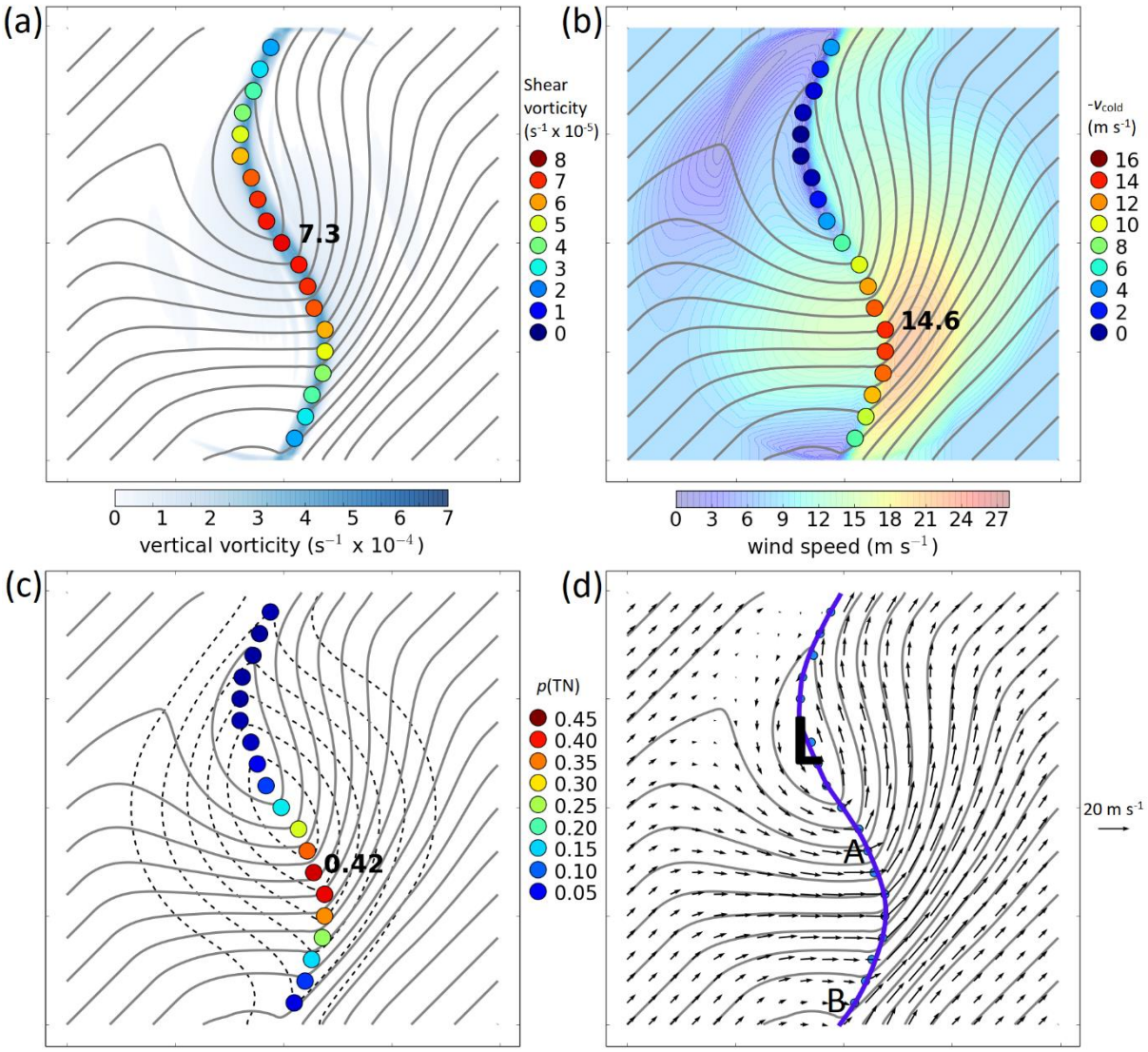

Figure 2.13: Idealised depiction of the pressure field (grey contours at 1 hPa intervals) in the early stages of frontal wave development along a trailing cold front (see Appendix E for details). Bulk measures of various parameters at on-front analysis points are shown by colour-shaded circles. (a) Vertical vorticity (shading) and shear vorticity (coloured circles); (b) Total geostrophic wind speed (shading) and $-v'_{cold}$ (coloured circles); (c) Pressure deficit from background (dashed contours; contour interval 1 hPa) and *p*[TN] (coloured circles). (d) Total wind field (vectors) and position of the frontal boundary (blue line). 'L' denotes centre of local pressure minimum associated with the frontal wave. Letters 'A' and 'B' denote regions of differing trough morphology on opposite sides of the meso-α-scale frontal bulge located down-front of the wave centre (following CP14). In panels (a)-(c), the maximum value of each bulk parameter is shown in bold type adjacent to the point at which the maximum occurs.

ii) Post-front normal flow, $-v'_{cold}$

In a situation with uniform background flow, and for an initially straight front, $-v'_{cold}$ is maximised down-front of the frontal wave due to the superposition of background

and anomaly flow fields. Down-front of the wave centre, the anomaly flow points towards the warm air and therefore contributes positively to $-v'_{cold}$ (Figure 2.13(b)). As discussed previously, and as depicted in Figure 2.13, the front tends to bulge forwards on the meso-α scale in this region, owing to the controlling influence of $-v'_{cold}$ on the front-normal forward motion. On the up-front flank of the wave, the anomaly flow contributes negatively to $-v'_{cold}$ and is associated with a local minimum in front-normal forward motion. The associated along-front variations in front-normal forward motion result, over time, in development of the characteristic 'S'-shaped inflection in the front.

Near the centre of the wave, the front rotates cyclonically as the wave amplifies. For an initially positively tilted front, the rotation is towards smaller positive tilt (i.e., from initial north-south (positive tilt) to northwest-southeast (neutral tilt) in the example illustrated, where the front is embedded in south-westerly large-scale flow). On the outer flanks of the S-shaped inflection, further up-front and down-front of the wave centre, the rotation is in the opposite sense i.e., the front rotates anticyclonically, and therefore becomes more positively tilted with time. This differential rotation in an initially positively tilted front results in troughs resembling CP14's type B structure (post-frontal pressure gradients << pre-frontal gradients) up-front of the wave centre and on the trailing section of front well down-front of the wave centre, and CP14's type A structure (post-frontal gradients ≈ pre-frontal gradients) immediately down-front of the wave centre (Figure 2.13(d)). In other words, the angle between the frontal trough and the background large-scale flow field has a controlling influence on the geometry of the trough (as seen in geopotential height or pressure fields), with modulation of this angle yielding the characteristic along-front variability in trough structure within and near frontal waves.

Given the initial positive tilt of the front, the cyclonic rotation near the wave centre causes the front to become orientated at a larger angle to the mean, large-scale flow (i.e., the cross-frontal component of the mean, large-scale flow increases), such that $-v'_{cold}$ will increase even in the absence of changes in the total wind field. A neutrally or negatively tilted front undergoing such rotation would conversely experience reducing $-v'_{cold}$. However, the latter situation appears to be highly atypical of NCFR-bearing fronts; only 1.2% of points in the current sample exhibited a local

orientation ≥90° (i.e., perpendicular to the flow, or negatively tilted). Median values of the angle between the front and the large-scale flow field in the filtered high-tornadic, tornadic and non-tornadic datasets were 56.5, 50.5 and 33.6°, respectively (Table 2.1).

Where the front possesses a strong ageostrophic transverse circulation, this circulation may also contribute to $-v'_{cold}$ immediately behind the front (i.e., in the lower branch of the circulation, where flow is directed towards the warm air). This aspect is not represented in the idealised fields in Figure 2.13 but, again, contributions might reasonably be expected to be maximised near the centre of the frontal wave in the early stages of wave development, where frontogenesis is maximised (as discussed in Section 2.3.7).

In summary, two processes contribute to the along-front maximum in geostrophic $-v'_{cold}$ near to frontal waves. Firstly, a contribution arises from the secondary cyclone's anomaly flow field. This is maximised down-front of the cyclone centre where the anomaly flow points towards the warm air. Secondly, a contribution arises from the local cyclonic turning of the front near the wave centre, in cases where the front exhibits an initial positive tilt (such that the rotation brings it closer to orthogonality to the large-scale flow). This contribution is maximised close to the wave centre. The sum of these effects is therefore maximised immediately down-front of the wave centre. Ageostrophic effects may also contribute to the total $-v'_{cold}$ where the frontogenesis is large, near the centre of the wave.

2.4.2. Influence of stability and its variation with tornadic NCFR type

CP14 showed that tornadic NCFRs with relatively small vertical vorticity tend to have smaller saturated static stability (N_S^2) in the pre-frontal environment, suggesting that in these cases buoyant instability may have played a greater role in driving NCFR updrafts and, potentially, in the tornadogenesis process. In order to investigate the distribution of stability in the current set of cases, surface–850 hPa N_S^2 was calculated at the warm air analysis point for all tornadic and near-tornadic points in tornadic and high-tornadic events. Results show that 78% of tornadic and near-tornadic points have pre-frontal N_S^2 > 0 (i.e., moist statically stable environments). Only a very weak positive correlation was found between N_S^2 and shear vorticity (r^2 = 0.06; not shown); however, a stronger positive correlation was found between N_S^2 and $\log_e$(total frontogenesis) (r^2 = 0.20;

Figure 2.14(a)). Furthermore, points from the eight cases conforming most obviously to the frontal wave scenario (inverted triangle symbols in Figure 2.14) tend to be characterised by larger frontogenesis and larger stability than those from the seven cases conforming most strongly to the north-westerly flow scenario (star symbols in Figure 2.14). The median N_S^2 for frontal wave events is 0.95 x 10^{-4} s^{-2}, which compares to 0.23 x 10^{-4} s^{-2} for north-westerly flow events. Median total frontogenesis is 14.2 x 10^{-10} K m^{-1} s^{-1} for frontal wave events and 5.4 x 10^{-10} K m^{-1} s^{-1} for north-westerly flow events, with differences significant at the 99% level ($p < 0.0001$). These differences are further illustrated by construction of smoothed kernel densities within the two-dimensional parameter space for points from each tornadic event type (colour shading in Figure 2.14(a)); the peak density in frontal wave cases is situated further towards the top, right-hand side of the parameter space than it is in north-westerly flow cases. Similar stability differences between tornadic event types were found when considering the surface–850 hPa lapse rate (not shown), for which median values in frontal wave and north-westerly flow cases were 5.15 and 6.66 K km^{-1}, respectively, with differences significant at the 99% level ($p = 0.008$).

Differences between tornadic event types are similarly evident when plotting points in the $-v'_{cold}$ versus $\log_e$(total frontogenesis) parameter space (Figure 2.14(b)) and the $-v'_{cold}$ versus shear vorticity parameter space (Figure 2.14(c)). Frontal wave cases show significantly larger bulk vorticity and slightly smaller $-v'_{cold}$ than north-westerly flow cases, though the spread of $-v'_{cold}$ amongst north-westerly flow cases is large.

In summary, the results presented in Figure 2.14 suggest that tornadic NCFRs occur in a wide range of stability conditions, but that statically stable environments predominate. Where the stability is large, the frontogenesis also tends to be large. One interpretation of these results is that, whilst frontal wave development (with associated large frontogenesis and increasing shear vorticity) is generally required for tornadogenesis in statically stable environments (due to the likely involvement of kinematic instabilities within the frontal shear zone, as discussed in the following section), this requirement relaxes as the stability decreases. This is likely because convective processes (specifically, those associated with buoyant instability, rather than forced ascent) begin to play a greater role as the stability decreases. These results may

be compared with the findings of Moore (1985), who demonstrated the existence of a buoyancy–shear hybrid instability for NCFRs in unstably stratified environments, as distinct from pure HSI in statically stable environments. Given the above results, we tentatively suggest that developing frontal waves of the type described in this study tend to produce environments supportive of pure HSI (given stable stratification in the large majority of cases), whereas north-westerly flow events produce environments that may, in at least some cases, be more supportive of the hybrid buoyancy–shear instability.

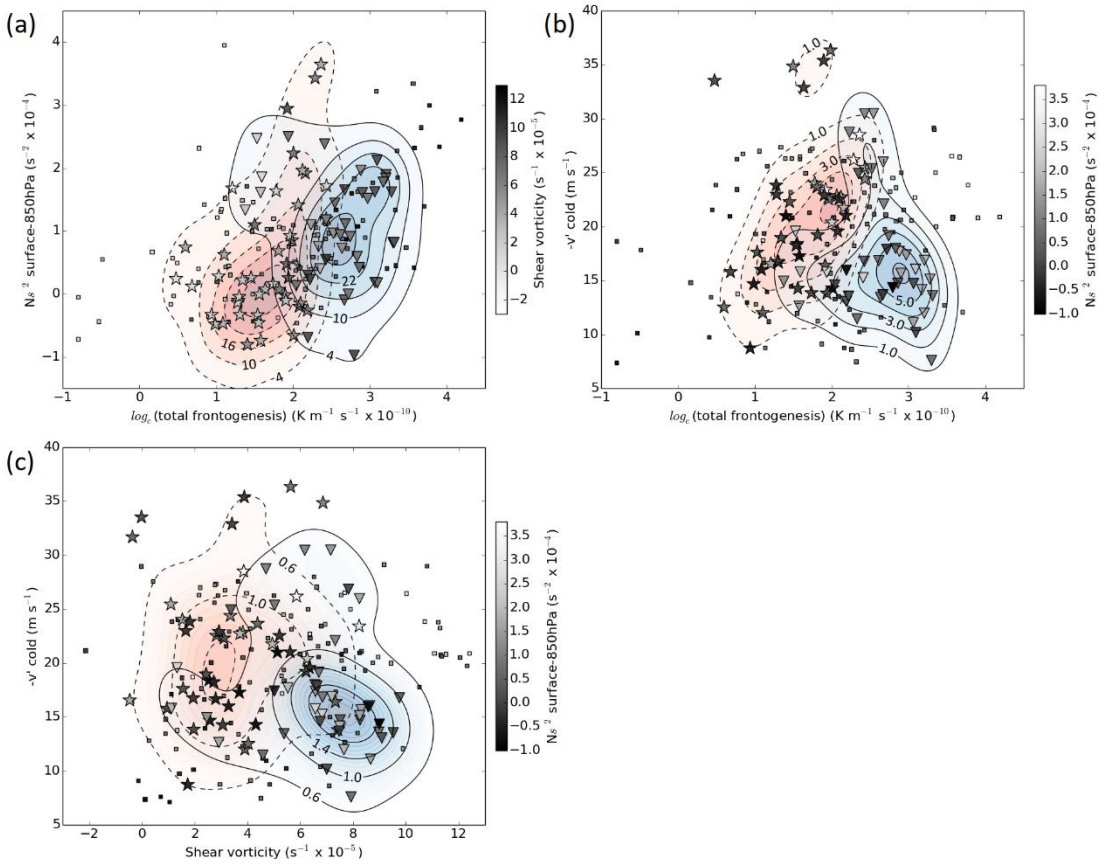

Figure 2.14: Scatterplots depicting parameter values for tornadic and near-tornadic points in tornadic and high-tornadic events. Triangles denote points belonging to the eight events conforming most closely to the frontal wave type, and stars denote points belonging to the seven events conforming most closely to the north-westerly flow type. Squares denote all other points. (a) $\log_e$(total frontogenesis) versus surface–850hPa saturated static stability, coloured by shear vorticity; (b) $\log_e$(total frontogenesis) versus $-v'_{cold}$ coloured by surface–850hPa saturated static stability; (c) shear vorticity versus $-v'_{cold}$ coloured by surface–850hPa saturated static stability. Solid (dashed) contours and blue (red) shading denote the smoothed density of points, per unit area of parameter space, in the frontal wave (north-westerly flow) events.

2.4.3. Hypotheses concerning the relevance of the environmental parameters to candidate vortex-genesis mechanisms

We now further consider how the identified environmental parameters may relate to known vortex-genesis mechanisms within NCFRs, and in QLCSs more generally. The discussion attempts to describe how the quantitative results obtained from the analysis of parameters can be related to various conceptual and theoretical models, and is included in the hope that it will stimulate further discussion and in order to show where future work could usefully be focussed. Some of the proposed mechanisms have been explored through analysis of high-resolution model datasets for two tornadic cases, the results of which will be presented in subsequent publications.

Radar studies show that NCFR tornadoes are often associated with misocyclones forming along a narrow zone of strong vertical vorticity coincident with the surface front and NCFR (Carbone, 1982, 1983; Clark and Parker, 2014). Horizontal shearing instability (HSI), in which an initially uniform sheet of vertical vorticity breaks down (or 'rolls up') into discrete vertical vorticity maxima separated by areas of weaker vertical vorticity, is generally invoked as the vortex-genesis mechanism (e.g., Carbone, 1983; Smart and Browning, 2009). In the non-supercell tornadogenesis mechanism described by Wakimoto and Wilson (1989) and Lee and Wilhelmson (1997), vertical stretching amplifies the vorticity to tornadic strengths when an updraft becomes collocated with the low-level vortex (albeit for shear zone vortices forming along thunderstorm outflow boundaries and other convergence zones, rather than NCFRs). On the other hand, a different mechanism – tilting of ambient horizontal vorticity – has been found to explain vortex-genesis along the leading edge of QLCSs in environments of large buoyant instability and large vertical wind shear (Trapp and Weisman, 2003; Weisman and Trapp 2003; Atkins and St. Laurent, 2009). Although the dynamics of QLCSs and NCFRs differ, the QLCS vortices appear at least kinematically similar to NCFR misocyclones, and so QLCS vortex-genesis mechanisms are also considered here.

i) Shear vorticity

One hypothesis is that this parameter relates to the potential for HSI, and the strength of resulting vortices, along the front. Buban and Ziegler (2016) show that the rate of

development and peak vertical vorticity of vortices forming as a result of HSI is directly proportional to the initial shear zone vorticity. Assuming that larger bulk shear vorticity generally equates to larger vorticity within the NCFR shear zone, this would suggest the potential for stronger and faster developing vortices where bulk shear vorticity is larger, in the event that HSI occurs along the shear zone. Furthermore, Dritschel *et al*. (1991) show that HSI is supressed within a vortex strip when the horizontal strain has a magnitude greater than one quarter of the vertical vorticity within the strip. In the environment of a frontal wave, the bulk confluence (one component of the two-dimensional strain field where the axis of contraction is initially aligned with the front) generally increases near the wave centre as the wave begins to develop, consistent with the large and increasing frontogenesis along this part of the front (e.g., Figure 2.10(d)). However, as the wave continues to amplify, the bulk confluence begins to reduce again along the cyclonically turning part of the front near the wave centre (consistent with the decreasing frontogenesis along this part of the front in the latter stages of wave development, as discussed in Section 2.3.7). The along-front dilatation, which is the other component of the two-dimensional strain, also tends to reduce in the same region as the wave develops (as reflected by the negative median values for tornadic and high-tornadic events; Table 2.1). In contrast, the shear vorticity near the wave centre increases throughout the early to early-mature stages of development (e.g., as in Figure 2.10(b), between Scotland and Norway). In other words, the shear vorticity begins to increase *relative to the strain*, such that an environment initially stable to HSI according to the Dritschel *et al*. (1991) criterion could transition to an unstable state as the frontal wave amplifies. Barotropic instability is known to be an important mechanism for the development of the frontal wave itself in some cases (e.g., Bishop and Thorpe, 1994; Dacre and Gray, 2006); our results suggest that this frontal-wave-scale instability may orchestrate the development of embedded barotropic instabilities at much smaller scales within the frontal shear zone itself. We suggest that this constitutes an important link between the sub-synoptic- and the meso-γ- to miso-scales in such cases.

Another question raised by the frequent presence of frontal waves in the analysed set of cases is why secondary cyclones are apparently more favourable for tornadoes than primary cyclones. The answer may relate to the fact that, in at least some secondary cyclones, the front has already collapsed to a narrow zone at the outset of wave development. In such cases, an NCFR is therefore likely to be present in the

tornado-favourable region in the early to early-mature developmental stages, when vorticity increases relative to the horizontal strain. In primary cyclones, the baroclinic zone is typically much wider at the outset of development, requiring a substantial period for collapse to a similarly narrow zone (e.g., Hoskins and Bretherton, 1972). Since the tornado-favourable region is collocated with the region of frontal fracture in Shapiro-Keyser type cyclones, frontal fracture in at least some primary cyclones may halt collapse before a narrow shear zone has developed, thereby preventing formation of an NCFR in the tornado-favourable region at any stage in the cyclone's development (consistent with the conceptual model of Browning and Roberts (1994), in which an NCFR is present only along the trailing cold front and back-bent front). The ability, or otherwise, for NCFRs to form or persist along the cyclonically rotating part of the front near and immediately down-front of the cyclone centre may therefore represent a key difference between cyclones of different types, and between primary and secondary cyclones in particular, in terms of their potential for hosting tornadic NCFRs.

ii) Post-front normal flow, $-v'_{cold}$

One hypothesis is that large (and in particular, increasing) $-v'_{cold}$ is favourable for intrusion of relatively dry, high PV air into the front from the cold side. A transient period of front-relative forward flow would be expected as $-v'_{cold}$ increases, but before the front-normal forward motion has fully adjusted to the new $-v'_{cold}$, given the correlation between this parameter and front-normal forward motion, and assuming the front-normal forward motion takes some finite time to adjust to evolving $-v'_{cold}$. This period of front-relative forward flow is clearly seen in the temporal evolution of front-relative $-v'_{cold}$ at the Lagrangian point passing through the tornadic part of the front in the 1 January 2005 case (Figure 2.11), with tornadoes occurring close to the time of peak front-relative forward flow[5]

Intrusions of dry air are well known to be associated with the local intensification of NCFRs and QLCSs (e.g., Johns, 1993; Browning and Reynolds, 1994; Yang and Houze, 1995; Browning and Golding, 1995; Browning *et al.*, 1997; Clough *et al.*, 2000), leading to the development of locally severe weather in some cases. The intrusion of dry air promotes evaporative cooling, which may lead to the development

[5] Note, however, that we cannot discount the possibility that this association between front-relative forward flow and tornadogenesis is coincidental in the analysed case.

of local downdraft and near-surface horizontal divergence maxima, or locally enhanced rear-to-front flow within the system. Enhanced convergence, and therefore stronger updrafts, may then occur along the convective line at the leading edge of these features. Atkins and St. Laurent (2009) demonstrate meso-γ-scale vortex-genesis through tilting of ambient horizontal vorticity on the flanks of the resulting updraft and downdraft maxima in such a scenario. An alternative possibility is that narrowing of the shear zone under the influence of the increased confluence, and associated increases in vorticity, could promote the release of HSI should the confluence (and therefore strain) subsequently relax. In NCFRs, the enhanced cross-frontal temperature differences and increased confluence would both act to enhance frontogenesis, which could lead to local intensification of the ageostrophic front-transverse flow, with associated further increases in $-v'_{cold}$. In some cases, this and other processes result in the surface front locally acquiring a density current like structure (e.g., Carbone, 1982; Koch and Kocin, 1991; Browning *et al*., 1997).

An alternative hypothesis as to the relevance of $-v'_{cold}$ (and therefore the front-normal forward motion) relates to the magnitude of the cross-frontal component of vertical wind shear, and its dependency on the strength of the cross-frontal geostrophic flow. Surface friction is known to increase the magnitude of the low-level vertical wind shear (e.g., Schenkman *et al*., 2016; Houser *et al*., 2016). Therefore, it is logical to expect the low-level cross-frontal vertical shear to be larger when the cross-frontal flow is larger, owing to friction acting on the stronger wind field ($-v'_{cold}$ is analysed here at 850 hPa, which is generally just above the friction layer). In support of this idea, wind profiler observations of a large subset of the events investigated herein (not shown) reveal a positive correlation ($r^2 = 0.1009$) between the front-normal forward motion and the cross-frontal component of vertical shear in the 0.5 – 1.5 km AGL layer on the warm side of the front. The cross-frontal component of vertical shear is relevant to the vortex-genesis mechanism of Trapp and Weisman (2003), in which crosswise horizontal vorticity is tilted into the vertical on the flanks of local updraft or downdraft maxima within the QLCS; stronger and deeper vortices were found by Weisman and Trapp (2003) to develop in environments possessing stronger low-level vertical wind shear.

A final hypothesis as to the relevance of $-v'_{cold}$ to the production of damaging meso-γ- or miso-scale shear zone vortices in NCFRs concerns its influence on the

translational velocity of these vortices. Since the frontal shear zone and embedded vortices are constrained to move approximately with the NCFR, larger $-v'_{cold}$ (and therefore larger front-normal forward motion) will equate to greater vortex translational velocity, assuming that the along-front component of translational velocity is relatively invariant. Due to superposition of translational and rotational velocities, and for a vortex of given rotational velocity, larger peak wind speeds will occur in the faster moving vortex where rotational and translational velocities are additive (e.g., on the southern flank of an eastward moving cyclonic vortex; Wakimoto *et al.*, 2006; Atkins and St. Laurent, 2009; Smart and Browning, 2009; Mahale *et al*., 2012). Therefore, for a vortex of given intensity, the damage potential may be greater when the translational velocity is greater.

2.5. Summary

Through analysis of a sample of 114 events, we have demonstrated that statistically significant differences exist between the environments of tornadic and non-tornadic NCFRs. In agreement with CP14, tornadic NCFRs tend to occur in environments with larger vertical vorticity and a larger front-normal component of flow on the cold side of the front ($-v'_{cold}$). A measure of the probability of tornadoes, *p*[TN], based upon the combined value of these parameters, has been derived. Since this measure requires knowledge only of the instantaneous wind field and the position of frontal boundaries, it could be calculated using standard operational model output, coupled with existing objective techniques for identifying the position of frontal boundaries (e.g., Hewson, 1997). The use of bulk measures, as defined in Section 2.2.3, should ensure that the results are robust to model resolution. In this way, a generalised measure of NCFR tornado risk may be forecastable with useful lead time. In view of the inherent unpredictability of some of the features found to have an influence on the timing and location of tornadoes, such as frontal waves, maximum benefit may be realised by applying the technique to output from ensemble models.

In order to complement the analysis of environmental parameters, synoptic situations resulting in high *p*[TN] were explored. Two synoptic situations were found to account for the large majority (>80%) of tornadic and high-tornadic NCFRs:

- Secondary cyclogenesis (i.e., a developing frontal wave) along a trailing cold front, usually in west to south-westerly large-scale flow (at least 54.5% of all tornadic cases, and 72.2% of high-tornadic cases)

- A strong mid-level jet streak approaching and eventually cutting across the front at a large angle to it, within an amplifying large-scale pattern, usually in north-westerly large-scale flow (at least 27.3% of all tornadic cases).

In the frontal wave scenario, tornadoes generally occur down-front of the centre of the secondary cyclone during the early stages of development, where frontogenesis is positive and $-v'_{cold}$ and shear vorticity (and therefore the conditional tornado probability, *p*[TN]) increase rapidly. Waves that evolve into fully fledged secondary cyclones often exhibit a transition to frontolysis down-front of the wave centre later in their lifecycles; associated dissipation of the NCFR (i.e., frontal fracture) effectively ends the period of tornado risk, in spite of the continued presence of large *p*[TN]. A refined measure of tornado probability, which takes into account the magnitude and sign of frontogenesis (and therefore likelihood of an NCFR) likely represents an improvement in this respect (as described in Appendix C). Our recommended approach in frontal wave cases is to use *p*[TN], or the *p*[NCFR]-weighted *p*[TN], as a first order assessment of risk, but to view this in context of the conceptual model described in Section 2.3.7. The estimate of tornado probability provided by *p*[TN] may be refined by considering the lifecycle stage of a given frontal wave at the time that it crosses the region of interest.

The second tornado-favourable situation involves a potent mid- to upper-level jet streak cutting across the front, at a large angle to the front. Tornadoes in this situation generally occur near the axis of the jet streak, or on its immediate cyclonic shear flank, where the front exhibits marked bulging. Most events of this type occurred in north-westerly flow. Large-scale amplification, characterised by upstream ridge building and down-stream trough extension, appears to be an important factor; veering and strengthening of the flow between the amplifying ridge–trough couplet facilitates the approach of mid- to upper-level disturbances originating in the cold air towards the

front. Analysis of stability parameters provided some limited evidence for weaker pre-frontal stability, or greater instability, in north-westerly flow cases compared to frontal wave cases. Together with the generally weaker frontogenesis in north-westerly flow events, this suggests that, on average, convective processes may play a greater role in NCFR development and tornadogenesis in north-westerly cases than in frontal wave cases.

Although we have speculated upon the possible relevance of the identified environmental parameters to vortex-genesis in NCFRs, this aspect remains an open question. Further insight is provided by subsequent analysis of high-resolution model data for a subset of cases, including examples of frontal waves and north-westerly flow events. Results of these investigations, which will be presented in future papers, clarify the nature of the links between frontal shear zone vortex-genesis and the evolution of the larger-scale environment, as suggested by the present study.

Acknowledgments

This study was inspired by the work of the Tornado and Storm Research Organisation (TORRO), and in particular by the early studies of Professor G. Terence Meaden and the late Professor Derek M. Elsom, in which the association of many cold-frontal tornado outbreaks with frontal waves was first noted, following several notable cases in the 1970s and 1980s. The authors are grateful to Paul Brown of TORRO for providing access to the UK tornado database, without which this study would not have been possible. We also wish to thank David Smart and two anonymous reviewers for their comments, which have led to improvements in the content and presentation of this paper. Parker has been supported in part by a Royal Society Wolfson Research Merit Award (2014-2018).

References

Apsley M, Mulder KJ, Schultz DM. 2016. Reexamining the United Kingdom’s greatest tornado outbreak: forecasting the limited extent of tornadoes along a cold front. *Wea. Forecasting* **31**: 853–875.

Atkins NT, St. Laurent M. 2009. Bow echo mesovortices. Part II: Their genesis. *Mon. Wea. Rev.* **137**: 1514–1532.

Ayrault F, Lalaurette F, Joly A, Loo C. 1995. North Atlantic ultra high frequency variability. An introductory survey. *Tellus* **47A**: 671–696.

Bishop CH, Thorpe AJ. 1994. Frontal wave stability during moist deformation frontogenesis. Part II: The suppression of nonlinear wave development. *J. Atmos. Sci*. **51**: 874–888.

Brooks HE, Doswell CA III, Davies-Jones R. 1993. Environmental helicity and the maintenance and evolution of low-level mesocyclones. *The Tornado: Its Structure, Dynamics, Prediction, and Hazards, Geophys. Monogr,* No. 79, Amer. Geophys. Union, 97–104.

Browning KA, Golding BW. 1995. Mesoscale aspects of a dry intrusion within a vigorous cyclone. *Q. J. Roy. Meteor. Soc.* **121**: 463–493.

Browning KA, Pardoe CW. 1973. Structure of low-level jet streams ahead of mid-latitude cold fronts. *Q. J. Roy. Meteor. Soc.* **99**: 619–638.

Browning KA, Reynolds R. 1994. Diagnostic study of a narrow cold-frontal rainband and severe winds associated with a stratospheric intrusion. *Q. J. Roy. Meteor. Soc.* **120**: 235–257.

Browning KA, Roberts NM. 1994. Structure of a frontal cyclone. *Q. J. Roy. Meteor. Soc.* **120**: 1535–1557.

Browning KA, Roberts NM, Illingworth AJ. 1997. Mesoscale analysis of the activation of a cold front during cyclogenesis. *Q. J. Roy. Meteor. Soc.* **123**: 2349–2375.

Buban MS, Ziegler CL. 2016. The formation of small-scale atmospheric vortices via horizontal shearing instability. *J. Atmos. Sci.* **73**: 2061–2084

Carbone RE. 1982. A severe frontal rainband. Part I. Stormwide hydrodynamic structure. *J. Atmos. Sci.* **39**: 258–279.

Carbone RE. 1983. A severe frontal rainband. Part II. Tornado parent vortex circulation. *J. Atmos. Sci.* **40**: 2639–2654.

Clark MR. 2012. Doppler radar observations of non-occluding, cyclic vortex-genesis within a long-lived tornadic storm over southern England. *Q. J. Roy. Meteor. Soc.* **138**: 439–454.

Clark MR. 2013. A provisional climatology of cool-season convective lines in the UK. *Atmos. Res.* **123**: 180–196.

Clark MR, Parker DJ. 2014. On the mesoscale structure of surface wind and pressure fields near tornadic and nontornadic cold fronts. *Mon. Wea. Rev.* **142**: 3560–3585.

Clark M, Smart D. 2016. Supercell and non-supercell tornadoes in the United Kingdom and Ireland. *Extreme Weather. Forty years of the Tornado and Storm Research Organisation (TORRO),* R. K. Doe, Ed., Wiley Blackwell, Chichester, UK, 31–59.

Clough SA, Lean HW, Roberts NM, Forbes RM. 2000. Dynamical effects of ice sublimation in a frontal wave. *Q. J. Roy. Meteor. Soc.* **126**: 2405–2434.

Dacre HF, Gray SL. 2006. Life-cycle simulations of shallow frontal waves and the impact of deformation strain. *Q. J. Roy. Meteor. Soc.* **132**: 2171–2190.

Dee DP, *et al.* 2011. The ERA-Interim reanalysis: configuration and performance of the data assimilation system. *Quart. J. Roy. Meteor. Soc.* **137**: 553–597.

Dritschel DG, Haynes PH, Juckes MN, Shepherd TG. 1991. The stability of a two-dimensional vorticity filament under uniform strain. *J. Fluid. Mech.* **230**: 647–665.

Elsom DM. 1983. Tornado at Bicester, Oxfordshire, on 21 September 1982. *J. Meteor. (UK)* **8**: 141–148.

Elsom DM. 1985. Tornadoes formed in association with a cold front: the example of the outbreak of 21 tornadoes on 8 February 1984. *J. Meteor. (UK)* **10**: 4–15.

Feuerstein B, Dotzek N, Grieser J. 2005. Assessing a tornado climatology from global tornado intensity distributions. *J. Climate* **18**: 585–596.

Gatzen C. 2011. A 10-year climatology of cold-season narrow cold-frontal rainbands in Germany. *Atmos. Res.* **100**: 366–370.

Godske CL, Bergeron T, Bjerknes J, Bundgaard RC. 1957. *Dynamic Meteorology and Weather Forecasting*. Amer. Meteor. Soc. 800 pp.

Godson WL. 1951. Synoptic properties of frontal surfaces. *Q. J. Roy. Meteor. Soc.* **77**: 633–653.

Hastie T, Tibshirani R, Friedman J. 2009. *The elements of statistical learning. Data mining, inference, and prediction.* (2nd Ed.). Springer–Verlag, New York, USA. pp. 763.

Hewson TD. 1997. Objective identification of frontal wave cyclones. *Meteor. Appl.* **4**: 311–315.

Hewson TD. 2009. Diminutive frontal waves—A link between fronts and cyclones. *J. Atmos. Sci.* **66**: 116–132.

Hoskins BJ, Bretherton FP. 1972. Atmospheric frontogenesis models: mathematical formulation and solution. *J. Atmos. Sci.* **29**: 11–37.

Houser JL, Bluestein HB, Snyder JC. 2016. A finescale radar examination of the tornadic debris signature and weak-echo reflectivity band associated with a large, violent tornado. *Mon. Wea. Rev.* **144**: 4101–4130.

James PK, Browning KA. 1979. Mesoscale structure of line convection at surface cold fronts. *Q. J. Roy. Meteor. Soc.* **105**: 371–382.

Johns RH. 1993. Meteorological conditions associated with bow echo development in convective storms. *Wea. Forecasting* **8**: 294–299.

Koch SE, Kocin PJ. 1991. Frontal contraction processes leading to the formation of an intense narrow rainband. *Meteorology and Atmospheric Physics* **46**: 123–154.

Lee BD, Wilhelmson RB. 1997. The numerical simulation of nonsupercell tornadogenesis. Part II: Evolution of a family of tornadoes along a weak outflow boundary. *J. Atmos. Sci.* **54**: 2387–2415.

Mahale VN, Brotzge JA, Bluestein HB. 2012. An analysis of vortices embedded within a quasi-linear convective system using X-band polarimetric radar. *Wea. Forecasting* **27**: 1520–1537.

Markowski, P. and Richardson, Y. (2010) *Mesoscale meteorology in midlatitudes*. Wiley Blackwell, Chichester, UK, 407 pp.

Meaden GT. 1976a. Tornadoes in Britain: their intensities and distribution in time and space. *J. Meteor. (UK)* **1**: 242–251.

Meaden GT. 1976b. Tornadoes of 12 January 1975 in England. *J. Meteor. (UK)* **1**: 187–193.

Meaden GT. 1978. Tornadoes in eastern England on 3 January 1978. *J. Meteor. (UK)* **3**: 225–229.

Meaden GT. 1979. Tornadoes on the cold front of 12 November 1978. *J. Meteor. (UK)* **4**: 54–55.

Meaden GT. 1983. Tornadoes and severe squalls of 21 September 1982. *J. Meteor. (UK)* **8**: 148–151.

Meaden GT, Rowe MW. 1985. The great tornado outbreak of 23 November 1981 in which North Wales, central and eastern England had 105 known tornadoes in about five hours. *J. Meteor. (UK)* **10**: 295–300.

Moore GWK. 1985. The organization of convection in narrow cold-frontal rainbands. *J. Atmos. Sci.* **42**: 1777–1791.

Mulder KJ, Schultz DM. 2015. Climatology, storm morphologies, and environments of tornadoes in the British Isles: 1980–2012. *Mon. Wea. Rev.* **143**: 2224–2240.

Sanders F, Hoskins BJ. 1990. An easy method for estimation of Q-vectors from weather maps. *Wea. Forecasting* **5**: 346–353.

Schenkman AD, Xue M, Dawson DT II. 2016. The cause of internal outflow surges in a high-resolution simulation of the 8 May 2003 Oklahoma City tornadic supercell. *J. Atmos. Sci.* **73**: 353–370.

Schultz DM. 2005. A review of cold fronts with prefrontal troughs and wind shifts. *Mon. Wea. Rev.* **133**: 2449–2472.

Schultz DM, Keyser D, Bosart LF. 1998. The effect of large-scale flow on low-level frontal structure and evolution in midlatitude cyclones. *Mon. Wea. Rev.* **126**: 1767–1791.

Shapiro MA, Keyser D. 1990. Fronts, jet streams and the tropopause. *Extratropical Cyclones, The Erik Palmen Memorial Volume*, C. W. Newton and E. O. Holopainen, Eds., Amer. Meteor. Soc. 167–191.

Smart DJ, Browning KA. 2009. Morphology and evolution of cold-frontal misocyclones. *Q. J. Roy. Meteor. Soc.* **135**: 381–393.

Trapp RJ, Tessendorf SA, Godfrey ES, Brooks HE. 2005. Tornadoes from squall lines and bow echoes. Part I: Climatological distribution. *Wea. Forecasting* **20**: 23–34.

Trapp RJ, Weisman ML. 2003. Low-level mesovortices within squall lines and bow echoes. Part II: Their genesis and implications. *Mon. Wea. Rev.* **131**: 2804–2823.

Turner S, Elsom DM, Meaden GT. 1986. An outbreak of 31 tornadoes associated with a cold front in southern England on 20 October 1981. *J. Meteor. (UK)* **11**: 37–50.

Wakimoto RM, Murphey HV, Davis CA, Atkins NT. 2006. High winds generated by bow echoes. Part II: The relationship between the mesovortices and damaging straight-line winds. *Mon. Wea. Rev.* **134**: 2813–2829.

Wakimoto RM, Wilson JW. 1989. Non-supercell tornadoes. *Mon. Wea. Rev.* **117**: 1113–1140.

Weisman ML, Trapp RJ. 2003. Low-level mesovortices within squall lines and bow echoes. Part I: Overview and dependence on environmental shear. *Mon. Wea. Rev.* **131**: 2779–2803.

Yang M, Houze RA Jr. 1995. Sensitivity of squall-line rear inflow to ice microphysics and environmental humidity. *Mon. Wea. Rev.* **123**: 3175–3193.

Chapter 3: Shear-zone vortex-genesis in a developing frontal wave

M. R. Clark[1,2,3], D. J. Parker[2,4] and K. E. Hanley[5]

[1]Met Office, Exeter, UK

[2]University of Leeds, Leeds, UK

[3]Tornado and Storm Research Organisation (TORRO), Oxford, UK

[4]NORCE Norwegian Research Center, Bjerknes Center for Climate Research, Bergen, Norway

[5]MetOffice@Reading, University of Reading, Reading, UK

A version of this Chapter is published in the *Quarterly Journal of the Royal Meteorological Society*: https://doi.org/10.1002/qj.4164

Abstract

High-resolution model simulations and radar observations are used to investigate the onset of vortex-genesis in a tornadic narrow cold-frontal rainband (NCFR). The timing and location of vortex-genesis was strongly constrained by a developing frontal wave, which tracked northeast across the UK and Ireland on 17 October 2011. In the simulations, vortices occurred preferentially during the early stages of wave development and just down-front of the wave centre, where large increases in vertical vorticity occurred in concert with decreases in the cross-frontal confluence. Vortex-genesis ceased as the frontal wave matured, due to the onset of frontal fracture.

Two distinct scales of vortex-genesis are documented: primary vortex-genesis on the meso-ɣ-scale, and secondary vortex-genesis on the miso-scale. We show that horizontal shearing instability is the most likely vortex-genesis mechanism, consistent with previous theoretical work on the stability of vertical vortex strips in the presence of horizontal stretching deformation. Secondary vortices occurred along the braid regions between primary vortices where the shear zone became particularly narrow and intense. In the model, these vortices developed extremely rapidly (from small perturbations to maximum vertical vorticity in 5 – 15 minutes) and the strongest exhibited near-surface vertical vorticity maxima approaching 10^{-1} s^{-1}.

Vortices of both scales were associated with characteristic local perturbations in the NCFR and we show, by comparison with radar reflectivity data, that primary and secondary vortices were likely present in the real NCFR. Tornado reports were associated with small NCFR perturbations like those associated with the secondary vortices in the model simulations. Analysis of the sub-structure of individual simulated vortices suggests that tornado-genesis is most likely within a region of intense near-surface vertical vorticity stretching at the north or northwest flank of the secondary vortices.

Keywords: tornado, narrow cold-frontal rainband, vortexgenesis, horizontal shearing instability, vortex strip, cold front.

3.1. Introduction

Recent climatologies suggest that the UK experiences an average of approximately 30 tornadoes *per annum* (Reynolds, 1999; Kirk, 2007; Mulder and Schultz, 2015), of which 40–50% are associated with precipitation systems exhibiting quasi-linear morphologies in radar rainfall imagery (Mulder and Schultz, 2015; Clark and Smart, 2016). An important type of quasi-linear precipitation system is the narrow cold-frontal rainband (NCFR) (Houze *et al*., 1976). These systems, which are responsible for approximately one-third of the UK's tornadoes, are characterised by strong but relatively shallow updrafts forced by horizontal convergence at the frontal boundary. In NCFR-bearing fronts the near-surface frontal boundary is marked by a narrow zone of strong cyclonic relative vertical vorticity (i.e., a vertical vortex sheet, or 'vortex strip') and large horizontal temperature gradient. Observational and modelling studies have shown that NCFR tornadoes are associated with meso-ɣ- to miso-scale vortices that develop along this vortex sheet[6]. Vortex-genesis has generally been attributed to horizontal shearing instability (HSI) (e.g., Matejka *et al*., 1980; Carbone 1982; 1983; Hobbs and Persson, 1982; Lee and Wilhelmson, 1997; Smart and Browning, 2009), though the mechanism of formation is not universally agreed upon and it may differ from case to case.

Clark and Parker (2020) (hereafter CP20) analysed a set of 114 NCFRs (44 tornadic) to identify synoptic situations favouring tornadoes and to find environmental parameters capable of distinguishing between tornadic and non-tornadic cases. At least 55% of tornadic NCFRs were found to be associated with secondary cyclogenesis (i.e., a developing frontal wave) along a trailing frontal system. Events producing ≥7 tornadoes showed an even stronger association with frontal waves (72% of cases). Wave development resulted in large spatiotemporal changes in the magnitude of environmental parameters found to have skill in discriminating between tornadic and non-tornadic events. In particular, a bulk measure of the cross-frontal shear vorticity (hereafter shear vorticity) increased rapidly near the wave centre, whilst the speed of the front-normal flow component on the cold side of the front (hereafter $-v'_{cold}$) increased

[6] In this study we use the mesoscale subdivisions of Orlanski (1975): meso-α-scale: 200 – 2000 km; meso-β-scale: 20 – 200 km; meso-ɣ-scale = 2 – 20 km. However, in the case of vortices of diameter ≤ ~ 4 km, we use the prefix 'miso-', to ensure consistency with existing nomenclature (i.e., 'misocyclones'; Fujita, 1981).

steadily down-front of the wave centre (i.e., in the along-front direction pointing towards higher geopotential height), where the front bulged forward on the meso-α-scale.

A generalised measure of tornado probability, *p*[TN], based on a combination of shear vorticity and $-v'_{cold}$ (see Figure 2.3) was found to reach a maximum immediately down-front of the wave centre, increasing rapidly during the early stages of wave development. CP20 suggested that increases in the shear vorticity, especially when coupled with decreases in the horizontal strain (i.e., stretching deformation), favoured the onset of vortex-genesis due to horizontal shearing instability (HSI) in this region, a hypothesis consistent with previous theoretical and modelling work on the stability of two-dimensional vortex strips in variable strain fields (Dritschel *et al*., 1991; Bishop and Thorpe, 1994). Tornado-genesis is assumed to occur in association with some of the resulting small-scale vortices, consistent with previous modelling and radar studies of tornadic NCFRs. If correct, the scenario described constitutes an important link between the synoptic and the meso-ɣ- to miso-scales in frontal waves. The purpose of this paper is to demonstrate in one case study, using observations and high-resolution model simulations, how a frontal wave constrains the timing and location of meso-ɣ- to miso-scale vortex-genesis, and therefore the area at risk of tornadoes, supporting the hypothesis of CP20 for tornadic NCFRs in frontal waves. The event under study, which occurred on 17 October 2011, produced at least two tornadoes over the UK (Brown and Meaden, 2012). Although the models used in this study are not capable of resolving a circulation on the scale of a typical NCFR tornado[7], we show that they produce numerous meso-γ- to miso-scale shear-zone vortices (i.e., with diameters in the typical range 1 – 10 km) in the area where tornadoes were reported in the real NCFR.

The remainder of the paper is structured as follows. The model setup is described in Section 3.2 and key parameters are defined. An overview of the synoptic-scale situation is given in Section 3.3, and the main features of frontal wave development are described using observations and output from a 1.5 km grid-length model. Primary shear-zone vortex-genesis and its relationship to the developing frontal

[7] A 100 m grid-length configuration of the same model was, however, shown to be capable of resolving the circulation associated with a large (~1 km diameter) tornado in a supercell thunderstorm (Hanley *et al*., 2016), demonstrating that it is capable of resolving features on a similar scale to cold-frontal misocyclones.

wave is described in Section 3.4, and the lifecycle of an individual primary vortex is described in Section 3.5. A more detailed exploration of primary and secondary shear-zone vortex-genesis, and of the three-dimensional structure of secondary vortices, is presented in Section 3.6 using output from a 300 m grid-length simulation, and associated perturbations in the modelled NCFR are compared with radar observations of the real NCFR near to the reported tornadoes. Discussion follows in Section 3.7 and a synthesis of the results is presented in Section 3.8, in the form of a conceptual model. Finally, a summary of the key findings is given in Section 3.9.

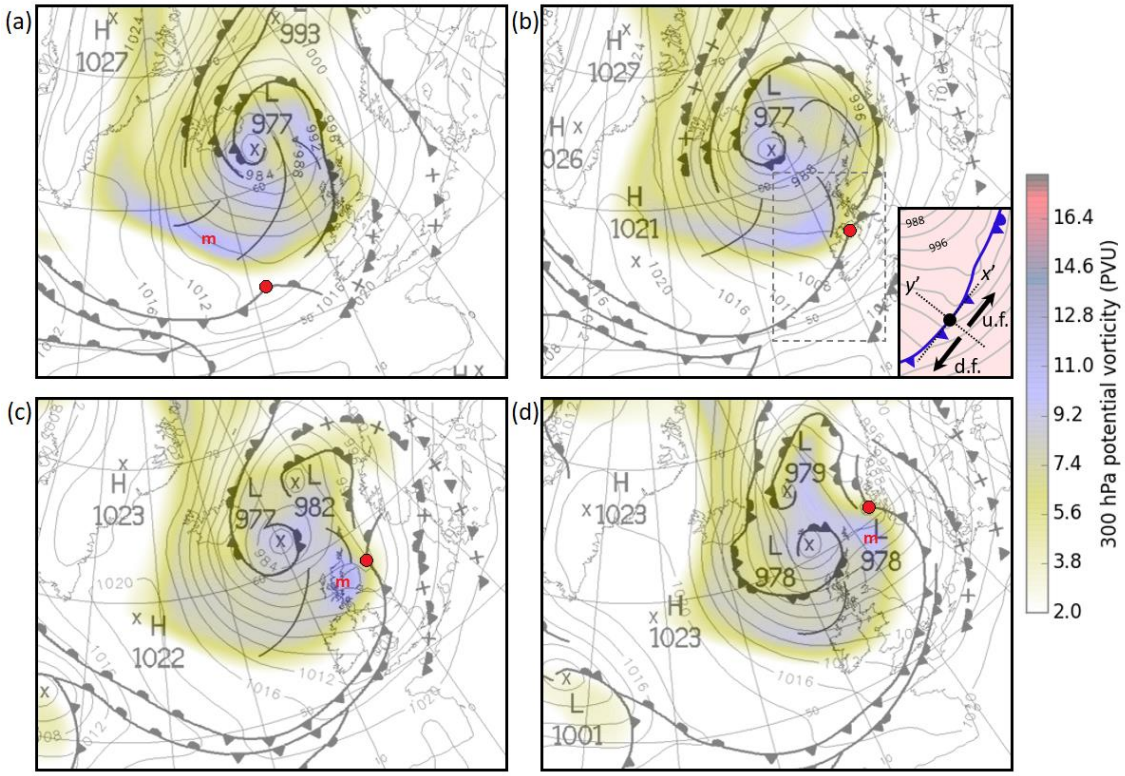

Figure 3.1: Sequence of Met Office surface analysis charts showing evolution of the frontal wave (the centre of which is marked by a red dot) on 17 – 18 October 2011. Shading shows ERAi 300 hPa potential vorticity (PV). 'm' denotes the approximate centre of the local PV maximum associated with frontal wave development. (a) 0600 UTC 17th; (b) 1200 UTC 17th; (c) 1800 UTC 17th; (d) 0000 UTC 18th. Inset in panel (b) shows axes of the natural coordinate system (dashed lines) at the point marked by the black dot, in which x' is tangential to the local front and y' is normal to the local front and points towards the cold air. Bold arrows and annotations 'u.f.' and 'd.f.' denote the up-front and down-front directions, respectively. Grey lines are isobars at 4 hPa intervals. For context, the domain of the inset panel is indicated by the dashed grey box in the main panel.

3.2. Data and methods

3.2.1 Model description

Data from two convection-permitting configurations of the Met Office's Unified Model (Davies *et al*., 2005; Wood *et al*., 2014) are presented in this study. Both were run using the Regional Atmosphere and Land 2.0 midlatitude configuration (RAL2-M). The first is the 1.5 km grid-length version, which is run for a domain spanning approximately 44 – 64°N and 26°W – 17°E. We use this model to explore the development of the frontal wave, its influence on the spatiotemporal evolution of shear vorticity, $-v'_{cold}$ and confluence at the cold front, and the wave-relative location and timing of meso-ɣ-scale vortex-genesis. The model uses a semi-implicit, semi-Lagrangian numerical scheme with a one-minute timestep and runs on a rotated latitude-longitude horizontal grid with Arakawa C staggering. In the vertical the grid is stretched and, close to the surface, terrain following, transitioning to horizontal at the model top (z = 40 km), with Charney-Phillips staggering and 70 vertical levels. The vertical grid length is smallest close to the surface and the vertical stretching is quadratic over much of the vertical extent of the domain. The first model level above the surface is at z = 2.5 m for the horizontal wind components and air density, and z = 5 m for other parameters. The model uses a Smagorinsky-type turbulence closure scheme. The lower boundary conditions, as described in Wood *et al*. (2014), impose surface stresses that can contribute to vorticity generation. The terrain is defined using a smoothed version of the 100 m resolution Shuttle Radar Topography Mission (SRTM) data. The 1.5 km model takes its boundary conditions from the global Unified Model, which for the purposes of this study was rerun using an initialisation time of 0000 UTC 16 October 2011, taking data from the Met Office global operational analysis. The global model was run at n768 resolution using the Global Atmosphere 6.1 configuration (Walters *et al*., 2017). Output is analysed for the period 0800 UTC 17 October to 0000 UTC 18 October (i.e., t + 32 hours to t + 48 hours, where t + 0 hours is the model initialisation time).

The second model has a horizontal grid-length of 300 m and a timestep of 12 seconds over a domain of 600 x 600 km centred on the Irish Sea. As with all configurations of the Unified Model, this uses semi-implicit, semi-Lagrangian discretisation of the deep atmosphere, non-hydrostatic Euler equations, which allows stable integrations with long timesteps. This fine-scale model was also initialised from

the 0000 UTC 16 October 2011 Met Office global analysis, but it takes its lateral boundary conditions from the 1.5 km model. Vertical levels are as for the 1.5 km model and the terrain is again defined using smoothed 100 m resolution SRTM data. We use this model to further explore the structure, development and evolution of primary (meso-ɣ-scale) and secondary (miso-scale) vortices, and for comparison of the associated structures in the rainfall field with radar observations of the real NCFR, especially near to the reported location of tornadoes.

3.2.2 Definition of bulk parameters

Bulk environmental parameter values are calculated from ERA-Interim (hereafter ERAi) data (Dee *et al*., 2011) and the 1.5 km model output fields using the methodology of CP20 (a full description can be found in Sections 2.2.2 and 2.2.3). A natural coordinate system is adopted in which x' is tangential to the local front and points towards lower geopotential height, and in which y' is normal to the local front and points towards the cold air. The term up-front will be taken as the positive x' direction i.e., pointing along the local front in the direction of lower geopotential height; an observer looking up-front would have the cold air on their left. The term down-front will be taken as the negative x' direction i.e., pointing along the front in the direction of higher geopotential height (for a graphical depiction of the coordinate system, see inset panel in Figure 3.1(b)). Analysis points are defined at regular intervals along the surface frontal boundary ('on-front analysis points'). For the analysis using ERAi data, frontal positions are taken from Met Office surface analysis charts. For the analysis using 1.5 km model data, the frontal boundary is taken to be the location of maximum near-surface vertical vorticity and collocated horizontal temperature gradient in the model fields. For convenience, analysis points are defined wherever the frontal boundary (as defined above) crosses a whole degree of latitude or longitude, though spacing is reduced to 0.5° latitude or longitude where the front exhibits substantial curvature, in order to adequately capture the shape of the front. At each point, finite differences are calculated between values at corresponding warm-air and cold-air analysis points located 150 km from the front in the local front-normal direction. To reduce the impact of small-scale variability in the 1.5 km model fields, the parameter value at each point is taken to be the mean value over nine grid squares centred on the analysis point (i.e., a square of 4.5 x 4.5 km). Whilst 150 km is rather far from the front, sensitivity studies

conducted using a range of separation distances between 25 and 600 km (not shown) revealed that the u' and v' winds are relatively insensitive to the choice of separation distance (i.e., the wind field is relatively uniform within the pre- and post-frontal air masses). The use of 150 km ensures consistency with CP20, where values were derived using ERAi data only.

A bulk measure of the cross-frontal vorticity (hereafter 'shear vorticity') is defined as the difference in the along-front wind component, u', between the warm and cold-air analysis points, divided by the distance between these points (positive where $u'_{warm} > u'_{cold}$, where positive u' points up-front). A bulk measure of the cross-frontal confluence (hereafter 'bulk confluence') is defined in a similar manner by analysis of the difference in the cross-front wind component, v' (positive where $v'_{warm} > v'_{cold}$ and where positive v' points towards the cold air). The parameter $-v'_{cold}$ is evaluated at the cold air point. The probability of tornadoes, p[TN], as defined by CP20, depends on the combined values of shear vorticity and $-v'_{cold}$, and describes the conditional risk of one or more tornadoes, derived from analysis of bulk measures for a large set of tornadic and non-tornadic NCFRs (see Figure 2.3; empirical formulae for the calculation of p[TN], given shear vorticity and $-v'_{cold}$, are given in Appendix B). The parameter is used here to highlight the region at risk of tornadoes and to show how the evolution of p[TN] relates to the development of the frontal wave.

The advantage of the bulk measures is that they are insensitive to the substantial small-scale variability in parameter values often observed along the shear zone, which tend to mask differences associated with the evolving synoptic- to meso-α-scale environment of the front, which are of interest to this study. Bulk parameters are calculated at the 1390 m AGL model level, selected because it is closest to the observed mean 850 hPa geopotential height over the UK in the current event, therefore ensuring consistency with values derived from ERAi fields here and in CP20. Furthermore, the 1390 m level is above the friction layer, but below the height of the top of the frontal updraft and shear zone over most of the domain, so that the bulk measures properly represent the horizontal wind differences across the vertical vorticity sheet at the front, without being unduly affected by the variable effects of friction over land and sea areas (which partially mask the along-front variability associated with the frontal wave at lower heights).

Dritschel *et al.* (1991) showed that the barotropic growth of vortices along a vertical vorticity strip (i.e., the release of HSI) is supressed when the stretching deformation acting on the strip exceeds one quarter of the magnitude of the vorticity within the strip. In the natural coordinate system defined above, and assuming the axis of dilatation is aligned with the front, the stretching deformation, D_s, is given by

$$D_s = \frac{\partial u'}{\partial x'} - \frac{\partial v'}{dy'} \qquad (4)$$

The first term represents dilatation in the along-front direction and the second term represents confluence in the cross-front direction. The shear zone at the front in the present case differs from the setup in Dritschel *et al*. (1991) in that it is characterised by large horizontal convergence in addition to large vertical vorticity (i.e., v' varies substantially across the narrow shear zone itself); in Dritschel *et al*. (1991), v' gradients are associated only with the larger-scale stretching deformation field. In the current case, the bulk measure of confluence, as described above, will include contributions from both the v' difference across the shear zone and the v' difference associated with the larger-scale stretching deformation field, where present. Inspection of the model fields shows the v' difference across the shear zone to be the larger of these two contributions, overall. For this reason, in the local environment of the front, the cross-frontal confluence is much larger than the along-front dilatation[8]. Physically, one would expect cross-frontal confluence to reduce the amplitude of perturbations, by flattening them in the cross-front direction, regardless of whether this confluence is a feature of the larger-scale environment (as with a stretching deformation field in which the axis of contraction is normal to the front) or localised to the strip, so we consider the results of Dritschel *et al*. (1991) relevant in spite of this difference. An approximate measure of the potential for the release of HSI along the strip may therefore be obtained using the bulk measures of shear vorticity and cross-frontal confluence, under the assumption that the local along-front dilatation is relatively small. The criterion, S_{HSI} , for barotropic vortex-genesis at the shear zone is thus approximated as:

[8] This is shown by calculation of the bulk measures of cross-frontal confluence and along-frontal dilatation using a range of separation distances from 600 km to 25 km. As the separation distance decreases, the bulk along-frontal dilatation becomes smaller relative to the bulk cross-frontal confluence. Near the lower limit of the tested range of distances, bulk confluence was ~15 times larger than the bulk along-front dilatation.

$$S_{HSI} = (4 \text{ x bulk confluence}) - \text{shear vorticity} \qquad (5)$$

Negative values of S_{HSI} indicate an environment favourable for the growth of vortices by the release of HSI, whilst positive values indicate an environment in which the growth of vortices is likely to be supressed by the cross-frontal confluence. Ostensibly, the method assumes that the axis of dilatation of the larger-scale stretching deformation field, where present, is aligned with the front (i.e., the axis of contraction is normal to the front). However, in practice, for constant stretching deformation, the bulk confluence will decrease as the angle between the front and the axis of dilatation increases from 0 – 90°. Therefore, the bulk confluence is sensitive both to changes in the magnitude of stretching deformation and changes in the angle of the axis of dilatation relative to the front.

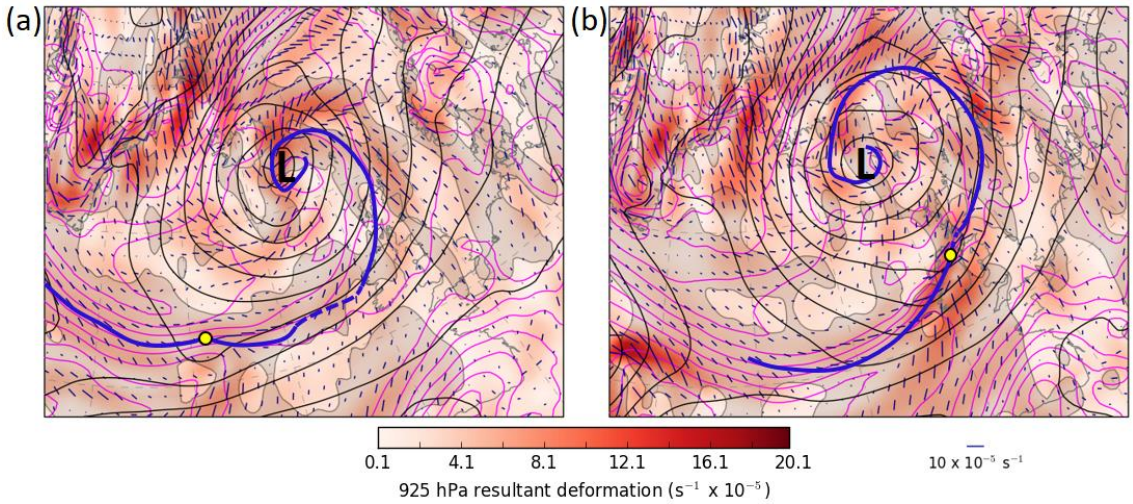

Figure 3.2: Resultant deformation of the horizontal wind field (colour shading) and axis of dilatation (dashes orientated parallel to the axis of dilatation, with dash length proportional to the magnitude of resultant deformation) at (a) 0000 UTC 17 October 2011 and (b) 1200 UTC 17 October 2011, analysed at 925 hPa using ERAi data. Magenta contours denote 925 hPa θ (contour interval 2 K) and black contours 925 hPa geopotential height (contour interval 4 DAM). Grey shading denotes areas where the isotherms are orientated at an angle of <40° to the local axis of dilatation. Bold, blue line indicates location of fronts as shown in Met Office surface analysis charts (only the trailing frontal system of interest is shown; dashed lines indicate sections of front not marked in the corresponding analysis charts (e.g., *cf*. Figure 3.1(b)), but included here for continuity of the trailing frontal system as suggested by the 925 hPa θ field). Yellow circle indicates the centre of the frontal wave and 'L' denotes the centre of the parent low pressure system.

3.3. Overview of wave development and reported tornadoes

In this section we provide an outline of frontal wave development on the synoptic- and meso-α-scales, describe the location of tornado reports relative to the wave, and compare the observed wave development with that in the 1.5 km model.

3.3.1 Synoptic overview

At 0600 UTC 17 October 2011, a primary cyclone of central pressure 977 hPa was located between Scotland and Iceland (Figure 3.1(a))[9]. The cyclone's trailing frontal system intersected north-western parts of the UK and Ireland where it was slow moving. An incipient frontal wave is evident further down front, to the southwest of Ireland. The environment of the trailing front was characterised, for a period of at least 12 hours prior to wave development and continuing through the early phases of development, by substantial resultant deformation, with the axis of dilatation orientated at a small angle to the front (Figure 3.2). Over the following 12 – 18 hours, the frontal wave moved northeast and deepened rapidly, crossing Ireland and northern parts of the UK between 1000 and 1900 UTC (Figures 3.1(b)-(c)). By 0000 UTC 18 October, the wave had matured into a discrete secondary cyclone of central pressure 978 hPa, centred just east of the Norwegian coastline (Figure 3.1(d)). Wave development was apparently induced by the approach of an upper-level potential vorticity (PV) maximum towards the front between 0600 and 1200 UTC (shading in Figure 3.1). After rounding the axis of an upper-level trough, the PV maximum moved northeast in tandem with the deepening surface frontal wave from 1800 UTC 17th to 0000 UTC 18 October (Figure 3.1(c)-(d)).

Bulk measures of relevant 850 hPa environmental parameters, as derived from 850 hPa ERAi fields, exhibit spatiotemporal evolution that closely follows the conceptual model described by CP20 for tornadic frontal waves (Figure 3.3; *cf*. Figures 2.11 and 2.12). Characteristic features include:

- Rapid increases in shear vorticity near the wave centre during the early stages of development (Figure 3.3(a)).
- Steady increases in $-v'_{cold}$ (Figure 3.3(b)) down-front of the wave centre over a swath several hundred kilometres wide, with an associated, amplifying, meso-α-

[9] Met Office surface analysis charts are created manually by operational meteorologists, using model output and satellite and surface observations (e.g., see Mulqueen and Schultz, 2015).

scale frontal bulge (wavelength of order hundreds of km); e.g., as over the North Sea in Figure 3.3(b). This bulge occurs due to the strong positive correlation between $-v'_{cold}$ and the forward speed of the front in the direction normal to its length (hereafter front-normal forward motion (FNFM); CP20).

- Rapid increases in *p*[TN] along a relatively narrow swath centred just down-front of the wave apex (i.e., between the developing shear vorticity and $-v'_{cold}$ maxima, and on the up-front flank of the meso-α-scale frontal bulge; Figure 3.3(c)).

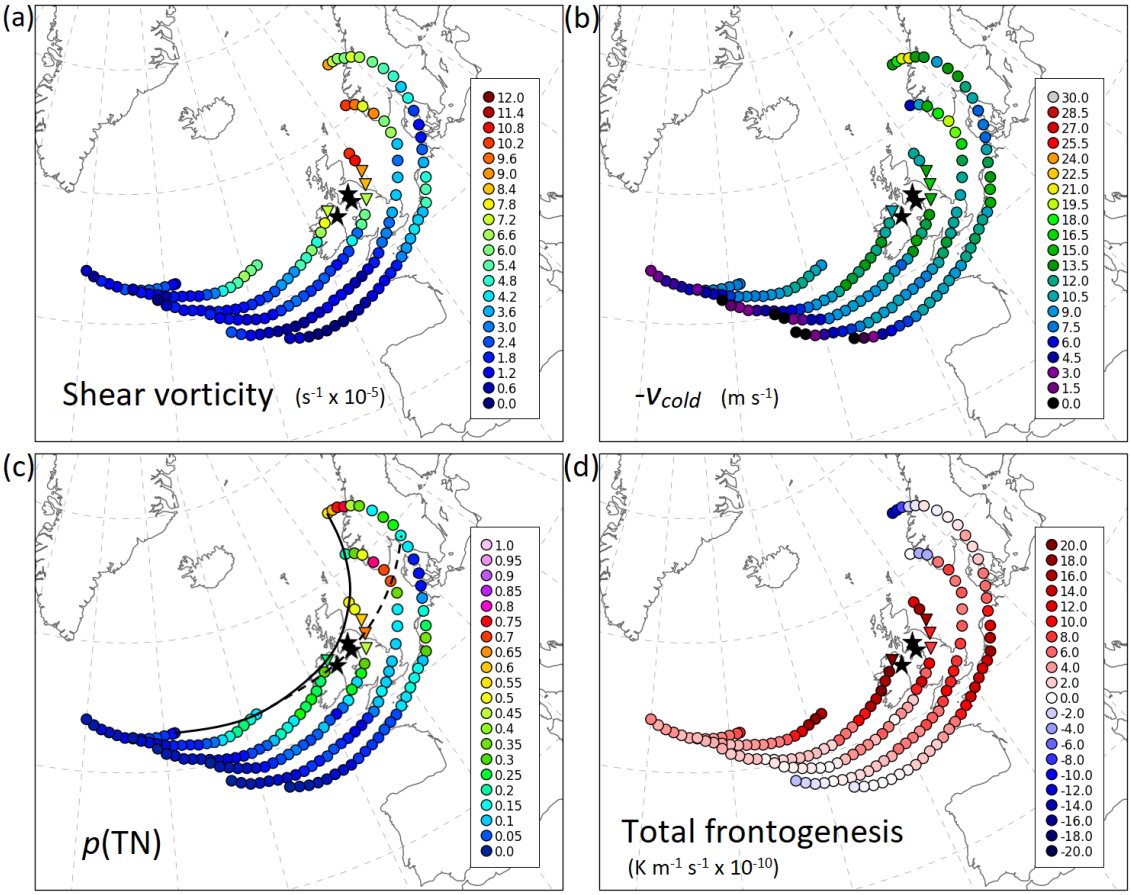

Figure 3.3: Evolution of bulk parameter values, calculated from ERAi reanalysis data, at on front analysis points at 6-hour intervals between 0000 UTC 17 October and 0600 UTC 18 October 2011, following the methodology of CP20. Frontal positions are taken from the corresponding Met Office surface analysis charts at each analysis time. (a) Shear vorticity; (b) $-v'_{cold}$; (c) *p*[TN]; (d) Total frontogenesis (horizontal, kinematic terms only). On-front analysis points are shown by the coloured dots (inverted triangles for points near to tornado reports), with the colour shading indicating the magnitude of the corresponding parameter (see scale within each panel). Star symbols mark the locations of reported tornadoes. In panel (c), solid black line denotes the track of the centre of the frontal wave, and dashed black line denotes the track of a pseudo-Lagrangian analysis point situated along the tornadic part of the front.

- Large and increasing frontogenesis near the wave centre during the early stages of development (e.g., over and to the west of Ireland in Figure 3.3(d)), followed by decreasing frontogenesis and eventual transition to frontolysis near the wave centre by the mature and dissipating stages of development (e.g., over Norway in Figure 3.3(d)).

3.3.2 Tornadoes of 17 October 2011

At least two tornadoes occurred in association with the frontal wave of 17 October 2011: at Templand, Dumfries and Galloway, just after 1500 UTC and at Whitehaven, Cumbria, at approximately 1540 UTC. A further possible tornado occurred at Killowen, Northern Ireland, at approximately 1300 UTC. Although video footage of the Killowen event showed an intense vortex making landfall from Carlingford Lough, it was classified by TORRO as an eddy whirlwind (Brown and Meaden, 2012), owing to the frequent occurrence at this location of vortices generated by the interaction of strong winds with the mountains surrounding the lough (the so-called 'Carlingford Kettle'), particularly in southerly flow as observed ahead of the cold front in the current case. For the purposes of this study, we choose to include this event as a possible tornado because the reported time closely matches that of NCFR passage at Killowen. However, confidence in the diagnosis of a tornado is lower in this case than for the other two reported tornadoes. The location of the three tornado reports is shown by star symbols in Figure 3.3. The tornadoes occurred immediately down-front of the wave centre, during the early stages of development when the wave was deepening rapidly, and where p[TN] was increasing rapidly.

3.3.3 Wave development in the 1.5 km model

The structure and evolution of the frontal wave may be analysed in more detail using output from the 1.5 km model. At 1300 UTC, the wave is centred over the Irish Sea between Northern Ireland and southwest Scotland (Figure 3.4). The frontal boundary is well-defined, marked by a sharp MSLP trough and a large vector wind difference across the trough axis, with associated strong cyclonic vertical vorticity and horizontal convergence. Coincident with this shear zone is a similarly narrow and well-defined baroclinic zone, across which temperatures typically differ by 4 – 5 °C and locally as much as 6 – 7 °C. Observations and model data show that the frontal boundary was narrow and well-defined both up-front and down-front of the wave centre at this time

(e.g., note the large wind direction and temperature differences across the front over both southern Scotland and Ireland in Figure 3.4), demonstrating that the trailing front had already collapsed to narrow cross-frontal scales (Hoskins and Bretherton, 1972) by the early stages of secondary cyclogenesis. This characteristic probably relates to the antecedent conditions; specifically, the substantial resultant deformation, in which the axis of dilatation was orientated at small angle to the front, before and during the early stages of wave development (Figure 3.2). This is consistent with the analysed positive frontogenesis along the full length of the front in the early stages of development (Figure 3.3(d)). The presence of such a 'pre-existing' narrow frontal shear zone was postulated by CP20 to be a key feature in tornadic frontal waves, since modulation of the along-front distribution of shear vorticity and stretching deformation during the early stages of wave development can only result in shear zone vortex-genesis if the shear zone is already narrow and well-defined in these early developmental stages.

Figure 3.5 illustrates the evolution of the wave in the 1.5 km model between 1200 and 2200 UTC 17 October. The wave centre is marked by a local MSLP minimum, initially elongated in the along-front direction, and a corresponding local vertical vorticity maximum along the shear zone (e.g., as over Ireland in Figure 3.5(a))[10]. As the wave moves northeast and matures, the pressure minimum becomes more circular and the largest values of vertical vorticity along the shear zone migrate towards the northern flank of the MSLP minimum. At the same time, a local along-front *minimum* in shear zone vertical vorticity develops near and immediately down-front of the wave centre (as shown by the break in the narrow zone of vertical vorticity > 1 x 10^{-3} s^{-1} (yellow shading) along the front in this region in Figure 3.5(f)), which is associated with the onset of frontal fracture (Shapiro and Keyser, 1990). The wave's central pressure decreases by 17 hPa over the 10-hour period ending 2200 UTC, due to a combination of pressure falls following the wave centre (i.e., genuine deepening of the wave) and translation of the wave towards lower background values of MSLP (i.e., up-front translation within the cyclonic pressure field associated with the primary cyclone). The modelled location of the wave centre, and values of central pressure at 1200 and

[10] In the calculation of these vorticity fields, the 845 m above ground level (AGL) wind field has been averaged over nine grid boxes in the x and y directions in order to smooth out some of the very small-scale variability along the shear zone. This small-scale variability is subsequently analysed in more detail using unsmoothed fields.

1800 UTC, agree very closely with the analysed locations and central pressures at the same times (e.g., *cf.* Figure 3.1(b)-(c)), suggesting that the 1.5 km model has an accurate representation of the wave's location, track, and rate of development. However, down-front of the wave centre, the south-eastward movement of the NCFR across the UK was slightly too slow, with frontal passage in the model occurring ~1 hour later than observed in most places.

Figure 3.6 illustrates the spatiotemporal distribution of bulk shear vorticity, $-v'_{cold}$ and S_{HSI} over the period 1000 UTC 17 October – 0000 UTC 18 October 2011, as constructed from hourly 1.5 km model wind fields at 1390 m AGL. Substantial variability is evident in the selected parameter values as the developing frontal wave moves across Ireland and the UK. In agreement with the ERAi values (Figure 3.3), shear vorticity is maximised close to the wave apex and increases steadily as the wave amplifies (i.e., from southwest to northeast along the wave's track; Figure 3.6(a)). The parameter $-v'_{cold}$ is maximised down-front of the wave, along a broad zone that tracks through southern Ireland, Wales and much of England, but remains much smaller north of the wave centre (Figure 3.6(b)). p[TN] (red contours in Figure 3.6) is maximised just down-front of the shear vorticity maximum and just up-front of the $-v'_{cold}$ maximum; a swath of p[TN] > 0.5 extends from ~50 km to ~250 km down-front of the wave centre, with peak values increasing gradually along the track of the wave. S_{HSI} is positive in most places along the front (suggesting an environment generally unfavourable for the development of vortices by the release of HSI), with values reaching a maximum where $-v'_{cold}$ is large, near the centre of the meso-α-scale frontal bulge, and in a separate region immediately up-front of the wave centre (Figure 3.6(c)). Between these regions, a minimum in S_{HSI} is evident, with values slowly decreasing as the wave develops. $S_{HSI} < 0$ (suggesting an environment favourable for the growth of vortices by HSI) occurs within a narrow swath immediately down-front of the wave centre (Figure 3.6(c)), appearing first over Northern Ireland and then tracking northeast close to the England–Scotland border, before moving into the North Sea[11]. The reported

[11] $S_{HSI} < 0$ is also evident over and near southwest Ireland, and in the far southwestern corner of the analysis domain. The former region is associated with a separate, weak frontal wave (as suggested by the presence of a shallow inflection in the frontal shear zone over far southwest Ireland) which fails to amplify and eventually becomes subsumed into the main wave development over the UK. The latter is likely explained by the fact that the shear zone depth is less than the 1390 m analysis height along the trailing part of the cold front, far down-front of the frontal wave centre.

tornadoes (black star symbols in Figure 3.6) occur within this S_{HSI} minimum. The reduced S_{HSI} in this region corresponds to reducing bulk confluence (not shown) and contemporaneous increasing shear vorticity. Bulk diffluence eventually develops near the wave centre by the time the wave reaches maturity, consistent with transition to frontolysis along the same part of the front in the ERAi fields (Figure 3.3(d)). This transition is associated with the onset of frontal fracture (as described subsequently).

In summary, analysis of bulk measures from the 1.5 km model shows that the tornadoes occurred within a narrow strip where relatively large and increasing values of p[TN] coincide with negative S_{HSI}.

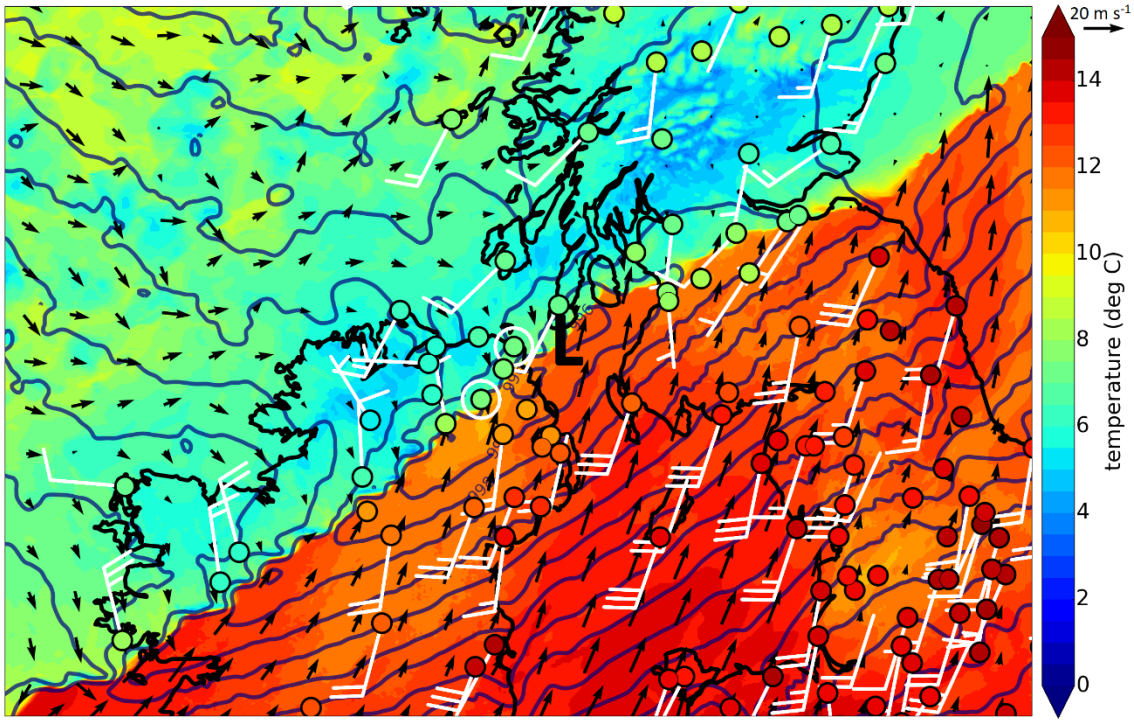

Figure 3.4: Surface wind vectors (black arrows), MSLP (navy blue contours at 0.5 hPa intervals) and temperature (shading), corrected to sea level assuming the dry adiabatic lapse rate) at 1300 UTC 17 October 2011 from the 1.5 km model. 'L' denotes the centre of the frontal wave. Met Office surface temperature observations (coloured circles) and wind observations (white barbs) at 1200 UTC 17 October 2011 are overlaid for comparison. Temperature circles use the same colour scale as for the model temperatures. Wind barbs are plotted using standard notation (one full barb for every 10 knots of wind speed, and half a barb for five knots, with open circles indicating calm conditions).

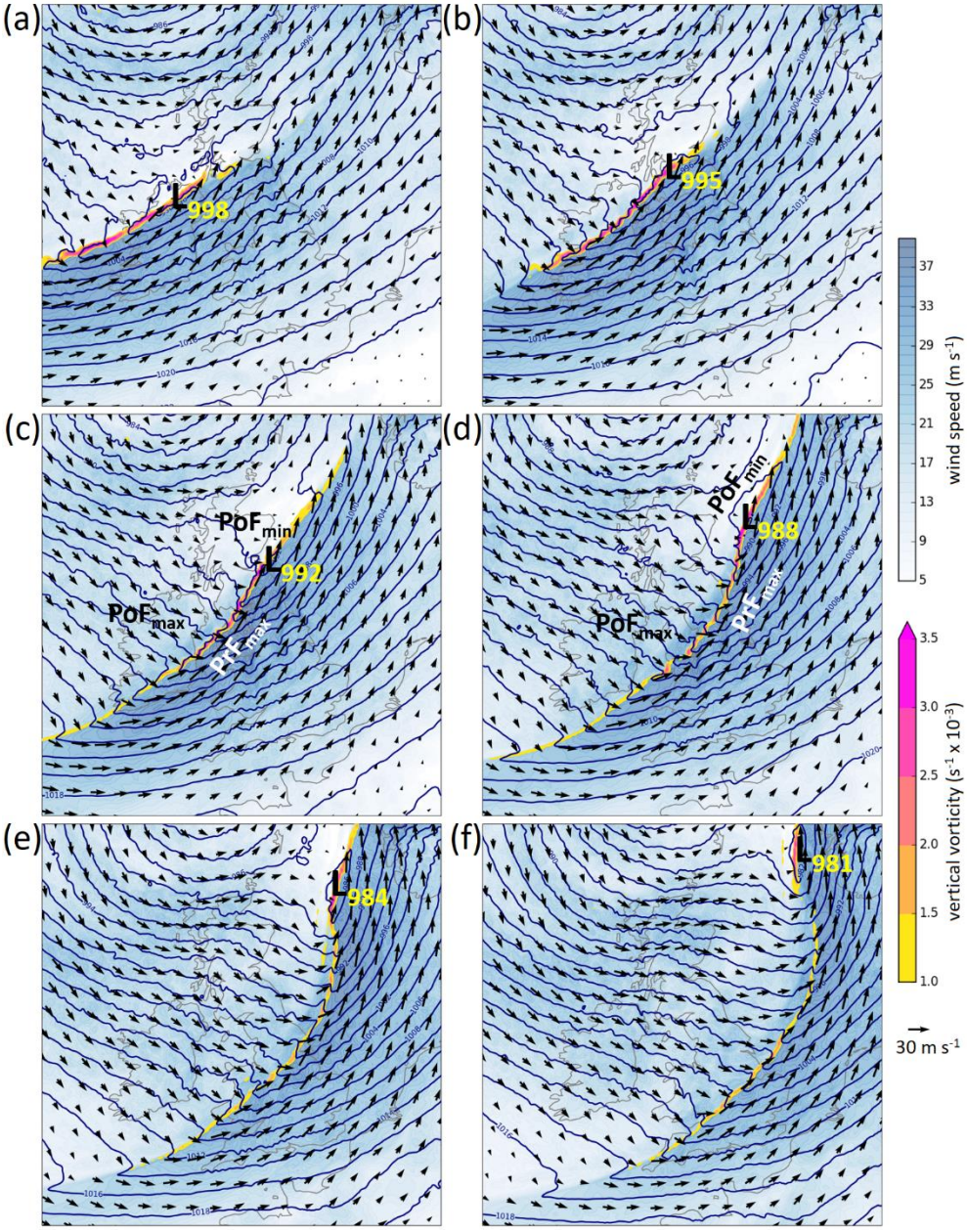

Figure 3.5: Wind vectors (arrows), MSLP (navy blue contours at 2 hPa intervals), wind speed (blue shading), and vertical vorticity (over-plotted, yellow–pink shading) at 845 m AGL from the 1.5 km model, showing evolution of the frontal wave at (a) 1200 UTC; (b) 1400 UTC; (c) 1600 UTC; (d) 1800 UTC; (e) 2000 UTC; (f) 2200 UTC 17 October 2011. Parameter fields have been smoothed by averaging over 9 x 9 grid boxes at the 1.5 km native model grid spacing. 'L' denotes the centre of the frontal wave at each time, with the central pressure (hPa) annotated. Additional annotations in panels (c) and (d) highlight various features of the flow pattern characteristic of frontal waves of the type described by CP20: a local minimum in wind speed and MSLP gradient on the cold side of the front near and immediately up-front of the frontal wave's centre (PoF_{min}); a local maximum in wind speed and pressure gradient on the cold side of the front, down-front of the wave centre (PoF_{max} in Figure 3.5(d)), in which winds are orientated nearly normal to the front and point towards the front (i.e., a maximum in $-v'_{cold}$); a local maximum in wind speed and MSLP gradient on the warm side of the front, near and down-front of the wave centre (PrF_{max} in Figure 3.5(d)), in which winds are orientated nearly parallel to the front. In the system-relative frame of reference, PrF_{max} constitutes part of the cyclone's warm conveyor-belt flow (Harrold, 1973).

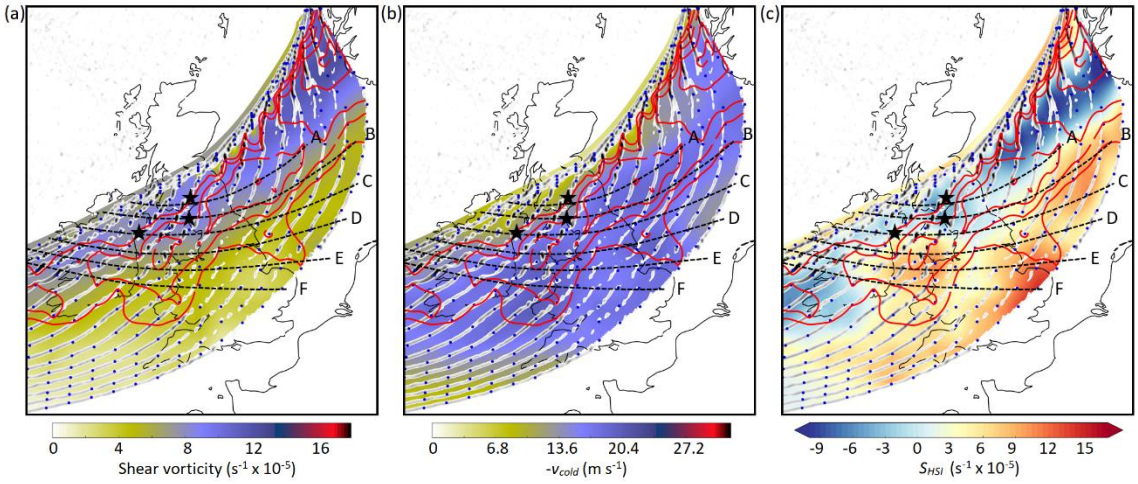

Figure 3.6: Bulk parameter fields analysed at 1390 m AGL (~850 hPa) from the 1.5 km model, derived by interpolation of bulk values at along-front points every hour over the period 1000 UTC 17 October – 0000 UTC 18 October 2011. (a) Shear vorticity; (b) $-v'_{cold}$; (c) Dritschel *et al*. (1991) criterion for the growth of vortices by HSI (S_{HSI}). Overplotted grey shading shows smoothed vertical vorticity at 75 m AGL, showing the location of the frontal shear zone at each hour; individual on-front analysis points are shown by blue dots. Red contours show *p*[TN] at intervals of 0.1, starting at 0.5. Black dashed lines show the tracks of selected perturbations along the shear zone (labelled A – F). Black star symbols denote the locations of reported tornadoes.

3.4. Vortex-genesis in the 1.5 km model

Having described the frontal wave development and associated spatiotemporal evolution of key environmental parameters, we now focus on the details of primary vortex-genesis and evolution in the 1.5 km model, identifying preferred regions for vortex-genesis. Figure 3.7(a) shows 75 m AGL vertical vorticity along the frontal shear zone at hourly intervals between 1000 and 2300 UTC 17 October 2011 from the 1.5 km model. Local perturbations in the shear zone, which are associated with the genesis and subsequent amplification of primary, meso-ɣ-scale vortices, are evident close to the wave centre and along the meso-α-scale frontal bulge, tracking through the Irish Sea and much of northern England and southern Scotland. The preferential development of vortices along this part of the front is best appreciated when inspecting vertical vorticity fields at individual analysis times, especially in the early stages of wave development (e.g., Figure 3.7(b)). A marked absence of similar perturbations is noted both up-front of the wave centre, and along the trailing part of the front, far down-front of the wave

centre, where the shear zone instead appears highly two-dimensional[12]. The section of the front exhibiting meso-ɣ-scale perturbations is therefore well-defined, bounded both up-front and down-front by a shear zone exhibiting a comparative absence of such structures.

The tracks of individual vortices and associated perturbations may be determined by inspection of vertical vorticity at the lowest model level at 5-minute intervals throughout the analysis period (not shown). Tracks of selected vortices are shown by dashed lines in Figure 3.7. In each case, the vortices originate as subtle vertical vorticity maxima along the shear zone, with associated small-amplitude perturbations developing soon after genesis. Over a period of several hours, the associated perturbations amplify whilst moving down-front relative to the wave centre. New vortices continue to develop near the wave centre, such that the along-front extent of the region with substantial perturbations increases with time. The tracks of individual perturbations diverge slightly, being orientated southwest–northeast over northern England and Scotland, compared to west–east or even west-northwest–east-southeast over central and southern England. The orientation of perturbation tracks, and its variability across the domain, agrees well with the tracks of the larger radar-observed perturbations in the real NCFR (Figure 3.8).

The apparent up-front movement of the wave relative to individual vortices and associated perturbations is explained by the differing along-front velocity components of the wave and the vortices. Relative to the front-normal direction, both the frontal wave and the individual vortices move up-front; however, the up-front movement of the wave is greater than that of individual vortices, with the consequence that individual vortices move down-front *relative to the wave*. The observed coupling between the wave centre and the 300 hPa PV maximum after ~1200 UTC (Figures 3.1(b)-(d)) suggests that the along-front movement of the wave is controlled by the velocity of the driving upper-level PV maximum, whilst the along-front velocity of shear zone vortices is likely controlled by the mean of the along-front wind component on each side of the

[12] More detailed analysis of unsmoothed fields (not shown) reveals that the front is not entirely two dimensional in these regions. However, perturbations are comparatively small, transient, and show limited up-scale growth.

shear zone, as previously suggested for vortices forming along NCFRs and other types of boundary (e.g., Parsons and Hobbs, 1983; Adlerman and Droegemeier, 2005)[13].

The wave-relative movement of vortices and the ongoing development of the frontal wave results in substantial Lagrangian changes in the bulk environmental parameters following individual vortices (hereafter 'pseudo-Lagrangian', since individual air parcels are not followed as in a true Lagrangian frame of reference), as depicted for selected vortices by the bold coloured lines in Figure 3.9. To provide a more complete picture of the evolution, values are plotted from 0800 UTC, which is approximately five, three and two hours prior to vortex-genesis for vortices A, B and C, respectively. Prior to vortex-genesis, local values are analysed at the point where the backward-extrapolated vortex track intersects the shear zone at each analysis time. In practice, since the FNFM is very small up-front of the wave centre, and because vortex-genesis occurs near to the wave centre in each case, the backward-extrapolated positions generally lie very close to the actual location of vortex-genesis. The evolution of environmental parameters is therefore analysed over the period that the frontal wave centre approaches, passes and then recedes up-front of each pseudo-Lagrangian analysis point.

At all points, *p*[TN] is initially small, but increases markedly as the frontal wave centre approaches and passes (Figure 3.9(a)-(b); recalling that the frontal wave moves up-front faster than individual vortices along the shear zone). Transition to large *p*[TN] occurs earliest at the pseudo-Lagrangian point of vortex C (hereafter point C), since the frontal wave centre is already close to this point at 0800 UTC, and latest at the pseudo-Lagrangian point of vortex A, which is located furthest up-front and therefore experiences later passage of the wave centre. The particularly low initial values of *p*[TN] at point A are representative of the environment ~200 – 300 km up-front of the wave centre. In the two-dimensional parameter space defined by shear vorticity and $-v'_{cold}$, traces for each vortex follow a curve, since shear vorticity and $-v'_{cold}$ increases occur at different times (i.e., in different locations relative to the wave centre). Initially, as the wave centre approaches, shear vorticity increases whilst $-v'_{cold}$ remains small. As the wave centre passes, shear vorticity reaches a peak and a rapid increase in

[13] This behaviour also arises in basic treatments of Kelvin–Helmholtz type instabilities (e.g., Kundu and Cohen, 2004; p. 489).

$-v'_{cold}$ ensues, with FNFM correspondingly beginning to increase. As the wave centre recedes up-front of the vortex, shear vorticity begins to decrease whilst $-v'_{cold}$ and FNFM continue to increase slowly, reaching a maximum as PoF_{max} (Figure 3.5(c)-(d)) approaches and then passes each pseudo-Lagrangian point. Thereafter, both parameter values begin to decrease as the wave recedes further up-front.

The period of large *p*[TN] is seen to be transitory, with values greater than 0.5 lasting only ~6 – 10 hours at each point (vortex A ends up in the frontal fracture region, and therefore dissipates whilst *p*[TN] is still large; however, even here, values are beginning to decrease by the time the vortex dissipates). The time of closest passage of each vortex to a reported tornado is shown by the triangle symbols in Figure 3.9(b). Tornadoes occurred during the period of rapidly increasing *p*[TN], rather than at the time of maximum *p*[TN]. This characteristic was also found for the frontal wave case of 1 January 2005 by CP20, suggesting that tornado-genesis may be more closely related to Lagrangian trends in *p*[TN] than its absolute value at any instant in time.

Evolution of the local environment of vortices A, B and C may also be described in terms of S_{HSI} (Figure 3.9(c)). In all cases, a transition from conditions unfavourable for the growth of vortices by the release of HSI (i.e., $S_{HSI} > 0$) to conditions favourable for such growth (i.e., $S_{HSI} < 0$) occurs around or just after the time of wave passage, which corresponds closely to the time of vortex-genesis. In vortices B and C, the transition to $S_{HSI} < 0$ is temporary, however, with a recovery to positive values as the wave recedes further up-front. In vortex A, values remain negative up to the time of vortex dissipation in the frontal fracture region. In all cases, the closest passage of the model vortex to a reported tornado in the real NCFR occurs close to or just after the time of minimum S_{HSI}.

In summary, the 1.5 km simulation shows that primary vortices develop preferentially near to the centre of the frontal wave in the early stages of wave development, with individual vortices moving down-front of the wave centre with time. The genesis of vortices is apparently orchestrated by the associated spatiotemporal variations in relevant environmental parameters. Vortex-genesis ceases as the frontal wave matures, due to onset of frontal fracture and associated dissipation of a well-defined shear zone in the high *p*[TN] region. The wave-relative location of vortex-

genesis in the model is consistent with the observed location and timing of reported tornadoes in the real NCFR.

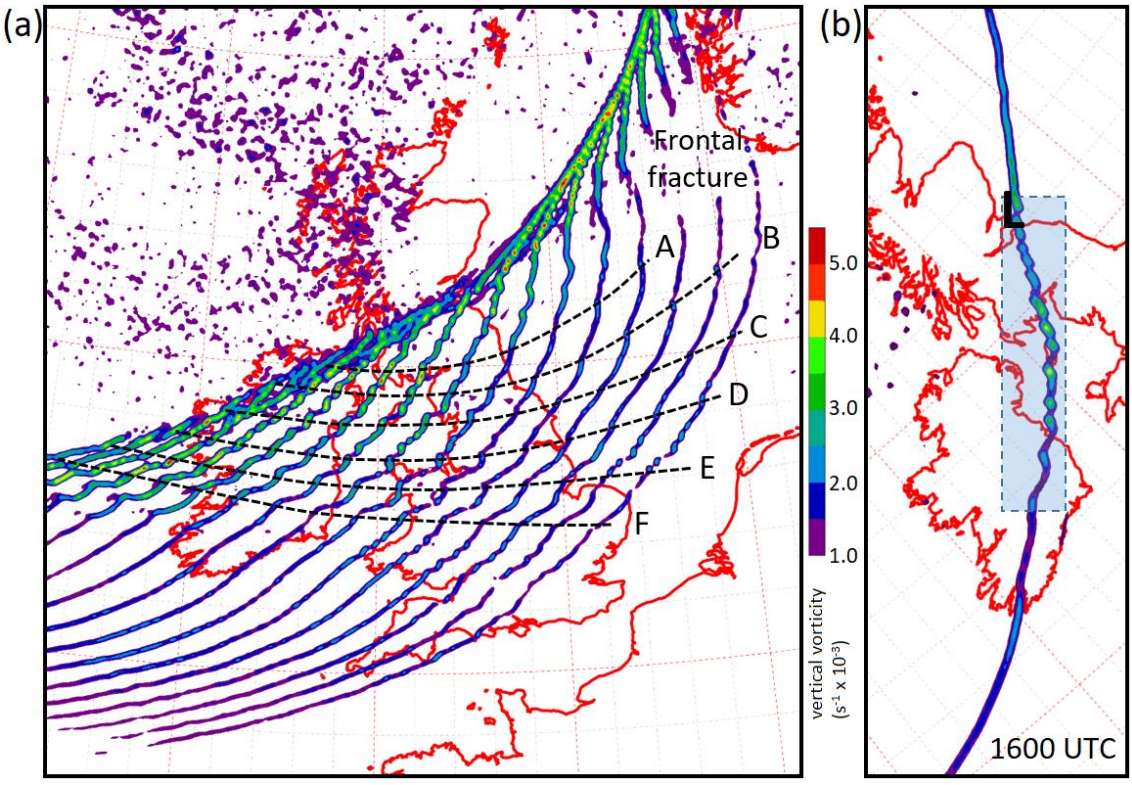

Figure 3.7: (a) Smoothed 75 m AGL vertical vorticity (colour shading) at hourly intervals from 0900 UTC 17 October to 0000 UTC 18 October 2011 from the 1.5 km model. Dashed lines show the tracks of selected vortices along the frontal shear zone, labelled A – F. (b) Smoothed 75 m AGL vertical vorticity from the 1.5 km model at 1600 UTC 17 October 2011 (colour shading). The section of front exhibiting substantial meso-ɣ-scale perturbations is highlighted by blue shading. 'L' denotes the modelled location of the wave centre.

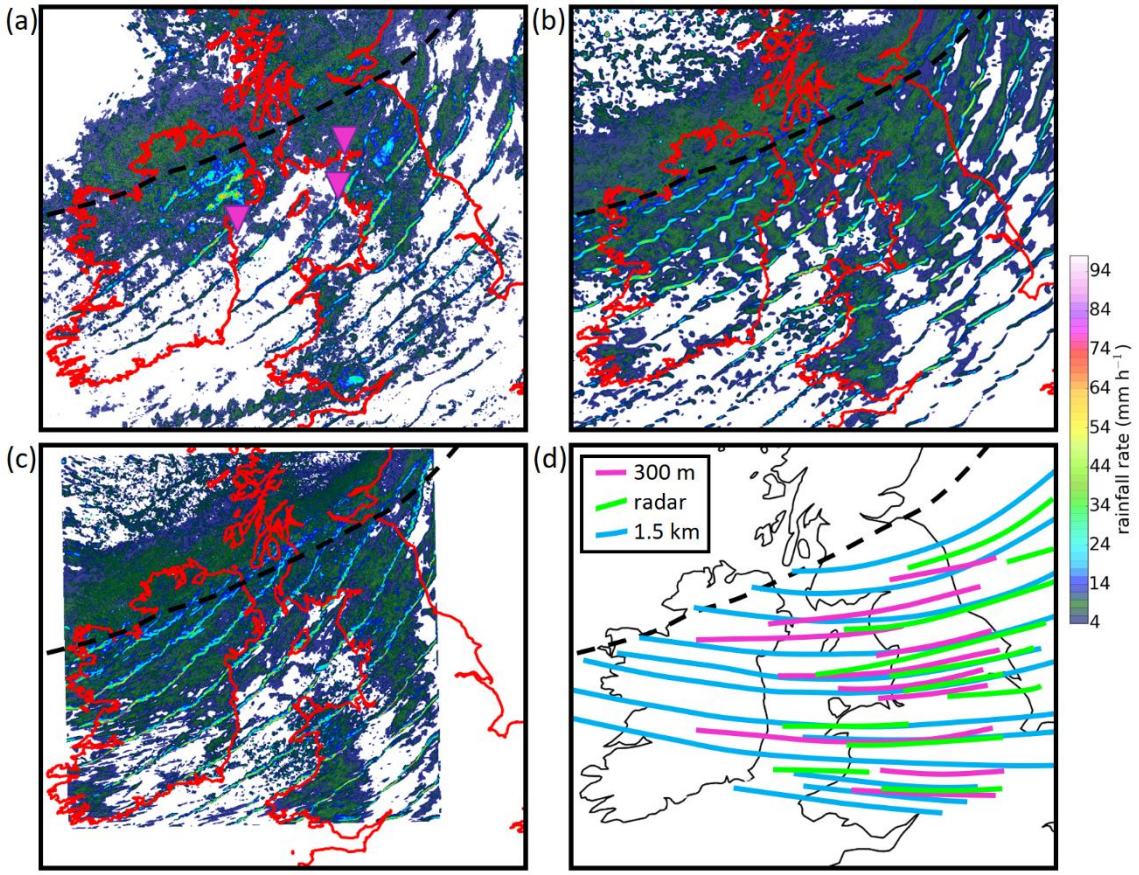

Figure 3.8: Comparison of instantaneous rainfall rates (composited at hourly intervals over the period 1000 UTC 17 October to 0000 UTC 18 October 2011) from (a) the UK and Ireland radar network; (b) the 1.5 km model; and (c) the 300 m model. The track of the modelled wave centre is shown by the bold, dashed line in each panel. (d) Tracks of prominent NCFR inflections and/or gaps in the radar data and the 1.5 km and 300 m model rainfall rate fields. Magenta inverted triangles in (a) show the location of tornado reports.

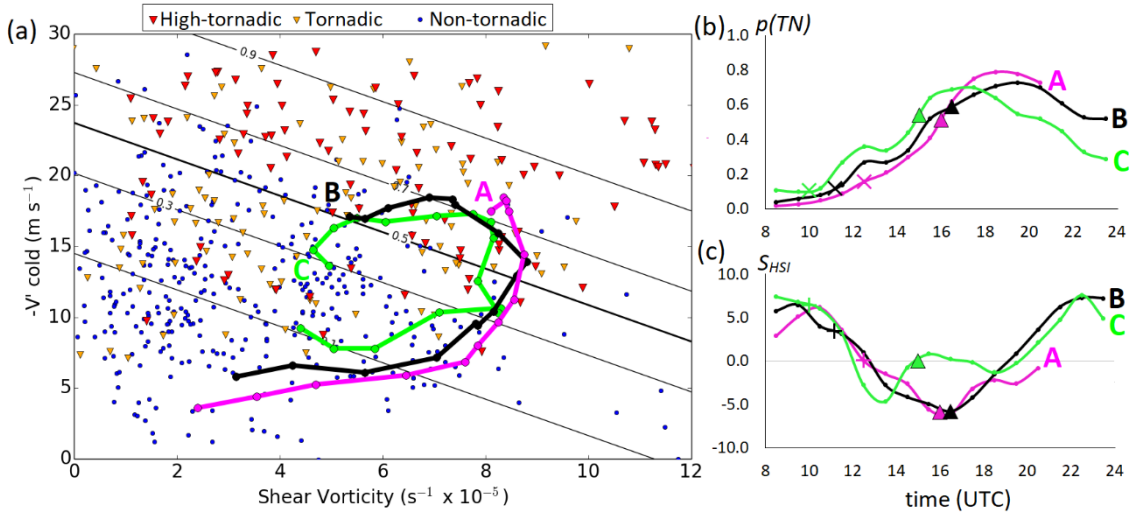

Figure 3.9: (a) Scatterplot of shear vorticity versus $-v'_{cold}$ for high-tornadic, tornadic and non-tornadic analysis points (red, orange, and blue markers, respectively) from the dataset analysed in CP20. Black contours denote the probability of a point being tornadic or high-tornadic across the two-dimensional parameter space (i.e., *p*[TN]), which is calculated using linear discriminant analysis (see CP20 for details). Bold, coloured lines show the temporal evolution of smoothed 1390 m AGL shear vorticity and $-v'_{cold}$ for three vortices (A, B and C) in the 1.5 km model (see Figure 3.7 for the tracks of these vortices). Values are computed every hour, by linear interpolation along the front where the vortex lies between on-front analysis points. Values are also averaged over two consecutive hours, then plotted at the half hour between (e.g., 1000 and 1100 UTC values averaged and plotted at 1030 UTC), to reduce the impact of noise in the individual hourly values. (b)-(c): Time-series of *p*[TN] and S_{HSI} at the locations of the same vortices over the period 0800 UTC 17 October – 0000 UTC 18 October 2011, again analysed at 1390 m AGL using 1.5 km model data. Triangles denote the time of closest passage of each vortex to a reported tornado. Cross symbols denote the approximate time of passage of the frontal wave centre.

3.5. Evolution of a primary vortex in the 1.5 km model

Using output from the 1.5 km simulation, we now explore in more detail the evolution of the shear zone near to primary vortex C (Figure 3.10; see Figure 3.7 for the location and track of this vortex). We describe how the relative movement up-front of the frontal wave impacts upon the local structure of the wind field near the NCFR, the evolution of the shear zone, and the timing of vortex-genesis. The influence of the vortex on the meso-ɣ-scale structure of the NCFR, which is later compared with radar observations of the real NCFR, is also explored throughout the lifecycle of the vortex. The morphology and evolution of vortex C is considered typical of the primary vortices in the 1.5 km simulation. The domain moves with the travelling shear zone and the centre is fixed near the vortex for all analysis times.

At the outset (Figure 3.10(a)), the domain is situated just up-front of the wave centre. The shear zone is already reasonably well-defined, with an abrupt decrease in wind speed across the frontal boundary (the area of light winds post-front is part of the region marked POF_{min} in Figure 3.5). An area of stronger, forward-directed flow is evident further rearward of the front (towards the top-left corner of the panels in Figure 3.10(a)), which catches up with the shear zone as the centre of the frontal wave passes through the domain (*cf*. Figures 3.10(a) and (b)). Horizontal convergence and vertical vorticity consequently increase substantially, with associated narrowing of the shear zone. A well-developed NCFR forms by 1200 UTC, with local rainfall maxima >30 mm h^{-1} (Figure 3.10(b)). Individual vortices begin to develop along the shear zone around this time.

Over the following 1 – 2 hours, localised NCFR perturbations develop as vortex C (and neighbouring vortices) continue to intensify. By 1400 UTC (Figure 3.10(c)), the perturbations are well defined and occur with fairly regular along-front spacing. Analysed over a larger domain, the mean spacing at this time is 37.9 km (range 31.6 – 44.3 km). Between the perturbation centres, clockwise-turned filaments (hereafter 'braids') develop, along which the shear zone becomes particularly narrow under the influence of increased horizontal convergence. Conversely, convergence decreases near the perturbation centres. A positive correlation exists between the magnitude of near-surface horizontal convergence, 1 km AGL updraft speed (not shown) and surface precipitation rate (e.g., as evident in the right-hand panels in Figures 3.10(c) and (d)), such that development of the vortices and associated along-front variability in horizontal convergence results in transition of an initially relatively unbroken NCFR (Figure 3.10(b)) to one exhibiting marked 'core–gap' morphology (e.g., Figure 3.10(d)). The cores, with rainfall rates locally > 50 mm h^{-1}, are located at the braids between primary vortices, where the updraft speeds are maximised, with NCFR gaps forming near the primary vortex centres. This core–gap morphology, and the clockwise orientation of individual cores relative to the mean orientation of the front, is consistent with numerous observations and modelling studies of NCFRs in the literature (e.g., James and Browning, 1979; Matejka *et al*., 1980; Hobbs and Persson, 1982; Parsons and Hobbs, 1983; Browning and Reynolds, 1994; Browning and Golding, 1995; Jorgensen *et al*., 2003; Kawashima, 2007; Smart and Browning, 2009; Clark and Parker, 2014).

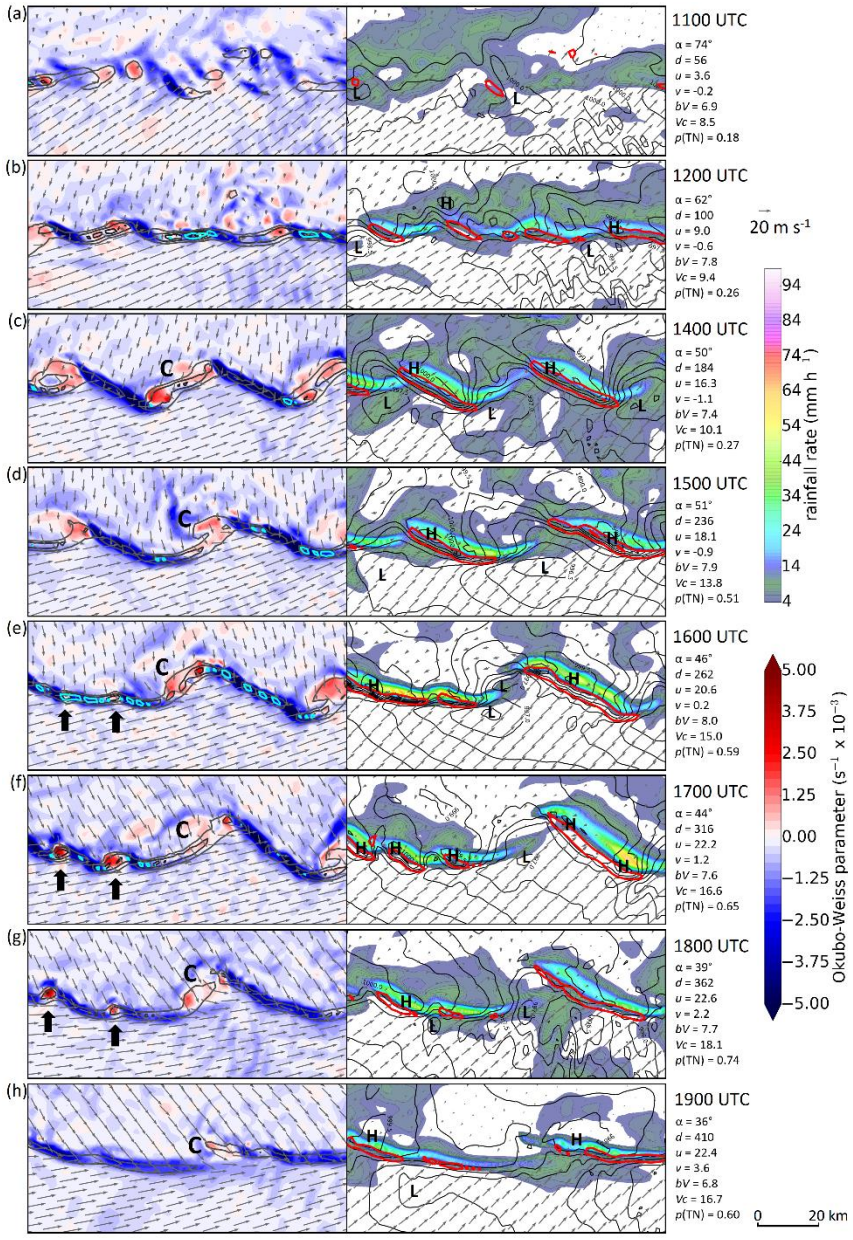

Figure 3.10: Evolution of MSLP, rainfall rate and 555 m AGL wind fields near vortex C (as labelled) over the period 1100 – 1900 UTC 17 October 2011 from the 1.5 km model. Left column: Okubo-Weiss parameter (shading), vertical vorticity (grey-black contours; contour interval 3 x 10^{-3} s^{-1} starting at 3 x 10^{-3} s^{-1}), ground-relative wind vectors (arrows, plotted every 4.5 km in the x and y direction). Cyan contours enclose regions with vertical vorticity stretching > 2 x 10^{-4} s^{-2}. Bold arrows in panels (e)-(g) denote locations of secondary vortices. Right column: rainfall rate (colour shading), vortex-relative wind vectors (arrows), MSLP (solid contours at 0.5 hPa intervals) and horizontal convergence (bold, red contours at intervals of 2 x 10^{-2} s^{-1}). 'L' and 'H' denote local MSLP minima and maxima, respectively. The domain shown has width 100 km and is rotated such that the x-axis is parallel to the local front at all times. Figures to the right of the panels indicate the local orientation of the front (α, degrees clockwise of a north–south line), down-front distance of domain centre from the frontal wave centre (*d*, km), x and y components of the vortex translational velocity (*u*, *v*, m s^{-1}), shear vorticity (*bV*, s^{-1} x 10^{-5}), $-v'_{cold}$ (*Vc*, m s^{-1}), and *p*[TN]. The latter three parameters are computed from the interpolated fields shown in Figure 3.6.

Over time, vertical vorticity at the braids increases as the shear zone narrows (e.g., immediately down-front of vortex C from 1400 to 1600 UTC; Figures 3.10(c)–(e)), and secondary vortices begin to develop in places, as shown by the presence of local vertical vorticity maxima with diameter ~3 – 4 km (marked by arrows in Figures 3.10(e)-(g)). In the 1.5 km model, these secondary vortices fail to exhibit upscale growth and decay slowly after ~1700 UTC, disappearing entirely by 1900 UTC (*cf.* Figures 3.10(f)-(h)). Consequently, the secondary vortices have little impact on the overall structure and evolution of the NCFR. In contrast, the secondary vortices are apparently better resolved in the 300 m simulation, and become important in the evolution of the NCFR, as described subsequently.

From ~1700 UTC vortex C begins to dissipate, as shown by a weakening and eventual loss of the local MSLP minimum and circulation centre near the vortex centre (*cf.* Figures 3.10(f) and (h)) and an associated reduction in local values of the Okubo-Weiss parameter. However, a step-like break persists in the NCFR, associated with a local minimum in cross-frontal wind, temperature and MSLP gradients (Figure 3.10(h)). Inspection of the precipitation rates over the full model domain, and comparison with radar data (e.g., as in Figure 3.8(b)), shows that these residual NCFR breaks may persist for several hours after the dissipation of the vortices originally responsible for their development.

3.6. Vortex-genesis and evolution in the 300 m simulation

Having described the genesis and evolution of primary vortices in the 1.5 km simulation, we now compare these findings with output from the 300 m simulation. We focus on the secondary, miso-scale vortices and their impact on the NCFR structure and evolution, comparing with radar observations of the real NCFR. Motivating this analysis is a desire for improved operational recognition of the radar signatures associated with rapidly developing secondary vortices, which we suggest are preferred locations for tornado-genesis (i.e., the secondary vortices constitute possible NCFR tornado parent vortices).

3.6.1 Comparison with 1.5 km simulation

On the scale of the frontal wave, the 300 m and 1.5 km simulations are similar, with both having the meso-α-scale NCFR bulge down-front of the wave centre over the Irish Sea, and evidence of long-lived meso-ɣ-scale NCFR perturbations associated with primary vortices and their remnants. Although structurally similar, the individual shear zone perturbations are smaller in the 300 m simulation and have smaller along-front spacing (*cf.* Figure 3.8(b) and (c)). A similar tendency for the size of various features to decrease with decreasing model grid length has been noted in previous modelling studies; for example, in simulations of frontal rainbands (e.g., Harvey *et al*., 2017), convective cells (Hanley *et al*., 2015) and individual updrafts (Nicol *et al*., 2015). In this respect, the 300 m model is closer to the radar observations in the current case (*cf.* Figure 3.8(a)). Another noticeable difference is that there is a much greater propensity for secondary vortex-genesis along the braid regions between existing vortices in the 300 m simulation. We suggest this is because the secondary vortices are better resolved in the 300 m simulation, though we cannot rule out the possibility that the increased vortex-genesis results from numerical noise (e.g., Dahl, 2020). Unlike in the 1.5 km simulation, most of these secondaries exhibit marked evolution and up-scale growth.

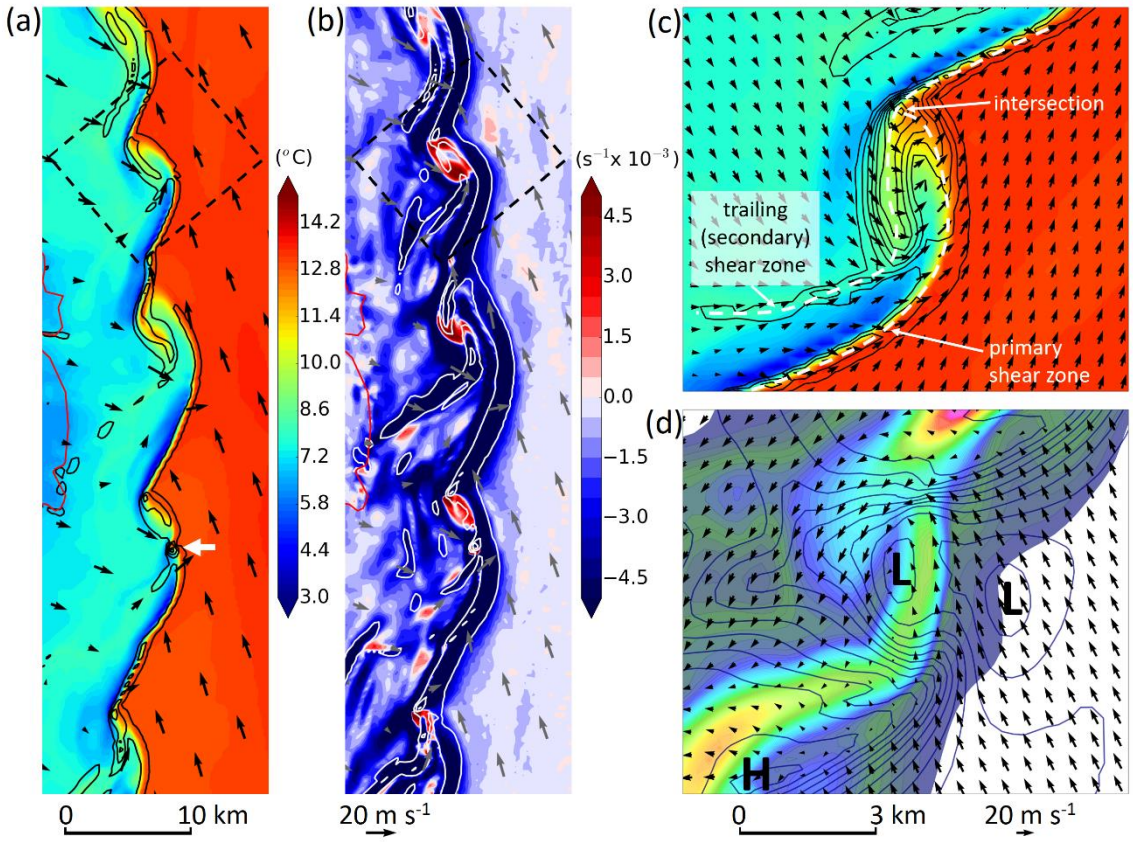

Figure 3.11: Primary vortices over the Irish Sea just to the east of Northern Ireland at 1500 UTC, from the 300 m model. (a) Surface temperature (colour shading), 10 m AGL vertical vorticity (black contours at intervals of 1.6 x 10^{-2} s^{-1}, starting at 0.4 x 10^{-2} s^{-1}) and wind vectors (arrows, plotted every 4.5 km in the x and y directions). (b) Okubo-Weiss parameter (colour shading), 10 m AGL horizontal convergence (white contours at intervals of 1.6 x 10^{-2} s^{-1}, starting at 0.4 x 10^{-2} s^{-1}) and wind vectors (arrows). Panels are rotated such that the y-axis is parallel to the local front. The coastline of Northern Ireland is shown in red. (c)-(d): closer view of one of the primary vortices over the area denoted in panels (a) and (b) by the dashed boxes. (c) Surface temperature (colour shading; scale as in panel (a)), ground-relative wind vectors (arrows, plotted every 0.6 km in the x and y directions) and vertical vorticity (black contours at intervals of 0.4 x 10^{-2} s^{-1}, starting at 0.2 x 10^{-2} s^{-1}). (d) Rainfall rate (colour shading; scale as in Figure 3.10), vortex-relative wind vectors (arrows) and MSLP (navy blue contours at intervals of 0.3 hPa).

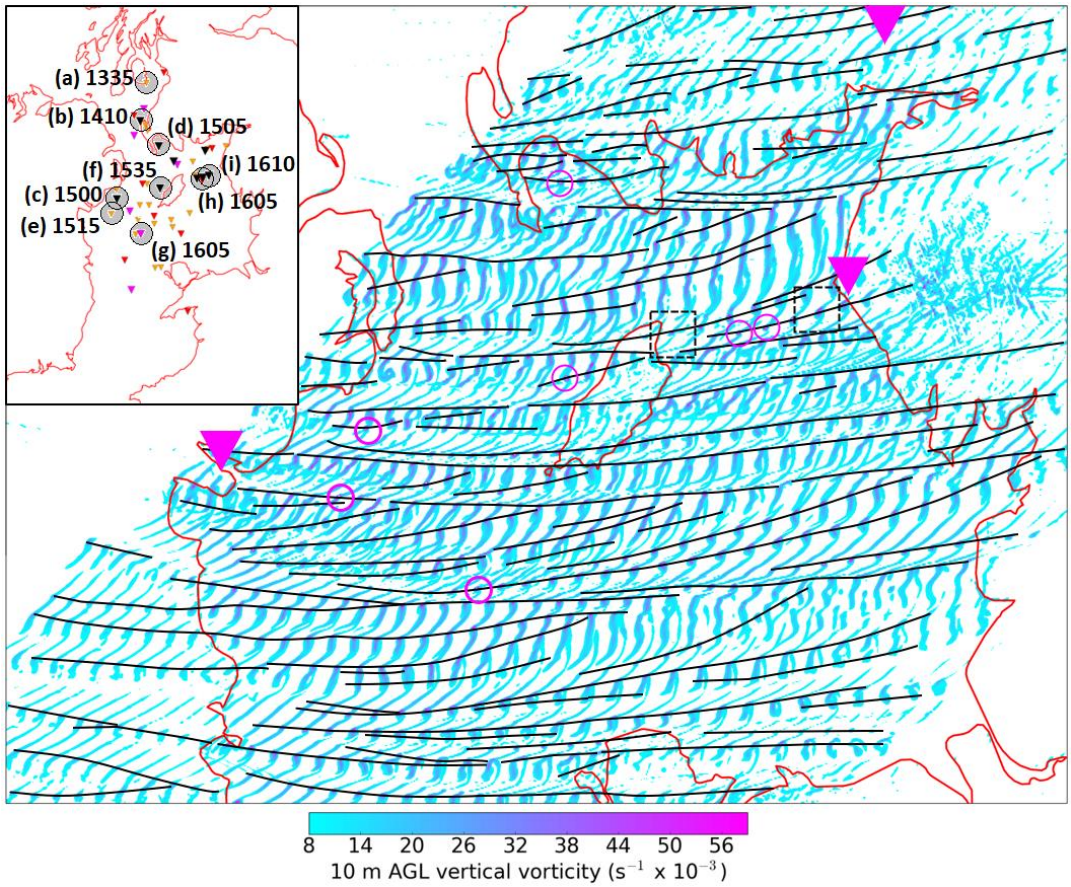

Figure 3.12: Relative vertical vorticity at 10 m AGL (colour shading) at 5-minute intervals over the period 1435 UTC – 1755 UTC 17 October 2011 from the 300 m model. Black lines show tracks of miso-scale vortices (subjectively analysed). Magenta circles highlight vortices having vertical vorticity > 7.5 x 10^{-2} s^{-1}. Magenta inverted triangles are tornado reports. Small, dashed boxes near the Isle of Man and the Cumbria denote, respectively, the area shown in Figures 3.13(a) and (g). Inset panel: Locations (inverted triangles) of 10 m AGL vertical vorticity stretching maxima exceeding 2.2 x 10^{-3} s^{-2} (orange), 2.4 x 10^{-3} s^{-2} (red), 2.6 x 10^{-3} s^{-2} (magenta) and 2.8 x 10^{-3} s^{-2} (black) from the 300 m model. Grey circles denote the locations of vorticity maxima > 7.5 x 10^{-2} s^{-1}. Overlaid text indicates the time of occurrence of each (in UTC), and the letter indicates the corresponding panel in Figure 3.14.

3.6.2 NCFR and shear zone structure prior to secondary vortex-genesis

Figure 3.11 shows a row of mature, primary vortices at 1500 UTC, before onset of widespread secondary vortex-genesis. These vortices developed in a manner closely resembling the early evolutionary stages of vortex C in the 1.5 km model (Figure 3.10(a)–(d)). The location of primary vortices is best seen by analysis of the Okubo–Weiss parameter, *O*, (Figure 3.11(b)), which is defined as the difference between the magnitudes of vertical vorticity and total horizontal strain (positive where vorticity

exceeds strain; Okubo, 1970; Weiss, 1991)[14]. Vorticity-dominant regions ($O > 0$, denoted by red shading in Figure 3.11(b)) comprise discrete, well-defined centres that occur at regular intervals along the shear zone (mean spacing 14.2 km; range 11.0 – 17.4 km). In contrast, strain is dominant ($O < 0$) along the braids. The mean spacing of primary vortices is just over one-third of that found in the 1.5 km model near to vortex C. We suggest the difference is symptomatic of the 1.5 km model's inability to simulate the true narrowness of the shear zone, given that linear theory predicts that the growth rate to be maximised for perturbations of wavelength ~7.5 times the thickness of the shear zone (Miles and Howard, 1964).

Near the primary vortices, the shear zone exhibits a complex structure; maxima in vertical vorticity generally occur along the flanks of the circulation centres, as noted in the 1.5 km simulation. A narrow filament of large vertical vorticity and relatively high temperatures is drawn out in the sheared flow on the rear flanks of each vortex (annotated in Figure 3.11(c)). Another elongated vertical vorticity maximum is drawn up-front on the forward flank of each vortex, intersecting the vorticity maximum along the braid region immediately up-front of the vortex (as annotated in Figure 3.11(c)). Secondary vortices in the 300 m simulation develop either along the braids, or near this intersection point of multiple shear zones on the flanks of primary vortices. An example of a strong secondary vortex at the shear zone intersection point on the flank of a primary vortex is highlighted by the white arrow in Figure 3.11(a).

[14] We use the definition of Schielicke *et al*. (2016) for the total horizontal strain, which comprises the sum of magnitudes of horizontal divergence, stretching deformation and shearing deformation. For clarity, we note that this differs from the Dritschel *et al*. (1991) horizontal strain, which comprises the stretching deformation only.

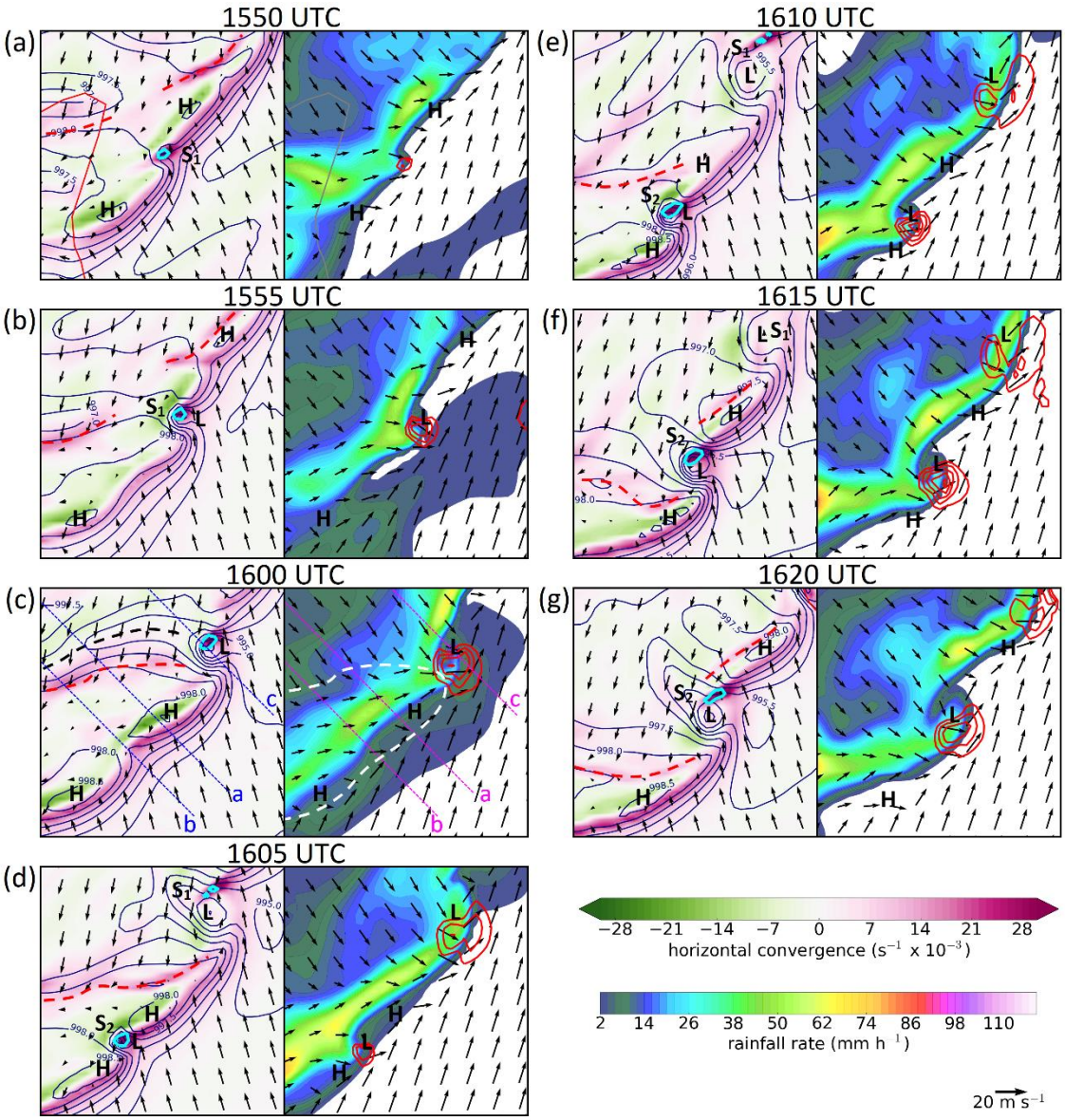

Figure 3.13: Evolution of surface fields near selected secondary vortices (labelled S_1 and S_2) from the 300 m model. Left-hand panels: horizontal convergence (colour shading), vortex-relative wind vectors (arrows, plotted every 1.2 km), MSLP (navy blue contours at 0.5 hPa intervals). Cyan contours enclose regions of vertical vorticity stretching > 1 x 10^{-3} s^{-2}. Red, dashed lines denote the position of the secondary shear zone. Black, dashed line in (c) denotes position of an MSLP trough located behind the secondary shear zone. Right-hand panels: rainfall rate (colour shading), ground-relative wind vectors (arrows, plotted every 1.2 km) and wind speed (red contours at intervals of 2 m s^{-1}, starting at 26 m s^{-1}). White, dashed line in (c) encloses the region of south-westerly winds (and weak flow in the system-relative frame of reference) between the primary and secondary shear zones. Blue and magenta dashed lines in panel (c) denote the position of the vertical sections in Figure 3.15, with the adjacent letters indicating the corresponding panel number of Figure 3.15. Note that the northwest end of each vertical section lies beyond the edge of the domain shown here.

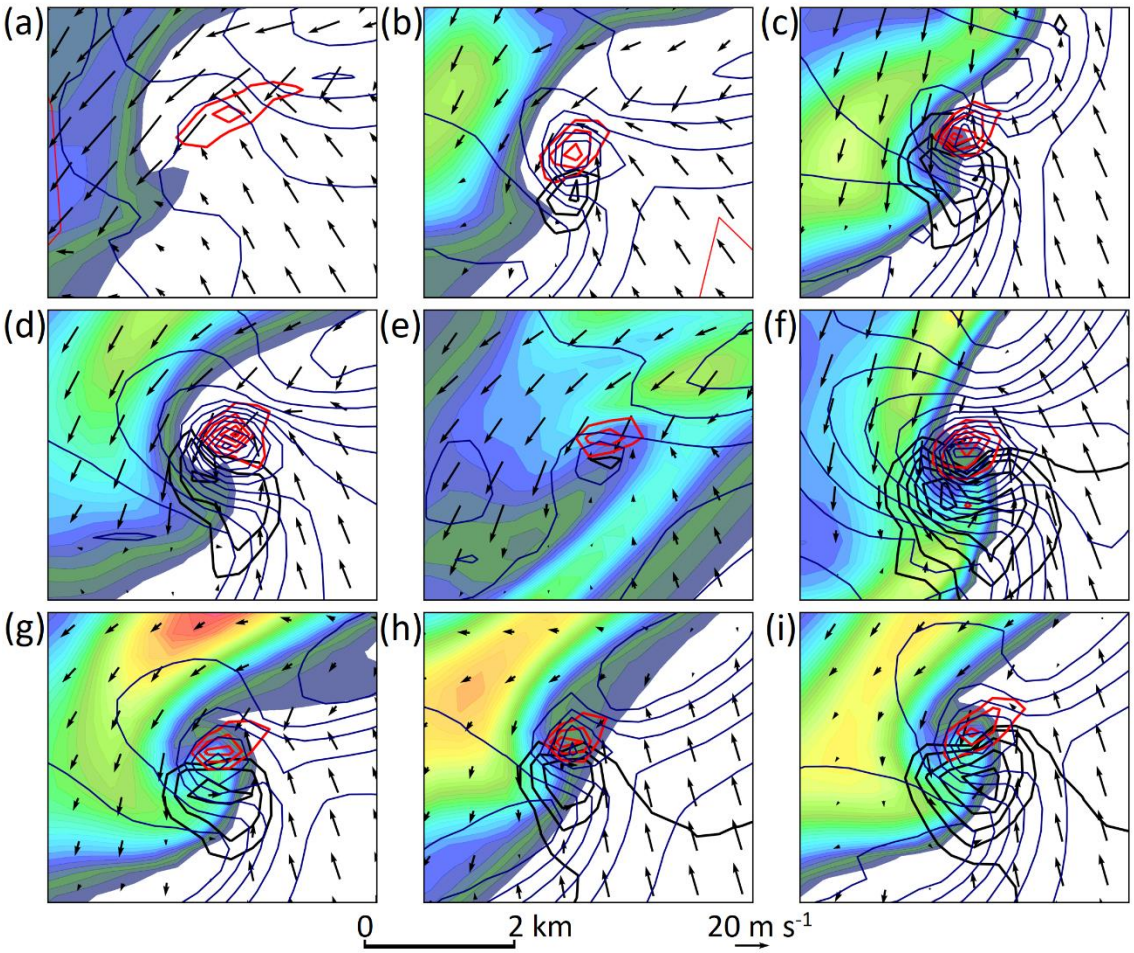

Figure 3.14: Surface fields near the nine strongest vertical vorticity maxima (vertical vorticity >7.5 x 10^{-2} s^{-1}) in the 300 m model, centred on the vorticity maximum in each case. Rainfall rate (colour shading, scale as in Figure 3.10), vortex-relative wind vectors (arrows, plotted every 0.6 km), MSLP (navy blue contours at 0.5 hPa intervals), wind speed (black contours at 2 m s^{-1} intervals, starting at 24 m s^{-1}) and vertical vorticity stretching (red contours at intervals of 0.8 x 10^{-3} s^{-2}).

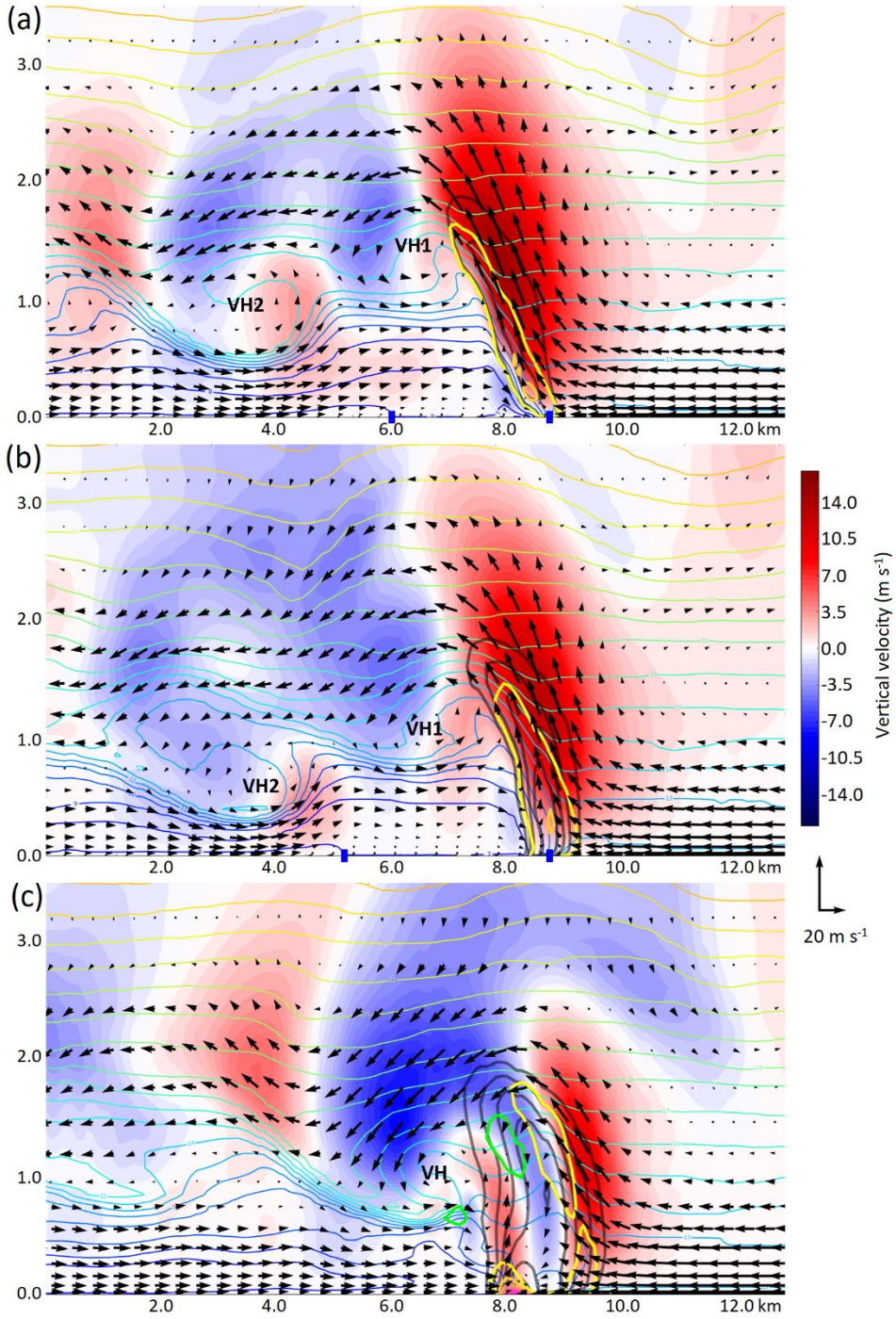

Figure 3.15: Vertical sections through the shear zone at 1600 UTC (see Figure 3.13(c) for the position of each) intersecting (a) the braid region between secondary vortices S_1 and S_2; (b) incipient vortex S_2; (c) mature vortex S_1. Vertical velocity (colour shading), θ (coloured contours at 1 K intervals), wind vectors parallel to the section (arrows, plotted every second model level in the vertical and every 0.36 km in the horizontal), vertical vorticity (grey contours at intervals of 1 x 10^{-2} s^{-1}), vertical vorticity stretching (yellow–pink contours at intervals of 4 x 10^{-4} s^{-2}, starting at 2 x 10^{-4} s^{-2}) and tilting of horizontal vorticity (lime contours at intervals of 4 x 10^{-4} s^{-2}, starting at 2 x 10^{-4} s^{-2}). 'VH' indicates the location of horizontal vortices near the interface between the forward-relative and rearward-relative flows behind the surface front, as discussed in the main text. Blue markers on the x-axis in panels (a) and (b) denote the positions of the leading and trailing zones of horizontal shear.

Table 3.1: Properties of the seven strongest secondary vortices (where strength is taken to be the maximum 10 m AGL vertical vorticity along the vortex track in the 5-minute fields) in the 300 m simulation (for locations of these vortices, see inset panel of Figure 3.12). Pressure deficit is relative to the local MSLP on the warm side of the front. Diameter is that at the time of maximum differential velocity. Position of vertical vorticity stretching maximum is relative to the centre of the MSLP minimum at the time of maximum vertical vorticity. Maximum wind speed, and all wind derivatives, are analysed at the 10 m AGL level.

Time of maximum vertical vorticity (UTC)	*Max. vertical vorticity (s^{-1} x 10^{-2})*	*Max. vorticity stretching (s^{-2} x 10^{-3})*	*Max pressure deficit (hPa)*	*Max. wind speed ($m\ s^{-1}$)*	*Max. differential velocity ($m\ s^{-1}$)*	*Diameter (km)*	*Translational velocity ($m\ s^{-1}$, degrees)*	*Position of vorticity stretching max.*
1410	8.29	2.97	0.9	28.3	23.4	1.53	17.3, 264	Collocated
1500	8.79	3.64	0.7	31.2	22.2	1.90	20.7, 264	W
1505	9.35	4.38	3.1	30.6	24.9	1.80	19.2, 270	NE
1515	7.73	2.40	-0.4	24.8	20.4	1.23	20.1, 275	N
1535	9.04	3.71	3.5	34.8	27.7	0.95	23.0, 244	N
1605	7.63	2.77	0.6	30.1	22.7	1.50	23.6, 262	N
1605	7.79	3.00	1.1	34.4	23.3	2.12	23.2, 259	NW
Mean	**8.37**	**3.27**	**1.4**	**30.6**	**23.5**	**1.58**	**21.0, 263**	**NNW**

3.6.3 Genesis and evolution of secondary vortices

After 1500 UTC, secondary vortex-genesis occurs in numerous places along the shear zone. Some idea of the variability in the development and evolution of vortices may be gained by inspection of vortex tracks, as inferred from 10 m AGL vertical vorticity fields at 5-minute intervals between 1435 and 1755 UTC (Figure 3.12), during which period the cold front tracked across the Irish Sea (vortex tracks are analysed mainly over sea areas, because topographical effects often complicate the near-surface vertical vorticity structure over land, which tends to obfuscate the analysis). The orientation of individual vortex tracks varies from west-northwest–east-southeast to southwest–northeast, sometimes over relatively small distances along the front. This reflects the variable tendency for secondary vortices to move towards and merge with the larger inflections associated with mature or decaying primary vortices. Over time it becomes impossible to distinguish between primary and secondary vortices, because many of the secondaries grow upscale to become the dominant feature along the local shear zone, whilst the primaries tend to become elongated in the along-front direction and ill-defined.

Detailed analysis of the development and evolution of individual secondary vortices is beyond the scope of the present paper, but we summarise a few key findings (also see Table 3.1):

- The strongest secondary vortices (circled in Figure 3.12) exhibited 10 m AGL vertical vorticity >7.5 x 10^{-2} s^{-1} and generally occurred along the braids between primaries (rather than at shear zone intersection points on the flanks of primaries).
- Most of these vortices occurred along the northern half of the meso-α-scale frontal bulge over the Irish Sea (i.e., just down-front of the frontal wave's centre). This corresponds closely to the region with tornado reports in the real NCFR, allowing for the land-sea issues alluded to above (reported tornado locations are shown by the large magenta inverted triangles in Figure 3.12).
- These vortices developed extremely rapidly, amplifying from subtle inflections along the braids to maximum vertical vorticity, with an associated closed circulation in the 10 m AGL wind field, in 5 – 15 minutes (Figure 3.13).
- Vortices were associated with characteristic miso-scale perturbations in the NCFR, including small bulges, hooks or appendage echoes at the NCFR leading edge near the southern flanks of the vortices, and inflow notches near the northern flanks (Figure 3.14)[15]. In the latter stages of vortex development, 'broken-S' rainfall signatures (McAvoy *et al*., 2000; Grumm and Glazewski, 2004; Lane and Moore, 2006) sometimes occurred, due to the development of a rainrate minimum near the vortex centre (as found for the primary vortices).
- The secondary vortices exhibited a core of >25 m s^{-1} ground-relative wind speeds on their southern flanks, where the rotational and background flow fields are additive, and a region of intense vertical vorticity stretching on their north or northwest flanks (Figure 3.14), where low-level (< 0.5 km AGL) updraft speeds are maximised.

[15] In one case these features occurred near the rear edge of the NCFR (Figure 3.14(e)).

Vertical sections through selected vortices (Figure 3.15) reveal that the secondary vortices are relatively shallow (commensurate with the shallowness of the NCFR, more generally), with large vertical vorticity (>1 x 10^{-2} s^{-1}) generally restricted to the lowest 2 km AGL; mature vortices exhibited a central downdraft with updrafts on both flanks of the vortex (e.g., Figure 3.15(c)). The intense vorticity stretching maximum on the north or north-west flank of the secondary vortices, which we suggest to be a preferred region for tornado-genesis, is evidently particularly shallow, with stretching > 2 x 10^{-4} s^{-2} extending to only ~250 m AGL (Figure 3.15(c)).

The vertical sections reveal that, at the scale of the secondary vortices, the shear zone exhibits a complex three-dimensional structure. For example, there is evidence of strong horizontal vortices near the interface of the rearward- and forward-relative flows above and below, respectively, the frontal boundary aloft (e.g., Figure 3.15(a) and (b)), which resemble the Kelvin-Helmholtz billows reported in laboratory and modelling studies of density currents. Similar structures were reported by Wakimoto and Bosart (2000) in high-resolution Doppler radar observations of an NCFR (see their Figure 17(e)), suggesting that these model features are at least plausibly realistic. Additional vertical sections (not shown) reveal that the horizontal vortices are horizontally contiguous; the rearward vortex (labelled ‘VH2’ in Figure 3.15(b)) is apparently associated with a secondary horizontal wind shift at the surface, on the immediate cold side of the front (i.e., a secondary horizontal shear zone; examples are marked by the dashed red lines in various panels of Figure 3.13) and a prominent local MSLP minimum (marked by the dashed black line in Figure 3.13(c), left panel). Beneath this horizontal vortex, the forward-directed, front-relative flow is locally enhanced and the potential temperature contours bunch together strongly and descend closer to the surface (indicating a shallower cold pool capped by a layer of very strong static stability; Figure 3.15(a)-(b)). Between the main and secondary shear zones, the cold pool is locally deeper than elsewhere in the vertical sections, and the NCFR-relative winds are light.

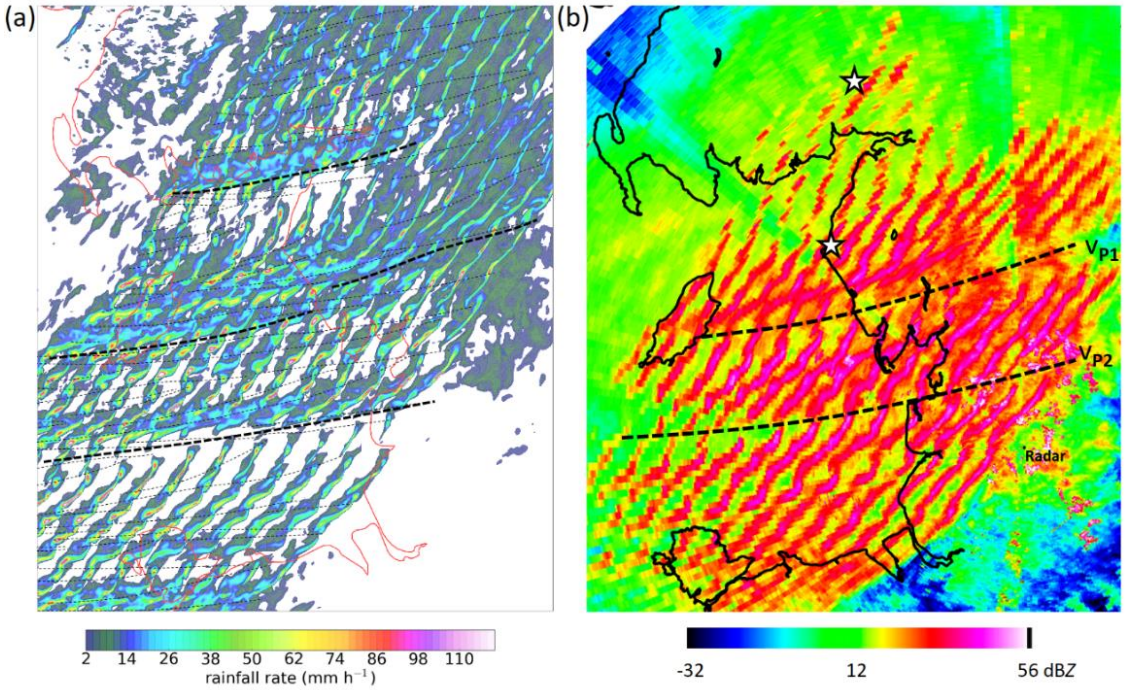

Figure 3.16: Comparison of (a) rainfall rate from the 300 m model and (b) raw reflectivity from 0.5° elevation-angle scans of the Hameldon Hill radar, showing evolution of the NCFR over northwest England and adjacent parts of the Irish Sea. Model data are plotted every 10 minutes over the period 1535 – 1755 UTC, and radar data every 10 minutes over the period 1500 – 1730 UTC. Tracks of larger NCFR inflections and gap regions are indicated by bold, dashed contours in each panel. Narrow, dashed contours in (a) are subjectively analysed tracks of shear zone vorticity maxima (as in Figure 3.12). White stars in (b) denote the location of confirmed tornadoes.

3.6.4 Comparison with radar observations

In order to aid operational recognition of miso-scale features potentially associated with NCFR tornadoes, and to support the suggestion that tornadoes in the real NCFR were associated with miso-scale vortices similar to the secondary vortices in the 300 m simulation, we now present a comparison of the modelled and observed structure of the NCFR over part of the region exhibiting the strongest secondary vortices in the 300 m simulation (Figure 3.16). The model and observations agree closely in several respects. Firstly, relatively large perturbations are evident at intervals of approximately 50 – 70 km in the along-front direction which, in the model, can be seen to be associated with the remnants of primary vortices, or regions where vortices have amalgamated and grown up-scale whilst weakening (the tracks of these perturbations are indicated by bold dashed lines in Figure 3.16, and labelled V_{P1} and V_{P2} in Figure 3.16(b)). The along-front

spacing of the larger inflections appears to be similar in the radar data and the 300 m simulation (*cf*. Figures 3.16(a) and (b)).

Secondly, smaller-scale perturbations, of typical wavelength 5 – 10 km, are evident in the modelled and observed NCFR between the tracks of the larger inflections. In the model, these perturbations are associated with the secondary, miso-scale vortices. The presence of vortices of equivalent size in the real NCFR cannot be confirmed, owing to a lack of Doppler radar observations over northern England at the time of the event. However, the radar reflectivity field (Figure 3.16(b)) exhibits similar small-scale perturbations, comprising line bulges and occasional hooks and small NCFR breaks, superimposed on the larger-wavelength pattern described above. These features are suggestive of the presence of secondary vortices in the real NCFR.

Closer analysis of reflectivity data from the Hameldon Hill radar near to the Whitehaven tornado report (Figure 3.17(a)-(e)) shows that the tornado occurred at the up-front flank of a developing miso-scale NCFR inflection, as shown by the tornado report's positioning just to the northwest of the track of the centre of the inflection. The inflection only becomes apparent in the 1545 UTC scan (Figure 3.17(b)), suggesting that the associated miso-scale vortex was at an early stage in its development when the tornado occurred. A subtle reflectivity minimum develops near the inflection centre by 1600 UTC, resulting in the 'broken-S' signature (Figure 3.17(e)). This signature becomes indistinct after 1600 UTC, suggesting that the tornado parent vortex was relatively short-lived.

A similar analysis for the Templand and Killowen tornadoes, using data from the nearest radars, also shows an association with developing miso-scale perturbations in the NCFR. For the Templand tornado, detailed analysis is precluded by the large range from radar, but the report is again situated close to a developing inflection and small NCFR break (Figure 3.17(f)-(j)). The (unconfirmed) Killowen tornado occurred near the centre of a shallow NCFR inflection, located immediately up-front of an intensifying reflectivity maximum (not shown). Therefore, all three tornadoes appear to have been associated with amplifying miso-scale NCFR perturbations resembling those associated with secondary vortices in the 300 m simulation.

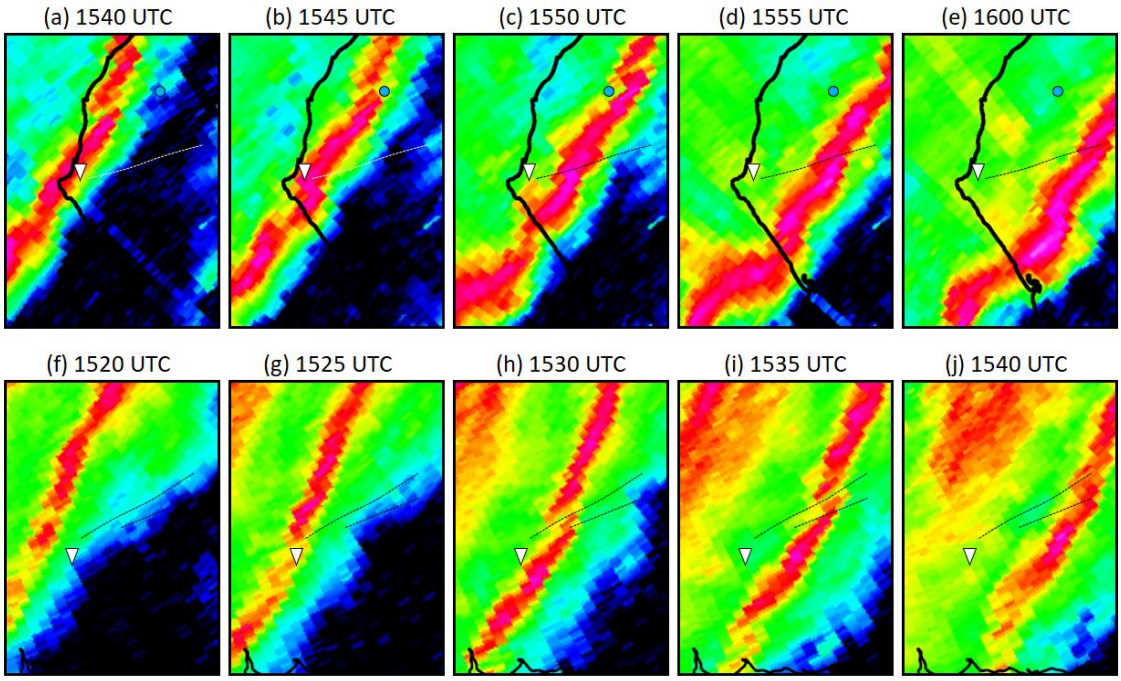

Figure 3.17: Sequence of 0.5° elevation angle radar reflectivity (colour scale as in Figure 3.16(b)) near to the two confirmed tornado reports (white inverted triangle in each panel). (a)–(e): data from Hameldon Hill radar showing evolution of the NCFR near the Whitehaven, Cumbria, tornado. Location of an additional, non-tornadic, wind damage report is shown by the blue circle. (f)–(j): data from Holehead radar showing evolution of the NCFR near to the Templand, Dumfries and Galloway, tornado. Area shown has width 62.5 km in all panels. Thin, dashed lines denote the tracks of NCFR gaps and inflections that pass close to the tornado reports. Coastlines are shown in black. Radar scan times are given above each panel.

3.7. Discussion

In the preceding sections we have explored how a developing frontal wave influences the timing and location of meso-γ- to miso-scale vortex-genesis along a vertical vortex sheet coincident with an NCFR, and we have described the structure and evolution of selected vortices. In this section we further consider the possible vortex-genesis mechanisms and compare our results with those of previous studies of meso-ɣ- to miso-scale vortices within NCFRs and QLCSs more generally.

Considering the various possible vortex-genesis mechanisms, we suggest HSI to be the most likely, as supported by the following evidence:

i. Primary vortices exhibited fairly regular along-front spacing, and vortices were like-signed (i.e., all cyclonic); no evidence of cyclonic–anticyclonic vortex pairs was found (such vortex pairs would be expected in the early stages of

development if tilting of horizontal vorticity were the relevant vortex-genesis mechanism; e.g., Weisman and Davis, 1998; Trapp and Weisman, 2003; Atkins and St Laurent, 2009).

ii. The spacing of primary vortices in the 1.5 km and 300 m simulations conforms closely to that predicted by linear theory for the most unstable mode (i.e., 7.5 x initial shear zone width; Miles and Howard, 1964). Details of the vortex-spacing calculations are presented in Appendix F.

iii. The associated pattern of roughly ovoid vortex cores (when viewed in horizontal section) separated by narrowing braids along which the horizontal convergence was maximised, and the breaking wave structure in low-level temperature and vorticity fields (e.g., Figure 3.11), strongly resemble the structures reported in idealised simulations of HSI (e.g., Figure 7 of Buban and Zeigler, 2016).

iv. In the pseudo-Lagrangian reference frame of individual vortices, primary vortex-genesis occurred close to the time of transition from positive to negative S_{HSI}. This is consistent with the release of HSI, in a situation where the release was formerly supressed by the large cross-frontal confluence, following the results of Dritschel *et al*. (1991)

A caveat to the final point is that the magnitude and sign of S_{HSI} has a strong height dependency, as revealed by calculation of values on different model levels between the surface and 3.5 km AGL (not shown). In general, S_{HSI} increases with decreasing height within the boundary layer due to surface friction (which acts to increase the horizontal convergence, relative to the vertical vorticity, along the shear zone). Down-front of the wave centre, in the region of $S_{HSI} < 0$ at 1390 m AGL, the height of transition to positive values is low compared to the mean depth of the shear zone; in other words, most of the shear zone experiences $S_{HSI} < 0$. In contrast, elsewhere along the front, the shear zone is shallower whilst the height of transition is greater, or S_{HSI} is positive at all heights, such that most or all of the shear zone is situated within $S_{HSI} > 0$. We are not aware of any studies pertaining to the stability of vortex strips in vertically varying stretching deformation fields, but it may be speculated that the release of HSI is more likely where the height of transition to $S_{HSI} < 0$ is low, relative to the depth of the shear zone, as is the case immediately down-front of the wave centre. These aspects are explored further in Appendix G.

In the current case, the radar-observed development of miso-scale NCFR perturbations including inflections, broken-S signatures and occasional hooks akin to those in the 300 m model strongly suggests that miso-scale vortices were present in the real NCFR (*cf*. Figures 3.16(a) and (b)) although, in the absence of Doppler radar observations, this cannot be confirmed. The association between miso-scale vortices, NCFR perturbations and tornadoes has been demonstrated in previous studies of tornadic NCFRs where Doppler radar data were available (e.g., Carbone, 1983; Clark and Parker, 2014), and is suggested in the current study by the proximity of tornado reports to developing NCFR perturbations. Whilst existing studies appear consistent in this respect, analysis of Doppler radar observations for a larger set of NCFR tornadoes would be beneficial for furthering our understanding of the association between tornadoes and miso-scale vortices, and of the positioning of tornadoes relative to the associated vortices and NCFR perturbations, more generally.

The observed sub-structure of the secondary vortices in the 300 m simulations agrees closely with that reported in previous simulations of miso-scale NCFR vortices. For example, in a real data simulation of the 24 September 2007 NCFR, Smart and Browning (2009) found a vertical vorticity stretching maximum at the northern flank of their modelled vortices, which they likewise suggested to be a potential location for tornado-genesis. Other similarities (*cf*. their Figure 7) include the relative shallowness of vortices (typical depth ~2 – 3 km), the occurrence of the largest vertical vorticity at low levels (<0.5 km AGL), the presence of a downdraft wrapping around the down-front flank of the vortex at low levels, the core of strong winds (> 25 m s^{-1}) on the down-front flank of the vortex, and the association of vortices with localised NCFR perturbations including inflections and broken-S-type structures. Apsley *et al*. (2016) similarly noted wind maxima on the equatorward flank of their simulated miso-scale vortices, in a reanalysis of the cold-frontal tornado outbreak of 23 November 1981. However, unlike in the present case, Apsley et al. (2016) reported the frequent occurrence of cyclonic–anticyclonic vortex pairs. This difference suggests that the vortex-genesis mechanisms may vary from case to case.

The development of > 25 m s^{-1} wind cores on the equatorward flanks of simulated miso-scale vortices provides a possible explanation for reports of localised non-tornadic wind damage in NCFRs, as previously suggested by Smart and Browning

(2009). An example is shown in Figure 3.17(a)-(e); the blue dot marks the location of localised non-tornadic wind damage, which occurred near the centre of a small NCFR bulge on the southern flank of a small broken-S signature. However, with typical diameters of 1 – 3 km, we suggest these cores are unlikely to explain the majority of NCFR tornado reports, since damage site investigations show the tornadoes to have typical track widths of around 50 – 100 m[16]. As noted by Smart and Browning (2009), the potential for both tornadic and non-tornadic wind damage in association with miso-scale vortices does highlight a need for careful investigation of individual NCFR damage reports, in order to ensure the proper classification of damage as tornadic or otherwise.

The similarity in the structure of the primary and secondary vortices in the 300 m simulation, and of the wind, temperature, and pressure fields in their vicinity (e.g., *cf*. Figures 3.11(d) and 3.13(g)), is striking. This similarity suggests that the sequential evolution of primary vortices, followed by smaller-scale secondaries along the braids between them, may be an example of the self-similar cascade of filament instabilities described by Scott and Dritschel (2014), wherein vortex sheet roll-up repeatedly occurs along the braids between existing vortices, down to very small scales. If so, a natural question arising is whether tertiary (and further) vortex-genesis might be simulated along the braids between the secondary vortices, given a model with sufficiently small grid spacing. This scenario raises the possibility that tornado-like vortices in NCFRs result from the development of braid instabilities at scales unresolved in the simulations presented here (rather than within the region of intense near-surface vertical vorticity stretching on the flanks of the secondary vortices, as previously suggested). Higher-resolution simulations (ideally, with grid spacing < 100 m) would be required to investigate these possibilities.

A noticeable characteristic of the larger NCFR perturbations (i.e., broken-S signatures and the residual NCFR gaps) in both the 1.5 km and 300 m simulations was

[16] Of the tornadoes associated with the set of 44 tornadic cold fronts analysed by CP20, maximum track width estimates are available in the TORRO tornado database for 51, where track width is recorded using an 11-point scale (see Table 1 of Kirk, 2007). The median and modal track width category of these tornadoes is W5 (maximum track width in the range 47 – 99 m). The minimum track width category (one tornado) was W1 (2.2 – 4.6 m) and the maximum track width category (3 tornadoes) was W7 (maximum track width in the range 216 – 414 m).

their longevity. The NCFR gaps often far outlived the vortices originally responsible for their development and they were associated with local minima in cross-frontal wind and temperature gradients, as found in previous observational studies (e.g., James and Browning, 1979). This longevity, coupled with down-front movement relative to the wave centre, meant that NCFR gaps eventually migrated towards the trailing part of the front several hundred kilometres down-front of the wave centre. The persistence of the NCFR gaps and the clockwise-turned NCFR cores between them may help to explain why this kind of core–gap morphology has been so widely reported in previous studies of NCFRs (e.g., Hobbs and Biswas, 1979; James and Browning, 1979; Hobbs and Persson, 1982; Browning and Roberts, 1996; Jorgensen *et al*., 2003; Kawashima, 2007). Whilst it has sometimes been suggested that NCFR gaps represent preferred locations for tornadoes, our results suggest a distinction should be made between the smaller, amplifying perturbations associated with rapidly developing vortices (especially the miso-scale secondary vortices) and the larger, slowly evolving, step-like features and NCFR gaps associated with decaying or decayed vortices; tornadoes appear possible with the former, but highly unlikely with the latter.

Previous studies show that NCFR tornadoes are more likely where CAPE is non-zero (e.g., Clark, 2013; Apsley et al., 2016), or where moist static instability exists in the pre-frontal environment (Clark and Parker, 2014). In the present case, the immediate pre-frontal environment near the wave centre was sampled by the 1200 UTC 17 October Castor Bay (Northern Ireland) sounding. Modification with 1200 UTC surface observations from various sites shows generally meagre CAPE (<~50 J kg^{-1}) at inland locations, but rather larger CAPE (typically 50 – 200 J kg^{-1}) close to windward coasts (with respect to the south-south-westerly pre-frontal wind direction). It is noticeable that the two confirmed tornadoes occurred within ~20 km of a windward coast (e.g., Figure 3.12). In light of these results, we suggest that, whilst the frontal wave provides the requisite conditions for vortex-genesis along the shear zone and determines the region at risk of tornadoes on the mesoscale, horizontal variability in pre-frontal CAPE may also act to modulate the tornado risk on smaller scales. The discussion of buoyant instability and its spatial variability is also relevant given the results of Moore (1985), who demonstrated the existence of a hybrid buoyancy–shearing instability in NCFRs under certain combinations of horizontal shear and static stability. Further research in this area would be beneficial to determine, for example,

whether transitions can occur between pure shearing instability and the buoyancy–shear hybrid mode in an individual NCFR, and if so, how such transitions might impact on the structure and intensity of vortices and the associated tornado risk.

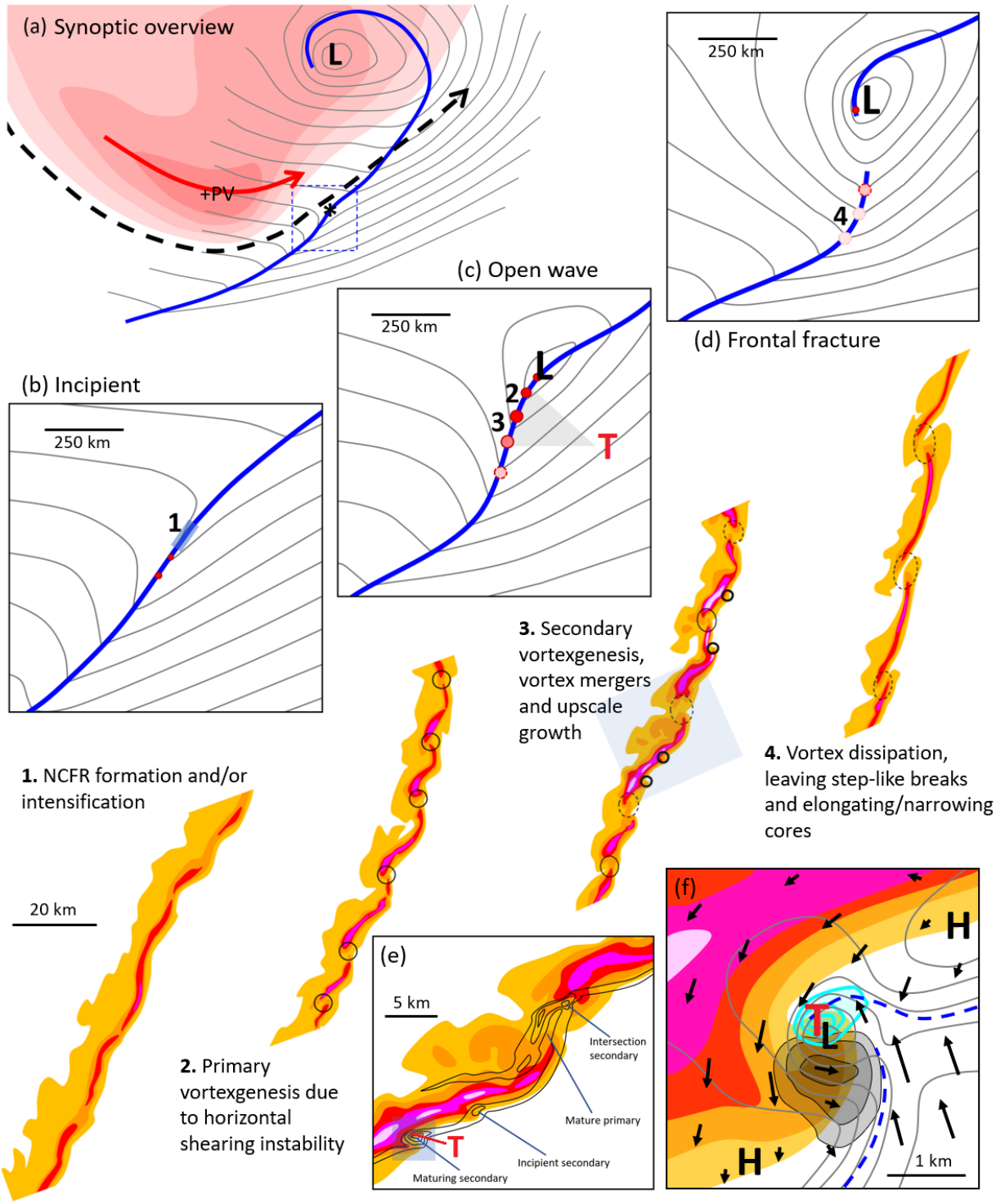

Figure 3.18 (previous page): Conceptual model depicting development in a tornadic frontal wave from the synoptic-scale (top, left) to the miso-scale (bottom, right). (a) Synoptic-scale overview at incipient stage of wave development. Red shading denotes region of large 300 hPa PV (darker shading for larger values); red arrow denotes the front-relative movement of PV maximum (+PV). Dashed arrow marks the upper-level jet axis. Grey contours are MSLP at ~4 hPa intervals. Bold blue line indicates the surface front. Dashed blue box is the domain in panel (b). 'L' and asterisk denote, respectively, the parent low pressure and frontal wave centres. (b)-(d) Evolution of the frontal wave on the meso-α-scale, showing three stages: (b) incipient; (c) open wave and (d) frontal fracture. MSLP (grey contours, plotted at ~2 hPa intervals). Bold blue line is surface front. 'L' indicates centre of frontal wave. Red/pink circles denote meso-γ- to miso-scale vortex-genesis (along-front spacing of individual vortices not to scale; deeper red shades indicate developing vortices and pink indicates decaying vortices or residual step-like NCFR breaks). In (c), the section of front prone to tornadoes is indicated by grey shading and letter 'T'. Main panel: Four stages of NCFR development, (1) – (4), as described by the annotations in the figure. Shading depicts near-surface rainfall rate (pink > magenta > red > orange > yellow). Blue shaded box at stage (3) is the domain shown in panel (e). Black circles indicate locations of vortices (dashed where vortices are weakening, and bold for secondary vortices). (e) Zoomed-in view of part of the NCFR during stage (3), showing the location of secondary vortices relative to the larger NCFR perturbations associated with a decaying primary vortex (see annotations for details). Blue shaded box is the domain in panel (f). 'T' indicates the most likely location for a tornado. Black contours denote near-surface vertical vorticity. (f) Zoomed-in view of one of the secondary vortices near peak intensity. Cyan contours depict the vertical vorticity stretching maximum, and grey contours the core of strong (> ~25 m s^{-1}) winds. Arrows are vortex-relative wind vectors near ground level. Yellow-red-pink shading denotes rainfall rate, and grey contours MSLP at ~0.5 hPa intervals. Dashed blue lines show the leading edge of the primary shear zone. 'T' indicates the most likely location for a tornado.

3.8. Conceptual framework

In this section we provide a synthesis of the results in the form of a conceptual model (Figure 3.18). Although this conceptual model is based largely on the findings of the current study, we are confident that it has some wider applicability. This is partly because the event was selected on the basis that it was a good example of the type of frontal wave found by CP20 to be associated with a majority of tornadic NCFRs, but also because many of the characteristic features were evident in similar (though less detailed) analyses of other frontal wave cases using 1.5 km model simulations, the results of which are not presented in the current paper.

Considering first the synoptic scale (Figure 3.18(a)), the initial condition is a trailing cold front, located underneath the forward flank of a broad upper-level trough and orientated at a shallow angle (<45°) to the upper-level flow, and in which the low-level flow pattern is at least weakly frontogenetic. The latter condition is necessary because the evolution described requires a well-defined surface cold front and

associated narrow zone of horizontal wind shear (i.e., a vertical vorticity strip) at the outset of frontal wave development; in other words, the narrow shear zone is 'pre-existing' in the context of the frontal wave development (or, at the least, minimal cross-frontal contraction is required to realise a narrow shear zone)[17].

An upper-level jet streak and associated positive PV anomaly move around the axis of the long-wave upper-level trough; as these features approach the trailing cold front, secondary cyclogenesis commences (Figure 3.18(b)-(d)). The associated frontal wave sets up mesoscale spatiotemporal variations in vertical vorticity and horizontal confluence that favour meso-γ- to miso-scale vortex-genesis along the shear zone near and just down-front of the wave centre as the wave amplifies (as signified by the pink and red dots along the front in Figure 3.18(b)-(d)), where the front begins to rotate cyclonically. In detail, the evolution in this region begins with increasing frontogenesis, cross-frontal confluence and vertical vorticity at the outset of wave development. With continued development, frontogenesis and cross-frontal confluence begin to decrease, whilst the vorticity continues to increase. Vortex-genesis by horizontal shearing instability occurs due to the contemporaneous increases in vertical vorticity and decreases in the cross-frontal confluence at this stage of wave development, which allows release of HSI in a situation where the release was formerly supressed by the large cross-frontal confluence (consistent with previous theoretical work on the stability of vortex strips in the presence of horizontal stretching deformation fields; e.g., Dritschel *et al*., 1991).

Frontolysis and cross-frontal diffluence eventually evolve in the vortex-prone region, resulting in frontal fracture and dissipation of the NCFR here (Figure 3.18(d)). Conversely, the NCFR tends to persist for longer along the trailing part of the front far down-front of the wave centre. This evolution means that vortex-genesis (and associated tornado risk) is generally restricted to the early developmental stages of the secondary

[17] Operational experience provides many examples of frontal waves (and indeed primary cyclones) in which a narrow frontal shear zone and associated NCFR fail to develop. In other cases, they may develop only along the trailing part of the cold front, well down-front of the wave centre, or at the developing bent-back front (e.g., Browning and Roberts, 1994; 1996), and therefore not in the otherwise tornado-favourable region. The lack of an NCFR immediately down-front of the wave centre in the early developmental stages therefore appears to constitute an important tornado-genesis failure mode. Analysis of the total frontogenesis within this part of the cyclone may be useful in this regard, as a measure of NCFR probability (as discussed in Appendix C).

cyclone's lifecycle[18]. In the analysed case, individual vortices moved down-front relative to the frontal wave; however, we suggest that the wave-relative movement of individual vortices may vary from case to case.

On the meso-β- to meso-ɣ-scales, vortex-genesis results in the transition of an initially fairly two-dimensional, unbroken NCFR (stage 1 in Figure 3.18) to one exhibiting marked core–gap structure near to, and just down-front of, the wave centre (stage 2). In practice, intensification of the NCFR may occur in tandem with the onset of secondary cyclogenesis (due to the increasing frontogenesis at this stage). The period with a relatively linear, unbroken NCFR may therefore be short-lived, and we suggest that it may not always be evident in radar data (especially where the wave moves rapidly and where the onset of wave development occurs at large range from the nearest radars). Notwithstanding this issue, the presence of amplifying perturbations within an NCFR, including newly developing NCFR gaps and associated broken-S reflectivity structures (McAvoy *et al*., 2000; Grumm and Glazewski, 2004; Lane and Moore, 2006), may be taken as an indication of the presence of developing vortices, with associated risk of tornadoes and localised non-tornadic wind damage.

On the other hand, residual inflections and gaps persist in the NCFR for a period of several hours following individual vortex merger and decay, resulting in a persistent core–gap structure in the trailing NCFR well down-front of the wave centre (stage 4). These residual inflections and gaps tend to evolve slowly and are associated with local minima in the cross-frontal temperature and wind gradients. For this reason, they are unlikely to be favoured locations for tornadoes or localised non-tornadic wind damage, and as such a distinction should be made between these residual perturbations and the rapidly evolving perturbations associated with developing vortices.

The largest values of near-surface vertical vorticity and vertical vorticity stretching, and we suggest the greatest potential for tornadoes, occur in association with miso-scale secondary vortices that develop and intensify extremely rapidly along the braid regions between existing primary vortices (stage 3; Figure 3.18(e)). These

[18] A few cases are known, however, in which vortex-genesis and tornadoes occurred after frontal fracture, near the tip of the developing bent-back front (at the location denoted by the northern red dot in Figure 3.18(d)). Such development appears atypical, and the few cases analysed to date all involved unusually small frontal waves with wavelengths on the order of tens of kilometres (e.g., Clark, 2012; Young and Clark, 2018).

secondary vortices therefore occur along the intense precipitation cores between the larger NCFR gaps or inflections associated with the primary vortices. Perturbations in the NCFR cores associated with the secondary vortices are small and may not be evident until after the time of tornado-genesis, but they include small hook or appendage echoes near the southern flank of vortices, and inflow notches on the northern flank (Figure 3.18(e)-(f)). Tornado-genesis appears most likely within a small zone of intense near-surface vertical vorticity stretching on the north, northwest, or west flanks of the secondary vortices (Figure 3.18(f)). This flanking stretching maximum is typically strongest during the developing and early-mature stages of secondary vortex evolution. Larger, though still highly localised, cores of strong winds (up to 25 – 35 m s^{-1}, with typical diameters of 1 – 3 km) develop along the down-front flanks of the same vortices during their mature to early dissipating stages of evolution, during which period the vortices often expand steadily whilst weakening. These wind maxima are a potential source of localised non-tornadic wind damage in NCFRs.

3.9. Conclusions

In this paper we have used observations and model output to investigate the structure and evolution of a tornadic NCFR within a frontal wave. The selected case is part of a significant class of tornadic NCFRs identified by CP20, suggesting that the results have some wider relevance. The results may be summarised as follows:

i. Secondary cyclogenesis (on the meso-α-scale) strongly modulates the risk of tornadoes along the NCFR
ii. As the wave develops, numerous primary (meso-ɣ-scale) and secondary (miso-scale) vortices develop along a narrow zone of strong vertical vorticity coincident with the surface front and NCFR, just down-front of the wave centre.
iii. Circumstantial evidence has been presented that HSI is the responsible mechanism for vortex-genesis on the meso-ɣ- and miso-scales. We suggest that the release of HSI is initially supressed by the substantial cross-frontal confluence (and therefore horizontal strain) at the trailing front (which is also instrumental in promoting development and/or maintenance of a narrow frontal shear zone in the first place); however, as wave development ensues,

simultaneous increases in vertical vorticity and decreases in cross-frontal confluence allow for release of HSI in a well-defined region down-front of the wave centre. Vortex-genesis ceases with transition to cross-frontal diffluence and associated frontal fracture.

iv. In the high-resolution simulations, the strongest near-surface vertical vorticity maxima and highest wind speeds were associated with miso-scale secondary vortices (typical diameters 1 – 3 km) that developed extremely rapidly at the leading edge of precipitation cores along the braid regions between larger perturbations associated with mature or decaying primary vortices.

v. These secondary vortices likely constitute preferred locations for tornado-genesis, as supported by analysis of radar data near to the two confirmed tornadoes in the real NCFR.

We suggest that the results presented herein, together with those of CP20, provide a provisional framework for the improved operational recognition of tornado-favourable environments in frontal waves, a situation that accounts for the majority of tornadic NCFRs (55%) and NCFR tornado outbreaks (73% of events producing ≥7 tornadoes) in the UK and Ireland. Whilst we are confident that the synoptic- to meso-scale evolution has some generality, the detailed sequence of meso-ɣ-scale primary vortex-genesis followed by miso-scale secondary vortex-genesis may be more case-dependent. Similar studies of other frontal wave NCFRs would therefore be desirable to assess the generality (or otherwise) of this behaviour. Remaining gaps in understanding include the possible variability in vortex-genesis mechanisms from case to case, the details of tornado-genesis within the miso-scale vortices, and the relevance of buoyant instability to the tornado-genesis process. Finally, although we have provided evidence that the miso-scale structures were captured credibly by the 300 m model, the miso-scale is only marginally resolved here (as discussed in Appendix F). For this reason, it would be desirable to nest to even higher resolution (grid spacing ≤100 m) in future simulations of tornadic NCFRs. Such simulations would permit a deeper exploration of the rich three-dimensional structure of the secondary vortices and of the frontal shear zone along which they form.

Acknowledgments

We are grateful to Paul Brown of the Tornado and Storm Research Organisation (TORRO) for providing access to the TORRO tornado database. We also thank David Dritschel and Kalli Furtado for useful discussions, and Helen Wells and Mike Molyneux for their comments on an earlier draft of this paper. We thank Johannes Dahl and an anonymous reviewer for their helpful and insightful comments and suggestions, which have led to improvements in the content and presentation of this paper.

References

Adlerman EJ, Droegemeier KK. 2005. The dependence of numerically simulated cyclic mesocyclogenesis upon environmental vertical wind shear. *Mon. Wea. Rev.* **133**: 3595–3623.

Apsley M, Mulder KJ, Schultz DM. 2016. Reexamining the United Kingdom's greatest tornado outbreak: forecasting the limited extent of tornadoes along a cold front. *Wea. Forecasting* **31**: 853–875.

Atkins NT, St. Laurent M. 2009. Bow echo mesovortices. Part II: Their genesis. *Mon. Wea. Rev.* **137**: 1514–1532.

Bishop CH, Thorpe AJ. 1994. Frontal wave stability during moist deformation frontogenesis. Part II: The suppression of nonlinear wave development. *J. Atmos. Sci*. **51**: 874–888.

Brown PR, Meaden GT. 2012. TORRO tornado division report: September-October 2011. *Int. J. Meteorol. (UK)* **37**: 27–30.

Browning KA, Golding BW. 1995. Mesoscale aspects of a dry intrusion within a vigorous cyclone. *Q. J. Roy. Meteor. Soc.* **121**: 463–493.

Browning KA, Reynolds R. 1994. Diagnostic study of a narrow cold-frontal rainband and severe winds associated with a stratospheric intrusion. *Q. J. Roy. Meteor. Soc.* **120**: 235–257.

Browning KA, Roberts NM. 1994. Structure of a frontal cyclone. *Q. J. Roy. Meteor. Soc*. **120**: 1535–1557.

Browning KA, Roberts NM. 1996. Variation of frontal and precipitation structure along a cold front. *Q. J. Roy. Meteor. Soc.* **122**: 1845–1872.

Buban MS, Ziegler CL. 2016. The formation of small-scale atmospheric vortices via horizontal shearing instability. *J. Atmos. Sci.* **73**: 2061–2084.

Carbone RE. 1982. A severe frontal rainband. Part I. Stormwide hydrodynamic structure. *J. Atmos. Sci.* **39**: 258–279.

Carbone RE. 1983. A severe frontal rainband. Part II. Tornado parent vortex circulation. *J. Atmos. Sci.* **40**: 2639–2654.

Clark MR. 2013. A provisional climatology of cool-season convective lines in the UK. *Atmos. Res*. **123**: 180–196.

Clark MR, Parker DJ. 2014. On the mesoscale structure of surface wind and pressure fields near tornadic and nontornadic cold fronts. *Mon. Wea. Rev.* **142**: 3560–3585.

Clark MR, Parker DJ. 2020. Synoptic-scale and mesoscale controls for tornadogenesis on cold fronts: A generalised measure of tornado risk and identification of synoptic types. *Q. J. Roy. Meteor. Soc*. **146**: 4195–4225.

Clark M, Smart D. 2016. Supercell and non-supercell tornadoes in the United Kingdom and Ireland. *Extreme Weather. Forty years of the Tornado and Storm Research Organisation (TORRO),* R. K. Doe, Ed., Wiley Blackwell, Chichester, UK, 31–59.

Dahl JML. 2020. Near-surface vortex formation in supercells from the perspective of vortex patch dynamics. *Mon. Wea. Rev*. **148**: 3533–3547.

Davies T, Cullen MJP, Malcolm AJ, Mawson MH, Staniforth A, White AA, Wood N. 2005. A new dynamical core for the Met Office's global and regional modelling of the atmosphere. *Q. J. Roy. Meteor. Soc*. **131**: 1759–1782.

Dee DP, *et al.* 2011. The ERA-Interim reanalysis: configuration and performance of the data assimilation system. *Q. J. Roy. Meteor. Soc.* **137**: 553–597.

Dritschel DG, Haynes PH, Juckes MN, Shepherd TG. 1991. The stability of a two-dimensional vorticity filament under uniform strain. *J. Fluid. Mech.* **230**: 647–665.

Fujita TT. 1981. Tornadoes and downbursts in the context of generalized planetary scales. *J. Atmos. Sci.* **38**: 1511–1534.

Grumm RH, Glazewski M. 2004. Thunderstorm types associated with the 'broken-S' radar signature. *Preprints, 22nd Conf. on Severe Local Storms,* 4–8 October 2004, Myannis, MA. American Meteorological Society: MA, USA. CD-ROM: P7.1.

Hanley KE, Barrett AI, Lean HW. 2016. Simulating the 20 May 2003 Moore, Oklahoma tornado with a 100-metre grid-length model. *Atmospheric Science Letters* **17**: 453 – 461.

Hanley KE, Plant RS, Stein THM, Hogan RJ, Nicol JC, Lean HW, Halliwell C, Clark PA. 2015. Mixing-length controls on high-resolution simulations of convective storms. *Q. J. Roy. Meteor. Soc*. **141**: 272–284.

Harrold TW. 1973. Mechanisms influencing the distribution of precipitation within baroclinic disturbances. *Q. J. Roy. Meteor. Soc*. **99**: 232–251.

Harvey B, Methven J, Eagle C, Lean H. 2017. Does the representation of flow structure and turbulence at a cold front converge on multiscale observations with model resolution? *Mon. Wea. Rev.* **145**: 4345–4363.

Hobbs PV, Biswas KR. 1979. The cellular structure of narrow cold-frontal rainbands. *Q. J. Roy. Meteor. Soc*. **105**: 723–727

Hobbs PV, Persson P. 1982. The mesoscale and microscale structure and organization of clouds and precipitation in midlatitude cyclones. Part V: The substructure of narrow cold-frontal rainbands. *J. Atmos. Sci*. **39**: 280–295.

Hoskins BJ, Bretherton FP. 1972. Atmospheric frontogenesis models: mathematical formulation and solution. *J. Atmos. Sci.* **29**: 11–37.

Houze RA, Hobbs PJ Jr., Biswas KR, Davis WM. 1976. Mesoscale rainbands in extratropical cyclones. *Mon. Wea. Rev.* **104**: 868–878.

James PK, Browning KA. 1979. Mesoscale structure of line convection at surface cold fronts. *Q. J. Roy. Meteor. Soc*. **105**: 371–382.

Jorgensen DP, Pu Z, Persson P, Tao, W-K. 2003. Variations associated with cores and gaps of a Pacific narrow cold frontal rainband. *Mon. Wea. Rev.* **131**: 2705–2729.

Kawashima M. 2007. Numerical study of precipitation core–gap structure along cold fronts. *J. Atmos. Sci.* **64**: 2355–2377.

Kirk P. 2007. UK tornado climatology, 1980–2004. *Int. J. Meteorol. (UK)* **32**: 158– 172.

Kundu PK, Cohen IM. 2004. *Fluid Mechanics* (3rd Ed.). Academic Press. pp. 758.

Lane JD, Moore PD. 2006. Observations of a non-supercell tornadic thunderstorm from terminal Doppler weather radar. *Preprints, 23rd Conf. Severe Local Storms,* St. Louis, MO. American Meteorological Society: MA, USA. CD-ROM: P4.5.

Lean HW, Clark PA. 2003. The effects of changing resolution on mesoscale modelling of line convection and slantwise circulations in FASTEX IOP16. *Q. J. Roy. Meteor. Soc*. **129**: 2255–2278.

Lee BD, Wilhelmson RB. 1997. The numerical simulation of non-supercell tornadogenesis. Part I: Initiation and evolution of pretornadic misocyclone circulations along a dry outflow boundary. *J. Atmos. Sci*. **54**: 32–60.

Matejka TJ, Houze RA Jr., Hobbs PV. 1980. Microphysics and dynamics of clouds associated with mesoscale rainbands in extratropical cyclones. *Q. J. Roy. Meteor. Soc*. **106**: 29–56.

McAvoy BP, Jones WA, Moore PD. 2000. Investigation of an unusual storm structure associated with weak to occasionally strong tornadoes over the eastern United States. *Preprints, 20th Conf. Severe Local Storms,* Orlando, FL. American Meteorological Society: MA, USA, 182–185.

Miles JW, Howard LN. 1964. Note on heterogeneous shear flow. *J. Fluid Mech.* **20**: 331–336.

Moore GWK. 1985. The organization of convection in narrow cold-frontal rainbands. *J. Atmos. Sci.* **42**: 1777–1791.

Mulder KJ, Schultz DM. 2015. Climatology, storm morphologies, and environments of tornadoes in the British Isles: 1980–2012. *Mon. Wea. Rev.* **143**: 2224–2240.

Mulqueen KC, Schultz DM. 2015. Non-classical extratropical cyclones on Met Office sea-level pressure charts: double cold and warm fronts. *Weather* **70**: 100–105.

Nicol JC, Hogan RJ, Stein THM, Hanley KE, Clark PA, Halliwell CE, Lean HW, Plant RS. 2015. Convective updraught evaluation in high-resolution NWP simulations using single-Doppler radar measurements. *Q. J. Roy. Meteor. Soc*. **141**: 3177–3189.

Okubo A. 1970. Horizontal dispersion of floatable particles in the vicinity of velocity singularities such as convergences. *Deep-sea Res*. **17**: 445–454.

Orlanski I. 1975. A rational subdivision of scales for atmospheric processes. *Bull. Amer. Meteor. Soc.* **56**: 527–530.

Parsons DB, Hobbs PV. 1983. The mesoscale and microscale structure and organization of clouds and precipitation in midlatitude cyclones. XI: Comparisons between observational and theoretical aspects of rainbands. *J. Atmos. Sci.* **40**: 2377–2397.

Reynolds DJ. 1999. A revised U.K. tornado climatology, 1960–1989. *J. Meteorol. (UK)* **24**: 290–321.

Scott RK, Dritschel DG. 2014. Numerical simulation of a self-similar cascade of filament instabilities in the surface quasigeostrophic system. *Physical Review Letters* **112**: 144505.

Schielicke L, Névir P, Ulbrich U. 2016. Kinematic vorticity number – a tool for estimating vortex sizes and circulations. *Tellus A* **68**: 29464.

Shapiro MA, Keyser D. 1990. Fronts, jet streams and the tropopause. *Extratropical Cyclones, The Erik Palmen Memorial Volume*, C. W. Newton and E. O. Holopainen, Eds., Amer. Meteor. Soc. 167–191.

Smart DJ, Browning KA. 2009. Morphology and evolution of cold-frontal misocyclones. *Q. J. Roy. Meteor. Soc*. **135**: 381–393.

Trapp RJ, Weisman ML. 2003. Low-level mesovortices within squall lines and bow echoes. Part II: Their genesis and implications. *Mon. Wea. Rev.* **131**: 2804–2823.

Wakimoto RM, Bosart BL. 2000. Airborne radar observations of a cold front during FASTEX. *Mon. Wea. Rev.* **128**: 2447–2470.

Walters D, *et al*. 2017. The Met Office Unified Model Global Atmosphere 6.0/6.1 and JULES global land 6.0/6.1 configurations. *Geoscientific Model Development* **10**: 1487–1520.

Weisman ML, Davis CA. 1998. Mechanisms for the generation of mesoscale vortices within quasi-linear convective systems. *J. Atmos. Sci.* **55**: 2603–2622.

Weiss J. 1991. The dynamics of enstrophy transfer in two-dimensional hydrodynamics. *Physica D* **48**: 273–294.

Wood N, Staniforth A, White A, Allen T, Diamantakis M, Gross M, Melvin T, Smith C, Vosper S, Zerroukat M, Thuburn J. 2014. An inherently mass-conserving semi-implicit semi-Lagrangian discretization of the deep-atmosphere global non-hydrostatic equations. *Q. J. Roy. Meteor. Soc*. **140**: 1505–1520.

Young MV, Clark MR. 2018. Development of localized damaging wind gusts associated with a frontal wave and mesoscale vortex across south Wales on 18 May 2015. *Meteor. Appl.* **25**: 139–150.

Chapter 4: A tornadic cold front in amplifying north-westerly flow

M. R. Clark[1,2,3]

[1]Met Office, Exeter, UK

[2]University of Leeds, Leeds, UK

[3]Tornado and Storm Research Organisation (TORRO), Oxford, UK

This chapter has been prepared as a submission to *Quarterly Journal of the Royal Meteorological Society*

Abstract

Processes leading to the localised intensification of a cold front and associated development of a tornadic narrow cold-frontal rainband (NCFR) across the UK on 20 November 2013 are explored using reanalysis data, high-resolution model simulations and observations. Physical links are found to exist across a wide range of spatiotemporal scales, such that the evolving large-scale flow field ultimately orchestrates the timing and location of tornado-genesis. The synoptic-scale flow pattern exhibited marked amplification, characterised by upstream ridge building and downstream trough extension. A prominent jet streak and associated positive PV anomaly and tropopause fold propagated rapidly south-eastward on the rear flank of the extending upper-level trough, the leading edge of these features eventually overspreading the surface cold front over the UK. Increasing 850 hPa frontogenesis underneath the left exit of the jet streak and an associated intensifying positive potential vorticity (PV) anomaly resulted in a strengthening front-transverse circulation, within which a filament of dry, high-PV air was extruded from the overlying tropopause fold. This dry filament eventually penetrated to low levels immediately behind the front, where it undercut the upper, rearward parts of the wide cold-frontal rainband. Diabatic cooling associated with sublimation of solid hydrometeors falling into the dry filament led to the development of local downdraft and near-surface divergence maxima and a prominent cold pool immediately behind the surface cold front over central England. Associated increases in horizontal convergence, updraft speed, and horizontal temperature gradients along the frontal boundary immediately ahead of the cold pool resulted in development of a locally well-defined surface front and NCFR, where the surface front was formerly (and elsewhere continued to be) relatively weak. Tornadoes occurred in association with miso-scale vortices that developed rapidly along an intensifying vertical vortex sheet at the NCFR.

Keywords: tornado, narrow cold-frontal rainband, cold front, dry intrusion, cold pool

4.1. Introduction

Current estimates suggest that 40 – 50% of the UK's tornadoes occur in association with precipitation systems exhibiting linear morphologies in radar rainfall imagery (e.g., Mulder and Schultz, 2015). The majority of these, and approximately one-third of all the UK's tornadoes, occur along well-defined cold fronts and (less commonly) occlusions (e.g., Clark and Smart, 2016). These narrow (cold)-frontal rainbands (NCFRs; Houze *et al*., 1976) are characterised by intense updrafts forced primarily by strong horizontal convergence within the boundary layer at the surface front (e.g., Browning and Harrold, 1970; Matejka *et al*., 1980; Hobbs and Persson, 1982). Although strong, NCFRs are shallow in comparison to other types of deep, moist convection, with updraft depths typically ranging from 1 to 3 km in the UK (Browning and Harrold, 1970; James and Browning, 1979). Radar and modelling studies show that tornadoes are often associated with miso-scale vortices developing along a narrow zone of intense horizontal wind shear (i.e., relative vertical vorticity) at the surface front (e.g., Hobbs and Persson, 1982; Carbone 1982; 1983; Smart and Browning, 2009; Clark and Parker, 2014; Apsley *et al*., 2016).

Clark and Parker (2020) (hereafter CP20) demonstrated that two synoptic setups are commonly associated with tornadic NCFRs in the UK. The first, which involves secondary cyclogenesis along a trailing front, accounted for 55% of tornadic NCFRs, and 72% of NCFRs producing ≥ 7 tornadoes, over the study period. Physical mechanisms associated with vortex-genesis were investigated for one case, using high-resolution model simulations, by Clark *et al*. (2021). The secondary cyclogenesis and associated frontal wave controlled the location and timing of vortex-genesis and tornado-genesis along the vertical vorticity sheet at the NCFR, by modulation of the relative magnitudes of vertical vorticity and horizontal strain. Contemporaneous increases in shear vorticity and decreases in cross-frontal confluence (one component of the horizontal strain field) near the wave centre resulted in the release of horizontal shearing instability, where the instability was formerly supressed by the large strain.

The purpose of the present paper is to provide a similarly detailed study of a case belonging to the second type of synoptic setup found by CP20 to be associated with tornadic NCFRs – namely, the north-westerly flow pattern. This setup, which accounts for ~27% of CP20's tornadic NCFRs, involves the approach towards the front

of a potent mid- to upper-level jet streak and associated potential vorticity (PV) maximum, in an environment characterised by large-scale amplification (ridge-building upstream, and trough extension and eventual disruption downstream)[19]. These events bear similarities to the 'type 2' tornadic NCFRs of Buckingham and Schultz (2020), in terms of the broadly zonal orientation of the cold front over the UK, diffluent flow aloft, and the typical position and track of the parent cyclone to the northeast of the UK[20].

CP20 showed that, in contrast to frontal wave cases, the jet streak in north-westerly cases approaches the surface front at a large angle (the major axis of the jet streak being orientated at ~90° to the surface front). Tornadoes generally occurred underneath the cyclonic-shear flank of the jet streak, around the time that the leading edge of the jet streak and associated PV maximum began to overrun the front. In this paper, the structure and evolution of the front in the vicinity of an overrunning jet streak and PV maximum are studied in more detail, to elucidate the physical mechanisms involved in generating an environment locally conducive to tornado-genesis. The cold front under study occurred on 20 November 2013. The associated NCFR produced at least five tornadoes as it tracked southeast across England.

The remainder of the paper is organised as follows. A description of the model is presented in Section 4.2, followed by an overview of the synoptic and mesoscale settings of the event in Section 4.3. A more detailed analysis of the mesoscale situation, the evolution of the front, and the along-front variability in cross-sectional structure of the front near the overrunning jet streak, is presented in Section 4.4, using output from the 1.5 km model and by comparison with observations. In Section 4.5, the fine-scale structure of the NCFR near to the reported tornadoes is explored, focussing on the miso-scale to meso-ɣ-scale vortices that were observed to develop along the frontal shear zone in this region, using both 1.5 km model data and radar observations. Tracks of radar-observed vortices are compared with the locations of reported tornadoes. Results are discussed in Section 4.6 and then summarized, in the form of a conceptual model, in Section 4.7. Conclusions follow in Section 4.8.

---

[19] The nomenclature reflects that most cases of this type occurred in north-westerly large-scale flow; however, a few cases were also noted in westerly flow.

[20] Indeed, Buckingham and Schultz (2020) present analysis of the synoptic setting and NCFR morphology for the current case (20 November 2013), as an example of their 'type 2' tornadic NCFR, and their classification system is based partly upon it.

4.2. Model description

Data from the operational, convection-permitting configuration of the Met Office's Unified Model (Davies *et al*., 2005), the UKV, are presented in this study. The following details relate to the model setup at the time of the event. The model uses the mixed-phase cloud microphysics scheme of Wilson and Ballard (1999), the radiation scheme of Edwards and Slingo (1996), the surface-layer scheme of Best *et al*. (2011), the non-local boundary layer scheme of Lock *et al*. (2000), and a Smagorinsky-type turbulence closure scheme. The model grid spacing is variable across the domain, from 1.5 km in the interior, which is centred on the UK and spans approximately 13° longitude and 11° latitude, to 4 km in the model's outer domain (Tang *et al*., 2012). The grid spacing varies smoothly between the inner and outer domains. The model uses a semi-implicit, semi-Lagrangian numerical scheme with a 50-second timestep and runs on a rotated latitude-longitude horizontal grid with Arakawa C staggering. In the vertical the grid is stretched and, close to the surface, terrain following, transitioning to horizontal at the model top (z = 40 km), with Charney-Phillips staggering and 70 vertical levels. The vertical grid length is smallest close to the surface and the vertical stretching is quadratic over much of the vertical extent of the domain. The terrain is defined using a smoothed version of the 100 m resolution Digital Terrain Elevation Data. The UKV takes its lateral boundary conditions from the global version of the Met Office's Unified Model, and initial conditions come from the model analysis, which is generated from the previous model cycle plus the latest available observations using three-dimensional variational (3DVAR) data assimilation. Output from the 0300 and 0900 UTC 20 November 2013 runs of the operational model are analysed in this study, over the period 0400 UTC to 1400 UTC 20 November 2013.

4.3. Overview of the case

4.3.1 Reported tornadoes

At least five tornadoes occurred along the cold front between 0900 and 1100 UTC 20 November 2013, as it moved southeast over central and southern England. The tornado reports were distributed mainly along a single, northwest–southeast-orientated line. This suggests that conditions only supported tornado-genesis along a very limited subsection

of the front, but that tornado-favourable conditions were maintained here for a period of at least two hours. The tornadoes were all short-lived and relatively weak (Table 4.1), and in these respects they are typical of NCFR tornadoes in the UK. Damage included the removal of numerous roof tiles, damaged fencing and outbuildings and the uprooting or snapping of trees (Brown and Meaden, 2014).

Table 4.1: Details of the five confirmed tornadoes on 20 November 2013. Intensities are as per the International Tornado Intensity (T) Scale.

Location	*Radar-estimated time*	*Track length*	*Maximum intensity*
Tutbury, Staffordshire	0901 UTC	unknown	T1
Ashby-de-la-Zouch, Leicestershire	0919 UTC	unknown	T0
Irthlingborough, Northamptonshire	1023 UTC	unknown	unknown
Milton Keynes, Buckinghamshire	1043 UTC	125 m	T2
Barton-le-Clay, Bedfordshire	1102 UTC	200 m	T1

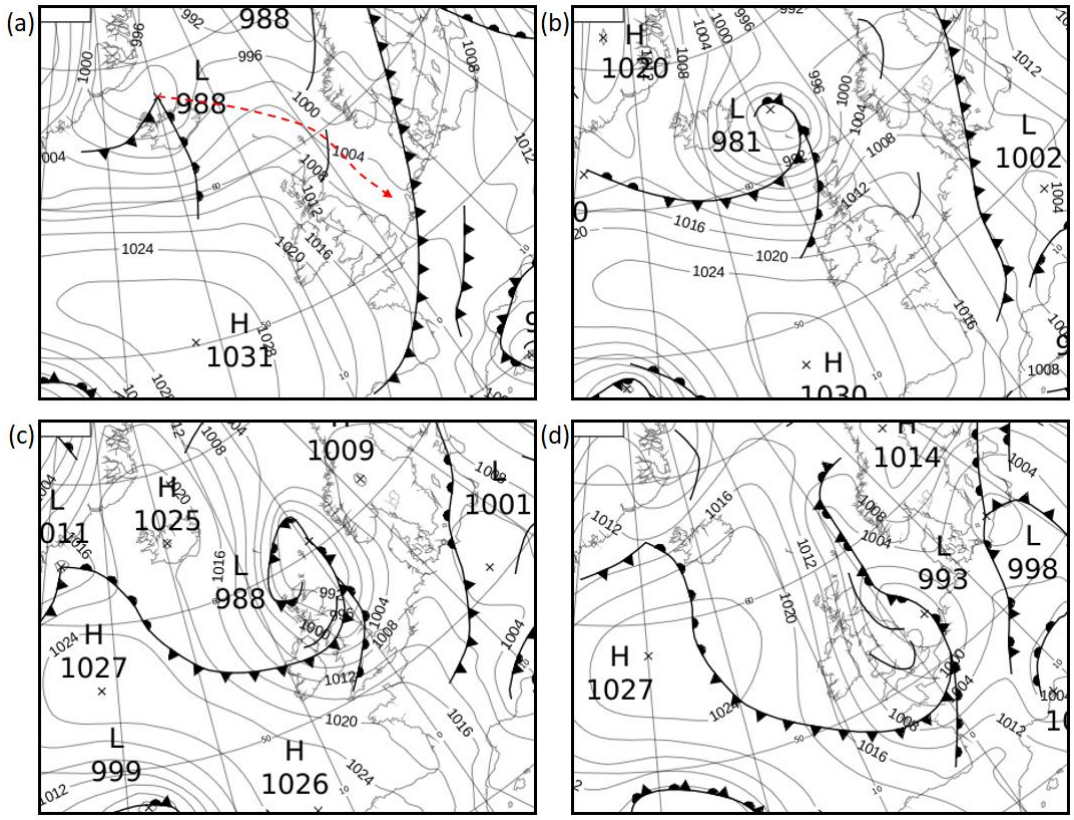

Figure 4.1: Sequence of Met Office surface analysis charts during 19 – 20 November 2013. (a) 0600 UTC 19th; (b) 1800 UTC 19th; (c) 0600 UTC 20th; (d) 1800 UTC 20th November. Fronts are shown using standard notation and isobars are drawn at 4 hPa intervals. Track of the parent low pressure centre over the period is shown by the dashed red line in panel (a).

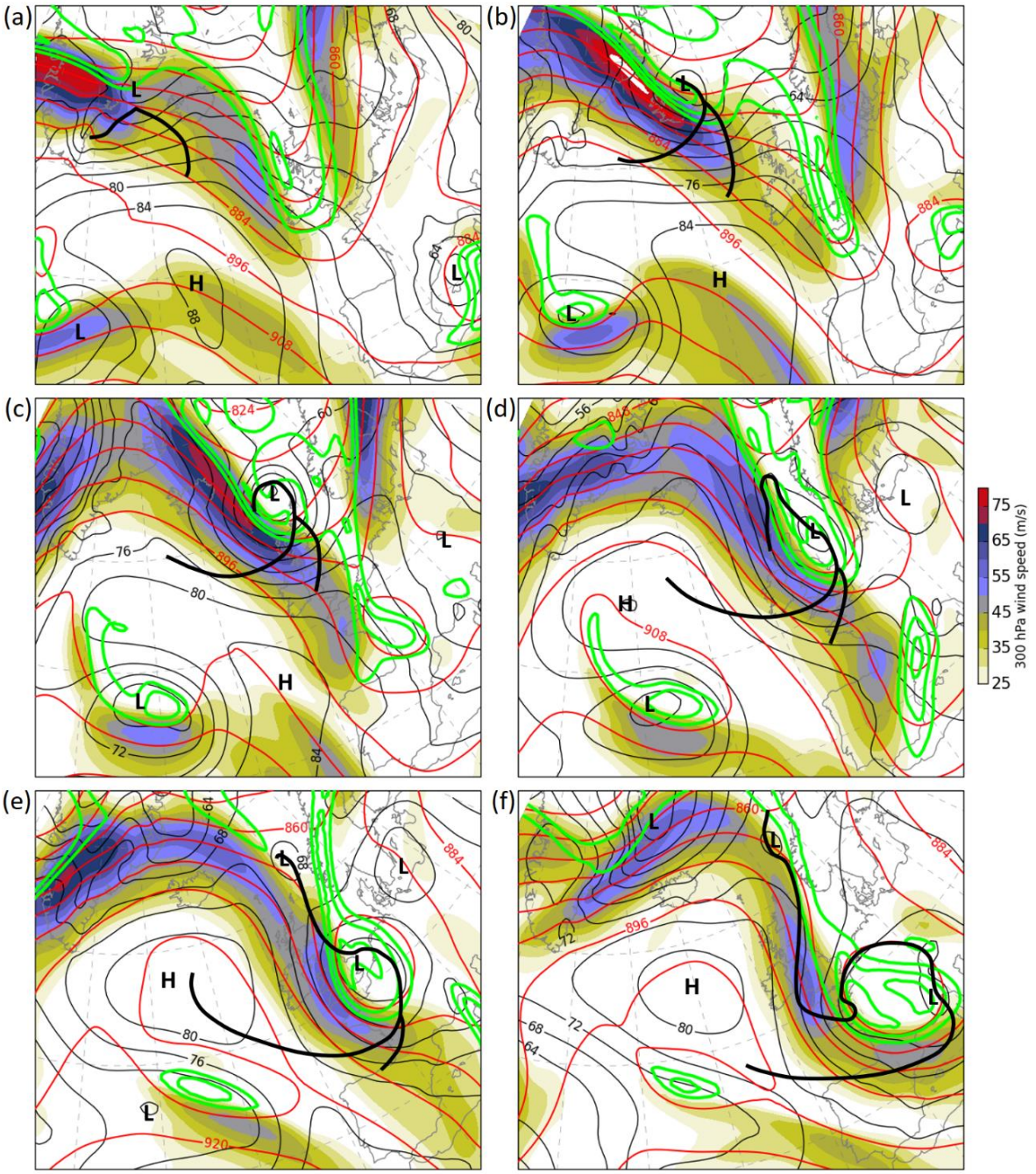

Figure 4.2: Sequence of ERAi reanalysis fields at 12 hour intervals showing 300 hPa wind speed (colour shading), 300 hPa geopotential height (red contours at intervals of 12 DAM), 300 hPa PV (lime green contours at intervals of 2 PVU, starting at 4 PVU), 925 hPa geopotential height (black contours at intervals of 4 DAM) and analysed surface fronts (bold, black lines; only those associated with the parent cyclone belonging to the cold front under study are shown): (a) 0000 UTC 19 November; (b) 1200 UTC 19 November; (c) 0000 UTC 20 November; (d) 1200 UTC 20 November; (e) 0000 UTC 21 November; (f) 1200 UTC 21 November 2013.

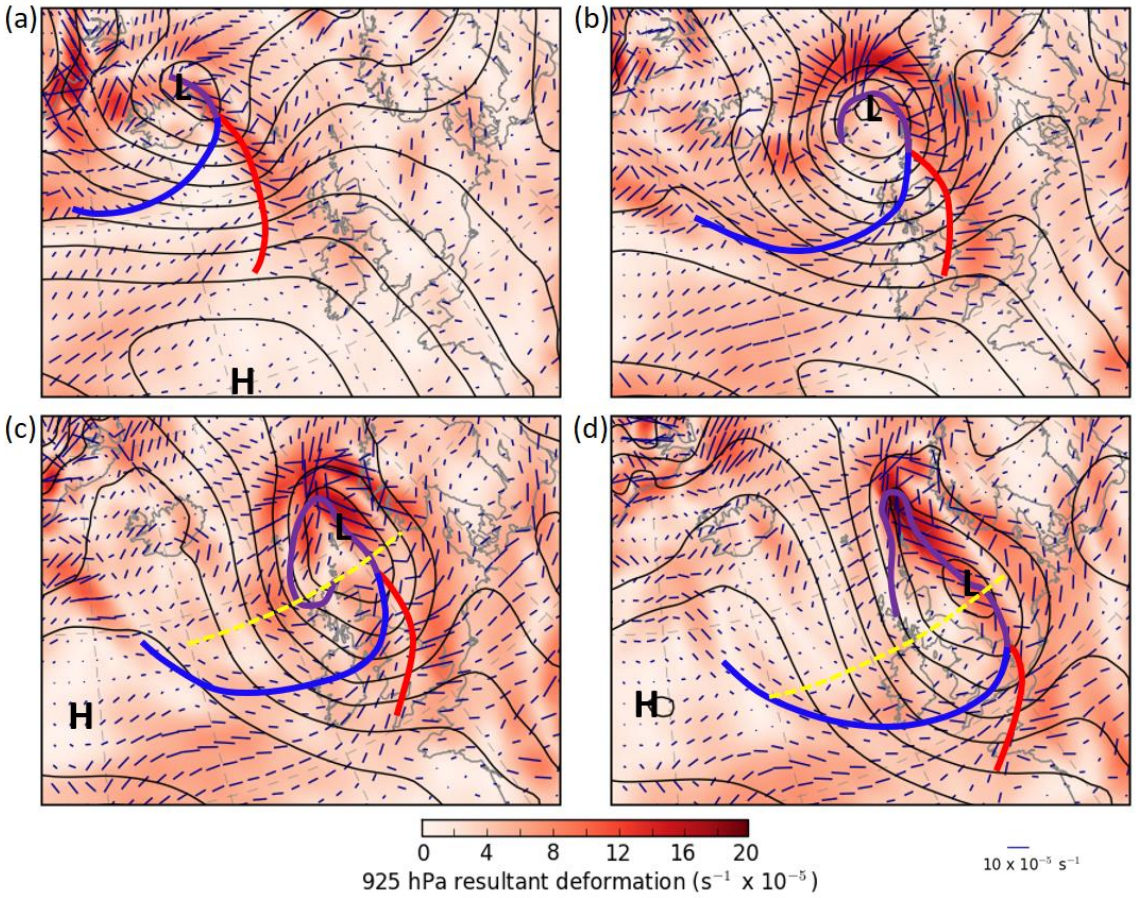

Figure 4.3: Resultant deformation of the 925 hPa horizontal wind field (colour shading) and axis of dilatation at the same level (dark blue dashes, in which the dash is orientated parallel to the axis of dilatation and the dash length is proportional to the magnitude of resultant deformation); (a) 1200 UTC 19 November; (b) 0000 UTC 20 November; (c) 0600 UTC 20 November and (d) 1200 UTC 20 November 2013. Bold, coloured lines indicate location of fronts as shown in Met Office surface analysis charts (purple, blue and red for occluded, cold and warm fronts, respectively). 'L' denotes the centre of the parent low pressure system. Dashed yellow lines in panels (c) and (d) mark the position of the vertical sections shown in Figures 4.5(a) and (b), respectively.

4.3.2 Synoptic-scale context

The period of interest commences late on 18 November 2013, with the onset of rapid cyclogenesis to the east of Greenland. The resulting surface depression moved eastwards to be centred near Iceland by 0600 UTC 19 November (Figure 4.1(a)). The cyclone subsequently moved south-eastwards, passing to the north of the UK, and reaching a minimum central pressure of 981 hPa at 1800 UTC 19 November, before filling slowly as it moved south-south-eastwards through the North Sea. The depression's occluding frontal system tracked southeast across the UK on 20

November. Although the surface depression was filling slowly by this time, pressure falls in the system-relative sense began to be focussed on the southwest flank of the parent low, close to the triple point of the frontal system. This process is evident in the development of a large region of slack pressure gradients to the southwest of the original low centre, and just to the northeast of the UK, by 0600 UTC 20 November (Figure 4.1(c)), with a corresponding increase in pressure gradients further west and southwest over the UK itself.

Between 0600 and 1800 UTC 20 November, the frontal system accelerated southwards over the UK in the strengthening, veering flow field at the southwest flank of the parent depression. Although the pressure falls near the triple point failed to result in the development of a secondary cyclone centre (at least at the resolution of the surface analysis charts), their impact is apparent in the direction and speed of propagation of the parent low, whose track curved to the right across the North Sea (looking down-track) with increasingly rapid movement after ~0600 UTC 20 November 2020 (dotted line in Figure 4.1(a)). By 1800 UTC 20 November, the occluding frontal system had moved south into mainland Europe, with pressure gradients around the now-mature surface cyclone decreasing steadily. The filling cyclone eventually became a slow-moving cut-off feature over southern Europe.

Geopotential height, wind speed and PV fields at 300 hPa (Figure 4.2) show that the initial phase of cyclogenesis on 18 – 19 November occurred underneath the left exit of an intense jet streak and associated positive PV anomaly embedded in the upper-level westerly flow, possibly augmented by lee troughing to the east of the Greenland plateau (Figures 4.2(a)-(b)). The large-scale flow pattern was dominated at this time by a prominent and relatively slow-moving long-wave, upper-level trough centred close to the UK, to the east of a ridge centred over the North Atlantic. Over the following 24 hours the pattern amplified, with substantial ridge-building over the North Atlantic and equatorward extension and narrowing of the trough near the UK. Trough disruption (i.e., the process by which a cut-off cyclone forms from a meridionally extending trough; e.g., Carroll, 1997) eventually occurred near the base of the trough over France (best seen in the PV field e.g., Figures 4.2(c)-(d)). The jet streak and associated PV maximum propagated rapidly south-eastwards towards the UK on the western flank of

the disrupting long-wave trough, the jet streak elongating slowly with time in the amplifying flow.

By 0000 UTC 20 November, the left exit of the jet streak had extended ahead of the parent low centre to be located close to the triple point of its frontal system (Figure 4.2(d)). The aforementioned surface pressure falls, near the triple point, were therefore likely associated with strong dynamic forcing for ascent underneath the left exit of the jet streak (the slow filling of the parent depression from this time likely relates to its increasing distance from the same forcing mechanism)[21]. Despite a slow weakening of the jet streak over the period (core wind speeds decreasing from ~80 m s^{-1} to ~60 m s^{-1} between 1200 UTC 19 November and 1200 UTC 20 November; *cf*. Figures 4.2(b) and (d)), the associated PV maximum intensified between 0000 and 0600 UTC 20 November as it tracked south-eastwards across the UK (*cf*. Figures 4.2(c) and (d)). This intensification marked the onset of a second disruption event in which the PV maximum eventually evolved into a well-marked cut-off over Europe, as the jet streak neared the base of the elongating long-wave upper-level trough (Figure 4.2(e)-(f)). The disruption culminated in a slow-moving PV maximum over Europe by 1200 UTC 21 November, with which the filling surface cyclone became collocated.

4.3.3 Evolution of 850 hPa deformation field near the cold front

In the early stages of the parent cyclone's development on 19 November (Figure 4.3(a)), the resultant deformation is strong along the cyclone's warm and back-bent fronts, with the axis of dilatation generally orientated at a shallow angle to these fronts, suggesting strong frontogenesis. In contrast, the deformation is weak along most of the cold front, except near the trailing end of the front where it links with the warm front of an upstream cyclone. This pattern of deformation, relative to the surface frontal positions, remains largely unchanged until ~0000 UTC 20 November (Figure 4.3(b)), consistent with the cold front being a relatively weak feature as it moved into the north of the UK just after midnight on 20 November. Thereafter, a marked increase in resultant deformation occurs along the part of the cold front crossing the UK. This culminates in the development of a well-defined deformation maximum, with the axis of dilatation

[21] This idea assumes the 'four quadrants' model of upper-tropospheric divergence and mid-tropospheric ascent associated with a straight jet streak (e.g., Bjerknes, 1951; Uccellini and Kocin, 1987), wherein ascent is expected underneath the left exit region. Although initially straight, the jet streak began to exhibit some curvature around the time that it moved across the UK (*cf*. Figures 4.2(c) and (d)).

orientated at a small angle to the cold front, over central parts of the UK by 0600 UTC 20 November (Figure 4.3(c)). As is subsequently shown, the associated increase in near-surface frontogenesis leads to a strengthening and deepening of the cold front's ageostrophic transverse circulation, which in turn becomes important in dictating the location and timing of tornado-genesis.

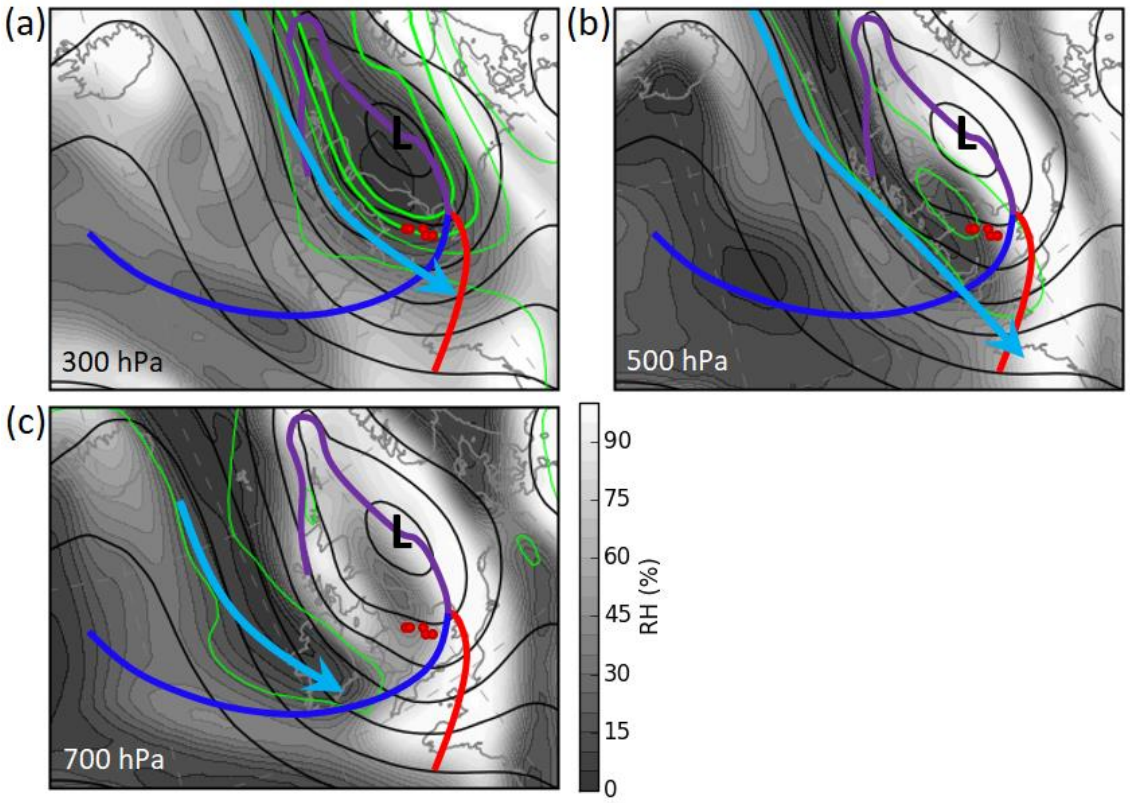

Figure 4.4: RH (shading), PV (lime green contours at intervals of 2 PVU, starting at 1 PVU; contours bolder for ≥5 PVU)) and position of the jet axis (blue arrow) on three pressure surfaces, from ERAi reanalysis, showing the vertical structure of the jet and associated PV maximum and tropopause fold at 1200 UTC 20 November 2013. (a) 300 hPa; (b) 500 hPa; (c) 700 hPa. Bold, coloured lines indicate location of fronts as shown in Met Office surface analysis charts valid at the same time (purple, blue and red for occluded, cold and warm fronts, respectively). Red dots are locations of confirmed tornadoes.

4.3.4 Mesoscale substructure over the UK

Further insight into the three-dimensional structure of the jet streak and PV maximum over the UK is provided by horizontal sections on various pressure levels, constructed using ERAi data (Figure 4.4). At 300 hPa, a tropopause depression, marked by the large region of very dry, high-PV air, is collocated with the axis of the extending upper-level trough just to the east of the UK (Figure 4.4(a)). The 300 hPa jet streak is situated at the

western flank of this tropopause depression (i.e., the associated PV maximum is located at the cyclonic-shear flank of the jet streak). At 500 hPa (Figure 4.4(b)), a narrower, north–south orientated tongue of dry, high-PV air extends over much of the UK, centred slightly to the west of the centre of the PV maximum at 300 hPa. This is part of a tropopause fold (Reed and Sanders, 1953; Reed, 1955) extending from the broader tropopause depression and penetrating into the middle to lower troposphere along a narrow, sloping zone. The tongue of dry, high-PV air associated with the tropopause fold is also evident at 700 hPa (Figure 4.4(c)), again located slightly to the west of the corresponding features at 500 hPa. At mid- to upper-levels, the jet axis (shown by the blue arrows in Figure 4.4) occupies the immediate western flank of the dry, high-PV air, and flow within the jet is approximately normal to the surface cold front.

The tropopause fold is clearly seen in east–west cross-sections over the UK at 0600 and 1200 UTC (Figure 4.5; the position of these sections is shown by the dashed yellow lines in Figures 4.3(c) and (d), respectively). Near the western edge of the fold, PV > 1 PVU and relative humidity (RH) < 25% extend as low as 1.5 – 2.0 km above ground level (AGL). The fold is collocated with a sloping baroclinic zone, consistent with observations and conceptual models of upper-level jet–front systems (e.g., Berggren, 1952; Reed, 1955; Reed and Danielsen, 1959; Danielsen, 1968; Keyser and Shapiro, 1986). Additional sections reveal that the tropopause fold had consistent cross-sectional structure along much of the length of the jet streak (not shown) and evolved only slowly (e.g., *cf.* Figures 4.5(a) and (b)). East–west cross-sections immediately to the south (i.e., on the warm-air side) of the front confirm that the leading edge of the jet and tropopause fold had extended ahead of the position of the surface front by 1200 UTC 20 November. As will be demonstrated in Section 4.4, the tropopause fold was instrumental in providing a source of dry, high-PV air into the mid-levels, from where some of this air could then be extruded, in the form of a much narrower dry filament, to even lower levels within the intensifying ageostrophic transverse circulation of the surface front.

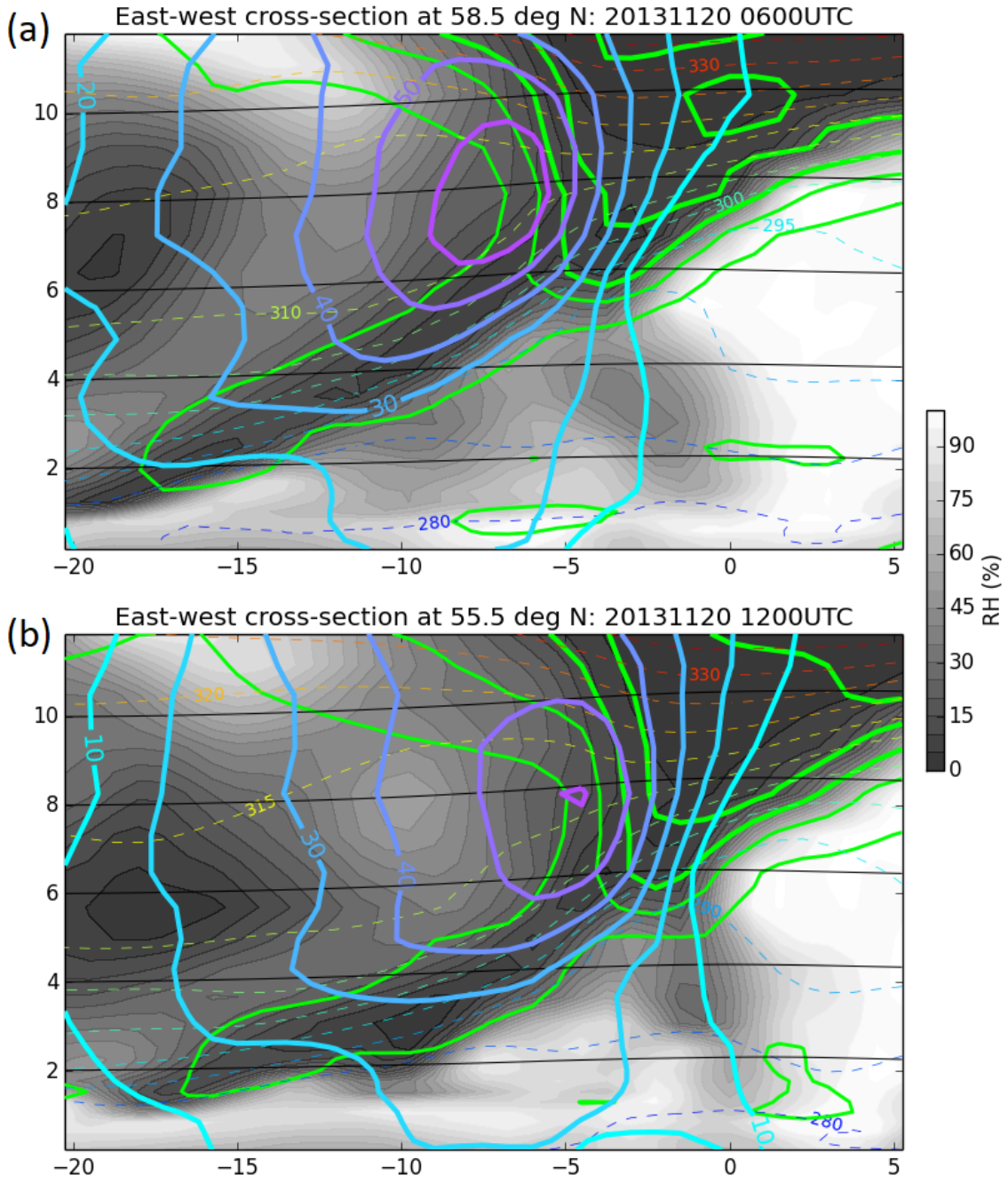

Figure 4.5: East-west vertical sections through the upper-level jet and associated tropopause fold at a position approximately 3° north of the southernmost part of the cold front at (a) 0600 UTC and (b) 1200 UTC 20 November 2013 (positions of the sections are shown by dashed yellow lines in Figures 4.3(c) and (d), respectively). RH (shading), PV (lime green contours at intervals of 2 PVU, starting at 1 PVU; contours bolder for ≥5 PVU) and $-v$ wind component (positive for flow out of the page i.e., from the north; blue–purple coloured contours, at intervals of 10 m s^{-1}), θ (dashed contours at intervals of 5 K) and height contours (thin black lines at intervals of 2 km). Note that the longitude of reported tornadoes over the UK was between -0.43° and -1.70°.

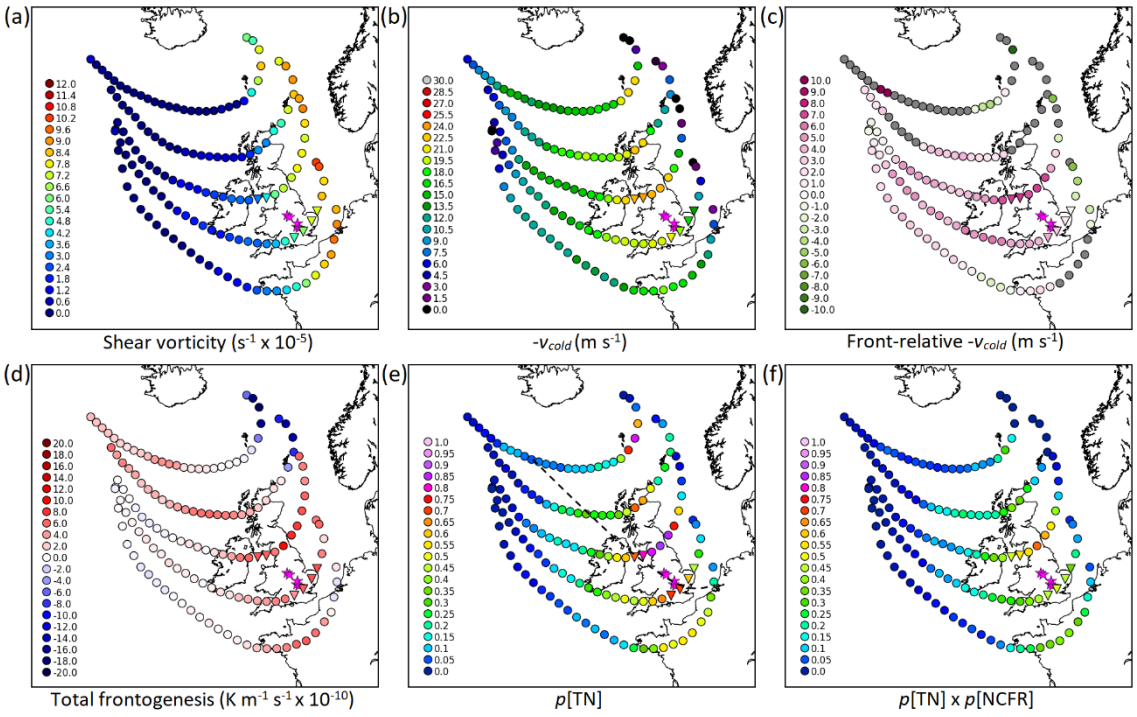

Figure 4.6: Bulk parameter values, calculated from ERAi data, at on-front analysis points (as defined by CP20) at 6-hour intervals between 1800 UTC 19 November and 1800 UTC 20 November 2013; (a) shear vorticity; (b) $-v'_{cold}$; (c) Front-relative $-v'_{cold}$; (d) Total frontogenesis (K m^{-1} s^{-1} x 10^{-10}); (e) p[TN]; (f) p[TN] x p[NCFR]. On-front analysis points are shown by the colour-filled symbols (dots for non-tornadic points and inverted triangles for tornadic or near-tornadic points, following the methodology of CP20), with the colour shading indicating the magnitude of the corresponding parameter as per the colour scale within each panel. In the case of front-relative $-v'_{cold}$, grey shading indicates on-front points at which the FNFM, and therefore front-relative flow fields, could not be calculated (see CP20 for details). Magenta star symbols denote the locations of confirmed tornadoes, as given in the Tornado and Storm Research Organisation (TORRO) tornado database. In panel (e), the dashed black line denotes the track of a Lagrangian analysis point passing through the tornadic part of the front.

4.3.5 Evolution of other relevant environmental parameters at 850 hPa

In an analysis of environmental parameters for a large set of tornadic and non-tornadic NCFRs, CP20 showed that a bulk measure of the cross-frontal vertical vorticity at 850 hPa (hereafter shear vorticity) and the front-normal component of the 850 hPa flow on the cold side of the front (hereafter $-v'_{cold}$; positive where the flow is towards the front) yielded the best discrimination between tornadic and non-tornadic NCFRs; tornadoes were more likely with larger values of each parameter. A measure of the probability of tornadoes, p[TN], based on the combined values of these parameters, was defined using linear discriminant analysis. Since CP20's event set only included fronts

exhibiting an NCFR, *p*[TN] is conditional on the presence of an NCFR. 850 hPa horizontal frontogenesis was found to be a useful proxy for the likelihood of an NCFR, as described by the parameter *p*[NCFR] (see Appendix C for details), and so CP20 recommended analysis of these parameters in conjunction with *p*[TN].

Figure 4.6 shows the distribution and evolution of relevant environmental parameters, calculated from 850 hPa ERAi fields using the methodology of CP20, at analysis points situated along the cold front and occlusion on 19 – 20 November 2013. Whilst the shear vorticity was largest close to the parent low pressure centre throughout the analysis period (Figure 4.6(a)), modest increases also occurred along the section of cold front crossing the UK. The parameter $-v'_{cold}$ was maximised where the cold front was orientated approximately normal to the large-scale 850 hPa flow, over central parts of the UK (Figure 4.6(b)), which also corresponds approximately to the position of the mid- to upper-level jet axis (*cf*. Figures 4.4(a)-(b)). Slight increases in $-v'_{cold}$ occurred up to ~0600 UTC 20 November, when the front was situated over northern England, with slight decreases thereafter. Increases in $-v'_{cold}$ and front-relative $-v'_{cold}$ (Figure 4.6(c)) along this part of the front are attributed to the aforementioned pressure falls near the triple point of the frontal system, which resulted in a strengthening of the low-level geostrophic wind field over the UK. Increases may also relate to the larger-scale veering associated with the amplifying synoptic-scale flow pattern, since veering tends to increase the angle between the front and the flow, and therefore the front-normal flow component, where initially < 90°.

The conditional probability of tornadoes, *p*[TN], increases rapidly between 0000 and 0600 UTC along the section of front crossing northern and central parts of the UK (Figure 4.6(e)), reaching a maximum over northern England at 0600 UTC. Values subsequently decrease, though a well-defined maximum is still evident at 1200 UTC over southeast England. Allowing for the movement of the front between analysis times, the tornadoes occurred near the position (along the front) of the *p*[TN] maximum, but just after the time of absolute maximum *p*[TN]. In a reference frame following the front and passing through the tornado reports (the trajectory of which is shown by the dashed line in Figure 4.6(e), constructed using the methodology of CP20), the tornadoes occurred just after the time at which *p*[TN] reached a maximum along the trajectory. Therefore, whilst *p*[TN] correctly highlighted the part of the front crossing England as

having an increased risk of tornadoes, the location of tornadoes (central England) did not correspond exactly to the location of maximum *p*[TN] (northeast England).

Frontogenesis was at least weakly positive along most of the frontal system throughout the analysis period, with frontolysis occurring only near the parent low pressure centre at earlier analysis times and (weakly so) near the trailing end of the front over the Atlantic Ocean at later analysis times (Figure 4.6(d)). However, frontogenesis was weak along the full length of the cold front early in the period ($< 5 \times 10^{-10}$ K m^{-1} s^{-1}), consistent with the relatively small total deformation near the front at these times (*cf.* Figures 4.3(a)-(b)). Substantial increases in frontogenesis occurred along the part of the front crossing the UK between 0000 and 0600 UTC 20 November. These increases are consistent with the increasing 850 hPa total deformation, in combination with an axis of dilatation orientated at a small angle to the front, over central parts of the UK by 0600 UTC (Figure 4.3(c)), near the approaching left-exit region of the upper-level jet and the PV maximum. The largest frontogenesis ($\sim 7 - 10 \times 10^{-10}$ K m^{-1} s^{-1}) occurred at 0600 and 1200 UTC along the section of front crossing northern and eastern England (Figure 4.6(d)), with values reducing rather rapidly along this part of the front after passage across the UK. The product *p*[TN] x *p*[NCFR] is maximised over northern England, but remains relatively large as the front tracks through central and southern England (Figure 4.6(f)).

4.4. Cross-sectional frontal structure and its along-front variability in the 1.5 km model

4.4.1 Overview and comparison between the model and observations

A key feature in the cold front of 20 November 2013 is a small intrusion, or filament, of dry, high-PV air that was extruded from the larger tropopause fold associated with the upper-level jet–front system, within the descending branch of the transverse ageostrophic circulation of the surface front. Although this filament is evident along a relatively broad swath of the cold front crossing the UK, it penetrates to low levels (<1 km AGL) only within a limited area over central England. As shown in Section 4.3.4, the tropopause fold slopes downwards to the west, whereas the PV filament slopes downwards towards the south. This somewhat counterintuitive situation arises because

the jet intersects the front at a large angle (almost 90°), such that the transverse circulation of the surface front is orientated almost orthogonal to that of the overlying jet–front system.

As will be shown subsequently, the transverse circulation associated with the surface cold front in the region where the dry filament eventually penetrated to low levels was initially weak, but intensified as the cold front moved southeast over the UK, consistent with the increasing 850 hPa frontogenesis along this part of the front (Figure 4.6(d)). Whilst intrusion of dry, high-PV air within the developing front-transverse circulation may also have been facilitated by the general increases in $-v'_{cold}$ and associated substantial *front-relative* forward flow (as postulated by CP20), this is apparently insufficient to explain the localised nature of the intrusion to low levels, since large $-v'_{cold}$ and front-relative $-v'_{cold}$ were present along a considerably wider swath of the front (Figures 4.6(b)-(c)), where much of the dry air aloft was in fact overrunning the surface front, as shown subsequently.

The relationship between the developing dry filament and the tropopause fold may be further understood by analysis of the lowest height of various RH surfaces in the 1.5 km model. Taking the RH = 45% contour (Figure 4.7(a)), evidence of the east–west-tilted tropopause fold is apparent equatorward of the front, where the fold is situated above a relatively moist pre-frontal air mass; the height of the RH = 45% contour decreases from ~7 km over the eastern part of the domain (mauve shades) to ~4.5 km over the western part of the domain (yellow–orange shades). The much smaller dry filament is evident immediately rearward (i.e., to the north) of the surface front over central England, where the lowest height of RH < 45% shows a north to south or north-northwest to south-southeast orientated gradient just behind the surface front (blue shades grading to green to the north or north-northwest)[22], locally reaching as low as 1 km AGL immediately behind the front.

Analysis of the RH = 70% contour (Figure 4.7(b)) provides a clearer picture of the locations where the dry filament penetrates closest to the surface, immediately to the rear of the surface front over central England. A smaller area is also evident over

[22] A second NNW-SSE tilted filament is also evident, further rearward of the front, in places. This appears to correspond to a dual structure in the cold-frontal rainband early on 20 November (evident in both model fields and radar observations; not shown); the rearward band merged with the forward band between 0400 and 0600 UTC as the front moved south across the UK.

extreme southeast Wales. The realism of the model features may be assessed by comparison with Meteosat Second Generation 7.3μm water vapour imagery (Figure 4.7(c)). In this channel, retrieved brightness temperatures are sensitive to the water vapour content in the middle to lower levels of the troposphere, provided there is an absence of dense medium- to upper-level cloudiness (e.g., Georgiev and Santurette, 2009). Comparison of the satellite imagery and model fields suggests that the model has a realistic depiction of the penetrating dry intrusion; a small region of higher brightness temperatures, locally near -10°C, is evident over central England, approximately corresponding to the area with the lowest height of the RH = 45% and 70% contours in the model (*cf*. Figures 4.7(a) and (b), respectively). The smaller region of penetrating dry air in the model over southeast Wales is perhaps also weakly evident in the satellite imagery. Within the main area of higher brightness temperatures over central England, a northwest to southeast orientated brightness temperature gradient can be discerned, broadly in agreement with the orientation of the gradient in the height of the RH = 45% contour in Figure 4.7(a). The highest brightness temperatures are displaced slightly poleward of the area with the lowest penetration of the RH = 75% contour in the model (notwithstanding the slightly later timing of the satellite imagery, relative to the valid time of the model fields). This discrepancy is likely explained by the fact that the dry air penetrates underneath moister layers where it approaches the surface front, as seen in cross-sections through the modelled front (e.g., Figure 4.8). The south-eastward extent of the dry air at low levels is therefore probably underestimated in the satellite imagery.

Near the leading edge of the area where RH < 75% reaches low levels over central England, the 1.5 km model depicts a region of enhanced downdrafts immediately behind the surface cold front (Figure 4.7(d)). Furthermore, updrafts are enhanced along the frontal boundary immediately ahead of these enhanced downdrafts. An association between regions of enhanced vertical velocity and the local intrusions of dry air is also seen over southeast Wales (though, as discussed, the region of penetrating dry air over southeast Wales is perhaps less prominent in the observations). A similar association between penetrating dry air and local downdraft maxima is evident in model fields valid at 1000, 1200 and 1300 UTC (not shown). The reasons for this association, and the impact of the penetrating dry filament and downdraft maxima on the near-surface temperature, wind and pressure fields, are explored further in Section 4.5.

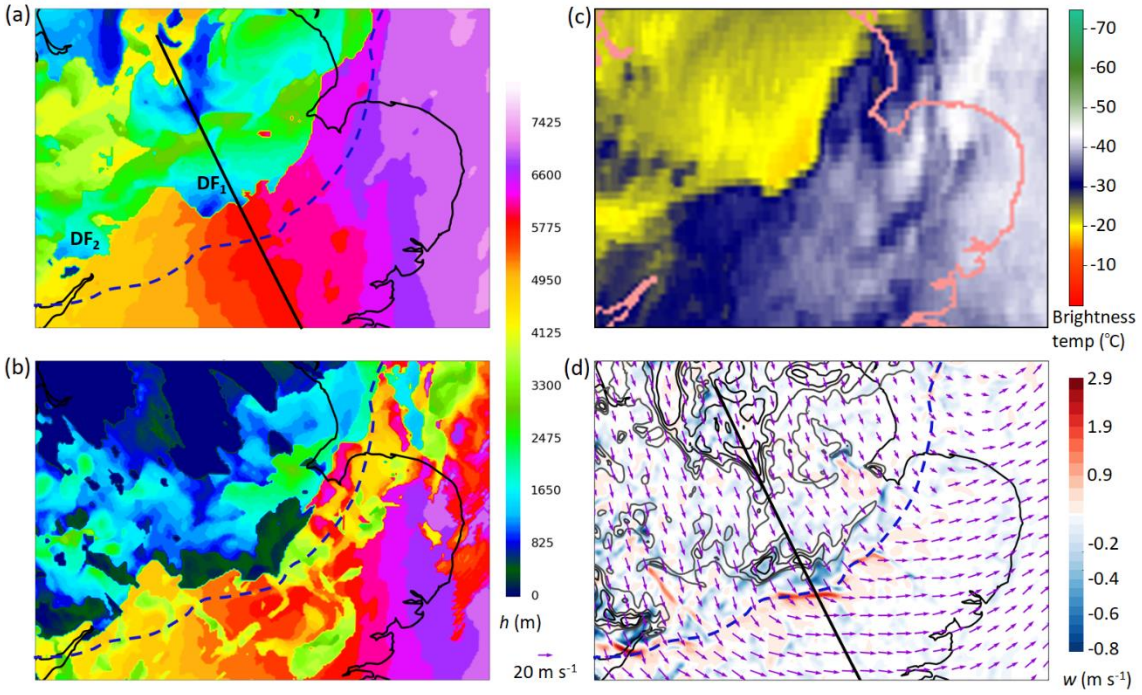

Figure 4.7: Model data (from the 0900 UTC 20 November run of the 1.5 km operational model) and satellite observations showing various structures on the mesoscale in the vicinity of the cold front over central England; (a) Lowest height, on model levels, of the 45% RH contour (colour shading) at 1100 UTC; (b) As in (a), except showing the lowest height of the 70% RH contour; (c) Colour-enhanced Meteosat Second Generation satellite water vapour image (7.3 μm channel) at 1130 UTC 20 November 2013; (d) 845 m AGL horizontal wind vectors (arrows), vertical velocity (red-blue shading, as per the colour scale), and RH (grey–black contours at intervals of 10%, from 50% to 80%, with darker shades indicating lower RH) from the 1.5 km model at 1100 UTC 20 November 2013. Dashed blue line in panels (a), (b) and (d) denotes the position of the surface front in the model fields. Solid black line in panels (a) and (d) denotes the position of the vertical section shown in Figure 4.8 (note that the southeast end of the section lies ~5 km beyond the boundary of the domain shown here). Annotations DF_1 and DF_2 in (a) indicate, respectively, the location of the main dry filament over the Midlands, and a secondary dry filament over southeast Wales.

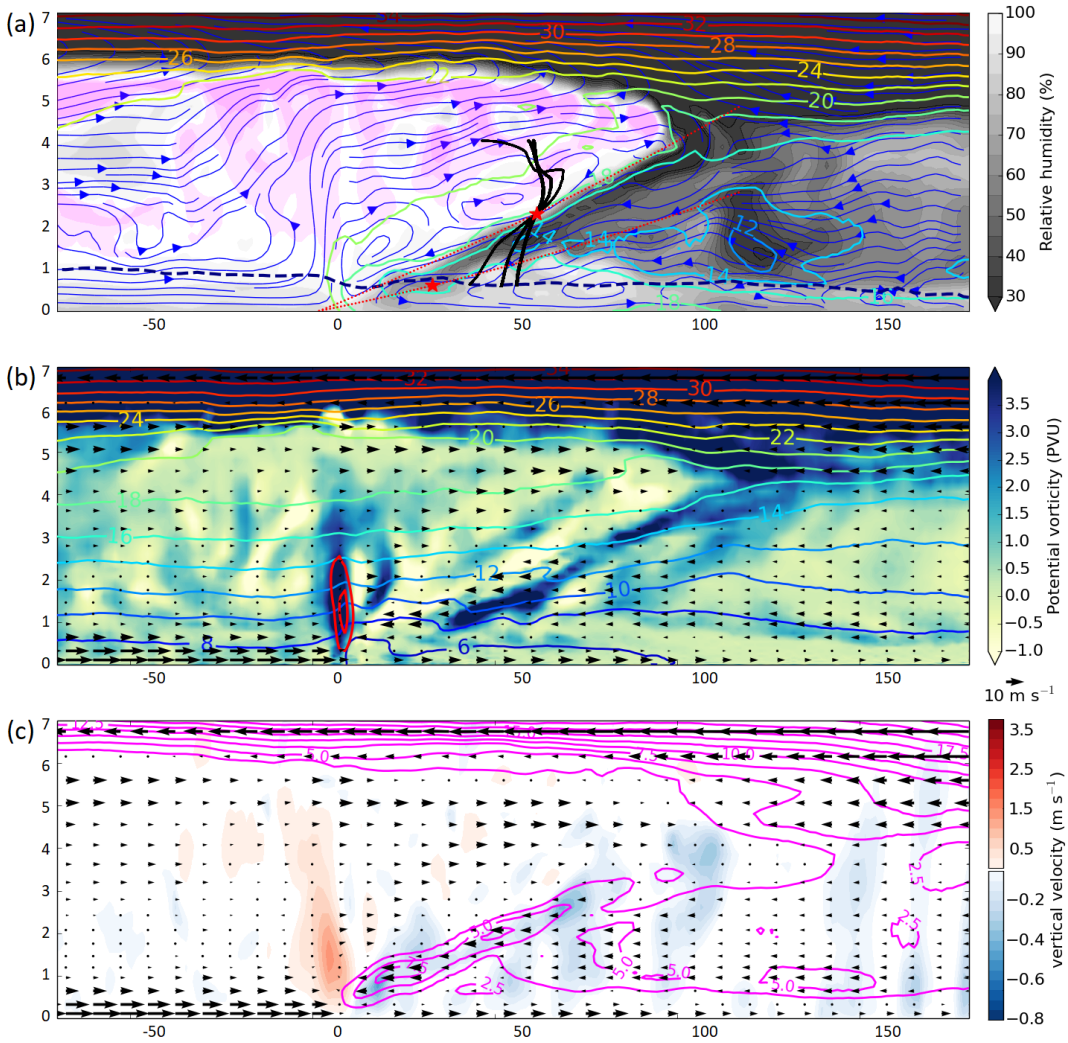

Figure 4.8: Southeast–northwest (152–332°) vertical cross-section through the cold front at 1100 UTC 20 November 2013, using output from the 0900 UTC 20 November 2013 run of the 1.5 km model, and intersecting the front at 52.08°N 0.60°W (see Figures 4.7(a) and (d) for position of section). Vectors are front-relative winds in the plane of the section, calculated using the observed local FNFM of 14.4 m s^{-1}. Horizontal axis shows distance (km) from the position of the surface frontal boundary (negative on the warm side of the front) and vertical axis shows height AGL in km. (a) RH with respect to ice (grey shading; pink areas denote supersaturation), equivalent potential temperature (coloured contours at 2 °C intervals) and streamlines (blue lines with arrows); (b) PV (shading), potential temperature (coloured contours at 2 °C intervals), positive vertical velocity (red contours at 0.5 m s^{-1} intervals starting at 1 m s^{-1}). (c) Vertical velocity (red–blue shading) and front-relative horizontal wind speed (bold, magenta contours for forward-relative flow at intervals of 2.5 m s^{-1}). In (a), the bold black lines represent fall trajectories for hydrometeors passing through the rear edge of the radar-observed wide cold-frontal rainband, using data from the 2° elevation-angle scan of the Chenies, Buckinghamshire, radar at 1117 UTC, assuming fall speeds of 1.0 (thickest line), 0.5, and 0.25 m s^{-1} (thinnest line). Trajectories are calculated from 4.0 km AGL to the model melting level. See main text for further details. Red star-shaped symbols denote the relative positions of the radar-observed rear edge of the wide cold-frontal rainband in the 1° and 2° elevation-angle scans at 1117 UTC (as also shown in Figures 4.13(a) and (b)), with the height of the front-normal radial also plotted for each beam (red dotted lines), after setting the radar location in the section equal to the distance of the radar from the surface front at the radar scan time.

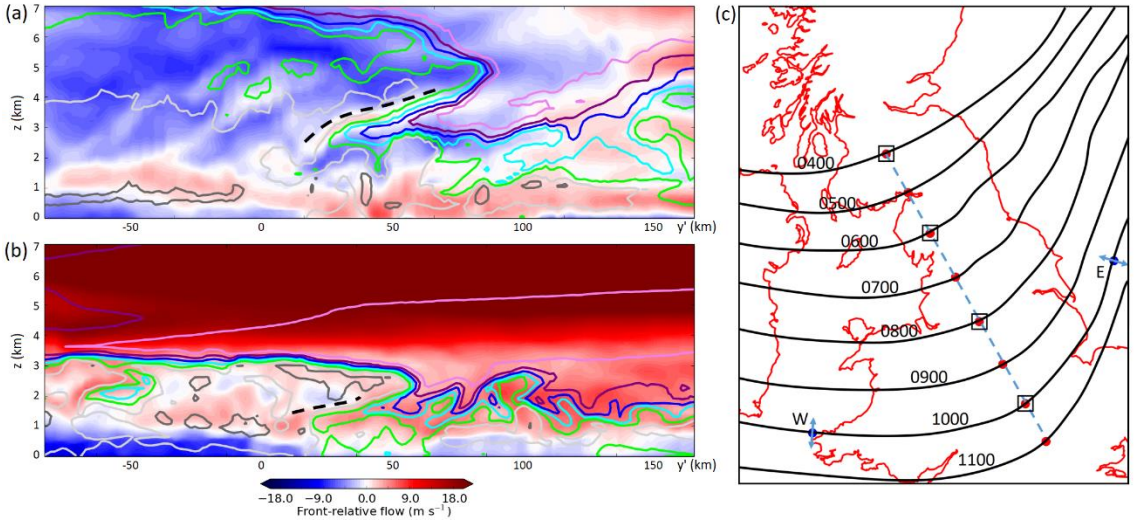

Figure 4.9: Front-normal vertical sections through the cold front at 1000 UTC 20 November 2013, using output from the 0300 UTC 20 November run of the 1.5 km model. (a) East-southeast to west-northwest (111–291°) vertical section intersecting the front at location 'E' in panel (c), which is up-front of the tornadic region; (b) South to north (185–005°) vertical section intersecting the front at location 'W' in panel (c), which is down-front of the tornadic region. Horizontal axis shows distance (km) from the position of the surface frontal boundary (negative on the warm side of the front). Colour shading denotes front-relative horizontal wind speed along the plane of the section (red and blue for forward- and rearward-relative flow, respectively) and bold, coloured contours denote RH with respect to water vapour (dark grey = 99%; light grey = 85%; lime green = 70%; cyan = 55%; dark blue = 40%; purple = 25% and violet = 10%). (c) Smoothed positions of the surface front, as shown in output fields of the 0300 UTC 20 November 2013 run of the 1.5 km model, at hourly intervals between 0400 and 1100 UTC (bold, black lines). The orientation and front-intersecting points of the sections in panels (a) and (b) are shown by the blue arrows and dots, respectively, marked 'E' and 'W' for the section up-front and down-front of the tornadic region, respectively. Blue dashed line and the red markers surrounded by squares indicate, respectively, the orientation and front-intersecting points of the sequence of sections shown in Figure 4.10. Front-relative winds in the sections in panels (a) and (b) have been calculated using FNFM = 11.0 m s^{-1} at 'E' and 17.0 m s^{-1} at 'W', as estimated by measuring the horizontal distance, in the front-normal direction, between the marked frontal positions at 0900 and 1100 UTC in the model fields. Bold, dashed lines denote the interface between sloping regions of rearward-relative above forward-relative flow.

4.4.2 Cross-sections near to the reported location of tornadoes

A southeast–northwest vertical section normal to the front at 1100 UTC, intersecting the front at 52.08°N 0.60°W (Figure 4.8), provides further insight into the structure of the high-PV filament near to the reported tornadoes. Above 5.5 km AGL, the air is extremely dry (RH < 30%) and exhibits large PV (>3 PVU) throughout the section. Flow is strongly equatorward relative to the moving front (forward-relative flow exceeding 15 – 20 m s^{-1} ≥7 km AGL). This overrunning dry air forms part of the

aforementioned tropopause fold, on the immediate cyclonic-shear flank of the mid- to upper-level jet. Within the smaller dry filament, RH of 40 – 50% (Figure 4.8(a)) and PV of 5 – 6 PVU (Figure 4.8(b)) reaches as low as 1 – 1.5 km AGL ~40 to 50 km rearward of the front, with pockets of RH < 80 % reaching the surface immediately behind the front. The dry filament is characterised by weak downdrafts of ~0.1 – 0.3 m s^{-1}, with pockets of stronger downdraft (up to 0.5 m s^{-1}) near the leading edge of the dry filament, ~10 km behind the surface front (Figure 4.8(c)). The magnitude of forward-relative flow within the dry filament (magenta contours in Figure 4.8(c)) generally increases towards the surface front, such that the strongest forward-relative flow (>7.5 m s^{-1}) is located ~10 – 20 km rearward of the front at ~1 km AGL. The forward-relative flow constitutes a well-defined rear inflow to the NCFR and comprises the descending part of the strong front-transverse circulation.

4.4.3. Along-front variability

Comparison of Figures 4.4 and 4.7 shows that the areas in which the dry filament and tropopause fold penetrate to their lowest levels do not correspond (e.g., note how, at 700 hPa, the axis of the dry, high-PV air associated with the fold is ~300 – 400 km west of the tornado reports; Figure 4.4(c)). As discussed earlier, due to the westward tilt of the fold, the overrunning dry, high-PV air reaches progressively lower levels down-front (i.e., to the west). However, the front-transverse circulation also becomes shallower and weaker with increasing distance down-front. The area over central England therefore represents a ‘sweet spot’ in which the transverse circulation associated with the surface front is deep and strong enough, and the dry air within the overlying tropopause low enough, to allow extrusion of dry air to low levels within the transverse circulation.

The associated along-front variability in the cross-sectional structure of the front is evident on comparison of cross-sections intersecting the front at locations up-front and down-front of the tornadic region at 1000 UTC (Figure 4.9). Up-front (i.e., east) of the tornadic region (Figure 4.9(a)), a well-defined dry filament is evident in mid-levels, even though the dry air within the fold only reaches ~7 km AGL in this region. However, the filament terminates some ~2 km AGL, apparently because the front-transverse circulation is rather ill-defined and also fails to extend to low levels (for example, there is only a small area of forward-relative flow aloft near the leading edge of the dry filament, and this is not clearly connected to the lower layer of forward-

relative flow below ~2 km AGL)[23]. Front-normal, front-relative flow is predominantly rearward, even at upper levels, which contrasts markedly with the strong forward-relative flow aloft in sections further down-front (as discussed below). This difference is attributable to the greater distance of this section from the mid- to upper-level jet axis, such that the upper-level flow is weaker, and to the smaller angle between the front and the jet axis here, such that the cross-frontal component of mid- to upper-level flow is smaller.

In contrast, the section located down-front (i.e., west) of the tornadic area is dominated by dry air and forward-relative flow (Figure 4.9(b)); dry air within the tropopause fold penetrates to ~3 km AGL and strongly overruns the front (forward relative flow > 15 m s^{-1}). The predominance of forward-relative flow may be explained by the fact that this section passes close to the jet axis at mid-levels (*cf.* Figure 4.4(b)), with the frontal boundary being orientated approximately normal to the jet here. The front-transverse circulation is weak and shallow (consistent with the slightly weaker 850 hPa frontogenesis along this part of the front, compared to further up-front; *cf.* Figure 4.6(d)) so that, again, dry air fails to reach low levels in the immediate post-frontal region. Rearward-relative flow is evident only in a shallow layer near ground level (likely associated with frictional effects in the boundary layer), and in the rearward-directed part of the weakly-defined front-transverse circulation (e.g., at around 2 km AGL between 10 and 30 km rearward of the surface front: Figure 4.9(b)). The shallow depth of the front, weak updrafts and predominance of forward-relative flow here are suggestive of a kata-type cold front (Sansom, 1951).

[23] Inspection of loops of satellite water vapour imagery suggest that the dry filament in this region may be a residual feature associated with an earlier downward penetration of dry air over northeast England (not shown).

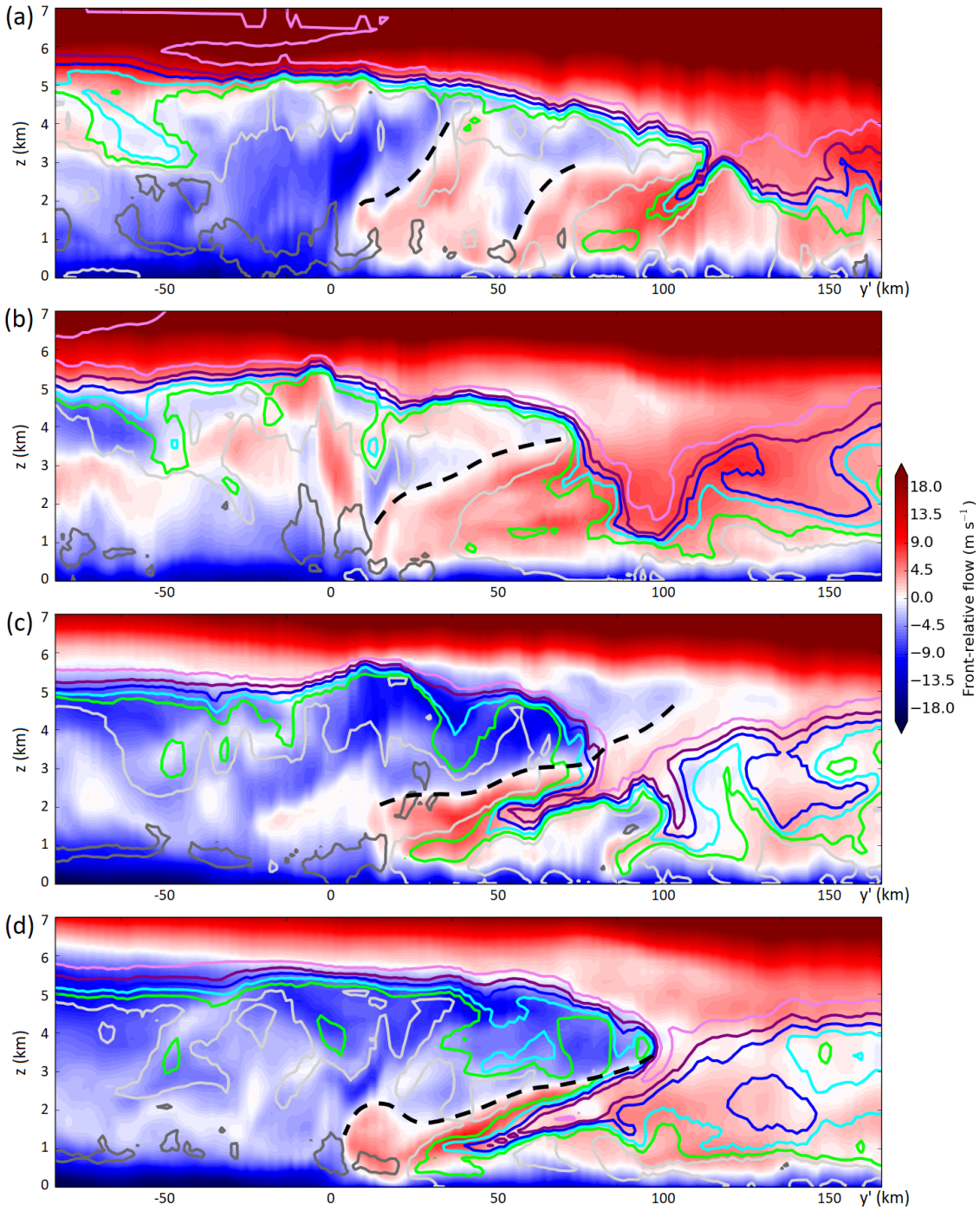

Figure 4.10: Sequence of southeast–northwest (153–333°) vertical cross-sections through the cold front at the locations shown in Figure 4.9(c) at (a) 0400 UTC; (b) 0600 UTC; (c) 0800 UTC; and (d) 1000 UTC 20 November 2013, using output from the 0300 UTC 20 November 2013 run of the 1.5 km model. Colour shading, coloured contours and horizontal distances are as in Figures 4.9(a) and (b). Bold, dashed lines denote the interface between sloping regions of rearward-relative above forward-relative flow.

4.4.4. Development and evolution of the dry filament

Inspection of cross-sections at two-hourly intervals between 0400 and 1000 UTC (Figure 4.10), shows that the dry filament developed rather rapidly as the front moved south across the UK. The timescale of evolution is much shorter than that of the larger tropopause fold and jet streak (e.g., *cf.* Figures 4.5(a) and (b)), suggesting that the development of the dry filament owes to the increasing 850 hPa frontogenesis along this part of the front (Figure 4.6(d)), rather than to changes in the structure of the overlying tropopause fold (though, as noted earlier, the increasing frontogenesis was itself apparently associated with the approach towards the surface front of the leading edge of the upper-level features). Evidence for the rapid development of the dry filament is also provided by satellite observations, which show an expanding cloud-free region and associated area of increasing brightness temperatures in 6.2 and 7.3 μm water vapour imagery (not shown) over the same period. The interpretation that the dry, high-PV filament is extruded from mid- to upper-levels by the front-transverse circulation (as opposed to developing *en route*) is supported by the timescale of evolution, given the typical magnitude of forward-relative flow within the intrusion (e.g., Figure 4.8(c)); a value of ~5 m s^{-1} implies ~70 km forward extension of the dry filament over the 4-hour period ending 1000 UTC (Figures 4.10(b)-(d)), which is close to the apparent extension over this period of ~65 km.

In the early stages (0400 UTC; Figure 4.10(a)), dry air reaches the mid-troposphere in broad region well to the rear of the surface front. This is part of the larger tropopause depression and associated fold. Although there are signs of a small dry filament at the leading edge of this feature (as shown by the fold in the RH = 55% surface near the 100 km distance marker in Figure 4.10(a)), there is no clear connection between this filament and the weak, shallow front-transverse circulation associated with the surface front at this time (between the distance markers -10 and 40 km, at altitudes of 1 – 4 km, in Figure 4.10(a)). The section also hints at two transverse circulations, consistent with the double banded structure evident in both the radar imagery and the model rainfall fields at this time (not shown).

By 0600 UTC, dry air has penetrated to lower levels well to the rear of the front; for example, the RH = 55% contour locally extends to ~1 km AGL ~100 km to the rear of the front (Figure 4.10(b)). There is evidence of a slight intensification in forward-

relative velocities within the forward-directed part of the front-transverse circulation, between the 0 and 100 km distance markers, compared to that at 0400 UTC (*cf*. Figures 4.10(a) and (b)). By 0800 UTC (Figure 4.10(c)), the dry filament has started to develop, as shown by the folding of the RH contours between distance markers 30 and 80 km and the approach of the RH = 70% contour (lime green) towards the surface front. The core of the developing filament is characterised by RH < 55%. The front-transverse circulation, located between the 20 and 70 km distance markers, has increased in strength relative to the earlier sections, with areas of >7 m s^{-1} forward-relative flow evident ≥ ~30 km rearward of the surface front (note that the interface between sloping regions of forward-relative flow and overlying rearward-relative flow, which are considered to form the main front-transverse circulation(s), are highlighted by bold dashed contours in Figures 4.9 and 4.10).

By 1000 UTC (Figure 4.10(d)), the dry filament is fully developed, with RH < 55% penetrating to ~1.0 km AGL only 30 km to the rear of the front. Forward-relative flow > 4 m s^{-1} extends to 0.5 km AGL and reaches the immediate post-frontal region. Forward-relative flow at upper levels and within the larger dry region further to the rear of the front has begun to decrease by this time, whereas rearward-relative flow occupies a larger region above and behind the surface front than in earlier sections (associated with the rearward-directed branch of the now well-defined front-transverse circulation). After 1000 UTC (not shown), the dry filament remains evident in cross-sections, but the front-transverse circulation begins to weaken, and the leading edge of the dry filament retreats slowly rearward of the surface front.

Figure 4.11 (following page): Observed (left column) and modelled (right column, using output from the 0900 UTC run of the 1.5 km model) 1.5 m AGL temperature (colour shading), 10 m AGL wind vectors (arrows) and MSLP (contours at intervals of 1 hPa) at 0900 UTC; (a,e), 1000 UTC (b, f), 1100 UTC (c, g) and 1200 UTC (d, h) 20 November 2013. Observed fields are obtained by interpolation of 1-minute temporal resolution observations from the Met Office's network of surface stations onto a regular 4 km grid using Delaunay triangulation, after time-compositing over a period of ±40 minutes from each analysis time. Time-compositing consists of spatial translation of off-analysis-time observations, using the observed velocity of the surface cold front near the centre of the domain, such that the front-relative location of translated observations is always the same as that of the observing site at each observation time (see Clark and Parker (2014) for details of the methodology). Inverted red (white) triangles denote the locations of confirmed (unconfirmed) tornadoes. Temperatures are corrected to sea level assuming the moist adiabatic lapse rate, since orographic effects otherwise complicate the post-frontal temperature field (particularly in the model), making it more difficult to discern the cold pool. Dashed red box in panel (g) indicates the area shown in Figure 4.12.

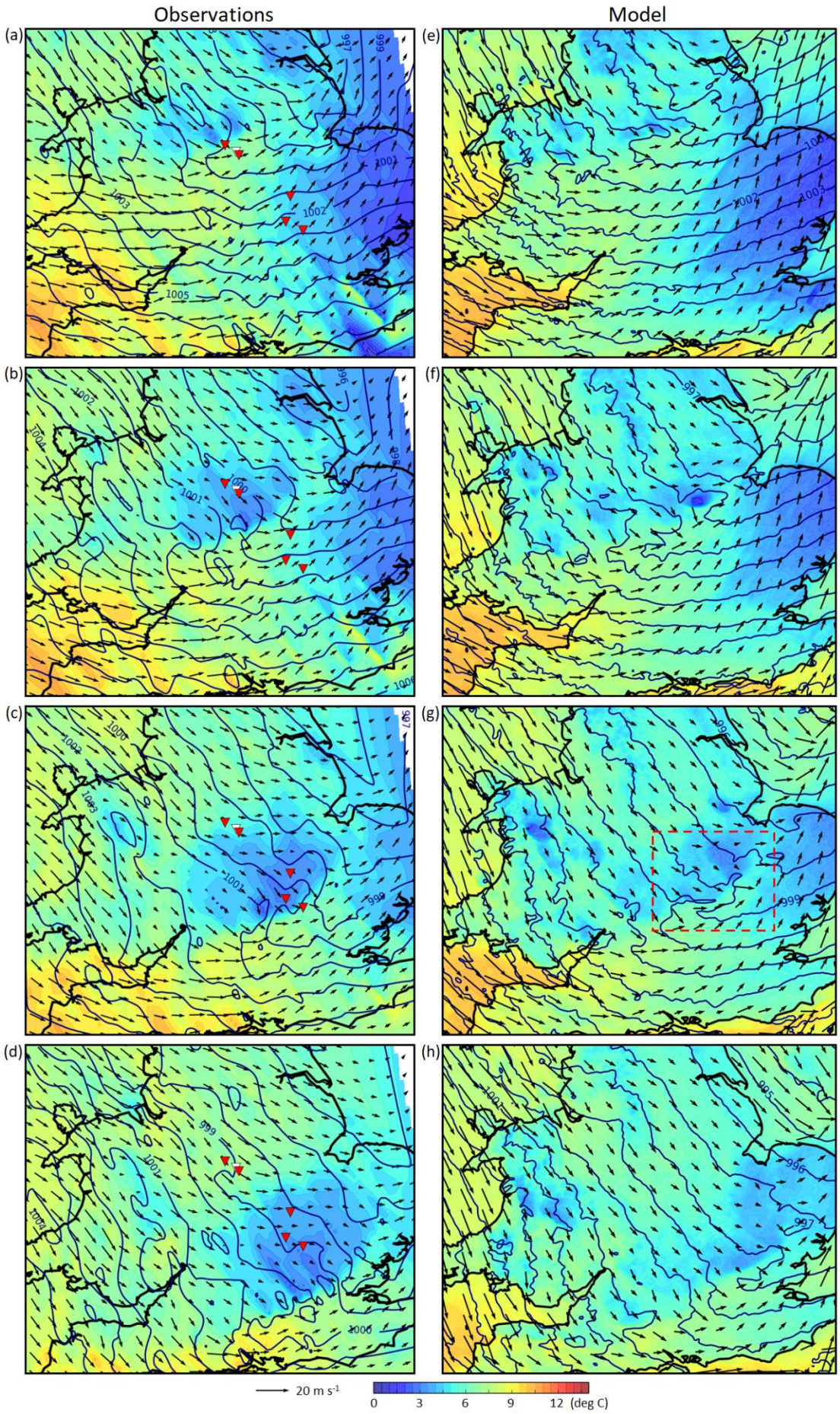
Observations
Model
(a)
(b)
(c)
(d)
(e)
(f)
(g)
(h)
20 m s-1
0
3
6
9
12 (deg C)

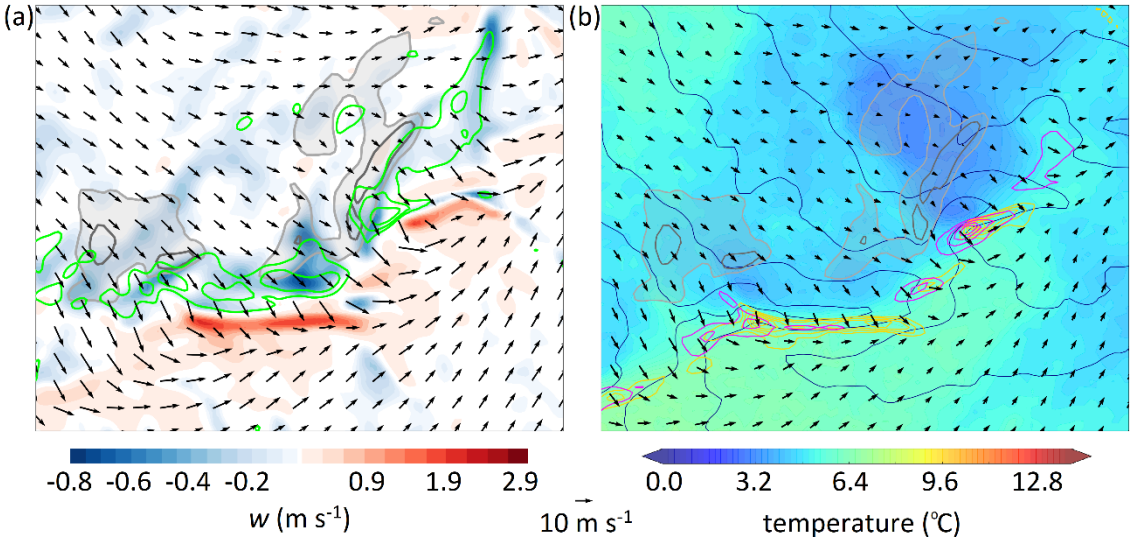

Figure 4.12: Zoomed-in view of surface and near-surface fields near the cold front over central England at 1100 UTC, from the 0900 UTC 20 November 2013 run of the 1.5 km model. (a) 645 m AGL vertical velocity (red-blue shading), 75 m AGL horizontal divergence (lime green contours), 75 m AGL ground-relative wind vectors (arrows); (b) 2 m AGL temperature (colour shading), 10 m AGL wind vectors (arrows), MSLP (navy blue contours; contour interval 0.5 hPa), 75 m AGL horizontal convergence (yellow contours, interval 0.5 x 10^{-3} s^{-1} starting at 1.0 x 10^{-3} s^{-1}) and 75 m AGL vertical vorticity (magenta contours, interval 1.0 x 10^{-3} s^{-1} starting at 1.0 x 10^{-3} s^{-1}). In both panels, RH at 325 m AGL is shown by the grey contours and grey shading (light grey contour = 75% and <75% shaded transparent grey; dark grey contour = 65%). Area of view has width ~135 km (see the dashed red box in Figure 4.11(g) for location of this area).

4.5. Near-surface structures and their relation to the intruding dry filament

4.5.1 RH, wind and temperature structures

The local penetration of dry air to low levels immediately behind the front has a marked impact on the surface temperature, wind and pressure fields in the model and observations (Figure 4.11), and on the local intensity of the surface front and its associated zone of strong horizontal wind shear (hereafter ‘shear zone’). In the model, a strong cold pool develops just behind the front over the northwest Midlands. The cold pool is characterised by surface temperatures of 1 – 3 °C, as compared to 5 – 7 °C elsewhere just behind the front. The cold pool expands as the front moves southeast across the Midlands and southern England between 0900 and 1200 UTC 20 November

(Figures 4.11(e)-(h))[24], eventually weakening and becoming ill-defined by the time that the front nears the south coast.

Gridded surface fields, derived from time- and space-interpolated one-minute resolution surface observations over the UK (Figures 4.11(a)-(d)), compare well with the model fields; a strong cold pool develops over the northwest Midlands by 0900 UTC, expanding as the front moves south-southeast across the Midlands. The five confirmed tornadoes occurred along the NCFR at the leading edge of this expanding cold pool (red inverted triangles in Figures 4.11(a)-(d)). The location, track, time of onset, and expansion of the cold pool all appear to be realistically depicted by the model, though the observations show that the cold pool was somewhat larger in reality, especially at later analysis times. Notwithstanding the differences in cold pool size, the model has evidently captured the pertinent structures in the vicinity of the cold front over central England, as also demonstrated in the earlier comparison of model RH fields and satellite water vapour imagery (Figure 4.7).

Horizontal sections through the modelled front just above the surface in the vicinity of the cold pool at 1100 UTC (Figure 4.12) reveal areas of enhanced horizontal divergence post-front (lime green contours in Figure 4.12(a)). These divergent regions are closely correlated with the areas of enhanced downdraft at 645 m AGL (blue shading in Figure 4.12(a)), suggesting that the divergence is associated with descending air reaching the surface and spreading out (i.e., $dw/dz < 0$ implying $(du/dx + dv/dy) > 0$). The horizontal sections further reveal that the areas of enhanced downdraft and horizontal divergence are closely associated with the leading edge of pockets of RH <85% (grey shading in Figure 4.12). Inspection of horizontal sections at progressively higher altitudes (not shown) reveals that the near-surface low-RH pockets are contiguous with a larger region of dry air at the tip of the intruding dry filament.

The suggested interpretation of these results is that diabatic cooling, associated mainly with sublimation of snow, is locally enhanced where the dry air reaches close to the surface, due to precipitation falling into the dry filament from the region of slantwise ascent above the sloping frontal boundary aloft. The cooled air sinks and

[24] Note that the larger area of surface temperatures < 3°C, over East Anglia, especially at earlier analysis times, is due to radiative cooling the previous night, and should not be confused with the developing cold pool.

spreads out on encountering the surface. The associated near-surface divergence forces a post-frontal forward acceleration that acts to increase the convergence, and therefore updraft speeds, along the frontal boundary at the leading edge of the cold pool. Narrowing of the shear zone and local veering of the winds immediately behind the front, near the leading edge of the cold pool, are associated with increases in vertical vorticity, which render the shear zone prone to miso- to meso-ɣ-scale vortex-genesis.

4.5.2 Evidence of snow sublimation in the dry filament

Observations in support of the sublimation of snow are provided by the Chenies (Buckinghamshire) Doppler radar. At 1117 UTC, the radar was positioned just south of the surface front (Figure 4.13). Along a line passing normal to the front, the rear edge of the wide cold-frontal rainband as observed in the 2° elevation angle radar scan at 1117 UTC was some ~40 – 50 km rearward (i.e., northwest) of that in the 1° elevation angle scan at the same time[25]. Some of this difference may be accounted for by drift of hydrometeors in the system-relative winds in the front-normal plane, over the height interval separating the radar beams. However, further calculations using the model wind fields suggest the difference is unlikely to be explained by drift alone (as also suggested by the large size of the area in which the 1° elevation angle reflectivity is substantially less than that in the 2° scan: Figure 4.13(c)). To perform these calculations, the height of the radar beam in each scan, along an azimuth normal to the front, has been superimposed on the model section in Figure 4.8(a), setting the front-relative location of the radar in the section equal to that of the radar at the time of the scans. The range (from radar) at which the rear edge of the wide cold-frontal band was observed in each scan has been marked in the same figure (red star symbols)[26].

Trajectories were calculated for particles originating at the position of the rear edge of the rainband in the 2° scan, assuming hydrometeor fall speeds of 0.25, 0.5 and 1.0 m s^{-1}, and using the model winds in the section (including the vertical velocities).

[25] Plan position indicator scans take ~17 seconds to complete, and the 1° and 2° elevation angle scans are performed consecutively in each scan cycle, such that the time difference between each is < 1 minute.
[26] It is noticeable in Figure 4.8(a) that the rear edge of the radar-observed rainband in the 2° scan lies close to the interface between high and low RH in the model section, whereas the rear edge of the rainband in the 1° scan lies well within the dry filament. Although this might ostensibly suggest a discrepancy between the model and the observations, an alternative explanation is that precipitation is falling further into the dry filament before completely sublimating at the point indicated in the 1° scan. This is feasible given that the precipitation within the wide cold-frontal rainband is generally heavier with decreasing distance rearward of the NCFR, as seen in Figures 4.13(a) and (b).

Trajectories were terminated at the model melting level (~0.7 km AGL). These fall speeds are deliberately conservative, compared to the accepted range for solid hydrometeors (e.g., see Figure 2 of Locatelli and Hobbs, 1974), so that the results reflect the largest drift that may reasonably be expected. The resulting trajectories (black lines in Figure 4.8(a)) suggest that drift cannot fully account for the distance between the rear edge of the rainband in the 1 and 2° elevation angle scans, or the size of the area with substantially lower reflectivities in the 1° elevation angle scan compared to the 2° (Figure 4.13(c)); even with a fall speed of 0.5 m s^{-1}, which is close to the lower limit of the range of solid hydrometeor fall speeds documented by Locatelli and Hobbs (1974), the drift only accounts for around one-third of this distance. The inference is that sublimation must also be occurring[27].

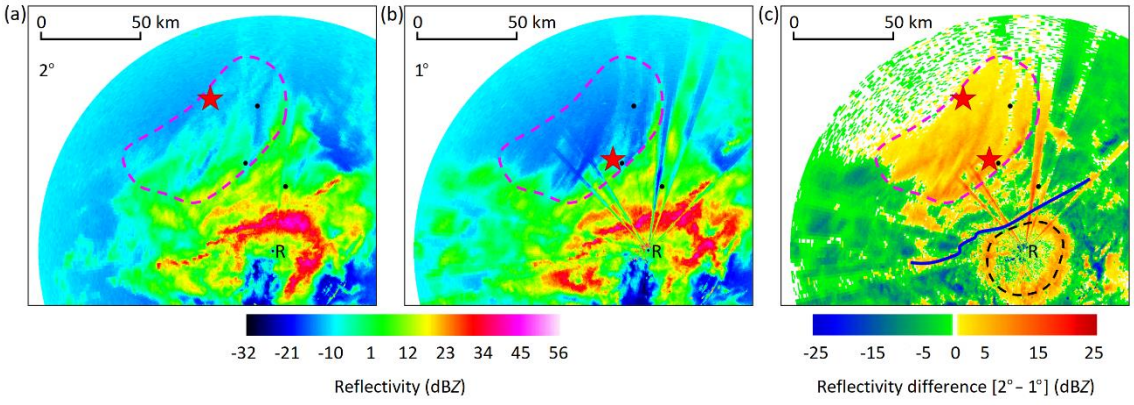

Figure 4.13: Data from the Chenies Doppler radar at 1117 UTC 20 November 2013 showing (a) 2° elevation angle reflectivity; (b) 1° elevation angle reflectivity; (c) reflectivity difference between the two scans (2° – 1°). In panel (c), position of the NCFR is shown by the blue solid line. The black dashed line indicates a ring of positive reflectivity differences due to the differing position of the bright band (associated with the melting layer) in each scan (the bright band being at greater range in the 1° elevation angle scan than in the 2° scan, owing to the lower beam height at given range), and not to be confused with the larger area of positive differences to the north-west of the radar (area enclosed by the magenta dashed line in each panel) which is suggested to be associated with sublimation of snow. Red, star-shaped markers in panels (a) and (b) indicate the rear edge of the rainband along the radial orientated normal to the front, corresponding to the red, star-shaped markers plotted in Figure 4.8(a). The linear features along some radials to the north of the radar in panels (b) and (c) are artefacts arising from partial occultation of the beam in the 1° elevation angle scan. 'R' denotes the radar location.

[27] This analysis also assumes that the model winds are close to those in the real front; unfortunately, no soundings or wind profiler observations are available over central England at the relevant time, so this assumption cannot be tested. However, if the modelled front-normal component of post-frontal winds was substantially in error, this would be reflected in the speed of advance of the front (due to the correlation between $-v'_{cold}$ and the front-normal forward motion (FNFM); e.g., Clark and Parker, 2020); the model and observations agree very closely in this respect (e.g., Figure 4.11), suggesting that the modelled front-normal winds are unlikely to be substantially in error.

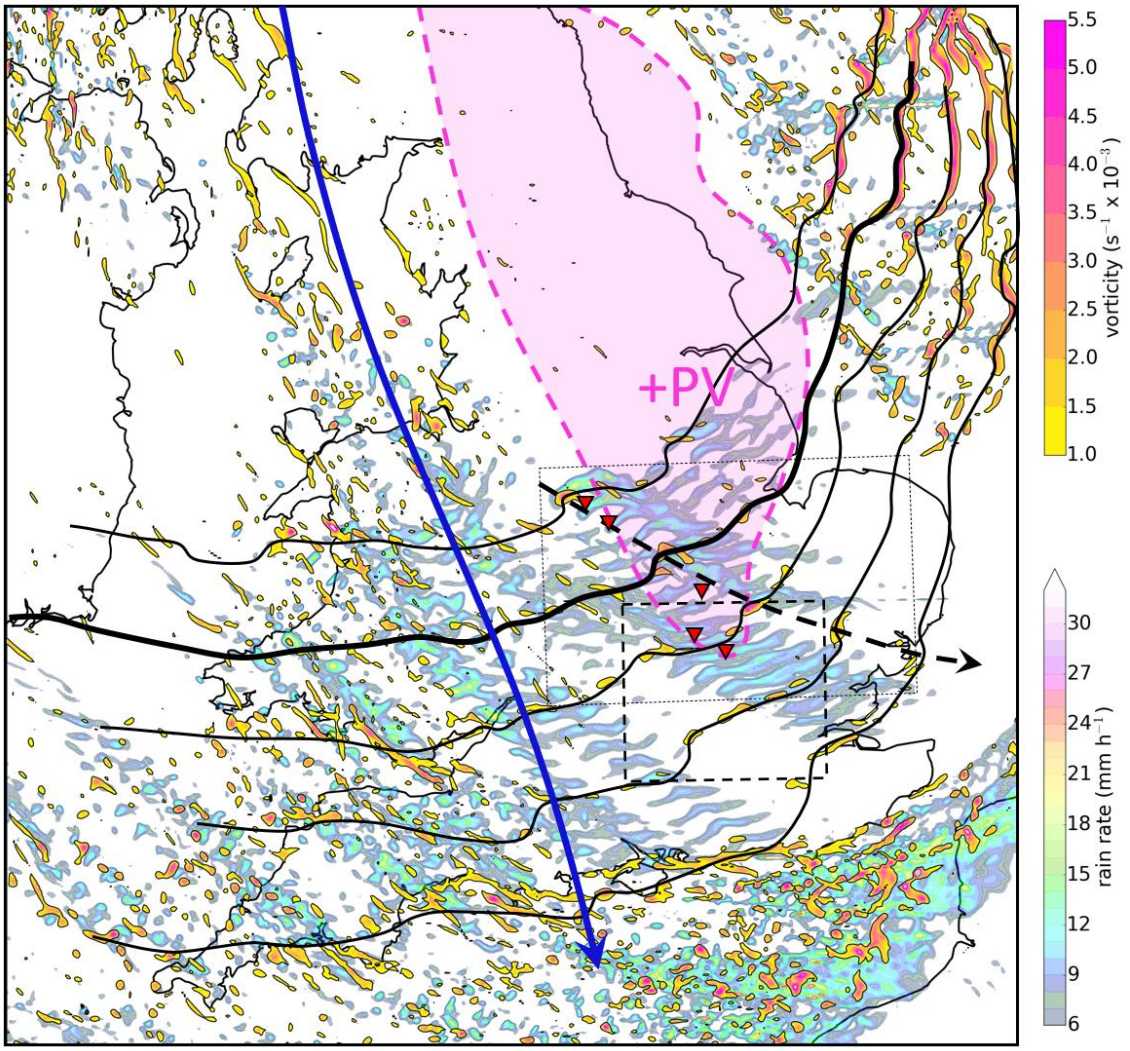

Figure 4.14: Sequence of surface precipitation rate at 15-minute intervals (colour shading) and 75 m AGL vertical vorticity at hourly intervals (overplotted, yellow–pink shading) between 0900 and 1300 UTC 20 November 2013, from the 0900 UTC run of the 1.5 km model. Bold black lines denote the approximate positions in the model of the surface front at hourly intervals over the same period. Bold blue arrow denotes the position of the jet axis at 7 km AGL, and the dashed magenta contour and shading denotes the extent of PV > 5 PVU at the same height. The track of the strongest overland vortex in the model is indicated by the black, dashed arrow. Locations of reported tornadoes are shown by the red inverted triangles. The fine dashed box denotes the area shown in Figure 4.16, and the smaller, bolder dashed box the area shown in Figure 4.17.

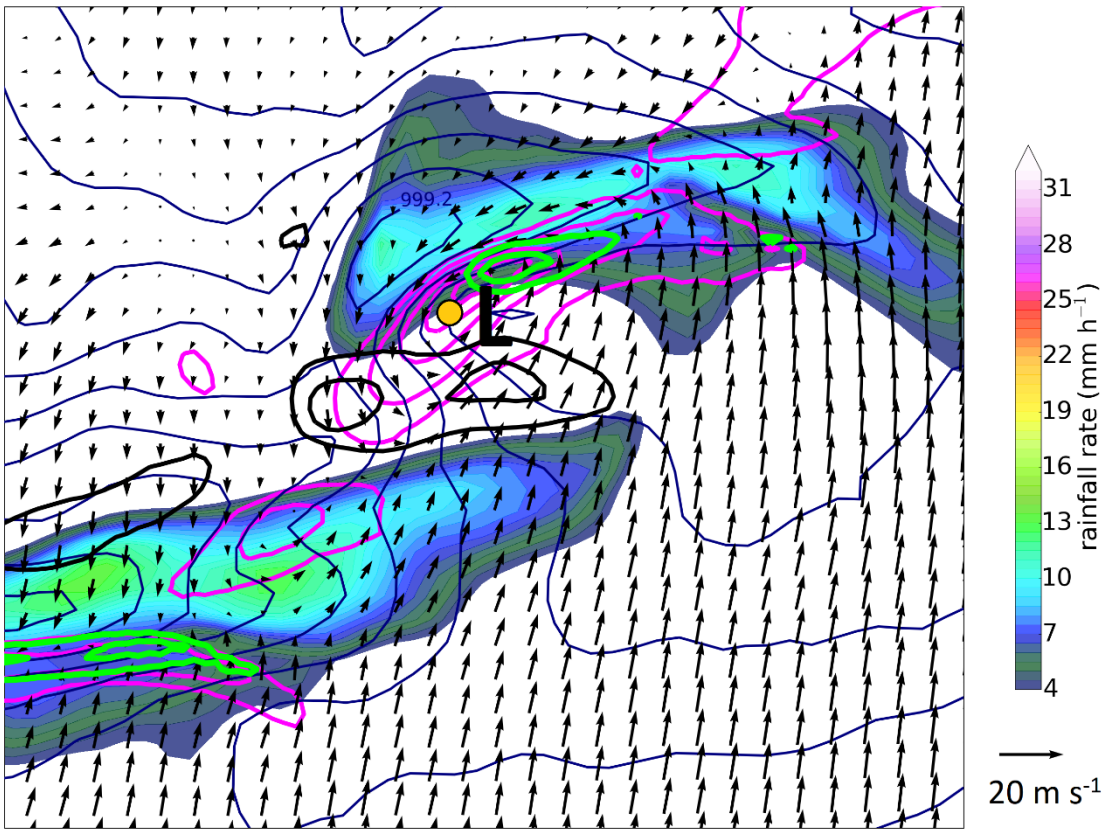

Figure 4.15: Zoomed-in view of the vortex associated with the strongest inland 75 m AGL vertical vorticity maximum in the 0900 UTC 20 November 2013 run of the 1.5 km model, valid at 1100 UTC 20 November 2013; MSLP (navy blue contours at intervals of 0.2 hPa), surface rainfall rate (colour shading), and 555 m AGL vortex-relative wind vectors (plotted every 2.25 km), vertical vorticity (magenta contours at intervals of 1 x 10^{-1} s^{-1}), vertical vorticity stretching (lime green contours at intervals of 0.25 x 10^{-5} s^{-2}) and ground-relative wind speed (black contours at intervals of 1 m s^{-1}, starting at 21 m s^{-1}). 'L' denotes the local MSLP minimum associated with the vortex, and the yellow dot marks the centre of the closed circulation in the vortex-relative wind field. The area shown has width 65 km.

4.5.3 Structure of the NCFR and embedded vortices in the model

Low-level vorticity and convergence fields from the model (e.g., Figure 4.12(b) and Figure 4.14) show that, whilst the shear zone at the surface front is generally characterised by much weaker vertical vorticity and horizontal convergence than found by Clark *et al*. (2021) in the frontal wave case of 17 October 2011 (e.g., 75 m AGL vertical vorticity generally < 1 x 10^{-3} s^{-1} over inland areas; *cf.* Figures 4.14 and 3.7), local maxima > 3 x 10^{-3} s^{-1} occur near the cold pool over central England and, to a lesser extent, near the feature over Wales. Similarly, the NCFR is coherent and locally intense along the leading edge of these cold pools, but relatively weak or absent elsewhere.

The strongest near-surface vertical vorticity maximum over land, which can be tracked from 0900 to 1400 UTC (as shown by the dashed arrow in Figure 4.14), is associated with a long-lived inflection in the NCFR. At times, this inflection resembles the broken-S reflectivity signature (McAvoy *et al*., 2000; Grumm and Glazewski, 2004; Lane and Moore, 2006), which is often associated with radar-observed NCFR vortices. In the broken-S signature, the up-front (down-front) NCFR core is slightly concave (convex) at the leading edge and positioned slightly rearward (forward) of the mean position of the surface front. A small NCFR break separates the two cores near the vortex centre (see also Figure 4.15). Closer inspection of the model rainfall rates at 5-minute intervals (not shown) suggests that the associated vorticity maximum may comprise a series of individual maxima, occurring in succession along the same part of the front, rather than a single maximum.

Cross-sections through the vortex centre near the time of maximum vertical vorticity (not shown) reveal a relatively shallow vortex (vertical vorticity > 1 x 10^{-3} s^{-1} extending only to ~1.7 km AGL, with the largest vertical vorticity (> 6 x 10^{-3} s^{-1}) occurring within the lowest 0.5 km AGL). The vortex centre is characterised by a local updraft minimum, consistent with the associated NCFR gap in model fields (near the centre of the 'broken-S' feature). Horizontal sections (Figure 4.15) reveal a closed circulation about the vortex centre in the system-relative reference frame. The circulation is centred near the western tip of the NCFR core comprising up-front half of the broken-S. In the immediate vicinity of the vortex, updraft speeds are maximised on the up-front (i.e., northeast) flank. Further away from the vortex, the down-front of the two NCFR cores comprising the broken-S feature exhibits the strongest and deepest updrafts anywhere along the front over the UK between 1000 and 1200 UTC, with updrafts extending to ~3 km AGL and updraft velocities reaching a maximum of ~2.7 m s^{-1} between 1.2 and 1.7 km AGL. Horizontal wind speeds at 10 m AGL are maximised on the immediate down-front flank of the vortex, where they locally exceed > 22 m s^{-1} (bold black contours in Figure 4.15). This wind maximum likely owes to superposition of the background wind field (itself enhanced by the cold pool) and the rotational velocity of the vortex, the two contributions being additive on the down-front flank of the vortex.

Although investigation of the vortex-genesis mechanisms is beyond the scope of the present study, analysis of the instantaneous magnitudes of the stretching and tilting terms in the vorticity equation at 1100 UTC shows that stretching is the larger of the two; a distinct stretching maximum is evident on the immediate up-front (i.e., northeast) flank of the vortex (bold, lime green contours in Figure 4.15), with the largest stretching (~2.8 x 10^{-5} s^{-2}) occurring between 0.1 and 0.15 km AGL. Large stretching also occurs near the leading edge of the strong NCFR core located immediately down-front of the vortex. In contrast, the largest tilting (~0.8 x 10^{-5} s^{-2}) occurs near the northeast end of the adjacent NCFR core down-front (i.e., well to the southwest of the vortex). The largest tilting magnitude in the immediate vicinity of the vortex (~0.4 x 10^{-5} s^{-2}) is on the northern flank above 0.75 km AGL, but the tilting here contributes negatively to the vertical vorticity. Negative tilting also occurs immediately behind the down-front NCFR core at 2.0 – 2.5 km AGL. Considering positive contributions only, the maximum stretching is therefore at least seven times larger than the maximum tilting. The presence of a stretching maximum on the up-front flank of the vortex is consistent with previous modelling studies of meso-ɣ- to miso-scale vortices within NCFRs (e.g., Smart and Browning, 2009; Clark *et al*., 2021), and this has been suggested to be a preferred location for tornado-genesis.

4.5.4 Structure of the NCFR and embedded vortices in radar observations

Composite radar data show evidence of NCFR cores along the surface cold front from ~0900 UTC 20 November 2013 (Figure 4.16), though the NCFR is not particularly strong or coherent at this time. Interpretation is hampered by bright banding near to several radars, and more generally by the shallowness of the NCFR (echo tops often near 1 km AGL), such that beam overshooting may account for some of the apparent NCFR gaps at large range from the nearest radar (e.g., over the Irish Sea and parts of northeast England). Notwithstanding these issues, the composite imagery shows that the NCFR intensified slowly as the cold front moved southeast, generally becoming strongest (core rainfall rates > 16 mm h^{-1}) and most coherent over central England and parts of central-southern and southeast England (Figure 4.16), corresponding to the track of the cold pool in the surface analyses (*cf*. Figure 4.11). Broken-S structures, suggestive of meso-ɣ- to miso-scale vortices (e.g., Smart and Browning, 2009), are apparent at times within this region. The structural and locational similarity between the

observed and modelled broken-S features is striking (*cf*. Figures 4.14, 4.16 and 4.17). However, the NCFR is evidently wider in the model (~10 km, as compared to ~5 km in the radar observations) and the broken-S structure is likewise larger (wavelength ~30 km as compared to ~14 km); *cf*. Figures 4.15 and 4.16. These issues likely relate to the model's inability to fully resolve the frontal shear zone, especially where it became particularly narrow and intense near to the expanding cold pool.

More detailed observations of the frontal shear zone at the leading edge of the expanding cold pool over central England are provided by the Chenies C-band Doppler radar (located at 51.69°N 0.53°W). Three of the five confirmed tornadoes occurred within range of this radar, the closest being 31.5 km away. The radar performs plan position indicator (PPI) scans at four elevations angles between 1° and 6° every five minutes. In Figure 4.17, data from 1° elevation angle scans have been composited by calculating the maximum value over the period 1012 to 1232 UTC, showing the evolution of the NCFR. The shear zone is rendered visible in the radial velocity field by the sharp azimuthal and radial gradients in velocities which indicate, respectively, horizontal shear normal to the beam, and horizontal convergence or divergence along the beam. The magnitude of these parameters is dependent on the orientation of the radar beam, relative to the local orientation of the shear zone, in addition to the true magnitude of the same parameters at the shear zone. In Figure 4.17(b), negative values of radial convergence and azimuthal shear (indicative of divergence and anticyclonic shear, respectively) have been set equal to zero, with the sum of the positive-only azimuthal shear and radial convergence then calculated. Since the frontal boundary is marked by both horizontal convergence and vertical vorticity, the summed quantity, which is termed 'positive azimuthal shear plus radial convergence' (hereafter PSPC) is less dependent on radar viewing angle, and therefore gives a more complete picture of the shear zone and its along-front variability than either of the constituent parameters in isolation.

The composited PSPC field (Figure 4.17(b)) shows that the shear zone is only adequately sampled within ~60 km of the radar, as suggested by the general lack of large PSPC at greater range. This is partly a consequence of beam broadening with increasing range, but also reflects the fact that the shear zone becomes less well defined with increasing height above the ground (the beam entirely overshooting the NCFR and

associated shear zone at large range from the radar). The maximum range to which features may confidently be detected (~60 km) is similar to the maximum range to which significant differences have been found between tornadic and non-tornadic vortices in convective systems in high-shear, low-CAPE environments (Davis and Parker, 2014) which, like NCFRs, tend to be shallower and smaller than their high-CAPE counterparts.

Within ~60 km of the radar, local perturbations in the shear zone are evident in both the reflectivity and PSPC fields, indicative of the presence of miso-scale vortices (i.e., misocyclones, with a typical diameter of 1 – 4 km). Some of these vortices are ongoing as the NCFR and shear zone come within ~60 km of the radar, whilst others develop at closer range. In the PSPC field, the perturbations consist of local inflections and notches, occasionally with local minima in PSPC near to the centre of the inflection. In the composited radar reflectivity field (Figure 4.17(a)), many of the perturbation centres are associated with local reflectivity minima, with several examples of the broken-S reflectivity signature. The approximately circular region of high reflectivity surrounding the radar is due to bright banding which, as mentioned in the discussion of the composite radar imagery, masks the reflectivity structure of the NCFR within ~20 km range of the radar.

Evolution of individual vortices and associated NCFR perturbations near to the two tornadoes closest to the Chenies radar (at Irthlingborough and Barton-le-Clay; Table 4.1) is shown in Figure 4.18. The vortex associated with the Irthlingborough tornado (hereafter vortex 1) is evident as a velocity couplet (i.e., a local maximum and adjacent local minimum in the radial velocity field, separated by a small distance in the azimuthal direction) between 1037 and 1057 UTC. A small reflectivity minimum develops near the centre of the associated amplifying NCFR perturbation at 1042 UTC, close to the time and location of tornado-genesis. This NCFR gap broadens after tornado-genesis, suggesting expansion of the parent vortex in its decaying stages. After 1107 UTC, the reflectivity structure becomes indistinct as the vortex moves into the region affected by bright banding.

The second tornado (at Barton-le-Clay) occurred in association with a separate vortex (hereafter vortex 2), initially located several kilometres up-front of vortex 1. The rate of advance of the shear zone is apparently locally reduced in this region (as

suggested by its lagging to the northwest of the adjacent parts of the shear zone), likely due to the southerly flow component on the eastern flank of vortex 1, and consistent with the local rearward position, relative to the mean position of the front, of the up-front NCFR core in the two cores comprising a broken-S reflectivity signature centred on vortex 1. A maximum in PSPC develops prior to tornado-genesis, as the shear zone narrows, and a velocity couplet is evident at 1042 and 1047 UTC. The reflectivity field evolves rapidly, with a well-defined broken-S signature in the 1052 UTC scan. Thereafter, perturbations in the reflectivity field appear to reduce for a time, as the vortex begins to merge with the expanding vortex 1. The tornado occurred at ~1102 UTC, near the south-western tip of a region of high reflectivity immediately up-front of the expanding NCFR gap associated with the merging vortices 1 and 2. Relative to the merged vortex and broken-S reflectivity signature, the tornado therefore appears to have occurred close to the location of the vorticity stretching maximum in the modelled vortex (*cf.* the 1102 UTC reflectivity panel in Figure 4.18 with Figure 4.15), though the merger of the two vortices complicates the picture somewhat. Reflectivity near the merged vortices reduces markedly after 1102 UTC, with a somewhat larger NCFR gap evolving by 1107 UTC. After this time, the reflectivity structures are masked by bright banding.

Several other prominent NCFR perturbations, sometimes with associated velocity couplets, are evident elsewhere along the shear zone near the leading edge of the expanding cold pool (as shown in Figures 4.17 and 4.18). There are no obvious differences, in terms of the strength and longevity of velocity couplets, between the vortices that produced tornadoes and those that apparently produced no damage.

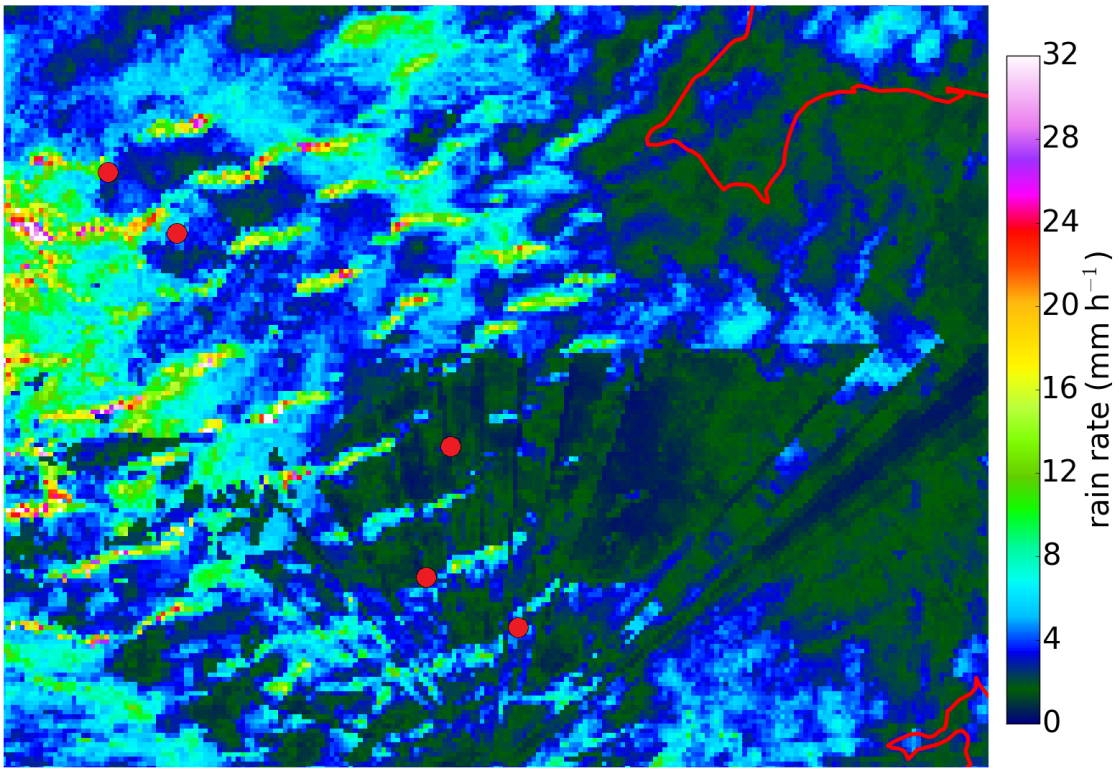

Figure 4.16: Composited radar rainfall rates at 15-minute intervals over the period 0900 to 1300 UTC 20 November 2013, showing the evolution of the radar-observed NCFR. The location of confirmed tornado reports is denoted by the red dots.

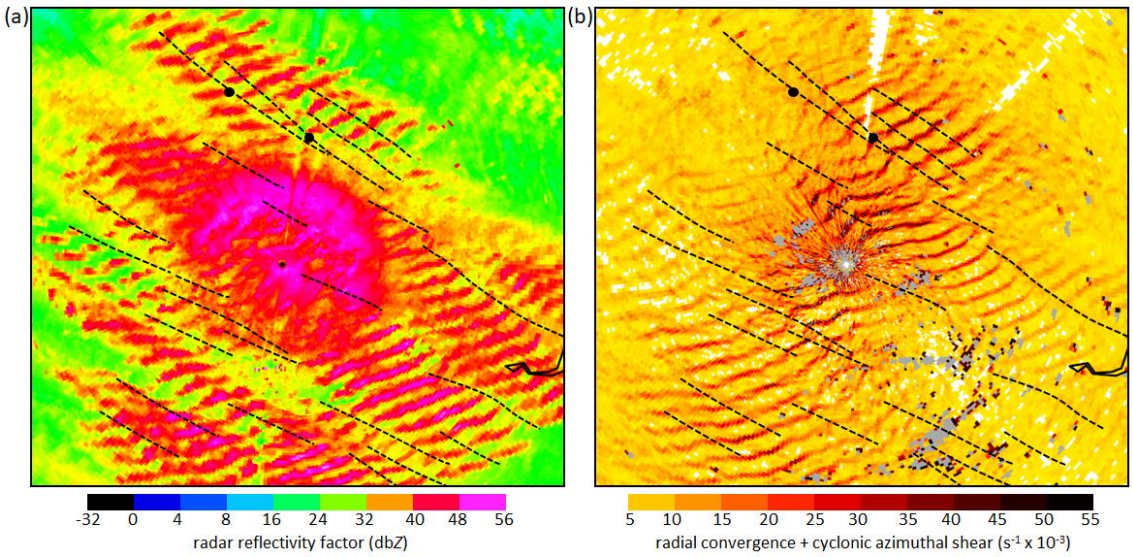

Figure 4.17: Composite fields from the Chenies, Buckinghamshire, Doppler radar, using 5-minute scans over the period 1012 to 1232 UTC 20 November 2013. (a) Radar reflectivity; (b) Sum of cyclonic azimuthal shear and radial convergence (PSPC). The radar location is shown by the small black dot in panel (a), and a white dot in panel (b). Tracks of individual miso-scale vortices, as inferred from inflections and broken-S signatures in the reflectivity field, and/or inflections in the PSPC field, are shown by dashed black lines. Larger black dots denote the locations of tornado reports. The area shown has width 130 km and corresponds to the bolder dashed box in Figure 4.14.

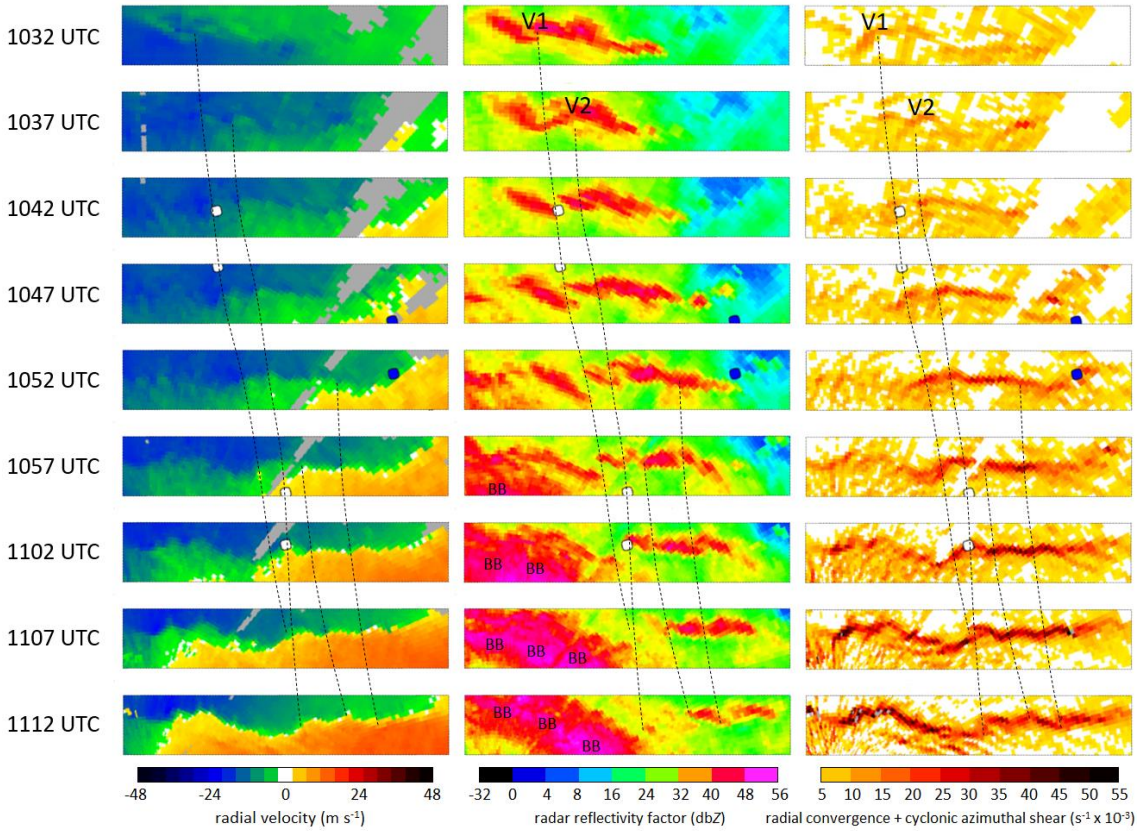

Figure 4.18: Radial velocity (left column), reflectivity (central column) and PSPC fields (right column) following the intense part of the shear zone ahead of the expanding cold pool over the period 1032 to 1112 UTC 20 November 2013, as observed in individual scans at 1° elevation angle (radial velocity and PSPC) and 2° elevation angle (reflectivity) from the Chenies Doppler radar. Locations of tornadoes and instances of non-tornadic wind damage are shown by white and blue dots, respectively. The tracks of radar-observed vortices, as shown by inflections in the shear zone in the reflectivity and PSPC fields, hook or broken-S signatures in the reflectivity field, or velocity couplets in the radial velocity field, are shown by dashed lines. Panels have been rotated so that the horizontal axis is approximately parallel with the front (a clockwise rotation of 31° from the original orientation in each case). Note that the vortex tracks are schematic, in that their location, relative to the data in each panel, is only exactly correct at the intersection with the shear zone; for clarity of presentation, the front-normal horizontal extent has been artificially extended by separation of the panels in consecutive timesteps, whereas in reality there is some overlap between the areas shown at consecutive time steps. Negative radial velocities (green–blue shades) denote flow towards the radar, and positive radial velocities (orange–red shades) denote flow away from the radar. The radar is located approximately to the south of the area shown in each panel (i.e., beyond the bottom, left-hand corner of the rotated panel, in most cases). The NCFR approaches the radar during the period shown. In the reflectivity panels, ‘BB’ denotes areas affected by bright banding. ‘V1’ and ‘V2’ denote vortices 1 and 2, respectively, as discussed in the main text.

4.6. Discussion

Processes leading to the development of locally tornado-favourable conditions at a cold front have been investigated through multiscale analysis of model data and observations. As for the frontal wave case investigated in Chapter 3, various features of the larger-scale flow field are found to play a controlling role in determining the timing and location of tornado-genesis. However, the mechanisms at work are different in the two cases. In the present case, the location and timing of tornadoes is explained by an interaction between upper-level features (i.e., a jet streak and associated positive PV anomaly and tropopause fold) and the intensifying front-transverse circulation at the surface cold front, underneath the left exit of the jet streak. The upper-level jet–front system was important not only in promoting local increases in low-level frontogenesis (via the associated forcing for ascent near the jet's left exit region), but also in that the associated tropopause fold provided a source of dry air in the mid-troposphere. As the front-transverse circulation intensified in the frontogenetic region, part of the dry air within the fold was extruded as a much smaller filament of dry, high-PV air, which eventually penetrated to low levels immediately behind the surface cold front. In the frontal wave case presented in Chapter 3, vortex-genesis, likely due to the release of HSI, apparently depended on the balance between horizontal strain and vertical vorticity (as assessed by analysis of bulk measures of shear vorticity and cross-frontal confluence, respectively) in a shear zone that was already narrow and well-defined at the onset of secondary cyclogenesis; intrusion of dry air appears not to have played a role in local intensification of the shear zone as in the current case.

The intruding dry filament had important ramifications for the intensity of the surface front, through its modification of the near-surface temperature and wind fields in the immediate post-frontal environment. Enhanced diabatic cooling, where precipitation from the wide cold frontal rainband fell into the dry filament, resulted in an expanding cold pool and region of enhanced descent and associated near-surface divergence near the tip of the dry filament. At the leading edge of these features, the frontal shear zone narrowed due to enhanced convergence, with an associated increase in the vertical vorticity and updraft speeds, and the development of a coherent and locally intense NCFR. Meso-ɣ- to miso-scale vortices developed along the intensifying shear zone, some of which spawned small tornadoes.

Outside of the region in which the dry filament penetrated to low levels, the cold front was generally rather diffuse and often lacked a coherent NCFR, both in the model simulations and in radar observations. The general lack of an NCFR likely relates to the weak 850 hPa frontogenesis away from the part of the front located underneath the left exit of the jet streak, and the antecedent weak frontogenesis along the cold front more generally (e.g., Figure 4.3). This is in stark contrast to the frontal wave case described in Chapter 3, in which a long period (>24 – 36 hours) of strong deformation and frontogenesis preceded the occurrence of tornadoes, such that the surface front was already narrow and well-defined by the time of onset of secondary cyclogenesis. Common to both cases, however, are local increases in frontogenesis along the tornadic part of the front, prior to tornado-genesis.

CP20 noted that amplification of the large-scale flow is a characteristic feature of north-westerly flow tornadic NCFRs. The amplification was suggested to facilitate the approach towards the front of disturbances in the mid- to upper-level flow. The present case is consistent with this idea, though the slow approach towards the front of the leading edge of the jet streak appears to have been due as much to its gradual elongation in the amplifying flow, as to the relative movement towards the front of the feature as a whole. Another relevant consideration in these cases is that north-westerly flow patterns are known to favour the birth of mobile upper-level troughs, in environments of substantial tilting frontogenesis (e.g., Reed and Sanders, 1953; Sanders, 1988; Schultz and Sanders, 2002). Indeed, the configuration and evolution of the large-scale flow pattern at mid- to upper-levels shows many similarities with Schultz and Sanders' (2002) study of mobile trough birth in north-westerly flow (*cf.* their Figure 1(a)-(b)). The pattern also conforms well to stage 2 of Shapiro's (1983) conceptual model of the evolution of an upper-level jet–front system as it propagates through a longwave trough; at stage 2, the jet streak is situated within north-westerly flow upstream of the major upper-level trough axis, the upper-level flow is markedly diffluent, and cold advection dominates (see Figure 19 of Keyser and Shapiro (1986)).

The amplifying large-scale flow pattern is associated with increasing $-v'_{cold}$ and *front-relative* $-v'_{cold}$ over a rather wide swath of the front (Figures 4.6(b) and (c)). Inspection of the ERAi fields suggests this is partly due to veering winds, such that the flow tends closer to orthogonality to the front, and partly due to increases in the wind

speed at all levels below the approaching mid- to upper-level jet streak. Whilst the increasing front-relative $-v'_{cold}$ might be expected to facilitate the intrusion of dry air into the rear of the front over a relatively broad swath, inspection of model cross-sections shows that dry air in fact overran the front in most locations. The intrusion of dry air to low levels immediately behind the front additionally required strong frontogenesis, because a well-defined and sufficiently deep front-transverse circulation was required for some of the otherwise overrunning dry air to be extruded to low levels behind the surface front, in the form of the dry filament. This again underlines the need, as originally suggested by CP20, for analysis of 850 hPa frontogenesis in conjunction with *p*[TN], to fully understand the risk of tornadoes in any given cold front.

Although not investigated herein, another mechanism that can lead to the intensification of slantwise flows within a frontal zone is the release of Conditional Symmetric Instability (CSI). This possibility may warrant further exploration (for example, by determining whether CSI existed in the frontal zone, or not, in the current case). However, as pointed out by Schultz and Schumacher (1999), where CSI is present in a frontal zone, it is often not possible to distinguish between the slantwise flow resulting from the release of CSI and that associated with the frontogenetic forcing.

In the region where the dry filament penetrated to low levels, the model and observations show the development of a well-defined cold pool that expanded as the front moved southeast across England. In the model, this cold pool was characterised by locally enhanced downdrafts and near-surface divergence, which in turn was associated with increased convergence and locally enhanced updrafts along the shear zone and NCFR just ahead of the cold pool. This association between post-frontal divergence and strengthening of the frontal shear zone and associated updrafts was evident in both the 0300 and 0900 UTC runs of the 1.5 km model (and indeed in observations, provided that the intensity of the NCFR can be understood as a proxy for the magnitude of updraft speed, as found in Chapter 3). In the model, these features were all slightly stronger in the 0900 UTC run than in the 0300 UTC run[28]. This suggests that there may

[28] This partly explains the use of both the 0300 and 0900 UTC runs of the model in the current study. The 0900 UTC run was too late to show the evolution prior to tornado-genesis, whilst the 0300 UTC run apparently produced a slightly weaker version of the pertinent features at the reported time of the tornadoes.

be a positive correlation between the intensity of the cold pool and the strength of the shear zone and associated vortices which, if true, lends further credence to the idea that the cold pool and associated enhanced post-frontal divergence are responsible for the localised intensification of the shear zone and subsequent vortex-genesis. Furthermore, the fact that the pertinent features were apparent in both model runs suggests the location and timing of the area at greatest risk of tornadoes may have been relatively predictable. This predictability probably relates to the close links between the (generally well-resolved) larger-scale flow features and the smaller-scale features responsible for localised severe weather, as similarly suggested by Browning and Golding (1995).

Close inspection of the near-surface wind fields (e.g., Figures 4.11 and 4.12) shows that increases in vertical vorticity along the shear zone near the cold pool are attributable both to localised veering and strengthening of near-surface winds just behind the leading edge of the cold pool, and narrowing of the shear zone as a result of the enhanced convergence just ahead of the divergent cold pool. Near the cold pool, the surface front was therefore transformed from one with an initially rather diffuse shear zone, characterised by limited cross-frontal wind veer, a weak pressure trough, and little cross-frontal temperature contrast, into a well-defined front characterised by a large wind veer (near 90°), well-defined pressure trough, strong post-frontal winds and large cross-frontal temperature gradient. Conditions therefore locally met the requirements for tornadic fronts as set by Clark and Parker (2014) (i.e., near-90° wind veer and post-frontal wind speeds of a similar magnitude to, or stronger than, pre-frontal wind speeds), even though, when analysed over a wider region, these requirements were not met.

In this study, it has been suggested that the penetrating dry air was important in promoting sublimation of solid hydrometeors where it undercut part of the wide cold-frontal rainband. Although this aspect is not investigated in detail, the suggestion is consistent with several previous studies of frontal rainbands (e.g., Koch and Kocin, 1991; Browning and Reynolds, 1994; Browning and Golding, 1995; Parker and Thorpe, 1995), post-frontal and ‘dry slot’ convective systems (e.g., Carr and Millard, 1985; Clark, 2011), and quasi-linear convective systems in high-shear, low-CAPE environments more generally (e.g., Johns, 1993). The association of sublimation with local intensification of the front suggests the choice of model microphysics scheme may

have an impact on the evolution, and ultimately on the extent to which tornado-favourable conditions are realised along the surface front, in the model.

Browning and Golding (1995) demonstrated a close link between penetration into the lower troposphere of a small, well-marked dry intrusion, and the formation of an intense squall line that produced two tornadoes in East Anglia. In their case, however, the dry intrusion and associated air of low wet-bulb potential temperature (ϑ_w) overran a shallow layer of high ϑ_w air in the lowest 1 km AGL, resulting in potential instability. The development and intensity of convection was attributed to the release of this potential instability. In contrast, there is no evidence that the dry filament overran pre-frontal air in the current case (e.g., see Figures 4.8 and 4.10) suggesting that, between cases, the mechanisms may differ in detail even when the synoptic to mesoscale setting appears similar. The possible importance of high PV, characteristic of the intruding dry air, has also been discussed by Browning (1999), who suggested it to be instrumental in driving small-scale 'cyclonic events'. In this respect, too, there are similarities with the present case; animated sequences of satellite water vapour imagery are suggestive of local centres of cyclonic rotation near to the dry filaments, especially over central England (not shown). This could also account for the observed local bulging of the front near to the cold pool (e.g., where the forward-relative flow is enhanced on the western flank of a small-scale cyclonic circulation).

Koch and Kocin (1991) drew attention to the importance of a deep region of descent, mid-tropospheric drying, and associated near-surface pressure rises post-front, in promoting marked intensification of a surface front. The pressure rises were associated with an isallobaric wind surge that contributed strongly to cross-frontal contraction processes at low levels, resulting in the sudden development of an intense NCFR. Isallobaric effects have not been considered specifically herein; however, the enhanced divergence in the cold pool, where MSLP was locally increasing in a system-relative frame of reference (e.g., as shown by the developing 'bulge' in the isobars within the cold pool in Figure 4.11) is at least qualitatively consistent with the pattern of winds that would be expected from isallobaric effects.

Doppler radar observations showed, in agreement with previous studies, that tornadoes were associated with miso-scale vortices developing along the frontal shear zone. Comparison of the radar observations, tornado report locations and the 1.5 km

model suggests, in agreement with Smart and Browning (2009) and Clark *et al*. (2021), that tornado-genesis may be favoured within a well-defined vertical vorticity stretching maximum at the up-front flank of the vortex, though evidence of the association is weak in the current case. Although the miso-scale vortex-genesis mechanisms remain, largely, an unresolved question, this association, and the much larger instantaneous magnitudes of the stretching term, relative to the tilting terms, in the vorticity equation near to the modelled vortex, lead to a tentative suggestion that stretching is the more plausible vortex-genesis mechanism. Furthermore, the radar observations show that the vortices forming near the leading edge of the cold pool were 'like-signed' (i.e., all cyclonic). The general absence of cyclonic–anticyclonic vortex pairs could be taken to support the suggestion that tilting is an unlikely explanation for vortex-genesis, since tilting results in cyclonic–anticyclonic vortex pairs; however, as noted by Atkins and St Laurent (2009), cyclonic vortices tend to grow in favour of the anticyclonic vortices, so that they may quickly come to dominate the vertical vorticity field even where tilting is operative. In light of the above considerations, it is concluded that tilting and stretching are both possible vortex-genesis mechanisms in the 20 November 2013 case (i.e., neither can be confidently ruled out). Higher resolution simulations of the current and additional cases are therefore required to provide additional insights into the vortex-genesis mechanisms.

Comparison of the results of the current case with those presented in Chapter 3 suggests that tornadic NCFRs of both types (i.e., frontal wave and north-westerly flow) have certain features in common. Firstly, both analysed events involved the approach of mid- to upper-level jet streaks and associated PV maxima towards the low-level frontal zone, although the configuration of the flow and the orientation of the upper-level features relative to the low-level front varied markedly (for example, the jet streak approached the surface front at a larger angle in the current case). Secondly, tornadoes tended to occur in both events just down-front of the location at which near-surface pressure falls were maximised (near the frontal wave apex on 17 October 2011, and near the triple point of the frontal system underneath the left exit of the upper-level jet streak in the current case). In some respects, both situations could be regarded as examples of secondary cyclogenesis, but in the current case this cyclogenesis was not synoptically evident (i.e., it was not associated with the development of a discrete

secondary cyclone, at the resolution of the operational analyses[29]). Possible reasons for this include weaker or more transient development, or the occurrence of development in a region with large ambient pressure gradients (which would tend to preclude the formation of a closed circulation) or along a part of the front exhibiting large pre-existing curvature (which would tend to preclude the development of an inflection in the front, which is otherwise characteristic of secondary cyclogenesis). A final similarity between analysed cases is that miso-scale vortices (and associated tornadoes) occurred where the frontal shear zone became particularly intense and narrow.

Figure 4.19 (following page): Schematic depicting the main features of a north-westerly flow tornadic NCFR and its environment. (a)-(c) Synoptic-scale evolution over ~24 – 36 hours, from (a), earliest, to (c), latest. 300 hPa wind speed and PV are shown by cyan and pink shading, respectively; darker shades indicate higher values in each case. MSLP is shown by grey contours and surface fronts by bold lines (blue, purple and red for cold, occluded and warm fronts, respectively). As the flow amplifies, trough extension and ridge amplification ('R' in panels (b) and (c)) occur to the east and northwest of the UK, respectively. A jet streak (cyan shading) and associated positive PV anomaly and tropopause fold propagate rapidly south-eastwards in the flow on the rear flank of the upper-level trough; the leading edge of these features gradually begin to overrun the surface front. Surface pressure falls and lower-tropospheric frontogenesis are focused along the cold front underneath the left exit of the jet streak (emphasised by the placing of a second low-pressure centre 'L' near the triple point of the frontal system). (d) Meso-α-scale view showing lower- to middle-tropospheric features of interest underneath the left exit of the jet streak. Local penetration of a dry filament into the lower troposphere occurs in this region, as shown by pockets of dry air immediately behind the surface front (areas of RH < ~70% at 1 km and 2 km AGL are enclosed by thick and thin dashed magenta lines, respectively; larger areas of dry air further rearward of the front are omitted for clarity). Sublimation of precipitation falling into the dry filament is associated with cooling and local downdraft maxima near the tip of the dry filament. The associated surface cold pool is depicted by blue shading. Approximate location of the upper-level jet axis is denoted by the thick, blue dashed line and arrow, and the upper-level PV maximum by pink shading (centre of the PV maximum is marked '+PV'). Bold blue line indicates the surface cold front, and grey shaded areas depict NCFR rainfall cores (darker shading for higher rainfall rates). Various morphological attributes of the NCFR, which vary with distance along-front, are annotated in the panel. (e) Meso-β-scale view showing near-surface features in the region of the penetrating dry filament. Lime green contours depict a region of enhanced near-surface divergence where downdrafts within the cold pool (blue shading) reach the surface and spread out. The NCFR becomes locally intense ahead of the cold pool (as shown by the along-front maxima in rainfall rates) due to the enhanced horizontal convergence and associated enhanced updraft speeds. The narrowing shear zone here is prone meso-ɣ- to miso-scale vortex-genesis, with associated risk of tornadoes. MSLP and surface wind field are shown by blue contours (1 hPa intervals), and magenta vectors, respectively. Grey shading indicates NCFR rainfall cores (darker shades for greater rainfall rates). 'M' denotes the location of a mature meso-ɣ-scale vortex, and red dots are developing miso-scale vortices. 'T' denotes the possible location of a tornado.

[29] In the conceptual model (Figure 4.19), this aspect has been emphasised by the placing of a second low pressure centre ('L') along the front underneath the left exit of the upper-level jet.

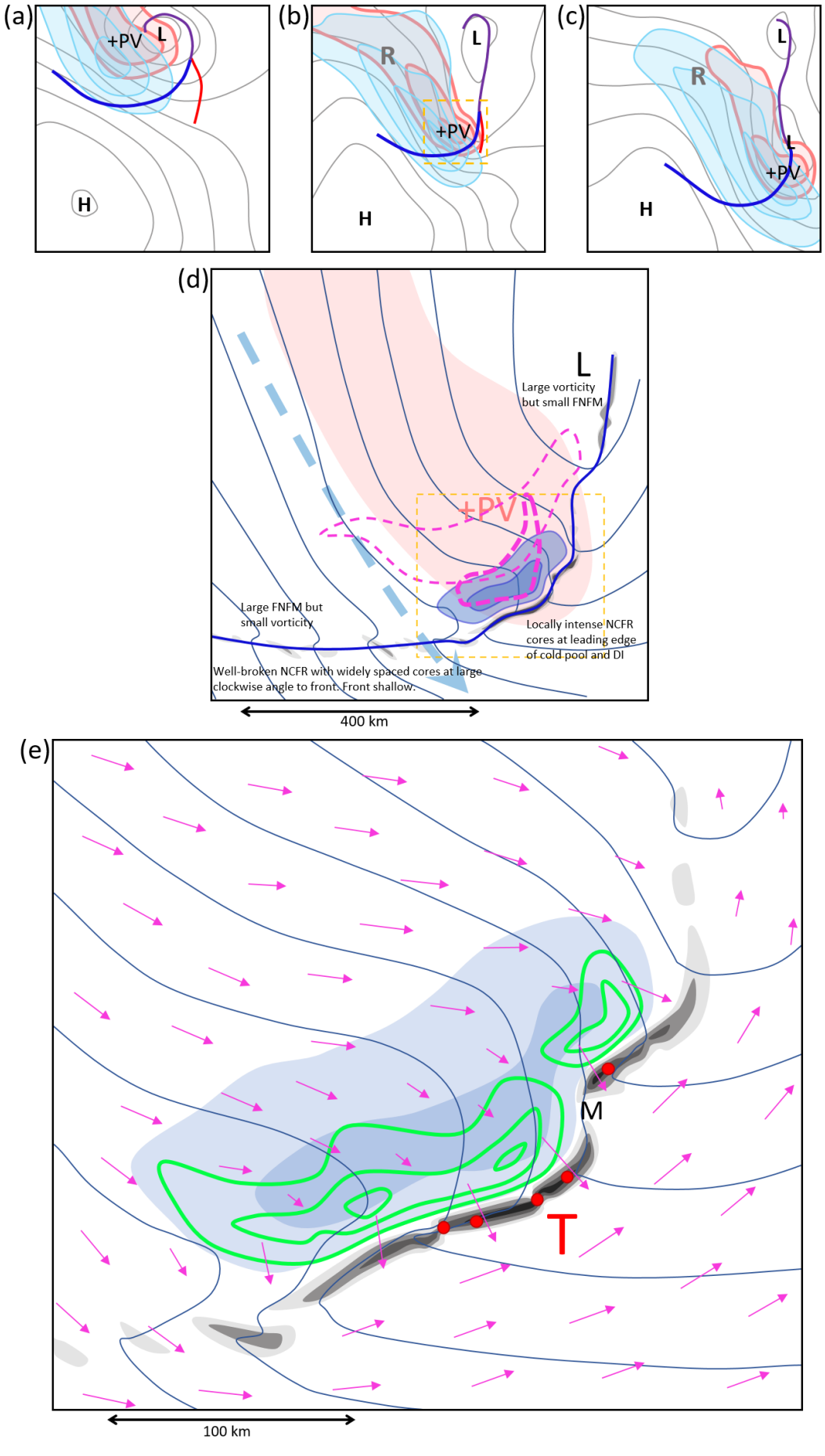
(a)
+PV
L
H
(b)
R
L
+PV
H
(c)
L
R
L
+PV
H
(d)
L
Large vorticity
but small FNFM
+PV
Large FNFM but
small vorticity
Locally intense NCFR
cores at leading edge
of cold pool and DI
Well-broken NCFR with widely spaced cores at large
clockwise angle to front. Front shallow.
400 km
(e)
M
T
100 km

4.7. Conceptual framework

Figure 4.19 provides a multiscale overview of the characteristic features in a north-westerly flow tornadic NCFR. On the synoptic scale, the mid- to upper-level flow exhibits a trough–ridge pattern of relatively large and increasing amplitude. The developments of interest occur on the rear (i.e., western) flank of the longwave upper-level trough, the trough itself being relatively slow-moving. A potent jet streak and associated positive PV anomaly develop upstream and propagate southeast on the rear flank of the trough, elongating slowly in the amplifying flow. At the surface, a depression develops underneath the left exit of the jet streak and moves southeast (for events in the UK, the track of the parent depression is typically to the north of the UK and then southeast or south through the North Sea). The associated frontal system tracks southeast or south, with the speed of advance of the fronts, in the direction normal to their length (i.e., FNFM), tending to increase within the veering and strengthening low- to mid-level flow field.

Over time, the leading edge of the extending jet streak and associated PV anomaly begin to move ahead of the centre of the surface depression, coming into closer proximity to the associated frontal system. Consequently, surface pressure falls and frontogenesis become focussed within a small area of the cold front, underneath the left exit of the jet[30]. Prior to this time, the cold front is likely to be characterised by relatively weak frontogenesis; it may therefore be rather diffuse and not necessarily accompanied by a well-defined surface trough or NCFR in the early stages of development.

On the mesoscale, the subsequent developments, which culminate in locally tornado-favourable conditions along a subsection of the surface cold front underneath the left exit of the jet streak, may be interpreted as an interaction between the overrunning jet streak (and associated features) and the developing transverse circulation at the surface front. The jet streak and PV maximum are associated with an

[30] Although not synoptically evident in the current case, some north-westerly flow cases exhibit a secondary cyclone centre along the cold front here (i.e., as suggested by a closed isobar in surface analysis charts). Attention is drawn to this feature in the conceptual model because surface pressure falls along this section of the front are apparently an important part of the evolution, regardless of whether or not a discrete secondary cyclone eventually forms.

upper-level front and tropopause fold within which dry, high-PV air intrudes into the mid-troposphere. The fold exhibits a dip direction towards the west or southwest (i.e., normal to the jet axis). Some of the dry, high-PV air within the fold begins to overrun the surface front where the extending jet–fold system cuts above the front. In response to the increasing low-level frontogenesis underneath the left exit of the jet streak, the cold front's ageostrophic, front-transverse circulation intensifies and deepens. Within the forward-directed part of this circulation, a filament of dry, high-PV air is extruded from the much larger reservoir of dry, high-PV air in mid- to upper-levels associated with the overrunning tropopause fold. Where the front-transverse circulation is strongest and deepest (i.e., underneath the left exit of the jet streak and near the leading edge of the associated positive PV anomaly), this dry filament eventually reaches the lower troposphere immediately behind the surface front, with dry (< ~70 – 80% RH), high-PV (>1 PVU) air locally penetrating to within 1 km of the surface.

The penetrating dry filament promotes diabatic cooling, due to sublimation or evaporation of hydrometeors, where it undercuts part of the cloud and precipitation associated with the wide cold-frontal rainband. The cooled air descends to the surface and spreads out, resulting in a well-marked cold pool and enhanced near-surface divergence immediately behind the surface front. Near the leading edge of the divergent cold pool, near-surface horizontal convergence is enhanced along the frontal boundary. Consequently, the frontal shear zone narrows and updraft speeds and vertical vorticity increase[31]. The above processes, which culminate in the development of a sharply defined and narrow frontal shear zone near the expanding cold pool, are accompanied by the development of a coherent and locally strong NCFR (again noting that the cold front may be a relatively diffuse feature elsewhere, and more generally prior to intrusion of the dry filament to low levels).

Near the expanding cold pool, meso-γ- to miso-scale vortices develop rapidly along the narrowing, intensifying shear zone. Associated NCFR perturbations typically present as subtle inflections which amplify into S-shaped structures. A reflectivity

[31] Although not demonstrated in the current study, a positive feedback may be envisaged at this stage, in which the enhanced cross-frontal temperature gradients and increased cross-frontal confluence near the leading edge of the cold pool act to further increase the frontogenesis. Associated strengthening of the front-transverse ageostrophic circulation could promote further intrusion of dry air within the filament, increasing evaporative cooling and leading to an even stronger cold pool and near-surface divergence field, with associated intensification of the front near to the leading edge of these features.

minimum often develops near the centre of the inflection in the mature stages of vortex development, resulting in the broken-S signature (McAvoy *et al*., 2000; Grumm and Glazewski, 2004; Lane and Moore, 2006). Some of these vortices spawn small tornadoes. In the context of individual vortices, tornado-genesis appears to be most likely during the period of amplification of the S-shaped inflection in the reflectivity pattern, and just prior to fracture of the NCFR and associated development of the broken-S reflectivity pattern. In the context of the cold pool and dry filament, vortex- and tornado-genesis appears to be most likely during the period that the cold pool is expanding and intensifying.

4.8. Conclusions

In this paper, insights have been provided into the physical mechanisms responsible for generating an environment locally favourable for NCFR tornadoes, in a case belonging to the north-westerly flow type as defined by CP20. The analysed case was selected partly on the basis that it was a good example of its type, lending confidence that the synoptic- to meso-scale setup and evolution have some wider applicability. However, on smaller scales, the evolution and physical mechanisms may vary from case to case. In the current case, the sequence of events may be described as follows:

- An intense jet streak and associated PV maximum and tropopause fold develop within the veering north-westerly flow on the forward flank of an amplifying upper-level ridge, and on the rearward (i.e., upstream) flank of an equatorward-extending upper-level trough.

- Continued amplification facilitates the approach of the leading edge of the jet streak, PV maximum and tropopause fold towards a surface cold front, whereupon the associated dynamic forcing for ascent induces low-level frontogenesis (due to surface pressure falls and associated cross-frontal convergence acting on the low-level baroclinic zone)

- Dry air originating within the tropopause fold becomes involved in the intensifying front-transverse circulation in this region, forming a narrow

filament of dry, high-PV air that eventually penetrates to low levels immediately behind the front, where it undercuts the rearward and upper parts of the frontal cloud band and associated wide frontal rainband.

- Diabatic cooling, due to sublimation or evaporation of precipitation near the leading edge of the penetrating dry filament, leads to the development of a mesoscale cold pool and associated local maxima in downdrafts and near-surface divergence immediately behind the surface front.

- Post-frontal divergence is associated with enhanced convergence and increased updraft speeds along the frontal boundary at the leading edge of the cold pool. The shear zone consequently narrows with formation of a well-defined NCFR.

- Meso-ɣ- to miso-scale vortices develop along the narrowing, intensifying shear zone. Some of the vortices spawn small tornadoes.

Taken together with the results presented in Chapters 2 and 3, this study provides a framework for the operational recognition of synoptic-scale and mesoscale situations favourable for tornadoes along NCFRs. Comparison with Chapter 3 shows that rather different physical mechanisms are at work in this north-westerly flow case than in the frontal wave case of 17 October 2011. This provides additional justification for CP20's definition of two distinct types of tornadic NCFR. However, further studies are required to understand whether these differences hold more generally between the two types of event.

Future work could usefully focus on detailed analysis of the low-level frontal structure and its evolution, in both high-resolution simulations and radar observations, near to overrunning jet streaks and intruding dry filaments in a larger set of cases. This could further clarify the sequence of events leading up to vortex- and tornado-genesis, providing insights that may help to improve operational nowcasting of tornado risk in NCFRs. Additional model simulations, using both 'real data' and idealised setups, would also be beneficial to provide insights into the vortex-genesis mechanisms, and

their variability or otherwise from case to case. Very high-resolution simulations (grid spacing ~50 m or less) will likely be needed to address these aspects.

References

Apsley M, Mulder KJ, Schultz DM. 2016. Reexamining the United Kingdom's greatest tornado outbreak: forecasting the limited extent of tornadoes along a cold front. *Wea. Forecasting* **31**: 853–875.

Atkins NT, St. Laurent M. 2009. Bow echo mesovortices. Part II: Their genesis. *Mon. Wea. Rev.* **137**: 1514–1532.

Best MJ, Pryor M, Clark DB, Rooney GG, Essery RLH, Mènard CB, Edwards JM, Hendry MA, Porson A, Gedney N, Mercado LM, Sitch S, Blyth E, Boucher O, Cox PM, Grimmond CSB, Harding RJ. 2011. The Joint UK Land Environment Simulator (JULES), model description –Part 1: Energy and water fluxes. *Geosci. Model Dev.* **4**: 677–699.

Berggren R. 1952. The distribution of temperature and wind connected with active tropical air in the higher troposphere and some remarks concerning clear air turbulence at high altitude. *Tellus* **4**: 43–53.

Bjerknes J. 1951. Extratropical cyclones. *Compendium of Meteorology*, T. F. Malone, Ed., Amer. Meteor. Soc., 577–598.

Brown PR, Meaden GT. 2014. TORRO tornado division report: November to December 2013. *Int. J. Meteorol. (UK)* **39**: 53–60.

Browning KA. 1999. Mesoscale aspects of extratropical cyclones: an observational perspective. In Shapiro MA, Grønås S (Eds). The life cycles of extratropical cyclones. American Meteorological Society, Boston, MA., pp. 265–283.

Browning KA, Golding BW. 1995. Mesoscale aspects of a dry intrusion within a vigorous cyclone. *Q. J. Roy. Meteor. Soc.* **121**: 463–493.

Browning KA, Harrold TW. 1970. Air motion and precipitation growth at a cold front. *Q. J. Roy. Meteor. Soc.* **96**: 369–389.

Browning KA, Reynolds R. 1994. Diagnostic study of a narrow cold-frontal rainband and severe winds associated with a stratospheric intrusion. *Q. J. Roy. Meteor. Soc.* **120**: 235–257.

Buckingham TJ, Schultz DM. 2020. Synoptic-scale environments and precipitation morphologies of tornado outbreaks from quasi-linear convective systems in the United Kingdom. *Wea. Forecasting* **35**: 1733–1759.

Carbone RE. 1982. A severe frontal rainband. Part I. Stormwide hydrodynamic structure. *J. Atmos. Sci.* **39**: 258–279.

Carbone RE. 1983. A severe frontal rainband. Part II. Tornado parent vortex circulation. *J. Atmos. Sci.* **40**: 2639–2654.

Carr FH, Millard JP. 1985. A composite study of comma clouds and their association with severe weather over the Great Plains. *Mon. Wea. Rev.* **113**: 370–387.

Carroll EB. 1997. Poorly forecast trough disruption shown in water vapour images. *Meteor. Appl.* **4**: 229–234.

Clark MR. 2011. Doppler radar observations of mesovortices within a cool-season tornadic squall line over the UK. *Atmos. Res.* **100**: 749–764.

Clark MR, Parker DJ. 2014. On the mesoscale structure of surface wind and pressure fields near tornadic and nontornadic cold fronts. *Mon. Wea. Rev.* **142**: 3560–3585.

Clark MR, Parker DJ. 2020. Synoptic-scale and mesoscale controls for tornadogenesis on cold fronts: A generalised measure of tornado risk and identification of synoptic types. *Q. J. Roy. Meteor. Soc.* **146**: 4195–4225.

Clark MR, Parker DJ, Hanley KE. 2021. Synoptic-scale and mesoscale controls for tornadogenesis on cold fronts: shear-zone vortex-genesis in a developing frontal wave. *Q. J. Roy. Meteor. Soc.*, under review.

Clark M, Smart D. 2016. Supercell and non-supercell tornadoes in the United Kingdom and Ireland. *Extreme Weather. Forty years of the Tornado and Storm Research Organisation (TORRO),* R. K. Doe, Ed., Wiley Blackwell, Chichester, UK, 31–59.

Danielsen EF. 1968. Stratospheric–tropospheric exchange based on radioactivity, ozone and potential vorticity. *J. Atmos. Sci.* **25**: 502–518.

Davies T, Cullen, MJP, Malcolm AJ, Mawson MH, Staniforth A, White AA, Wood N. 2005. A new dynamical core for the Met Office's global and regional modelling of the atmosphere. *Q. J. Roy. Meteor. Soc.* **131**: 1759–1782.

Davis JM, Parker MD. 2014. Radar climatology of tornadic and nontornadic vortices in high-shear, low-CAPE environments in the mid-Atlantic and southeastern United States. *Wea. Forecasting* **29**: 828–853.

Edwards J, Slingo A. 1996. Studies with a flexible new radiation code. Part I: Choosing a configuration for a large-scale model. *Q. J. Roy. Meteor. Soc.* **122**: 689–719.

Georgiev CG, Santurette P. 2009. Mid-level jet in intense convective environment as seen in the 7.3 μm satellite imagery. *Atmos. Res.* **93**: 277–285.

Grumm RH, Glazewski M. 2004. Thunderstorm types associated with the 'broken-S' radar signature. *Preprints, 22nd Conf. on Severe Local Storms*, 4–8 October 2004, Myannis, MA. American Meteorological Society: MA, USA.

Hobbs PV, Persson P. 1982. The mesoscale and microscale structure and organization of clouds and precipitation in midlatitude cyclones. Part V: The substructure of narrow cold-frontal rainbands. *J. Atmos. Sci*. **39**: 280–295.

Houze RA, Hobbs PJ Jr., Biswas KR, Davis WM. 1976. Mesoscale rainbands in extratropical cyclones. *Mon. Wea. Rev.* **104**: 868–878.

James PK, Browning KA. 1979. Mesoscale structure of line convection at surface cold fronts. *Q. J. Roy. Meteor. Soc.* **105**: 371–382.

Johns RH. 1993. Meteorological conditions associated with bow echo development in convective storms. *Wea. Forecasting* **8**: 294–299.

Keyser D, Shapiro MA. 1986. A review of the structure and dynamics of upper-level frontal zones. *Mon. Wea. Rev.* **114**: 452–499.

Koch SE, Kocin PJ. 1991. Frontal contraction processes leading to the formation of an intense narrow rainband. *Meteorology and Atmospheric Physics* **46**: 123–154.

Lane JD, Moore PD. 2006. Observations of a non-supercell tornadic thunderstorm from terminal Doppler weather radar. *Preprints, 23rd Conf. Severe Local Storms*, St. Louis, MO. American Meteorological Society: MA, USA.

Locatelli JD, Hobbs PV. 1974. Fall speeds and masses of solid precipitation particles. *Journal of Geophysical Research* **79**: 2185–2197.

Lock AP, Brown AR, Bush MR, Martin GM, Smith RNB. 2000. A new boundary-layer mixing scheme. Part I: Scheme description and single-column model tests. *Mon. Wea. Rev.* **128**: 3187–3199.

Matejka TJ, Houze RA Jr., Hobbs PV. 1980. Microphysics and dynamics of clouds associated with mesoscale rainbands in extratropical cyclones. *Q. J. Roy. Meteor. Soc.* **106**: 29–56.

McAvoy BP, Jones WA, Moore PD. 2000. Investigation of an unusual storm structure associated with weak to occasionally strong tornadoes over the eastern United States. *Preprints, 20th Conf. Severe Local Storms,* Orlando, FL. American Meteorological Society: MA, USA, 182–185.

Mulder KJ, Schultz DM. 2015. Climatology, storm morphologies, and environments of tornadoes in the British Isles: 1980–2012. *Mon. Wea. Rev.* **143**: 2224–2240.

Parker DJ, Thorpe AJ. 1995. The role of snow sublimation in frontogenesis. *Q. J. Roy. Meteor. Soc.* **121**: 763–782.

Reed RJ. 1955. A study of a characteristic type of upper-level frontogenesis. *Journal of Meteorology* **12**: 226–237.

Reed RJ, Danielsen EF. 1959. Fronts in the vicinity of the tropopause. *Arch. Meteor. Geophys. Bioklim.*, A11, 1–17.

Reed RJ, Sanders F. 1953. An investigation of the development of a mid-tropospheric frontal zone and its associated vorticity field. *Journal of Meteorology* **10**: 338–349.

Sanders F. 1988. Life history of mobile troughs in the upper westerlies. *Mon. Wea. Rev.* **116**: 2629–2648.

Sansom HW. 1951. A study of cold fronts over the British Isles. *Q. J. Roy. Meteor. Soc.* **77**: 96–120.

Schultz DM, Sanders F. 2002. Upper-level frontogenesis associated with the birth of mobile troughs in northwesterly flow. *Mon. Wea. Rev.* **130**: 2593–2610.

Schultz DM, Schumacher PN. 1999. The use and misuse of Conditional Symmetric Instability. *Mon. Wea. Rev.* **127**: 2709–2732.

Shapiro MA. 1982. Mesoscale weather systems of the central United States. CIRES/NOAA Tech. Rep., University of Colorado, 78 pp.

Smart DJ, Browning KA. 2009. Morphology and evolution of cold-frontal misocyclones. *Q. J. Roy. Meteor. Soc.* **135**: 381–393.

Tang Y, Lean HW, Bornemann J. 2012. The benefits of the Met Office variable resolution NWP model for forecasting convection. *Meteor. Appl.* **20**: 417–426.

Uccellini LW, Kocin PJ. 1987. The interaction of jet streak circulations during heavy snow events along the east coast of the United States. *Wea. Forecasting* **2**: 289–308.

Wilson DR, Ballard SP. 1999. A microphysically based precipitation scheme for the UK Meteorological Office Unified Model. *Q. J. Roy. Meteor. Soc.* **125**: 1607–1636.

Chapter 5: Further Interpretation, Discussion and Conclusions

In this chapter, a summary of the results detailed in Chapters 2 – 4 will be given, along with a critical discussion of the limitations of the work. The wider implications of the results will also be explored, bringing in ideas from additional case studies and existing conceptual models. Further interpretation of the results will be provided in light of these additional case studies and related observations. Finally, a set of priorities for future research into tornadoes on narrow cold-frontal rainbands will be offered.

5.1 Summary of results, including new insights and analysis techniques

In the preceding chapters, the current understanding of NCFR tornadoes has been summarised, and then extended by analysis of a large set of NCFRs, leading to the identification of environmental parameters that have skill in discriminating between tornadic and non-tornadic events. Furthermore, two distinct types of tornadic NCFR have been identified: frontal wave and north-westerly flow. One example of each type has been explored in detail using high-resolution model simulations and observations, demonstrating the existence of physical links across a wide range of spatiotemporal scales. The results show that, via these links, the synoptic- and meso-α-scale settings strongly constrain the timing and location along the front of meso-ɣ- to miso-scale vortex-genesis and associated tornado-genesis. The case studies suggest that the nature of the links across scales, and possibly the vortex-genesis mechanisms themselves, differ between event types, which partly justifies the definition of the different tornadic event classes, but also has implications for the operational approach when attempting to forecast NCFR tornado risk in the different event types.

Environmental parameters were evaluated using a bulk measures approach, also developed as part of the current work, in which relevant parameter values (e.g., the along- and cross-front wind components, u' and v') are analysed within the air masses on each side of the front, at a set front-normal distance, $\Delta y'$. Where applicable, finite differences are calculated between values at corresponding points on each side of the front (e.g., $-\Delta u'/2\Delta y'$ for bulk shear vorticity), rather than gradients being calculated at a single point on the front itself[32]. The derived values are insensitive to small errors in the analysed location of the front, and to small-scale variability along the frontal

[32] The exception is total frontogenesis which, for simplicity, was calculated at the on-front points.

boundary itself (relevant when using higher-resolution datasets, as demonstrated in the case studies), which might otherwise mask the along-front variability on synoptic- to meso-α-scales.

Of 22 analysed parameters, a bulk measure of shear vorticity, and the front-normal wind component on the cold side of the front, $-v'_{cold}$ (which is strongly positively correlated with FNFM i.e., the speed of advance of the front), yield the best discrimination between non-tornadic and tornadic events; both parameters show significantly larger values in tornadic events (at the 99% level). In other words, tornadic NCFRs tend to have a stronger front-normal component of post-frontal flow, advance more rapidly, and have larger vertical vorticity, than non-tornadic NCFRs. These attributes were even more apparent in the high-tornadic cases (i.e., NCFRs producing outbreaks of ≥7 tornadoes). For the first time, a composite parameter describing NCFR tornado probability, *p*[TN], has been obtained, using the distribution of points within the two-dimensional parameter space defined by shear vorticity and $-v'_{cold}$. The ability of this parameter to identify tornado-favourable time periods and subsections of the front in individual events has been demonstrated (e.g., Figures 2.10, 3.3 and 4.7). *p*[TN] has already been trialled during the winters of 2018-19 and 2019-20 by operational meteorologists at the Met Office, identifying a high probability of tornadoes over southeast England on 29 February 2020, which verified when a tornado occurred in Kent (Matthew Lehnert, Pers. Com.). However, these trials also revealed an important tornado-genesis failure mechanism not captured by *p*[TN], as discussed subsequently.

Improved operational recognition of NCFR tornado-favourable environments is also facilitated by the conceptual models, developed for each of the identified types of tornadic NCFR (Chapters 3 and 4). The conceptual models complement *p*[TN] in that they allow forecasting by pattern recognition i.e., they provide a qualitative approach that may be used in parallel with *p*[TN]. The conceptual models allow the tornado-prone region(s) to be described relative to features already displayed in forecast surface charts, and they provide a way of fitting these events within the context of existing conceptual models for cyclogenesis and cyclone life cycles, as discussed subsequently.

In summary, an overriding aim of this work has been to address the gap in our current understanding of NCFR tornado environments, as compared to that of supercell tornadoes. By providing diagnostics and other tools tailored specifically to NCFRs, the

current work represents a substantial step forward in addressing this knowledge gap, and in providing a possible way forward for the operational forecasting of these events.

5.2 General limitations of the study

The main limitation of the study as a whole, notwithstanding the large number of analysed cases, is the relatively short period from which cases were drawn (10 years, except for the high-tornadic cases, for which events back to 1979 were additionally included), and the relatively small number of cases fitting each identified tornadic NCFR type. The record of tornadoes in the UK and Ireland is comprehensive back to at least the 1970s, thanks to the work of TORRO (albeit, subject to the normal limitations of such records e.g., Doswell and Burgess, 1988; Feuerstein *et al.*, 2005). Over the period of the reliable record, large variability is apparent in tornado frequency on annual to decadal timescales. Since the current study encompasses a period of only 11 years (2004 – 2014, inclusive), this raises questions as to how representative the chosen period is in context of the longer record. Burt (2021) showed that a marked decrease in the annual number of thunderstorm days in southern England since ~2005 is related to a reduction in the frequency of occurrence of certain large-scale flow patterns; it seems plausible that similar variability may exist for the large-scale regimes associated with tornadic NCFRs of each type. These considerations suggest that a very long period of study (at least several decades) would be required to properly quantify the long-term frequency of events, and to be confident that all possible event types have been identified.

A further limitation is that in-depth analysis has only been performed for one tornadic NCFR of each type. Each case was chosen as appearing typical of its class, but detailed analysis of more cases is required, since the vortex-genesis mechanisms, and possibly the nature of the physical links across the spatiotemporal scales, may vary between events of the same type[33]. A related question is whether it is possible for the various mechanisms, as identified in the two case studies, to occur together within a

[33] However, preliminary analysis of 1.5 km model fields for additional frontal wave events (not shown) reveals similarities to the 17 October 2011 case analysed herein, in terms of the along-front variability of key parameters and the sub-structure of individual shear zone vortices (in particular, the vertical vorticity stretching maximum on their up-front flank).

single event. Suggestive of this possibility is the frequent presence of meso-β-scale perturbations superimposed on the meso-α- to synoptic-scale perturbation associated with the secondary or parent cyclone (an example is shown in Figure 5.1; see also Figures 3 and 4 of CP14). Although, as shown in Chapter 3, such perturbations may result from the upscale growth and merger of vortices along the shear zone, another possible cause is localised post-frontal wind maxima (e.g., Wakimoto and Bosart (2000); CP14; Chapter 4). Mesoscale bulges superimposed on a frontal wave could therefore be indicative of localized intrusion of dry air, with associated local cool pools and $-v'_{cold}$ maxima, in these cases too. Another possibility is topographic influences: it is not uncommon to observe NCFR bulges over or downwind of major estuaries or bays (an example is shown in Figure 5.2), perhaps owing to the differing surface roughness values over sea and land, which could result in local differences in $-v'_{cold}$ within the boundary layer. Detailed observational and modelling studies of further NCFRs would therefore also be useful for improving our understanding of the range of mechanisms responsible for the development of meso-β-scale perturbations along NCFRs.

5.3 Further interpretation of the results

5.3.1 Meso-β-scale NCFR perturbations and implications for localised release of HSI

The meso-β-scale perturbations described in the previous section are of potential significance to vortex- and tornado-genesis, because small changes in the angle of the frontal boundary, relative to the pre- and post-frontal wind fields on larger scales, may alter the balance of vertical vorticity and horizontal convergence at the boundary, as may be demonstrated using idealised flow fields (Figure 5.3). The along-front variability associated with these features is generally not resolved in the bulk parameter values in the current work (recalling the typical along-front spacing of points is ~110 km). Nevertheless, such perturbations could help to dictate where and when vortex-genesis by the release of HSI occurs, as for the larger-scale perturbations associated with a frontal wave, as described in Chapter 3.

Strong anecdotal evidence of such localised release of HSI is occasionally found in radar observations (e.g., Figures 1.10 and 5.4). In the latter example, individual NCFR elements (i.e., rainfall cores) move slowly up-front relative to the meso-β-scale

NCFR bulge. Given the configuration of vertical vorticity and horizontal convergence in the idealised fields (Figure 5.3), an individual NCFR element rounding the apex of the bulge and moving towards its northern flank would experience decreases in horizontal convergence, and increases in vertical vorticity; such an evolution could support release of HSI near the apex of the bulge, assuming the horizontal convergence to be large enough, relative to the vertical vorticity, to supress the release on the southern flank of the bulge. It is noticeable that NCFR fractures develop close to the apex of the bulge in Figure 5.4, where most of the tornadoes were also reported, suggestive of the release of HSI. Furthermore, the NCFR is generally intense and close to two-dimensional (i.e., few perturbations and gaps) on the southern flank of the bulge, where the horizontal convergence would be expected to be large relative to the vertical vorticity, following Figure 5.3. Future work might therefore usefully focus on these smaller-scale NCFR perturbations, in order to better understand how they may impact upon the location and timing of release of HSI.

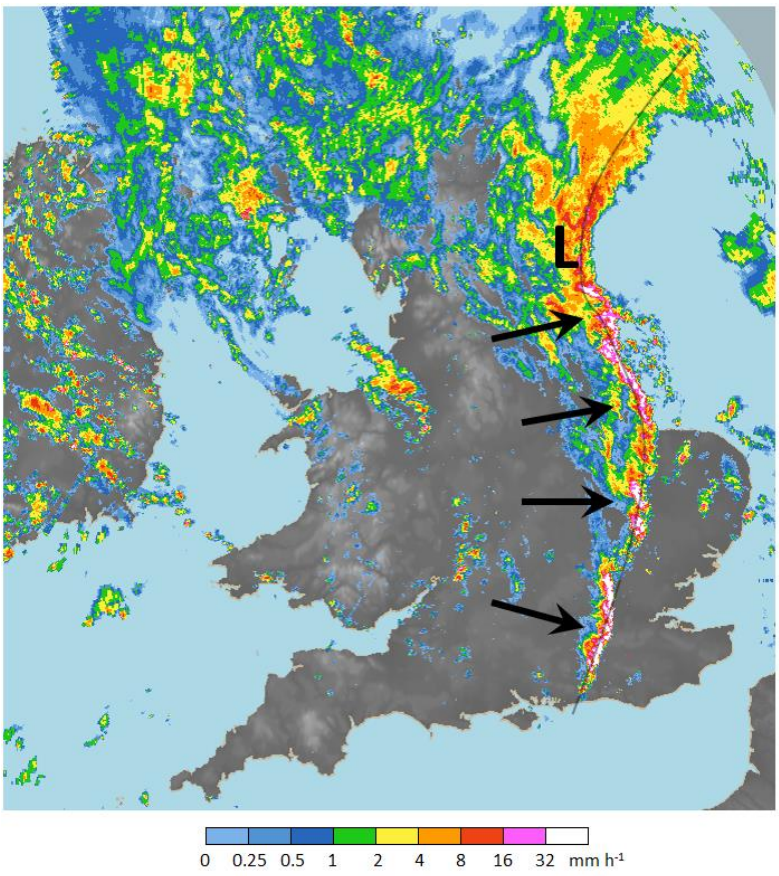

Figure 5.1: Composite radar imagery at 1330 UTC 10 August 2014, showing embedded meso-β-scale NCFR bulges (arrowed) superimposed on the meso-α-scale perturbation associated with the parent cyclone (as traced by the transparent grey line). 'L' denotes centre of parent cyclone.

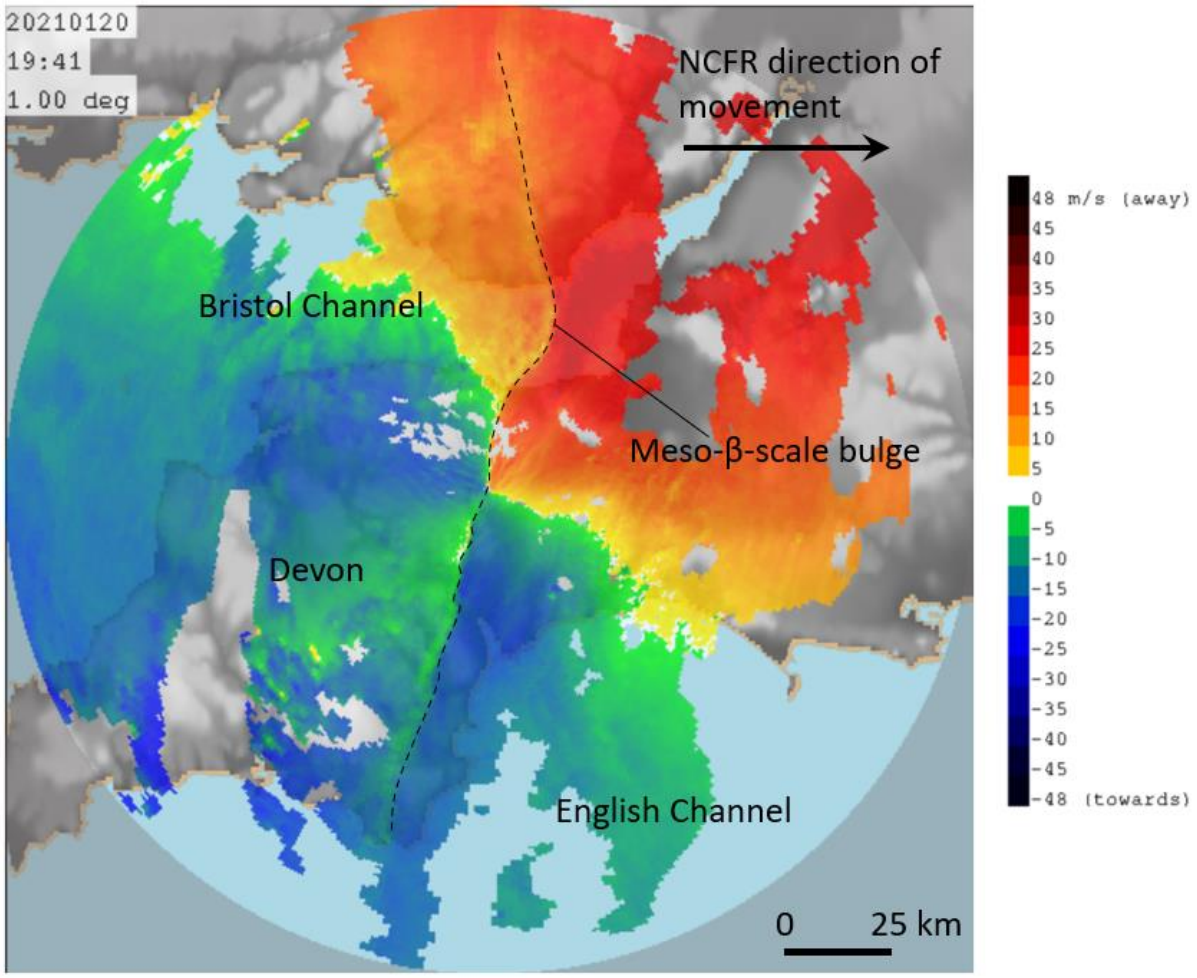

Figure 5.2: Radial velocities from a 1° elevation-angle scan of the Cobbacombe Cross, Devon, Doppler radar at 1941 UTC 20 January 2021, showing a meso-β-scale bulge, over the Bristol Channel, in the line of strong radial velocity gradients (dashed line) collocated with an NCFR moving eastwards across the region.

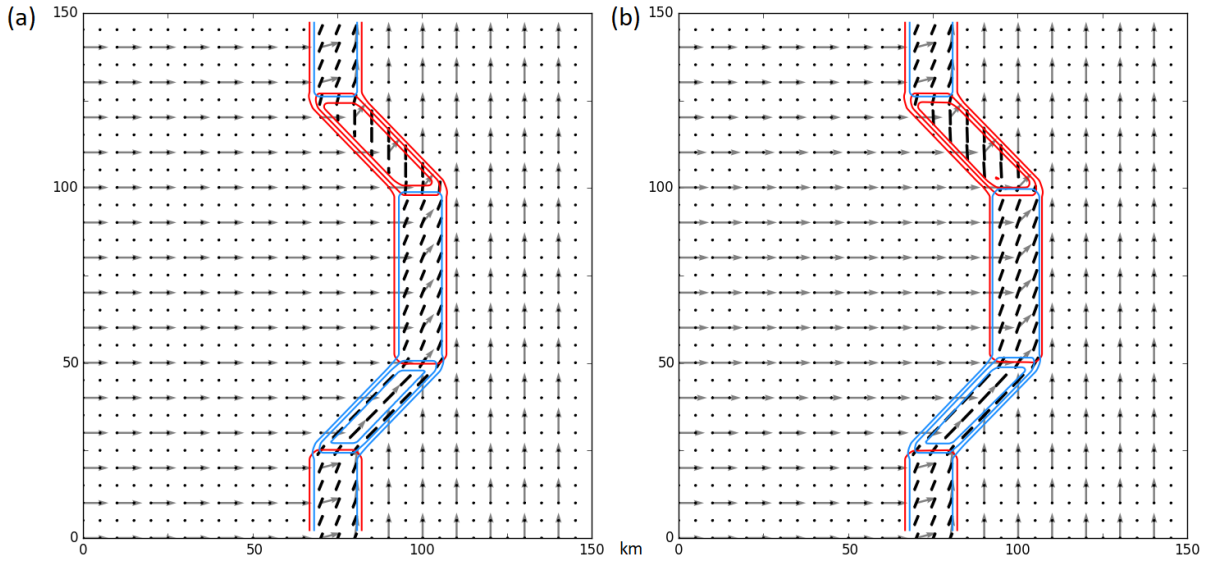

Figure 5.3: Idealised flow fields depicting a meso-β-scale bulge superimposed on a frontal shear zone of width 15 km, illustrating the variation in vertical vorticity (red contours at intervals of 4 x 10^{-4} s^{-1}, starting at 3 x 10^{-4} s^{-1}) and horizontal convergence (blue contours at intervals of 4 x 10^{-4} s^{-1}, starting at 5 x 10^{-4} s^{-1}) on opposite flanks of the bulge. The frontal boundary is characterised by a 90° wind veer, with pre-frontal winds parallel to the unperturbed boundary, and pre-frontal wind speed = post-frontal wind speed = 10 m s^{-1} (i.e., CP14's tornado-favourable wind configuration, which approximates well to the observed wind fields in the 29 November 2011 case illustrated in Figure 5.4). The unperturbed boundary therefore contains both positive vertical vorticity and horizontal convergence, with vertical vorticity = horizontal convergence. In (a), pre- and post-frontal wind fields are uniform over the whole domain. In (b), an additional perturbation post-frontal, front-normal wind of 2 m s^{-1} has been added behind the bulging section of the shear zone, decreasing linearly to zero away from the bulging section (this perturbation cross-frontal flow could generate the depicted bulge, which protrudes 25 km forward of the unperturbed boundary, in ~3.5 hours, assuming a strong correlation between $-v'_{cold}$ and FNFM, as found in Chapter 2). Note that the perturbation wind, even though relatively large (20% of the unperturbed post-frontal wind speed) has little impact on the overall pattern of vertical vorticity and horizontal convergence on the flanks of the bulge (*cf.* panels (a) and (b)). Black dashes lie parallel to the axis of dilatation, with length proportional to the resultant deformation. Grey arrows are the wind vectors.

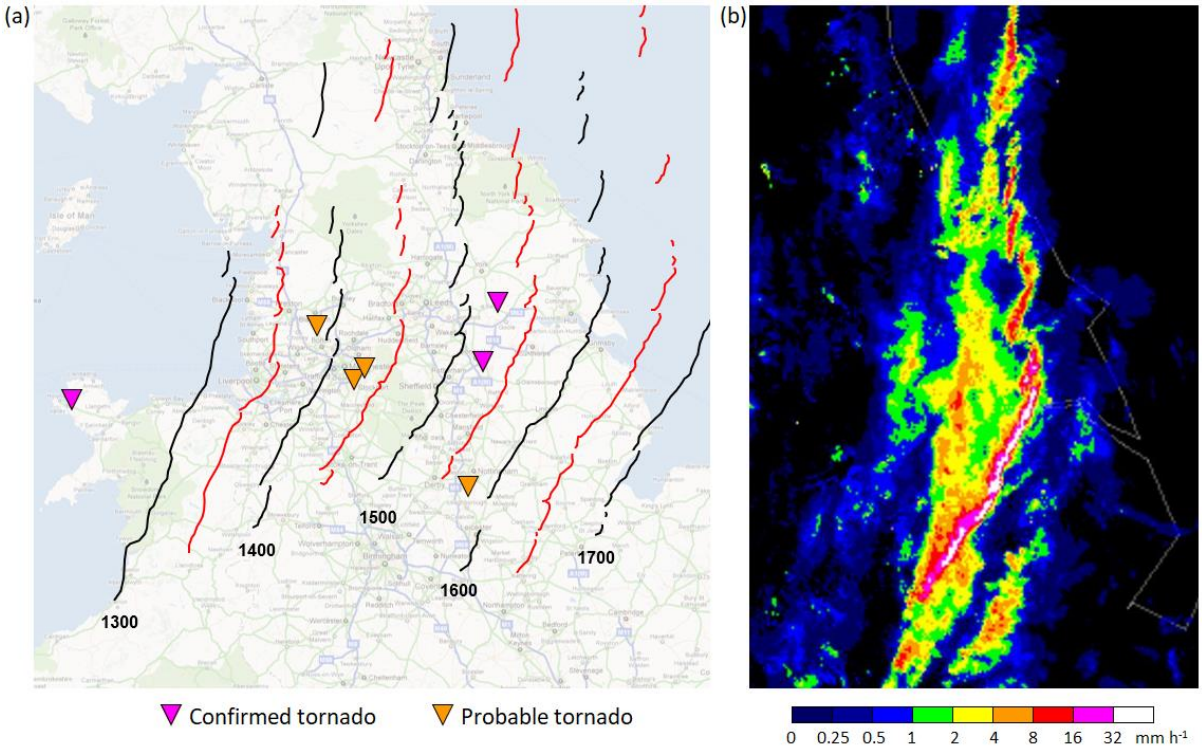

Figure 5.4: A meso-β-scale NCFR bulge over northern England on 29 November 2011. (a) Subjectively analysed positions of NCFR elements (i.e., precipitation cores) at 30-minute intervals over the period 1300 – 1700 UTC (black and red lines). Tornado reports are shown by the inverted triangles. (b) Composite radar rainfall imagery at 1530 UTC, showing the wide cold-frontal rainband and embedded NCFR.

5.3.2 Geometry of frontal troughs and links with the results of CP14

Consideration of the basic geometry of frontal troughs, and the associated distribution of geostrophic wind fields, provided further insight into the results of CP14, in that fronts exhibiting CP14's 'type A' structure, characterised by large vorticity and wind speed ratios near 1.0 (where the ratio is defined as the wind speed at the cold air point divided by that at the warm air point), were shown to occur when the frontal trough is deep *and* orientated nearly normal to the background flow (as discussed in Section 2.4.1). On the other hand, troughs of CP14's 'type B' structure were found to arise when the trough is deep but is positively tilted with respect to the background flow (these characteristics may be further illustrated using simple MSLP and associated geostrophic flow fields, in which a frontal trough is superimposed on uniform background flow, and the depth of the trough and relative direction of the large-scale flow are varied; Figure 5.5). Furthermore, in frontal wave events, it was shown that 'type A' troughs tend to arise just down-front of the wave centre, where an initially

positively tilted front rotates cyclonically relative to the large-scale flow, whereas ‘type B’ troughs are more characteristic of trailing fronts far from the wave centre, where rotation is in the opposite sense (Figure 2.13(d)). Given that tornadoes tend to occur just down-front of the wave centre, this is consistent with CP14’s finding that tornadic NCFRs are generally associated with ‘type A’ troughs.

The results of CP14 are confirmed to hold generally for the set of events analysed herein, by consideration of the variation of the angle between the front and the mean flow, within the shear vorticity versus wind speed ratio parameter space (Figure 5.6(a)); for positive shear vorticity, the angle between the front and the large-scale flow is strongly stratified by the wind speed ratio; for given (positive) shear vorticity, the angle between the front and the large-scale flow tends to increase as the wind speed ratio increases. Furthermore, for given shear vorticity, the tornadic points tend to be associated with larger values of wind speed ratio and a greater angle between the front and the mean flow than non-tornadic points (i.e., troughs closer to the ‘type A’ structure, in agreement with CP14; although, when shear vorticity is particularly large, some tornadic events show wind speed ratios as low as 0.4 – 0.5). The association of well-marked ‘type A’ troughs (i.e., large shear vorticity and wind speed ratio near 1.0), with relatively strong post-frontal winds also becomes apparent by analysis of the variation of wind speed ratio within the shear vorticity versus $-v'_{cold}$ parameter space (Figure 5.6(b)). Since NCFRs are usually associated with well-marked frontal troughs, the differences between ‘type A’ and ‘type B’ troughs tend to be easily seen in surface analysis charts (e.g., Figure 5.7), and so the trough type is found to be a useful proxy for the relative risk of tornadoes in NCFR-bearing fronts.

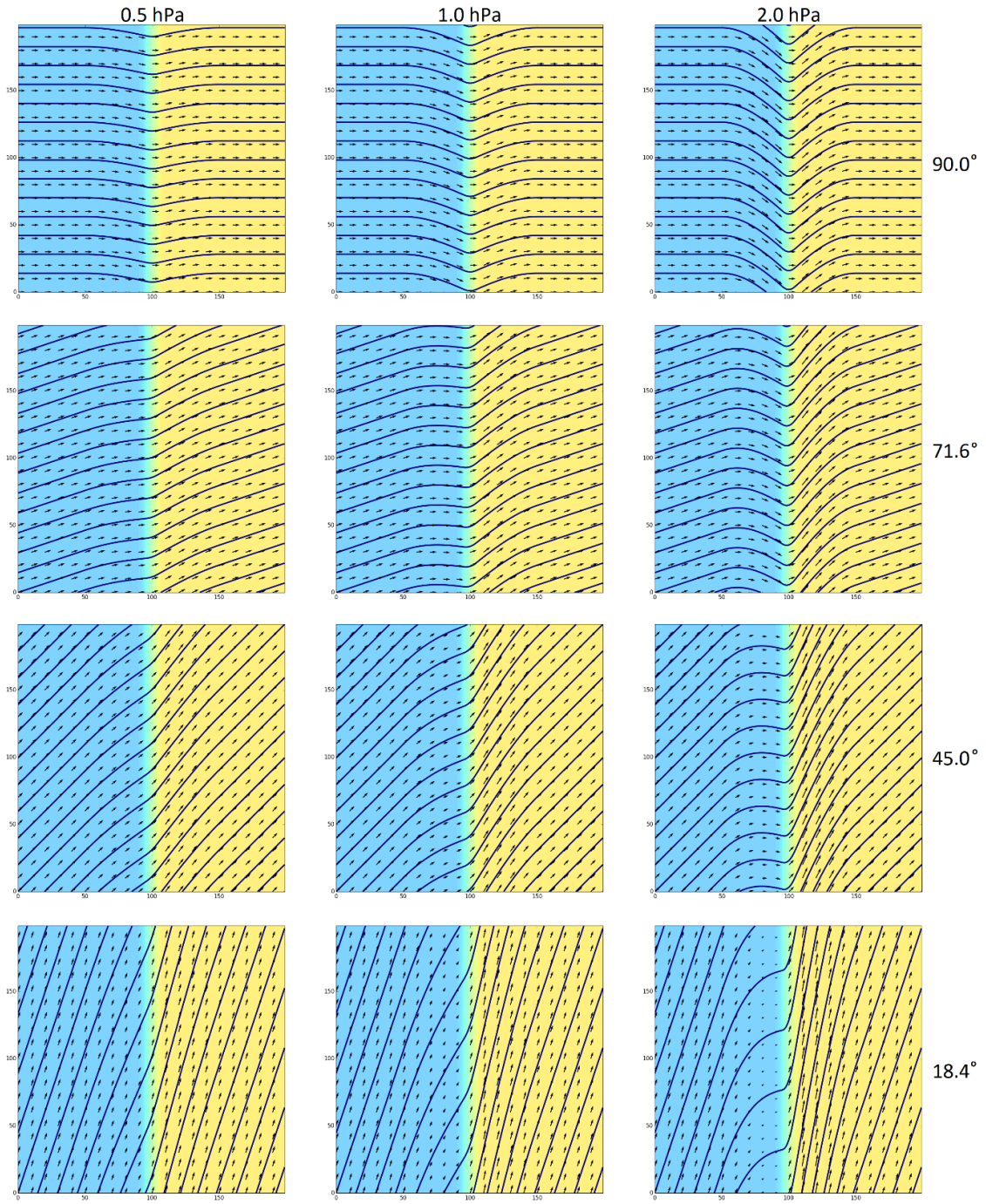

Figure 5.5: Idealised MSLP (navy blue contours) and geostrophic wind (vectors) fields showing the dependency of the trough geometry and associated flow structure on the trough depth and orientation, relative to the large-scale flow. The trough has fixed width and a cross-sectional profile as described by the equation in bullet point (2) of Appendix E. The trough depth is constant in each column of panels and increases towards the right-hand side within each row. Trough depth is defined as the pressure deficit, relative to the background, at the trough axis, as indicated at the top of each column. The angle between the front and the large-scale flow (indicated to the right of each row) is constant within each row of panels and decreases towards the bottom row within each column. Shading is included to illustrate, schematically, the cross-frontal temperature differences (blue for the cold air mass, yellow for the warm air mass).

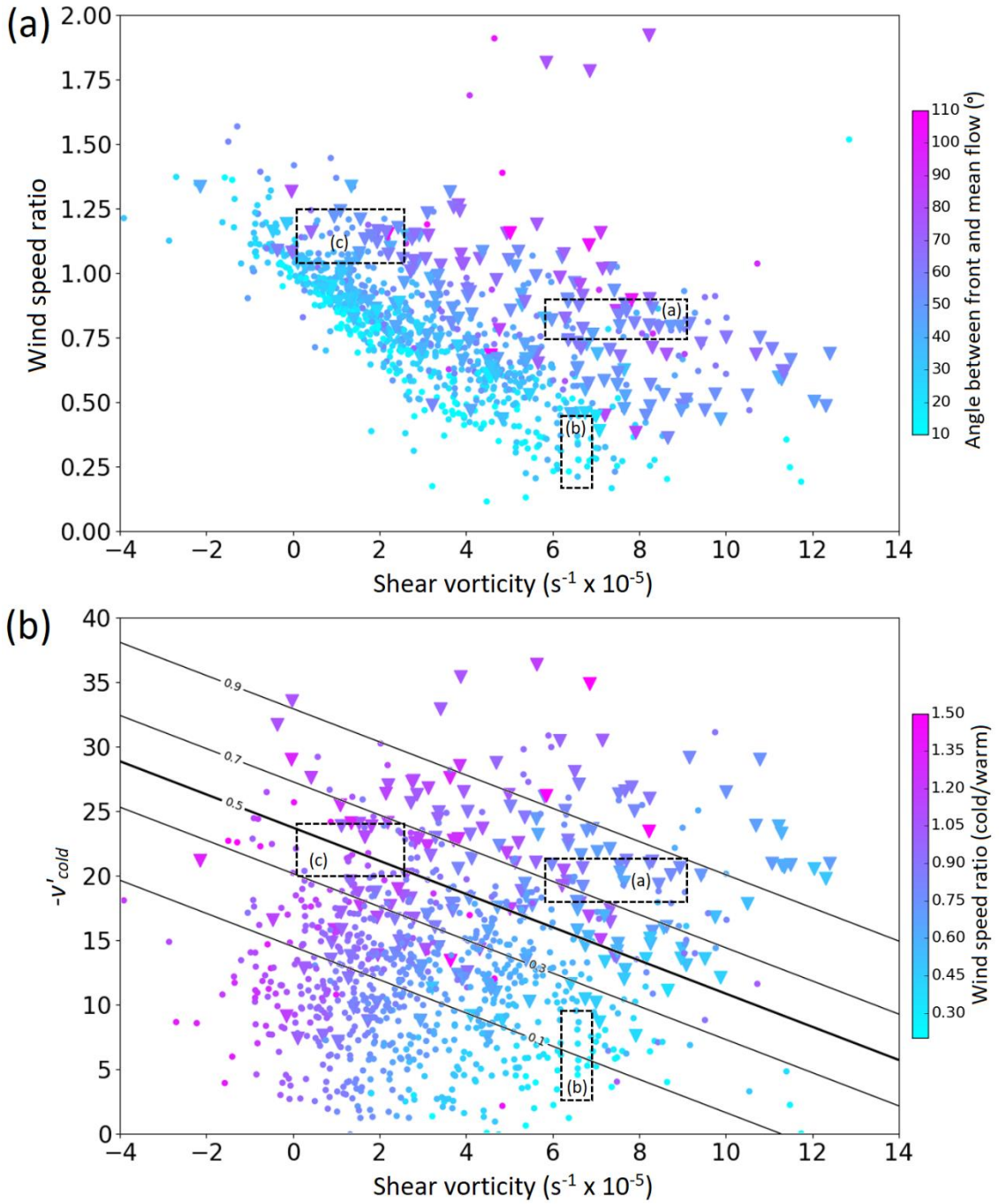

Figure 5.6: Scatterplots of tornadic and non-tornadic points in the two-dimensional parameter space defined by (a) Shear vorticity and wind speed ratio, coloured by the angle between the front and the mean flow, and (b) Shear vorticity and $-v'_{cold}$, coloured by wind speed ratio. Dashed boxes indicate the range of values, within the two-dimensional parameter space, for analysis points situated along the highlighted sections of the example fronts shown in Figure 5.7 (the letters correspond to the panel numbers in that figure). For non-tornadic points, all analysis points over UK and Ireland land areas are shown (rather than only those where the front exhibited an NCFR, as in Figure 2.3(a)), since the variability across the domain is best seen using the larger dataset. However, the *p*[TN] isolines in (b) relate to the dataset used in Chapter 2 (i.e., calculated using only those non-tornadic points over UK and Ireland land areas with an NCFR) so that the position of the example cases can be seen in the *p*[TN] parameter space, as originally defined.

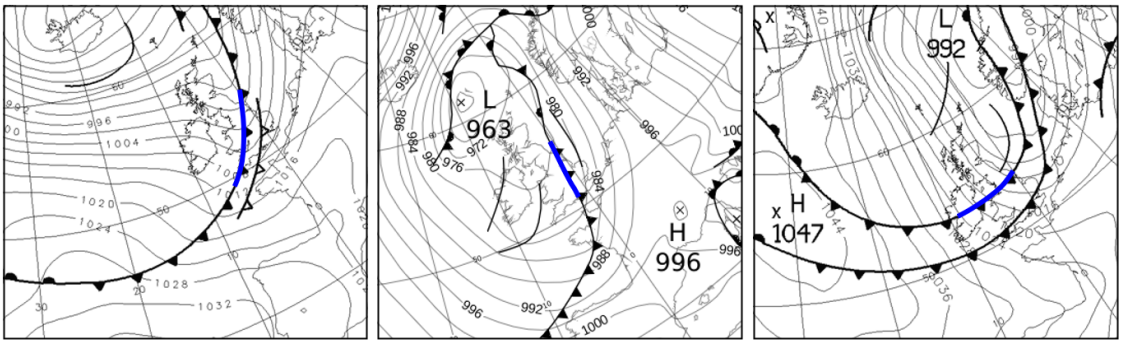

(a) 0000 UTC 28 December 2004 (b) 0000 UTC 1 November 2012 (c) 1200 UTC 24 November 2005

Figure 5.7: Surface analysis charts for example cases situated within different areas of the two-dimensional parameter spaces shown in Figure 5.6. Cases (a) and (c) are examples of CP14's 'type A' troughs (though with relatively weak shear vorticity (i.e., CP14's sub-type 'A_{sv}') in the latter case), and case (b) is an example of CP14's 'type B' troughs. The sections of front corresponding to the values plotted in Figure 5.6 (dashed boxes in that figure) are highlighted by the bold, blue lines.

5.3.3 Relationship between the identified tornadic NCFR types and 'triple point' tornado outbreaks

One type of tornadic NCFR not studied in detail herein, but mentioned in passing in Chapters 2 and 3, is that associated with a prominent meso-β-scale depression (hereafter mesolow), embedded within a cold front or occlusion. Events of this type are now discussed further, in part to complete the survey of all known types of tornadic NCFR in the UK, but also to consider how these events relate to the types identified in the current work. Existing case studies (e.g., Clark, 2012; Young and Clark, 2018) show the mesolow has a diameter of ~30 – 60 km and is therefore intermediate in scale between the meso-ɣ- to miso-scale shear-zone vortices (diameters 1 – 10 km) and most secondary cyclones (wavelength ~1000 km). In Clark (2012), the mesolow and associated tornadoes developed close to the left exit of a mid-level jet streak (therefore having some similarities with the north-westerly flow cases described herein).

As the mesolow develops, the NCFR becomes distorted, leading to a broken-S radar signature. This subsequently evolves into a long-lived hook-shaped echo at the northwest flank of the mesolow, as the southern half of the 'S' fractures and dissipates. Tornadoes occur in association with misoscale vortices forming near the inner, concave edge of the hook-shaped echo, with individual vortices rotating around the west and southwest flanks of the mesolow before dissipating. Tornadoes therefore tend to be distributed along a single, extended track of damage following the track of the mesolow

(this may be contrasted with the development, as shown in Chapter 3, of miso-scale vortices along a much wider swath of the front down-front of a meso-α-scale frontal wave). In the context of the present work, it has been suggested that these cases may represent a sub-type of the frontal wave class, in which the scale of secondary cyclogenesis is unusually small.

It interesting to consider how so-called 'triple point' tornadoes and tornado outbreaks (e.g., Meaden, 1991; Pike, 1992, 1993), relate to the above-mentioned mesolow cases, and to the event types identified in the current study. Pike (1993) analysed several cases and, although not all were associated with NCFRs along well-defined frontal systems (some being associated with more cellular convection in warm-season 'thundery lows'), tornadoes were generally noted to occur within ~100 km of the analysed triple point (i.e., the point of occlusion in surface analysis charts), and usually along the cold front. Furthermore, small secondary depressions were sometimes noted near the triple point, reminiscent of the mesolows in the above-mentioned cases. These attributes suggest that some of these events are likely to be examples of frontal wave tornadic NCFRs (indeed, the events of 21 September 1982 and 25 December 1990, two of Pike's (1993) analysed cases, both appear in the set of high-tornadic cases defined here, and the former is listed in Section 2.3.8 as one of the eight events conforming most closely to the frontal wave type).

Classification of an event as 'triple point' or otherwise carries some difficulty. Pike (1993) located the triple point using carefully constructed mesoanalyses, looking for spatiotemporal continuity in its location. However, even with such detailed analysis, the exact location of the triple-point is often open to doubt, especially where the warm front is rather weak and diffuse (e.g., Pike, 1992). This presents a practical difficulty for a classification system dependent upon the positioning of tornadoes relative to the analysed triple point. Given these issues, it is suggested that triple-point storms, where associated with NCFRs along well-defined frontal systems, could usefully be regarded as members of the frontal wave class.

Some of the above points are illustrated by another example of a meso-β-scale frontal wave and associated mesolow. A swathe of severe wind damage, including at least 10 embedded tornadoes, occurred along the track of a mesolow on 17 November 2016 (refer forward to Section 5.7.2 for further discussion of this case). Surface analysis

charts show that the frontal system developed as an 'instant occlusion' (McGinnigle *et al.*, 1988). In the early stages of development, the disturbance is shown as an open frontal wave (Figures 5.8(a) and (b)), with a separate trough immediately to the north of the wave tip. By 1200 UTC (Figure 5.8(c)), the trough is marked as an occlusion and is contiguous with the frontal wave, giving rise to the instant occlusion and a triple point. By 1800 UTC (Figure 5.8(d)), a small back-bent occlusion has formed, and the triple point has moved down-front relative to the centre of the secondary depression.

Radar imagery suggests that the system is difficult to interpret from the point of view of conventional frontal analysis (Figure 5.9). The disturbance associated with the tornadoes is first evident around 0700 – 0800 UTC near the south coast of Ireland (Figure 5.9(a)); at this time the storm is close to the analysed tip of the frontal wave (*cf.* Figure 5.8(b)), allowing for movement of the wave in the intervening two hours. By 1130 UTC (Figure 5.9(d)), the hook-shaped echo associated with the mesolow is clearly visible over northeast Wales, and a more coherent band of rainfall has developed along the cold front to its south, with embedded NCFR cores. At 1200 UTC, the tornadic storm is more-or-less collocated with the analysed triple point (*cf.* Figure 5.8(c)). By 1400 UTC (Figure 5.9(f)), the hook-shaped precipitation region associated with the mesolow has expanded considerably whilst an extensive NCFR has developed along the trailing cold front over southeast England. Extrapolation of the track of the hook-shaped precipitation region[34] places it close to the centre of the analysed secondary cyclone at 1800 UTC (Figure 5.8(d)). The radar data therefore show that the mesoscale circulation associated with the tornadic storm developed prior to the development of the instant occlusion (and therefore the triple point) and that the disturbance effectively expanded to become the secondary cyclone, by which time the triple point was located ~300 km further down-front. Considering these observations, the secondary cyclogenesis and associated mesolow appear to be more reliably collocated with the tornadic storm than the triple point, as analysed[35].

[34] Extrapolation is required because the hook moved out of radar range from ~1500 UTC.

[35] This suggestion is not meant to imply, however, that analysis of triple points in the context of tornadic convection is *never* useful; for example, tornadic supercells have been shown to occur preferentially near triple points (e.g., Knightley, 2006), where it could be argued that the triple point constitutes a boundary intersection. Such intersections can focus convection initiation and may be associated with local enhancement of storm-relative helicity and low-level vertical wind shear (i.e., ingredients known to be supportive of tornadoes in supercells) (e.g., Weckwerth *et al.*, 2008; Tang *et al.*, 2016).

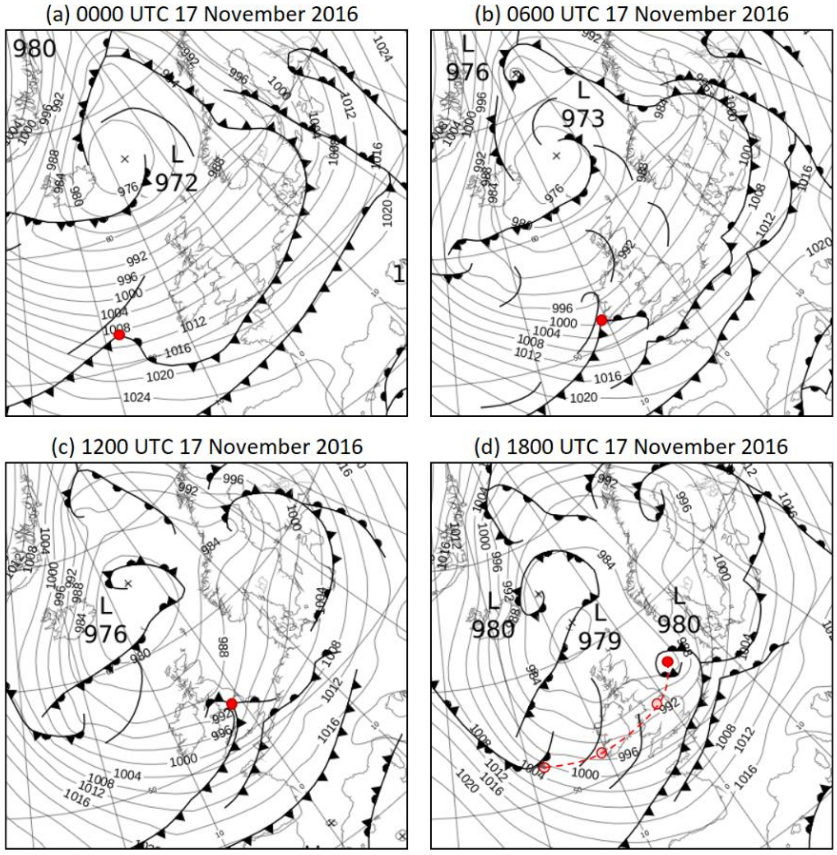

Figure 5.8: Met Office surface analysis (ASXX) charts showing the development of a frontal wave and associated 'triple point low' on 17 November 2016. Red dot shows the location of the disturbance in question. Pink circles and red dashed line in (d) show, respectively, positions of the disturbance at previous analysis times, and track of the disturbance.

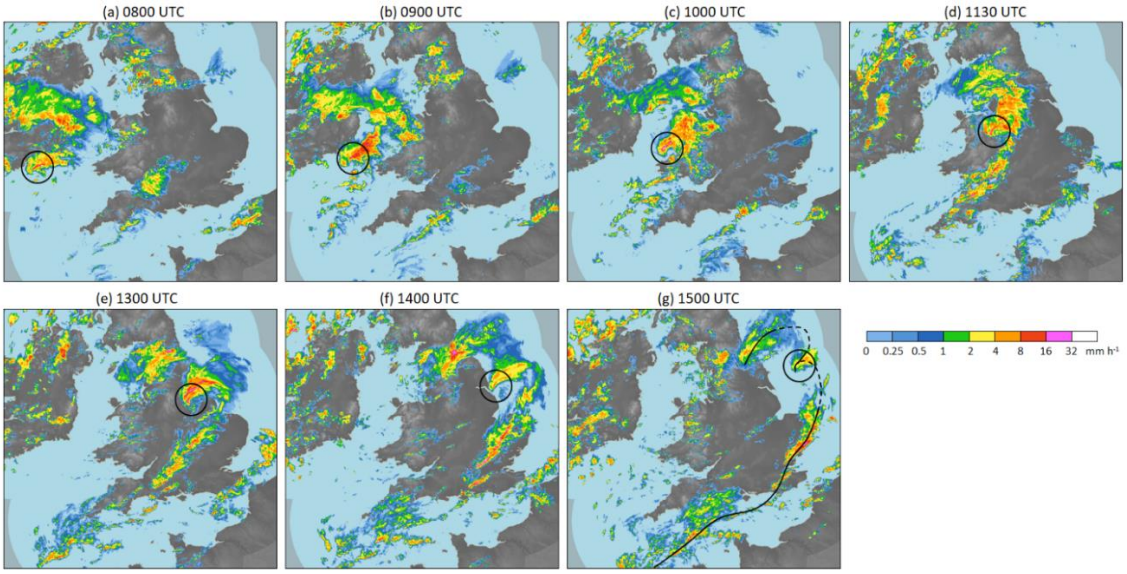

Figure 5.9: Composite radar imagery at specified times on 17 November 2016, showing development of a hook-shaped precipitation region (the tornadic storm) associated with a meso-β-scale cyclone (circled) embedded within a frontal rainband. The solid line in (g) indicates the suggested position of the main surface front (dashed where ill-defined) at 1500 UTC.

5.4 Critical discussion of *p*[TN] as a measure of NCFR tornado risk

5.4.1 Strengths and weaknesses of composite parameters in general, and p[TN] specifically

In the case of supercells and supercell tornadoes, composite environmental parameters have proven ability to draw the forecaster's attention to areas and time periods favourable for severe weather. However, composite parameters and associated indices also have important limitations (e.g., Doswell and Schultz, 2006), which are relevant in the case of *p*[TN]. Firstly, the link to relevant physical processes is not always obvious, especially where several component parameters feed into the composite parameter (e.g., Hart and Cohen, 2016). A related issue is that a single composite parameter is unlikely to capture all relevant physical processes, and the relative contribution of component parameters may vary between cases. These issues can hinder proper assessment of individual supporting or mitigating factors in any given event (e.g., consider a situation in which *p*[TN] is high, but no NCFR is likely to be present, such as in the frontal fracture region of a secondary cyclone). Although it is acknowledged that the NCFR vortex- and tornado-genesis mechanisms remain to some extent unresolved questions, an attempt to address these issues has been presented in Sections 2.4.1 and 2.4.3, where the possible relevance of *p*[TN]'s component parameters to candidate vortex-genesis mechanisms in NCFRs is discussed. Plausible links to physical mechanisms also arise from the case studies in Chapters 3 and 4. Consideration of the possible tornado-genesis failure modes and tornadic cases with low *p*[TN], in Appendix C, is intended to draw attention to processes not captured by *p*[TN], which need to be borne in mind when using the parameter in an operational environment.

Secondly, threshold values are often applied to composite parameters, giving the impression that the hazard in question is likely to occur when the threshold value is met, and unlikely to occur otherwise. *p*[TN] avoids this issue in that is it a *probability* i.e., tornado risk increases as the parameter value increases, and so by definition there is no clear cut-off between tornadic and non-tornadic events. Naturally, this raises the possibility of operationally awkward events with intermediate probabilities, but this is considered preferable to the application of rigid thresholds, for the above-mentioned reason. Strictly, *p*[TN] relates to the probability of one or more tornadoes occurring within an area of size determined by the distance travelled by the front between the

ERAi analysis times (i.e., as dictated by the speed of advance of the front, which is variable across the analysed dataset), and the along-front spacing of analysis points. Furthermore, the linear discriminant analysis, used to derive the probabilities, makes certain assumptions about the constituent parameters (such as that each has a Gaussian distribution). How *p*[TN] relates to the actual point probability of tornadoes, which is potentially a more useful forecast metric, is therefore unclear. These considerations also raise questions as to whether the overall probability of tornadoes is higher if the region with high *p*[TN] extends a greater distance along the front or persists for longer. Another issue, highlighted by the fact that tornadoes may occur when *p*[TN] is rapidly increasing, rather than at the time of its maximum (e.g., Figure 2.11), is that tornado-genesis is likely best explained by Lagrangian changes in the relevant parameters (i.e., following the front), whereas *p*[TN] is a Eulerian measure, based on analysis of parameter values at a single time. For these reasons, it is suggested that the parameter is best used for understanding the relative risk at different locations along a front, and at different times during its lifetime, rather than as a strictly quantitative measure of tornado risk. As stated in Section 2.5, the best results are likely to be achieved when *p*[TN] is used in conjunction with the conceptual models.

The case studies presented in Chapters 3 and 4 show that the physical links between larger and smaller scales, and possibly the meso-ɣ- to miso-scale vortex-genesis mechanisms, vary between the event types. For example, in the frontal wave case of 17 October 2011, vortex-genesis was apparently controlled by the balance between vertical vorticity and horizontal strain, consistent with previous studies on the stability of vortex strips in variable strain fields (e.g., Dritschel *et al*., 1991; Bishop and Thorpe, 1994). *p*[TN] captures the variability in vertical vorticity through the bulk shear vorticity component, but it does not account for the variability in strain. In the same case, the parameter $-v'_{cold}$ was maximised some distance down-front of the tornadoes, though in the quasi-Lagrangian framework it was increasing rapidly near the location of the tornadoes. The physical relevance, or otherwise, of $-v'_{cold}$ in this case is therefore unclear. In the north-westerly flow case, localised intrusions of air into the rear of the front, which might reasonably be expected to be associated with local increases in $-v'_{cold}$, were found to be important in producing local contraction of the front and intensification of the vertical vorticity sheet, providing one possible explanation as to

the physical relevance of this parameter. However, unlike in the frontal wave case, vertical vorticity was otherwise relatively small (as also noted by Buckingham and Schultz (2020) in their type 2 tornadic NCFRs), which calls into question the relevance of the bulk measure of vertical vorticity in north-westerly flow cases.

These considerations may help to explain why individual component parameters apparently vary systematically between the tornadic event types (e.g., shear vorticity is generally larger in frontal wave cases, and $-v'_{cold}$ is especially large in some of the north-westerly flow cases; Figure 2.14), though confidence in this result is low given the large spread in parameter values and relatively small number of events of each type in the analysed dataset. Similar issues apply to other composite parameters; for example, in the case of the Significant Tornado Parameter (Thompson *et al*., 2003), the relative importance of the various component parameters has been shown to vary with the synoptic-scale regime (Garner, 2013), suggesting there is merit in analysis of the component parameters separately. Ultimately, *p*[TN] was derived empirically using a set of events that included both frontal wave and north-westerly flow cases; as such, it represents a compromise between the parameters most relevant to both types of event. In other words, it performs reasonably well across all cases, but fails to account for all the relevant physical mechanisms in individual events. This highlights the additional value of the case studies and derived conceptual models, in furthering understanding of the likely physical mechanisms and in drawing out the differences between event types.

A further measure of the utility of *p*[TN] is its ability to identify exceptional events: in short, are values of *p*[TN] exceptional in NCFRs producing exceptional numbers of tornadoes? This question can be investigated by analysis of the four largest tornado outbreaks within the studied event set. In all cases, *p*[TN] at the tornadic part of the front exceeds the 90th percentile of the distribution over the full set of 8212 analysis points, and so the metric does appear to show potential in this respect[36]. Furthermore, analysis of the constituent parameters, and other key parameters such as the total

[36] Also noticeable is that the tornadic part of the front, on 23 November 1981 and 8 February 1984, traversed almost as wide a swath of land as is possible in the UK for fronts travelling from the west or northwest; this may provide part of the explanation for the exceptionally large number of reported tornadoes. Likewise, lower numbers in some of the other events may be due to the tornadic part of the front traversing a narrower part of the country (e.g., as on 29 November 2011; Figure 5.4), rather than necessarily indicating a difference in the prevailing environmental conditions. Regional differences in the reporting of tornadoes (e.g., due to population bias) could also be important in this respect.

frontogenesis, lend additional support the idea of systematic differences between event types. For example, in the infamous outbreak of 104 tornadoes on 23 November 1981 (Figure 5.10), in which an incipient wave is evident just up-front of the region with tornadoes, shear vorticity and total frontogenesis are exceptionally large; for the latter parameter, this event includes 13 of the 20 highest values in the entire dataset. $-v'_{cold}$ increases from initially unexceptional values to become unusually large (5 analysis points above the 95th percentile) along the bulging section of front down-front of the wave centre during and after the latter stages of the tornado outbreak. Conversely, in the outbreak of 19 tornadoes on 8 February 1984, which is the largest outbreak amongst the north-westerly flow cases in the analysed dataset (Figure 5.11), $-v'_{cold}$ is exceptionally large throughout (14 analysis points at or above the 99th percentile), whereas shear vorticity and total frontogenesis are relatively unexceptional (generally near or below the 80th percentile). The other two largest outbreaks (not shown), of 29 tornadoes on 20 October 1981, and 24 tornadoes on 21 September 1982, were both associated with frontal waves, and yield results similar to those on 23 November 1981 (i.e., unusually large frontogenesis and bulk vorticity, and strong but generally unexceptional $-v'_{cold}$).

The ability of *p*[TN] to identify tornado-favourable areas at longer lead times (> ~1 day) is subject to uncertainty in the model's depiction of the relevant larger-scale features. For example, in frontal waves, although the *potential* for wave development may be relatively predictable up to several days in advance, the timing, position and rate of development is often relatively unpredictable, even up to short lead times (e.g., Parker, 1998; Young and Hewson, 2012; Schemm and Sprenger, 2015; Priestley *et al*., 2020). In practice, this is likely to limit the lead time to which *p*[TN] is useful. These considerations suggest that it would be beneficial to adopt a probabilistic approach to the computation of *p*[TN] (i.e., computing values for all members in an ensemble, and then analysing the mean and spread of values), as is already routinely done for other types of localised high-impact weather, such as the point probability of high rainfall totals or wind gusts.

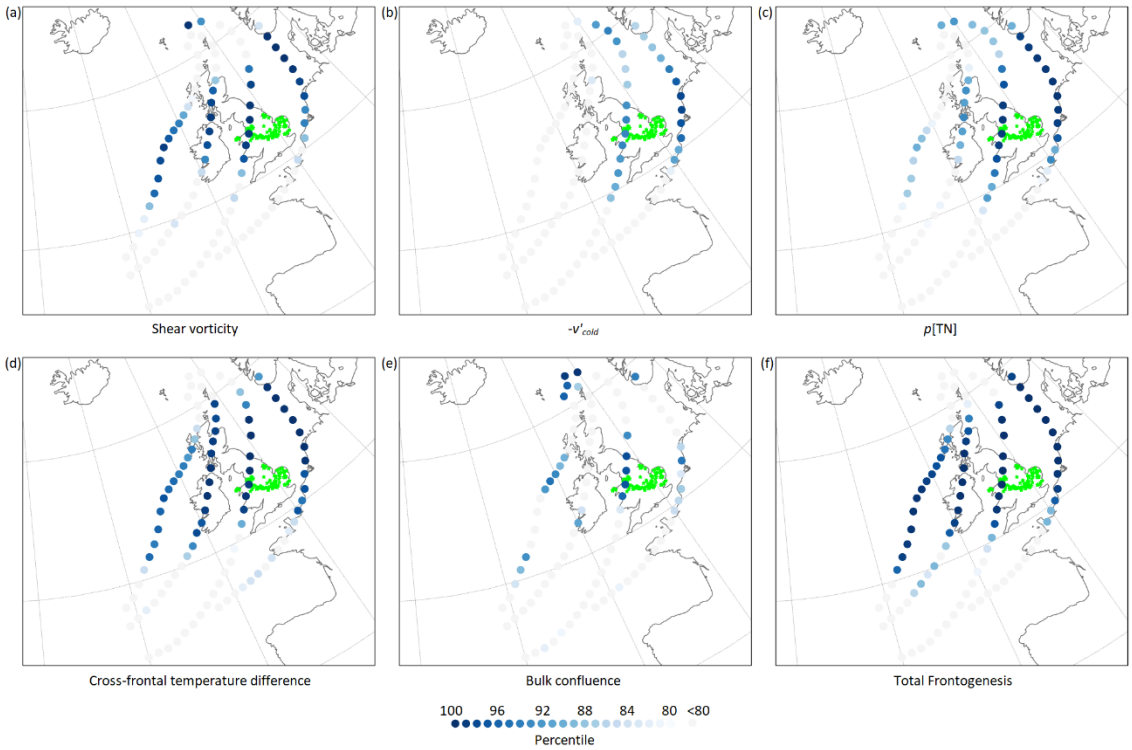

Figure 5.10: Bulk parameter values at on-front analysis points (calculated using ERAi fields and the methodology described in Section 2.2.3) for the high-tornadic case of 23 November 1981. Values are shown at 6-hourly intervals between 0000 and 1800 UTC 23 November 1981. Shading indicates the percentile of each parameter value, within the full set of 8212 analysis points for the 114 analysed cases (see colour scale). Green markers are tornado reports from the TORRO tornado database.

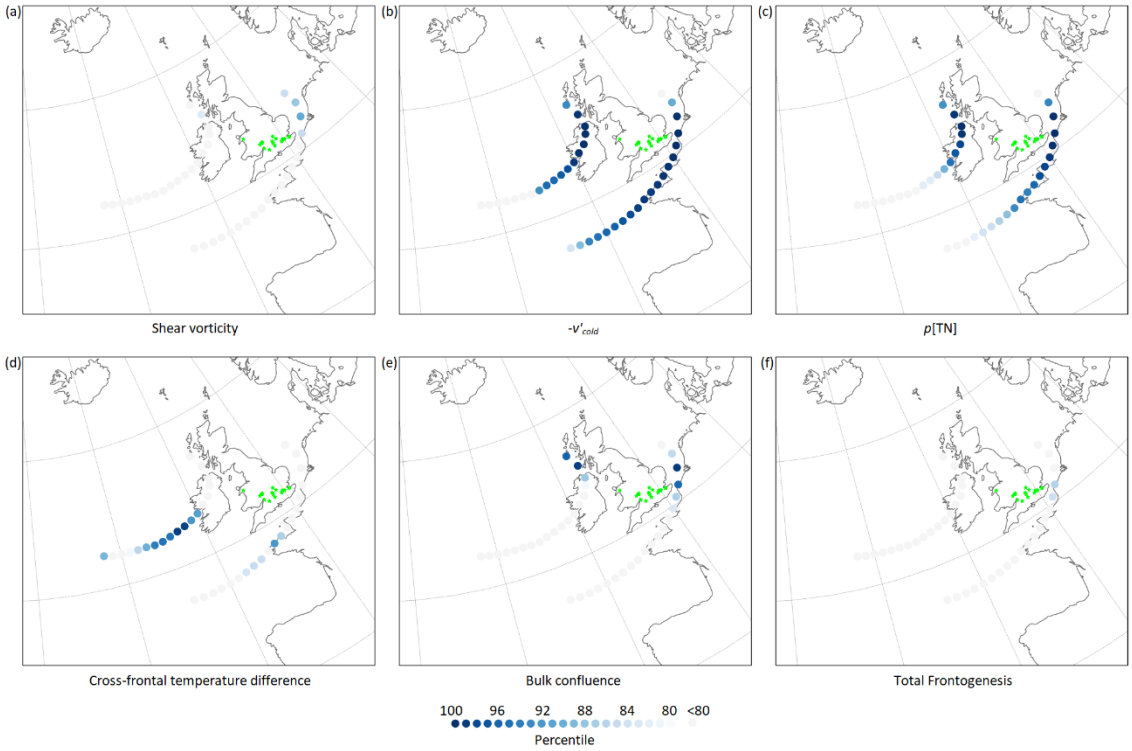

Figure 5.11: As in Figure 5.10, but for the high-tornadic case of 8 February 1984, with values shown at 0000 and 0600 UTC.

5.4.2 Tornado-genesis failure modes in cases of high p[TN]

During early operational trials of *p*[TN], an important failure mode was identified in which large values occurred in cases with multiple shear zones (and associated NCFRs). In these cases, the total horizontal wind shift across the frontal zone is partitioned between the individual shear zones, such that the vertical vorticity at each is smaller than if there were only one shear zone, given the same bulk shear vorticity (assuming some fixed shear zone width). Similarly, $-v'_{cold}$ immediately behind the leading shear zone is smaller than the bulk value of $-v'_{cold}$ (i.e., that analysed at ~150 km to the rear of the front). Operational experience suggests it is not uncommon for two shear zones to exist (Figure 5.12(a)); the leading zone is marked by an abrupt wind veer and transition from strong, nearly front-parallel winds characteristic of the pre-frontal environment to relatively weak winds behind (e.g., see the green-shaded area in Figure 5.12(a)). The trailing zone is marked by a transition from relatively weak winds to somewhat stronger winds with a larger cross-frontal component, and often a secondary wind veer. In cases where these two shear zones merge, the tornado-favourable configuration (CP14) may arise of a near-90° wind veer and a strong cross-frontal component of flow towards the warm air on the immediate cold side of the front. However, where the shear zones remain separate, this favourable configuration is not achieved at either shear zone, with the implication that tornado-genesis is less likely than is suggested by *p*[TN].

The above discussion demonstrates an important limitation of *p*[TN], and the bulk parameters approach more generally; it assumes a single shear zone, and relatively uniform wind fields within the air masses on each side of the front. Provided these assumptions are valid, and given some fixed shear zone width, the bulk measures (e.g., bulk shear vorticity) are directly proportional to the local magnitude of the equivalent parameters (e.g., vertical vorticity) along the shear zone itself. Otherwise, the relationship between bulk and local values of the component parameters breaks down. Complicating the issue are cases in which multiple, initially separate, shear zones subsequently collapse into a single, intense shear zone (e.g., Figure 5.12(b)). In the illustrated case, merger was complete (in the model and observations) by the time the front exited southeast England, and a tornado occurred over Kent around the time of the merger. The collapse, or otherwise, of a relatively diffuse frontal zone with multiple shear zones to a single, narrow shear zone likely relates to the presence or absence of

cross-frontal contraction processes (e.g., Koch and Kocin, 1991), and so a plausible hypothesis is that the horizontal deformation frontogenesis, and related parameters such as the cross-frontal confluence, are relatively weak in cases that fail to exhibit collapse. These considerations again argue for analysis of the total frontogenesis (or the related *p*[NCFR]; see Appendix C) in conjunction with *p*[TN].

In Chapters 2 and 3, it was suggested that the buoyant or static stability may influence the probability of tornadoes, with tornadoes becoming more likely as the buoyant instability increases (and/or the static stability decreases). Although not captured within *p*[TN], this idea is consistent with Figure 18 of CP14, which suggests that tornado-genesis requires larger vertical vorticity as the stability increases. A question that naturally follows is whether tornado-genesis can be prevented, even in large *p*[TN] environments, by particularly large static stability. Moore (1985) noted that pure horizontal shearing instability (as opposed to a buoyancy–shear hybrid instability) is possible in shear zones with aspect ratio (height divided by width) greater than unity. In the high-resolution simulations presented in Chapter 3, aspect ratios of 2 – 3 were noted along some of the braids between primary vortices. Moore's results, and the presence of narrow, deep shear zones in the real data simulations, together suggest that HSI should be possible in at least some statically stable NCFR environments; however, it is unclear whether HSI becomes less likely as the stability increases, in already stable environments. Further work is therefore required to understand the impact of static stability on the likelihood vortex-genesis and associated tornado-genesis in otherwise kinematically favourable environments.

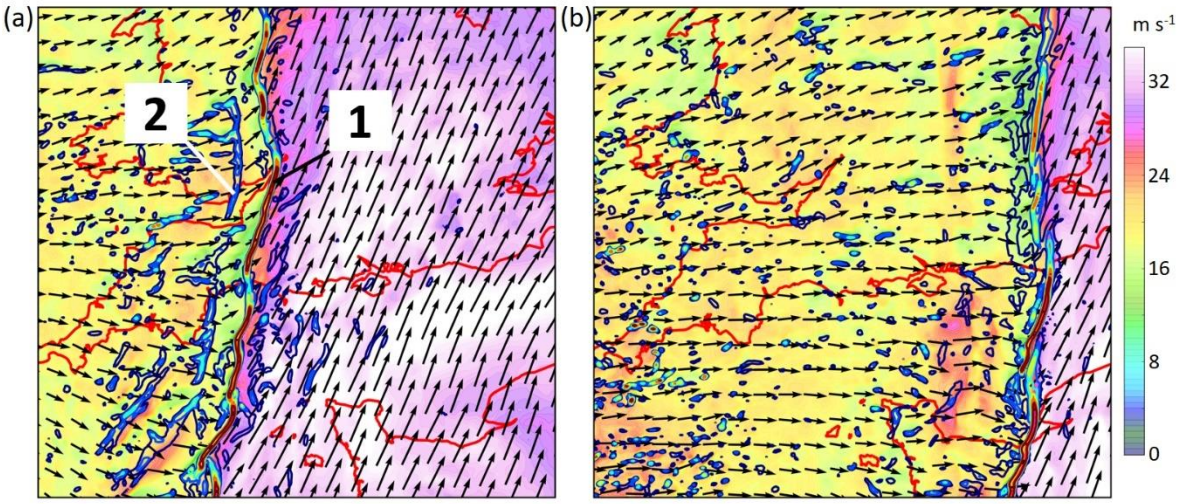

Figure 5.12: Wind fields at 1195 m AGL from the 0900 UTC 28 February 2020 run of the Met Office 1.5 km model, showing the process of collapse of two initially separate shear zones (labelled 1 and 2 in panel (a)) to a single shear zone (collapse almost complete in panel (b)). Shading indicates wind speed, according to the colour scale, and arrows are the wind vectors. Coloured contours are vertical vorticity plotted at intervals of 1 x 10^{-3} s^{-1}. Forecast wind fields are valid at (a) 0400 UTC and (b) 0800 UTC 29 February 2020.

5.5 Conceptual models: comparisons with existing cyclone paradigms

Conceptual models developed for each identified type of tornadic NCFR show substantial differences in terms of the large-scale flow patterns and the cross-sectional structure of the fronts near to the tornadoes. Some similarities exist between the NCFR types identified herein and the QLCS types of Buckingham and Schultz (2020). Characteristics of each identified type are summarised in Table 5.1 and illustrated schematically in Figure 5.13. These characteristics are now compared with existing conceptual models of cyclogenesis and cyclone lifecycles.

Young *et al*. (1987) suggested the existence of two upper-level jets near to major longwave troughs. Both tornadic NCFR types appear to be associated with the approach towards a surface cold front of jet ‘J2’, originating on the upstream side of the trough and typically associated with a PV maximum (Young *et al*., 1987). However, interaction between the jet and front apparently occurs at different locations relative to the axis of the longwave trough; in the north-westerly flow setup, it occurs on the upstream flank of the trough, whereas in the frontal wave setup, it occurs as J2 rounds the axis of the upper-level trough and interacts with the main polar front on the

downstream side of the trough. This difference may be viewed in context of Shapiro's (1983) lifecycle model of upper-level jet streaks (e.g., see Figure 19 of Keyser and Shapiro, 1986), in which a jet streak and associated shortwave trough, originating on the upstream flank of the longwave trough, propagate around the longwave trough axis. North-westerly flow cases resemble stage 2, when the upper-level jet streak intensifies on the upstream flank of the longwave trough, in strongly diffluent flow. Frontal wave cases resemble stage 3, during which the jet streak propagates around the axis of the long-wave trough, with nearly neutral flow tending towards confluent (by stage 4). The developments are both examples of the 'type B' cyclogenesis of Petterssen and Smebye (1971), and what Semple (2003) describes as 'multi-body' cyclogenesis, in that development involves an interaction between upper-level and lower-level features (as opposed to 'type A', or 'single-body', cyclogenesis, involving only one element in the flow, such as an amplifying hydrodynamic instability along a surface cold front e.g., Moore and Peltier, 1987; Schär and Davies, 1990; Joly and Thorpe, 1990; Dacre and Gray, 2006).

Browning (1997, 1999) describes two types of cyclogenesis, according to the configuration of the upper-level flow and characterised by different configurations of system-relative flow within the cyclone (Figure 5.14). This classification is based on the work of Young (1993; 1994) and Browning and Roberts (1994). Confluent flow cyclogenesis (Figure 5.14(a)) is characterised by a relatively elongated warm conveyor-belt and trailing cold front. Frontal fracture occurs only within a small region near the cyclone centre. The upper-level flow, and flow within much of the dry intrusion, are orientated approximately parallel to the trailing portion of the front. Diffluent flow cyclogenesis (Figure 5.14(b)) exhibits a greater extrusion of a secondary warm conveyor-belt flow poleward of the main polar front cloud band; the surface cold front bounding the poleward and upstream edge of this flow is of the split-front type (Browning and Monk, 1982); air within the dry intrusion flows approximately normal to the surface cold front in this region and overruns it. The case studies explored in Chapters 3 and 4 broadly fit these two classes of cyclone, in that the 17 October 2011 frontal wave case, occurring in neutral or weakly confluent flow aloft, exhibited characteristics of the confluent flow type cyclogenesis, such as the elongated cold front and relatively limited region of frontal fracture (e.g., Figure 3.5(e)-(f)). The 20 November 2013 case, exhibiting strongly diffluent flow aloft, exhibited the split-front

characteristics and overrunning jet, within which flow was orthogonal to the surface front, of the diffluent-flow cyclogenesis model.

A potentially related explanation for the differing large-scale setups is barotropic shear in the mean zonal wind. Using a semi-geostrophic model, Davies *et al*. (1991) showed that distinctly different structures arise in cyclones forming in ambient anticyclonic and cyclonic shear (*cf*. Figures 5.15 and 5.16). The relevant differences, at the mature stage of the resulting cyclones, may be summarised as follows:

Anticyclonic shear (Figure 5.15):

- Strong, elongated cold front, relatively straight except near the trailing end.
- Strong cyclonic relative vorticity along surface front (Figure 5.15(e)).
- Relatively elongated surface cyclone sandwiched between two large and almost circular anticyclones; surface trough is everywhere positively tilted relative to the large-scale background flow (i.e., southwest–northeast orientated).
- A relatively weak front-normal component of geostrophic flow post-front, especially along the trailing front far from cyclone centre.
- Somewhat less extensive push of cold air on rear flank of cyclone.

Cyclonic shear (Figure 5.16):

- Strong warm and back-bent fronts and relatively weak cold front; cold front strongly curved (convex on warm-air side).
- Relatively weak cyclonic relative vorticity along cold front (Figure 5.16(e)).
- Relatively circular surface cyclone, lagging to the west of the warm sector further down-front (i.e., surface trough is negatively tilted near cyclone centre).
- A relatively strong front-normal component of geostrophic flow post-front.
- Stronger equatorward push of cold air on rear flank of cyclone.

Furthermore, the upper-level flow in the anticyclonic shear case exhibits a strongly confluent, positively tilted upper-level trough, compared to a diffluent, somewhat negatively tilted (i.e., northwest–southeast-orientated) upper-level trough in the cyclonic shear case (*cf*. panels (b) and (f) in Figures 5.15 and 5.16); agreement therefore exists with the diffluent- and confluent-flow cyclogenesis conceptual models of Browning

(1997) and Young (1994), as described above. The anticyclonic and cyclonic shear patterns resemble, respectively, the large-scale setup in frontal wave and north-westerly flow cases, especially just prior to the tornadic period (i.e., prior to the onset of secondary cyclogenesis in the former type, and prior to the jet streak cutting across the cold front in the latter type). This raises the possibility that differences in the subsequent developments, associated with upper-level jet streak J2 (Young *et al*., 1987) approaching the front from the upstream side and culminating in locally tornado-favourable conditions along the surface front, relate entirely to the pre-existing differences in the parent cyclone structure, associated with the large-scale barotropic shear. On the other hand, since the large-scale shear influences the structure and relative location of the upper-level jets, it may also have an impact on the proximity of jet J2, where present, to the trailing surface cold front, and therefore on the likelihood of the required interaction between upper- and lower-level features.

Notwithstanding these unknowns, the similarities between the large-scale patterns arising from the semi-geostrophic simulations and those associated with the two types of tornadic NCFR identified herein are striking, suggesting that the possible influence of the large scale barotropic shear on the tornadic NCFR type merits further investigation. Comparisons may also be drawn, both in terms of the upper-level trough structure and tilt, and various attributes of the surface frontal zones, with the LC1 anticyclonic, and LC2 cyclonic, cyclone paradigms of Thorncroft *et al*. (1993), which are in many ways comparable with the Davies *et al*. (1991) exemplars. The tornadic NCFR types identified in this thesis therefore appear to fit rather neatly into existing cyclone paradigms.

Several authors (e.g., Ayrault *et al*., 1995; Schemm and Sprenger, 2015; Graf *et al*., 2017) have demonstrated that the relative frequency of cyclones of different types varies geographically. For example, Ayrault *et al*. (1995) noted the existence of maxima in ultra-high-frequency variability slightly down-track and equatorward of the main storm tracks in both the Atlantic and Pacific basins. The main source of this high-frequency variability was frontal waves[37]. These results could help to explain the high frequency of tornadoes in the UK (located equatorward of the end of the North Atlantic storm track), relative to many other midlatitude countries, given that over half of all

[37] Other identified sources were cold air cyclogenesis and other small-scale developments.

tornadic NCFRs, and over three-quarters of NCFR tornado outbreaks, were found to be associated with frontal waves in the current study. If correct, this suggests that tornado-favourable NCFR environments of this type may occur frequently in other regions, such as parts of western North America, equatorward of the eastern end of the Pacific Storm track. This hypothesis could be tested by calculation of *p*[TN] using global reanalysis datasets, in conjunction with objective classification methods for identification of fronts and associated waves (e.g., Hewson, 1997; 2009).

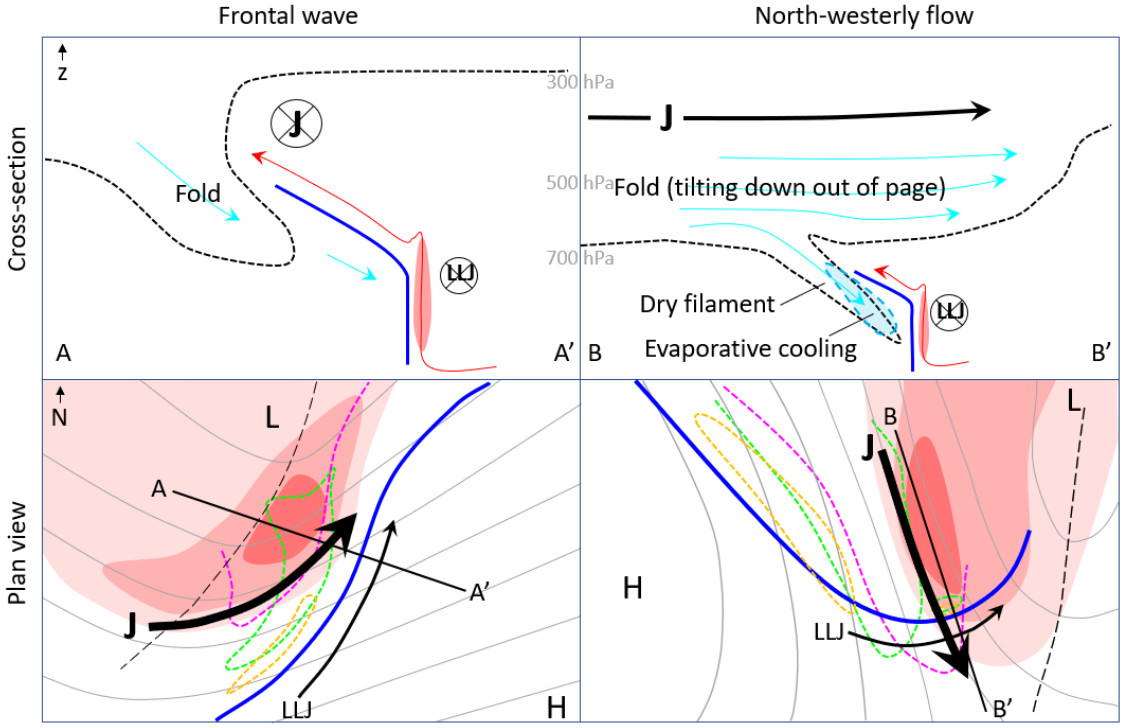

Figure 5.13: Schematic cross-sections (top row) and plan views (bottom row) for frontal wave (left column) and north-westerly flow (right column) tornadic NCFRs. In the vertical sections, bold blue lines indicate the frontal boundary, and thin coloured arrows the front-relative airflows. Bold black arrows and 'J' denote the upper-level jet, and thinner black arrows and 'LLJ' the pre-frontal low-level jet. Black dashed lines indicate the approximate boundary of the driest air aloft (relative humidity < ~ 75%), and red shading denotes strong updrafts associated with the NCFR at the surface front. Note that in the north-westerly flow setup, the horizontal and vertical extent of the rearward-sloping ascent above the frontal boundary (red arrow in the cross-sections) tends to increase with time, over several hours prior to tornado-genesis, such that it may become deeper and wider than is shown here. In the plan view panels, the bold, blue line is the surface front, red shading signifies the PV distribution at 300 hPa (deeper red shades denoting larger PV), coloured, dashed lines denote the approximate boundaries of the driest air at 500 hPa (magenta), 700 hPa (lime green) and 850 hPa (gold), plotted in order to depict the three-dimensional structure of the tropopause fold. The approximate positions of the vertical sections are shown by the lines A – A' and B – B' (see corresponding labels in the vertical sections); section length is ~1000 km. Thin grey lines are 300 hPa height contours, and the thin, black dashed line marks the approximate position of the 300 hPa trough axis.

Table 5.1: Comparison of the characteristics of frontal wave and north-westerly flow tornadic NCFRs and their environments.

Characteristic	*Frontal wave*	*North-westerly flow*
Position relative to longwave upper-level trough	Near axis or downstream (i.e., forward) side	Upstream (i.e., rearward) side
Orientation of mid- to upper-level flow relative to surface front (in tornadic region)	Near-parallel, but tending towards a larger angle as the frontal wave amplifies	Near-orthogonal
Mid- to upper-level flow and/or trough configuration	Near-neutral or confluent	Diffluent
Cyclone paradigms	Confluent flow (Browning, 1997; 1999); Anticyclonic large-scale shear (Davies *et al*., 1991); LC1 (Thorncroft *et al.*, 1993)	Diffluent flow (Young, 1993); Cyclonic large-scale shear (Davies *et al*., 1991); LC2 (Thorncroft *et al.*, 1993)
Cyclogenesis type	Interaction of upper-level and surface features i.e., Type B of Petterssen and Smebye (1971)	Interaction of upper-level and surface features i.e., Type B of Petterssen and Smebye (1971)
Cold front paradigms (near location of tornadoes)	Rearward sloping; conforms well to the classic ana cold-front cross-section of Browning (1990)	Hybrid (generally split or forward-sloping, with dry air overrunning at mid- to upper-levels, but increasingly rearward sloping in tornadic region).
Surface frontal characteristics	Well-marked, narrow shear zone. Sharp pressure trough, large vertical vorticity, sharp temperature decrease; some similarities to surface fronts in ‘type 1’ tornado outbreaks of Buckingham and Schultz (2020)	Generally weak and diffuse shear zone, except near tornadic region. Relatively weak pressure trough and small vertical vorticity, except near tornadic region; generally small temperature decrease; some similarities to surface fronts in ‘type 2’ tornado outbreaks of Buckingham and Schultz (2020)
Intrusion of dry air and evaporative cooling	Limited in early stages of cyclogenesis	Marked, especially in small region near to tornadoes
Antecedent environment (in quasi-Lagrangian frame of reference following the front)	Long history (>24 – 48 hours) of large deformation strain and frontogenesis; increases with onset of wave development, followed by decreases immediately prior to tornado-genesis	Weak deformation strain and weak frontogenesis, except near tornadic part of front and within ~6 – 12 hours of tornado-genesis

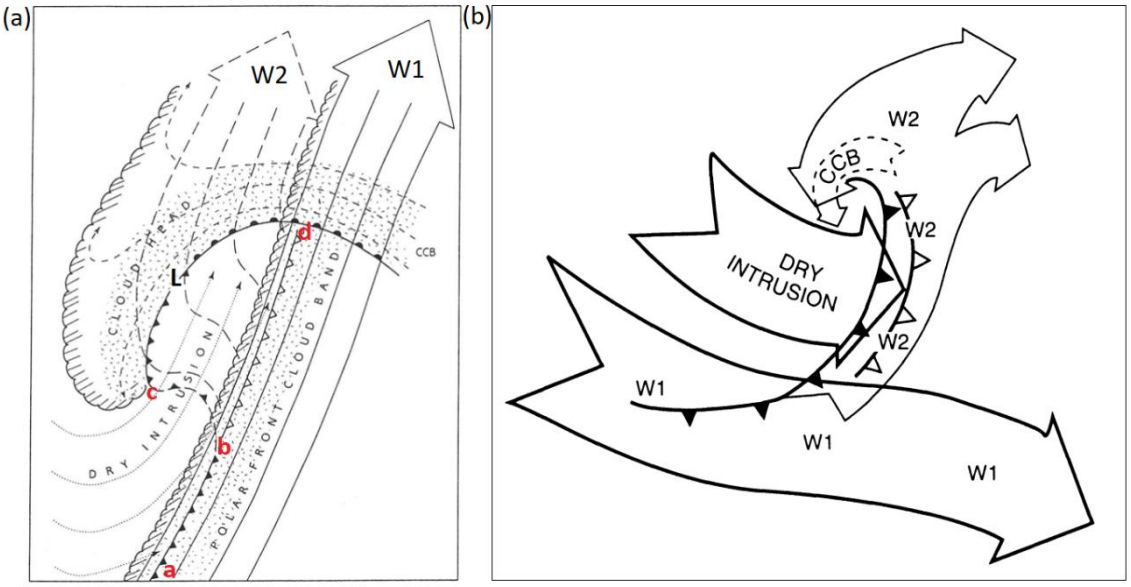

Figure 5.14: Comparison of the main system-relative flows and frontal positions in confluent and diffluent flow cyclones. (a) Structure of a developing extratropical cyclone (confluent-flow type) based on Browning and Roberts (1994). The cyclone centre (L) is travelling toward the top right. The surface warm front is shown conventionally. Part of the back-bent front (cd) is plotted as a cold front with closely spaced frontal symbols. The main surface cold front (ab) is shown similarly. In between the two sharp surface cold fronts (bc) there is a diffuse surface cold front drawn dashed with widely spaced frontal symbols. The cold front drawn with open symbols (bd) is an upper cold θ_w-front (UCF) marking the leading edge of the dry intrusion. Principal airflows, drawn relative to the system, are the main warm conveyor belt (W1) (solid lines), the secondary warm conveyor belt (W2) (long-dash lines), the cold conveyor belt (CCB) (short-dash lines), and the dry intrusion (dotted lines). The cold-air sides of the main cloud features are drawn scalloped. (b) Conceptual model showing system-relative airflows within a cyclone forming ahead of a strongly diffluent trough (after Young, 1994). The arrows labelled W1 and W2 are warm conveyor belts. The dashed arrow labelled CCB is a shallow cold conveyor belt, which forms a hook of low cloud around the cyclone centre. Figure and caption reprinted with permission from Browning (1999) in M. A. Shapiro *et al*. (eds.), *The Life Cycles of Extratropical Cyclones* (Figures 4 and 5, pages 269 and 270).

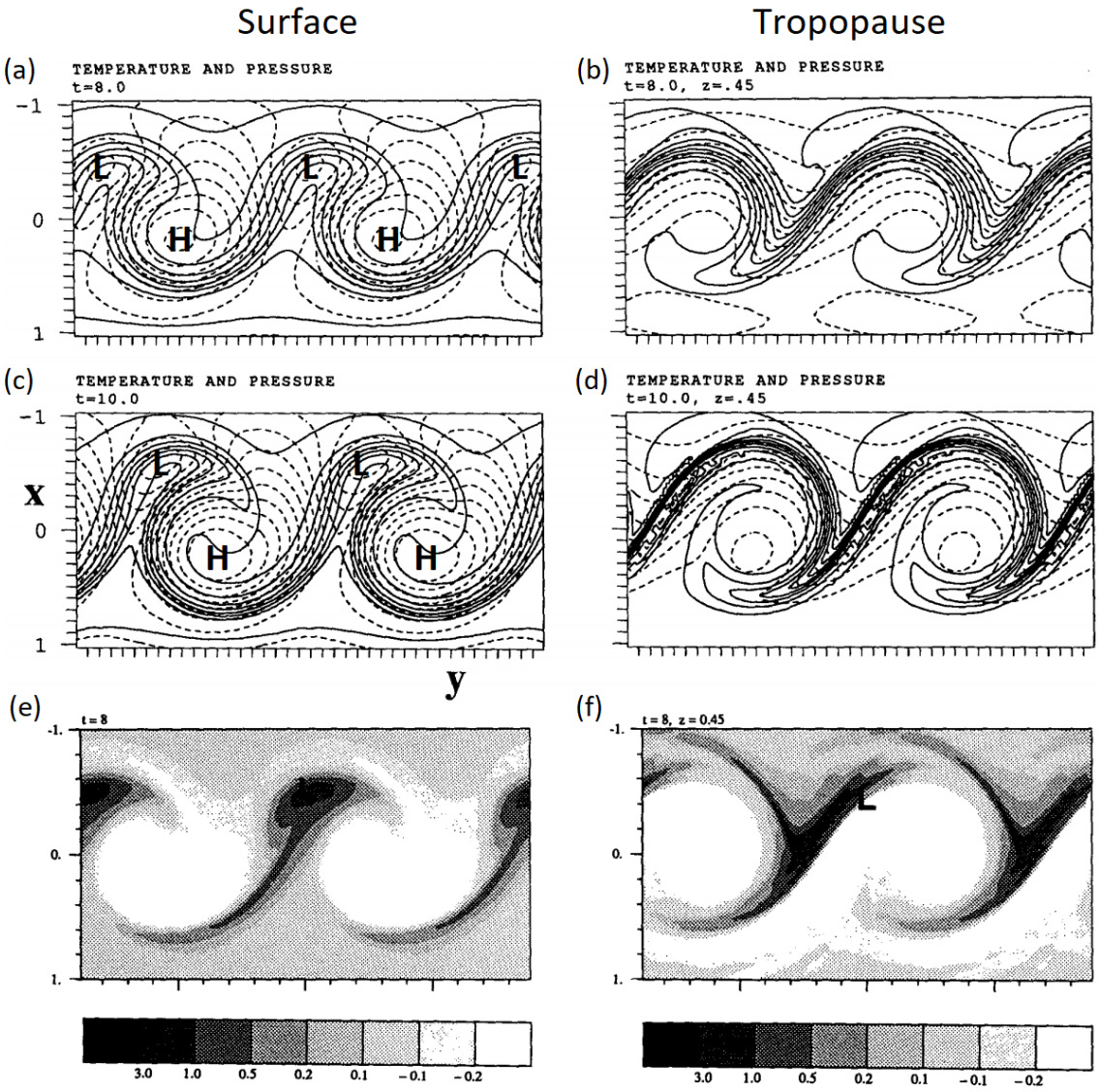

Figure 5.15: The nonlinear normal-mode development for the anticyclonic shear case at the surface (on the left) and the tropopause (on the right) in a semigeostrophic idealised simulation (see Davies *et al*. (1991) for details). The fields are displayed in physical space. (a)-(b): fields at time t = 8 (~day 4); (c)-(d): fields at time t = 10 (~day 5). The isoline spacings are 0.15 (~2 K) for the isentropes (solid lines), and 0.03 (~3 hPa) for the pressure (dashed lines) at the surface and 0.06 (~4.2 hPa) for the "tropopause" pattern. 'L' and 'H' denote the surface low- and high-pressure centres, respectively. (e)-(f): Relative vorticity patterns, at the surface (e) and tropopause (f), for the same case at time t = 8 (~day 4), displayed in physical space. The vorticity has been scaled in units of the Coriolis parameter, *f*, with cyclonic regions darker and anticyclonic regions brighter (see colour bar below panels). "L" denotes the position of the surface low pressure centre. Adapted from Figures 8 and 10 of Davies, H.C., Schär, C. and Wernli, H. (1991) The palette of fronts and cyclones within a baroclinic wave development. *J. Atmos. Sci.*, 48, 1666–1689. © American Meteorological Society. Used with permission.

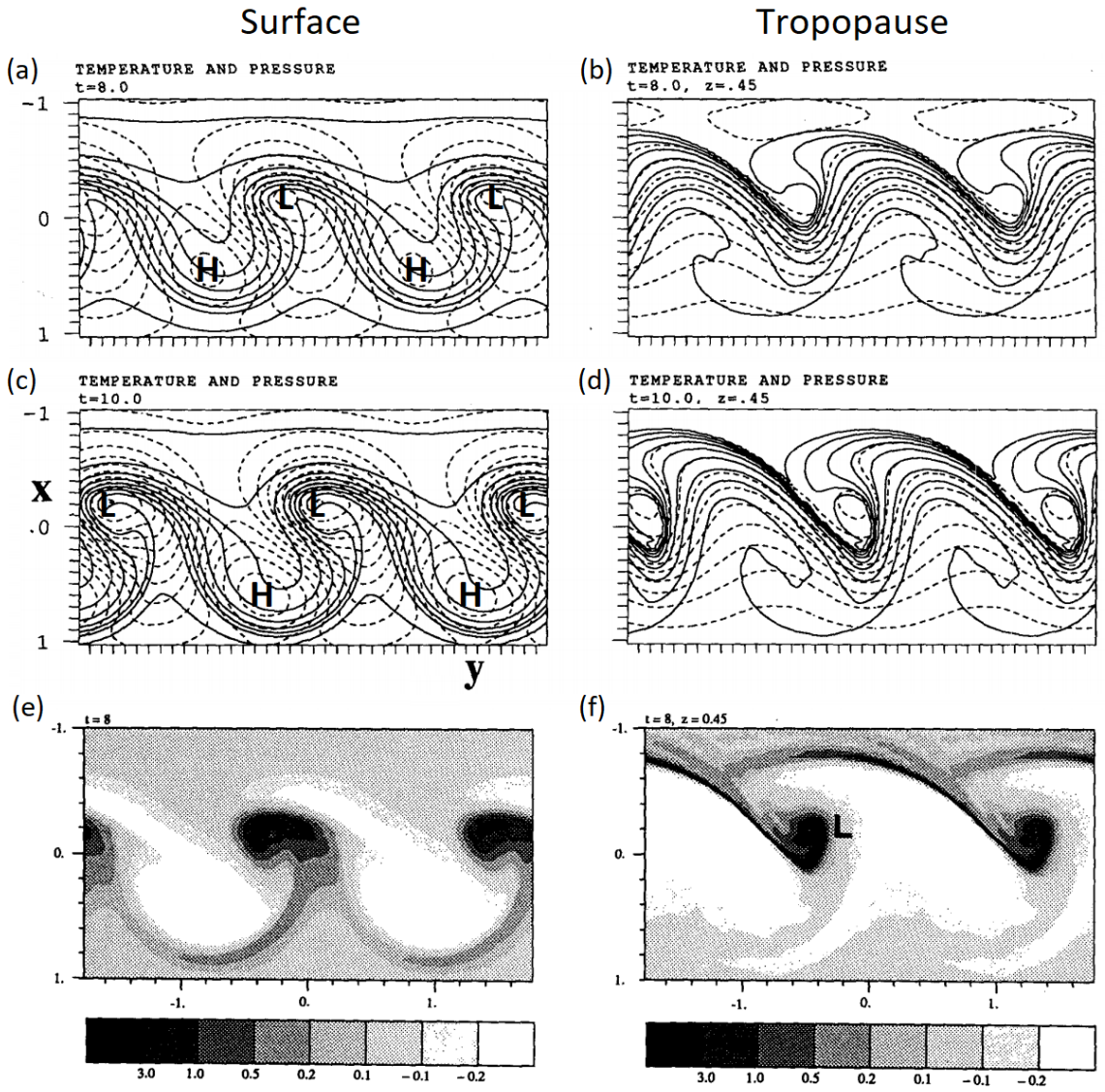

Figure 5.16: As in Figure 5.15, but for the cyclonic shear case. Adapted from Figures 9 and 10 of Davies, H.C., Schär, C. and Wernli, H. (1991) The palette of fronts and cyclones within a baroclinic wave development. *J. Atmos. Sci.*, 48, 1666–1689. © American Meteorological Society. Used with permission.

5.6 Variability in frontal structure: further interpretation and considerations

The case studies presented in Chapters 3 and 4 demonstrate, in agreement with previous studies (e.g., Browning and Roberts, 1996), that cold fronts may exhibit a wide range of cross-sectional structures, sometimes even over relatively short distances along a single front. Of the two fronts studied in Chapters 3 and 4, that on 17 October 2011 is closer to the ‘classical’, deeply rearward-sloping structure of Browning (1990), in that the tropopause fold and its associated transverse circulation were approximately aligned

with the transverse circulation at the surface front. This configuration arises because the upper-level jet was orientated nearly parallel to the surface front (Figure 5.13, left column). Assuming this configuration to be typical of frontal wave cases (as suggested by the composite analysis in Figure 2.12), it seems probable that some frontal waves will exist in which the upper- and lower-level transverse circulations are more strongly coupled, such that dry high-PV air from the tropopause fold intrudes to low levels immediately to the rear of the surface front. Therefore, although apparently not important on 17 October 2011, cooling by evaporation or sublimation of precipitation (e.g., Parker and Thorpe, 1995) could become dynamically important in some frontal waves, as found in the north-westerly flow case of 20 November 2013. This possibility again highlights a need for detailed analysis of further examples of each type.

In contrast, the 20 November 2013 case exhibited a rather non-classical frontal structure, in which the tropopause fold associated with the mid- to upper-level jet–front system descended towards the west i.e., in the along-front direction, with respect to the section of surface cold front over England (Figure 5.13, right column). Therefore, the transverse circulation associated with the mid- to upper-level jet–front system was orientated approximately normal to that associated with the surface front in the same region. This configuration implies that dry air within the tropopause fold could not have intruded 'directly' into the rear of the surface front as in the classical case (*cf.* left and right columns of Figure 5.13). Indeed, most of the dry air within the fold overran the surface front and its associated (generally rather shallow) transverse circulation; the tilt of the larger fold explains the decrease in the base height of this overrunning dry air towards the west (i.e., down front) over the UK (Figure 4.7(a)). Yet, perhaps counterintuitively, intrusion of dry air to low levels immediately behind the surface front was locally important in this case, in the form of a much smaller filament of dry air underneath the left exit of the jet streak, where near-surface frontogenesis was maximised. This filament was extruded from the overlying tropopause fold within the surface front's intensifying transverse circulation, descending along a slope orientated normal to that of the larger fold, and undercutting the developing rearward-sloping ascent region and some of the associated precipitation (Figure 5.13, right column).

Browning (1997; 1999) suggested the existence of a spectrum of frontal types between pure ana and pure kata (see Figure 1.8). The current study supports this idea;

for example, the 20 November 2013 front generally exhibited split characteristics, in that there was strong overrunning of dry air aloft (e.g., Figure 4.10(a)). However, as discussed above, local rearward-sloping ascent also occurred beneath this overrunning dry air near the tornadic region, as part of the intensifying front-transverse circulation. The cross-sectional structure in this region therefore conforms to an intermediate stage in Browning's spectrum of frontal types (Figure 1.8(b)), tending towards the ana end of the spectrum. This result has relevance to operational forecasting because it is sometimes assumed that NCFRs (and related hazards) occur only in 'classical' rearward-sloping fronts. A related issue is the rule-of-thumb that such classical fronts and their associated NCFRs occur only with confluent upper-level flow and/or troughs, an idea apparently drawn from classical treatments of deformation frontogenesis (e.g., Hoskins and Bretherton, 1972). One problem with this rule-of-thumb is that horizontal deformation represents only one of at least two commonly occurring upper-level frontogenesis mechanisms; the other involves tilting in north-westerly flow regimes upstream of a longwave trough (e.g., Uccellini *et al*., 1985; Schultz and Sanders, 2002), a situation often associated with neutral or diffluent upper-level flow patterns reminiscent of that on 20 November 2013 (see also Table 5.1). A second issue surrounds whether strong upper-level frontogenesis is necessarily associated with strong low-level frontogenesis, the latter being important for development of the NCFR. Whilst the NCFR was more extensive and longer-lived in the 17 October 2011 case, the results presented in Section 4 demonstrate that NCFRs and related hazards are also possible with strongly diffluent upper-level flow patterns and in cold fronts that appear somewhat non-classical; such events would be missed if relying only on the above-mentioned 'rules-of-thumb'.

5.7 High-resolution simulations: achievements, limitations and further considerations

5.7.1 Summary of findings and limitations

The case studies presented in Chapters 3 and 4, which incorporate output from the high-resolution simulations, provide new insights into the physical mechanisms leading to meso-γ- to miso-scale vortex-genesis in NCFRs. Furthermore, they confirm the

existence of physical links across a wide range of spatiotemporal scales, which help to explain how the large-scale flow ultimately constrains the timing and location of tornado-genesis along a given front. The high-resolution simulations also provide insights into the typical structure and evolution of the NCFR near to developing meso-ɣ- to miso-scale vortices, which could be of practical use for the operational nowcasting of NCFR tornadoes using radar data.

The primary limitation of the case studies, aside from the question of the generality of the results, remains the model resolution; the grid length was too large to resolve tornadic circulations explicitly, and therefore to provide any direct insights into the tornado-genesis process. Furthermore, the studies cannot give a definitive answer as to the question of the parent vortex-genesis mechanisms, even though circumstantial evidence of HSI is strong in the 17 October 2011 case (as discussed in Section 3.7). Trajectory analysis was not performed in Chapters 3 and 4, since the three-dimensional wind fields in the 300 m simulation were only output at hourly intervals, but such analysis could provide further clues. A 'frozen' trajectory approach was attempted, however, using the three-dimensional model wind field at a single output time, for an array of trajectories ending in the vorticity maximum associated with secondary vortex S_2 on 17 October 2011 (Figure 5.17). Substantial vortex evolution is evident on these timescales (e.g., Figure 3.13), and so equivalence of the frozen trajectories to full trajectories computed using the time-varying wind fields cannot be assumed. However, with these limitations in mind, the frozen trajectories show stretching of vertical vorticity to be much larger than tilting of horizontal vorticity almost throughout the trajectory (Figure 5.17(b)) which, if taken at face value, suggests that the tilting mechanism (e.g., as described for QLCSs in high-CAPE environments; Figure 1.6) is unlikely to have been the primary vortex-genesis mechanism in this case. A similar result was found when constructing frozen trajectories ending within nascent vortex S_1 (not shown).

In terms of tornado-genesis within the miso-scale secondary vortices, the results in Chapter 3 present two possibilities. Firstly, tornado-genesis may occur within the small area of intense near-surface vertical vorticity stretching at the north, northwest or west flank of analysed secondary vortices. Secondly, tornado-genesis may be the result of the cascade of filament (i.e., braid) instabilities (e.g., Juckes, 1995; Scott and

Dritschel, 2014) to smaller (and herein unresolved) scales. Tornado-like vortices are plausible in the cascade scenario because the magnitude of vertical vorticity along the braids is larger than at the original shear zone prior to the initial release of HSI, and the strength of vortices resulting from the release of HSI is known to be proportional to the initial vorticity along the unperturbed shear zone (Buban and Ziegler, 2016), noting that the braid constitutes the unperturbed shear zone in the case of the smaller-scale instabilities. Higher-resolution simulations (ideally with grid-spacing ~10 m) would be required to investigate which, if any, of the above-mentioned mechanisms is responsible for tornado-genesis, and whether this varies from event to event.

5.7.2 Insights provided by other case studies

Although observational data are usually insufficient to provide direct insights into the vortex- and tornado-genesis mechanisms in NCFRs, owing to the small spatiotemporal scales involved, some potentially relevant results have been found in the case of 17 November 2016. As discussed in Section 5.3.3, this was an example of an unusually small frontal wave associated with a long-lived tornadic storm. The resulting damage over Shropshire and surrounding areas was mapped in the field over a 6-day period. The damage patterns were then compared with radar observations of the parent storm, including a dual Doppler analysis and surface meso-analyses constructed through time-composited surface data from Met Office and privately-owned automatic weather stations (see Clark *et al*. (2018) for details of the methodology). The damage survey revealed a swath of general wind damage on the southern flank of the mesolow, which extended for over 150 km in length. Embedded within this swath was a repeating pattern of much narrower, intense damage swaths, likely due to tornadoes, originating near the northern edge of the general damage swath and sometimes merging with it (Figure 5.18(a). Comparison with radar data shows that the narrow damage swaths originated near the tip of a hook-shaped NCFR core occupying the northwest flank of the mesolow (Figure 5.18(b)).

Dual Doppler analysis reveals a core of > 40 m s^{-1} winds on the southern flank of the mesolow (Figure 5.19(a)) and a well-marked system-relative vortical flow (Figure 5.19(b). An elongated vorticity maximum is evident on the southwest flank of the mesolow, at the northern edge of the wind maximum (Figure 5.19(c)). Embedded within this vorticity maximum is a smaller region of strong vertical vorticity stretching near the

tip of the hook-shaped echo (Figure 5.19(d)), and therefore close to where the narrow damage tracks originated. The inference is that the tornadic vortices were developing within this flanking vertical vorticity stretching maximum, and then tracking around the larger mesoscale circulation, consistent with their gently curving tracks[38], before dissipating in a region of horizontal divergence on the southeast flank of the mesoscale vortex.

Although the mesoscale circulation is substantially larger than the miso-scale secondary vortices noted in the 300 m grid-length simulation of the 17 October 2011 case, and as observed by radar in many other NCFR cases, the similarity between the model and dual Doppler analysis, in terms of the existence and relative size of the stretching maxima on the flanks of the respective parent vortices, is of interest (*cf.* Figures 5.19 and 3.14). The repeated occurrence of tornado-genesis near or within the flanking vorticity stretching maximum could be taken as evidence of the first suggested scenario above (i.e., spin-up of tornadoes within a vertical vorticity stretching maximum on the flanks of a larger parent vortex). However, since the observations pertain to only one case, and given the differences in scale, modelling and in-depth observational studies of further cases are required to confirm or refute this idea, with particular focus on the miso-scale vortices more typical of tornadic NCFRs.

5.7.3 Flanking vorticity stretching maxima in a simple model

Flanking vertical vorticity stretching maxima, which appear at least superficially similar to those described in the model simulations in Chapters 3 and 4, may also be produced using a simple two-dimensional model, in which a horizontal shear zone is advected by the horizontal flow around a vertical vortex centred on the shear zone (Figure 5.20). In the simple model, two flanking maxima appear as the original shear zone distorts, on the northwest and southeast flanks of the vortex; the intensity of the flanking maxima increases as the shear zone continues to distort. In the real-data simulations, a flanking maximum is generally only evident on the up-front (i.e., north, northwest or west) flank of the vortex, as described in Chapter 3, rather than on both flanks as in the simple model. This difference may relate to the neglect of three-dimensional aspects of the vortex structure in the simple model; in particular, a tendency for descending

[38] Similar curved tornado damage tracks, and movement of miso-scale vortices around the larger mesoscale circulation, were found in the 3 November 2009 case (Clark, 2010; 2012).

trajectories (Smart and Browning, 2009) and extremely strong vertical wind shear on the southern flank of the vortices at low levels, owing to friction acting on the strong ground-relative winds in this region, which tend to be detrimental to maintenance of a well-defined zone of strong vertical vorticity here. Notwithstanding the limitations of such a simple model, these results suggest that a flanking maximum of vertical vorticity stretching could arise simply from the perturbation of an initially linear shear zone by a vortex growing along it, which could explain why flanking maxima appear to be ubiquitous in the real data simulations of miso-scale vortices. The simple simulation also appears to reproduce the clockwise-turned horizontal convergence maxima that (in real NCFRs) are associated with the clockwise-turned updraft maxima and precipitation cores between primary vortex centres, and the divergence maximum associated with the NCFR gap near the vortex centre (these along-front differences in horizontal convergence relate to the local reorientation of the boundary, relative to the larger-scale pre- and post-frontal wind field, as described earlier in relation to meso-β-scale perturbations along the front; Figure 5.3).

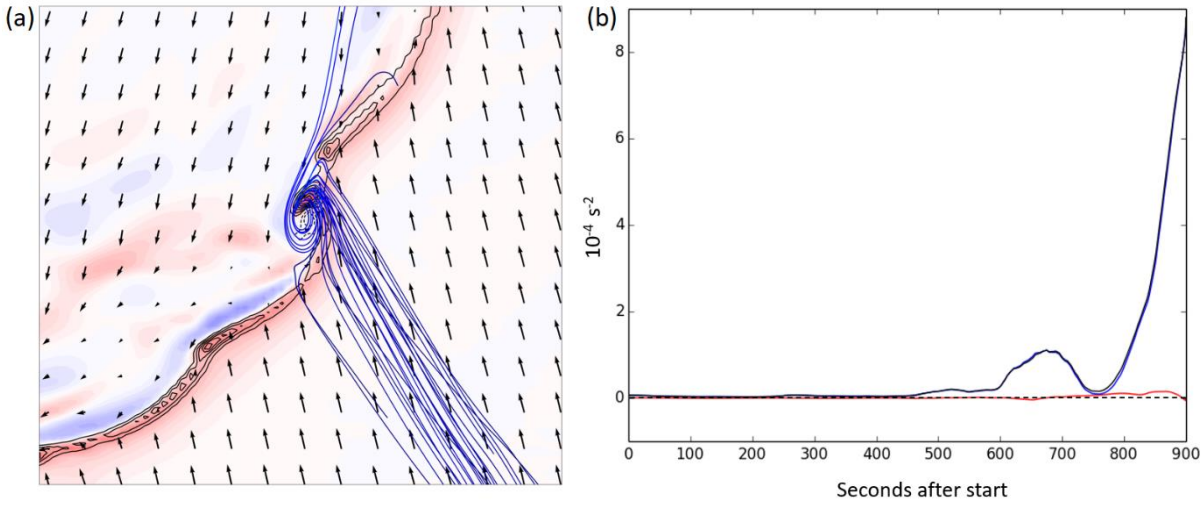

Figure 5.17: (a) Trajectories (thin blue lines) for a bundle of parcels ending at 45 m AGL in the miso-scale vortex S_2 (see Figure 3.13 for location of this vortex, and additional details) from the 300 m model simulation. Fields are valid at 1600 UTC 17 October 2011 and the vortex is located over the Irish Sea. Shading shows vertical velocity at 45 m AGL (red = ascent; blue = descent; contour interval = 0.1 m s^{-1}) and thin black contours are vertical vorticity stretching (contour interval 2 x 10^{-4} s^{-2}; dashed lines indicate negative values, and zero contour is not shown). Arrows are 45 m AGL vortex-relative wind vectors, plotted every 1.2 km in the horizontal. Note that the trajectory origin points lie outside of the area shown here. (b) Instantaneous values of stretching (blue) and tilting (red) terms of the vorticity equation, averaged over all trajectories shown in (a) and computed every 1 second along the trajectory over a period of 15 minutes. Black line shows the sum of the two terms.

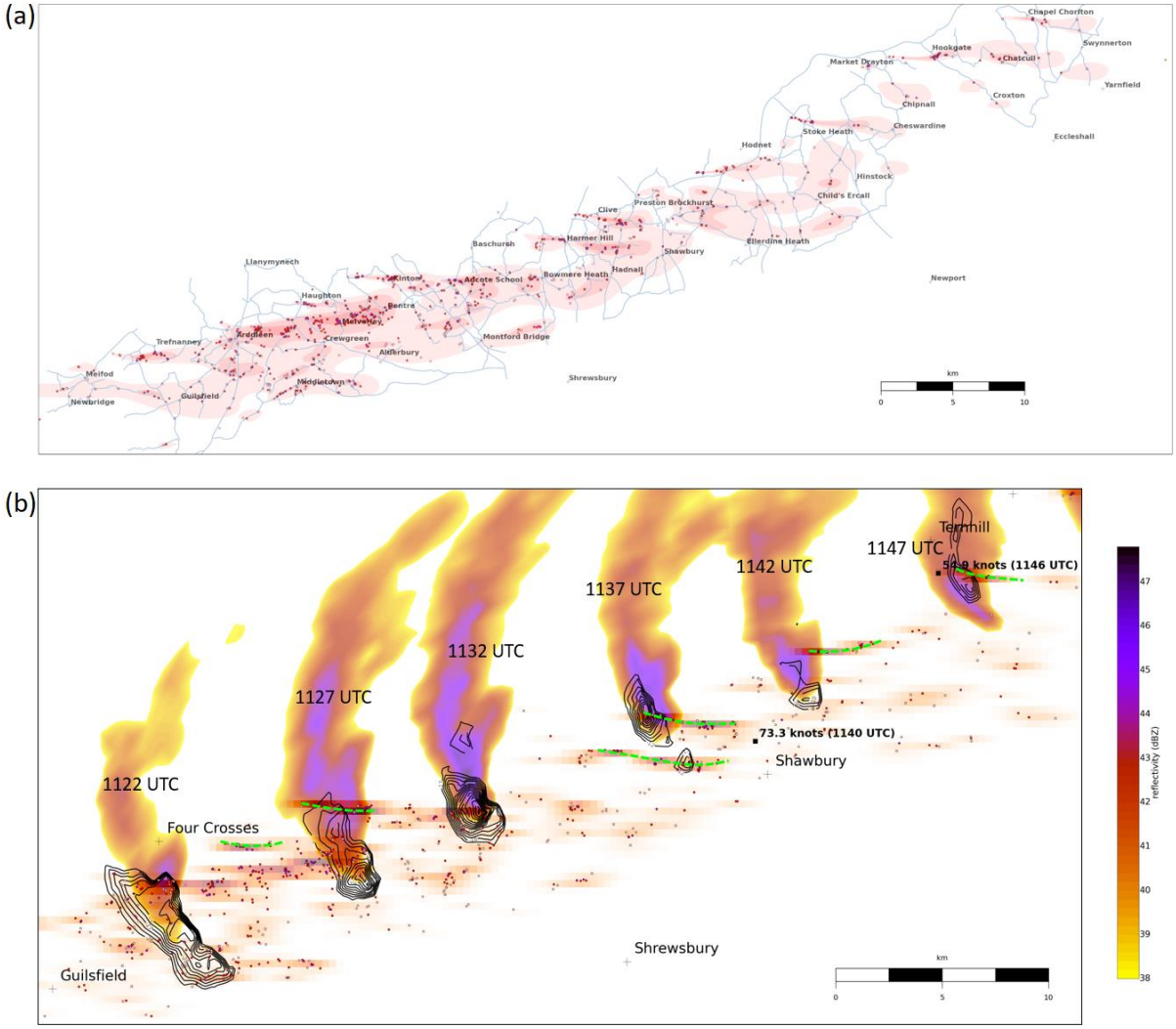

Figure 5.18: (a) Subjective assessment of damage tracks in Shropshire and surrounding areas, following the storm of 17 November 2016. Red shading indicates the damage area (deeper colours for more intense damage). Blue lines are roads covered during the survey. (b) Overlay of part of the damage area on data from the Clee Hill radar. Shading denotes radar reflectivity and black contours are radial velocity (contour interval 0.5 m s^{-1} for approaching velocities exceeding a threshold value; this threshold varies according to the scan time, in order to pick out areas of strongest approaching velocities in each scan). Scan times are indicated in the panel. Orange–red shading is a quantitative measure of the damage on a 0.33 km grid, in which the shading relates to the number of damage points in each grid square multiplied by the mean intensity of damage points in the same square (see below for details of the intensity scale). Lime green, dashed lines denote narrow, intense damage swaths associated with tornadoes. In both panels, coloured circles are individual damage points at three intensity levels: pink (approximately equivalent to T0 – T1 on the International Tornado Intensity Scale), red (~T1 – T2) and purple (~T2 – T3). Other annotations show the maximum gust speed, and the time at which it was recorded, at two Met Office surface stations located within the wider damage swath.

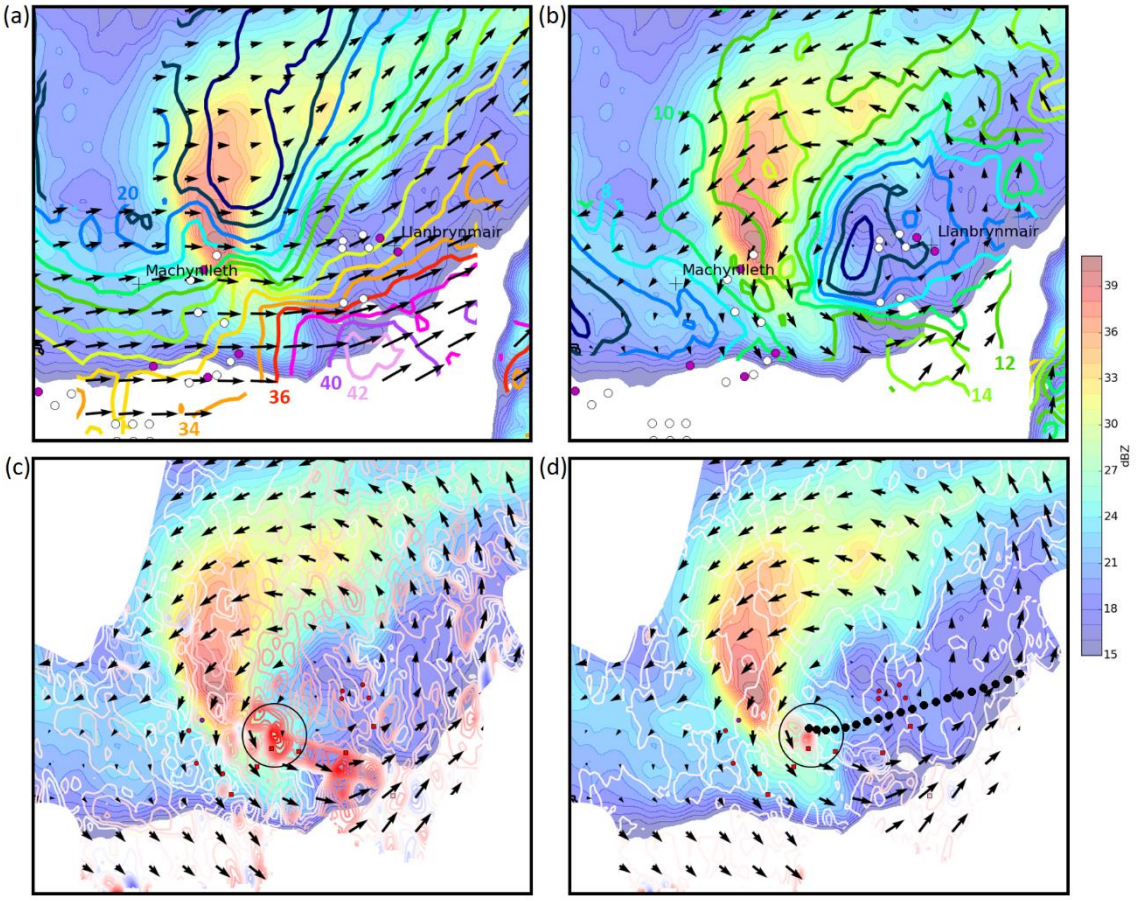

Figure 5.19: Dual-Doppler analysis, using data from the Crug-y-Gorllwyn and Clee Hill radars, over a part of mid Wales at 1052 UTC 17 November 2016. The beam height near the centre of the circulation is ~1.9 km AGL for the Crug-y-Gorllwyn radar, and ~1.7 km AGL for the Clee Hill radar. (a) Ground-relative wind vectors (arrows, plotted every 2 km in the x and y directions) and wind speed (coloured contours; contour interval 2 m s^{-1} starting at 16 m s^{-1}; blue colours indicate the lowest values and pink the highest values) overlaid on radar reflectivity (colour shading) from Crug-y-Gorllwyn radar. (b) As in (a) but showing storm-relative wind vectors and wind speeds (lowest contour 2 m s^{-1}). (c) As in (b) but showing vertical vorticity (red–blue contours; red denoting positive values and blue negative; contour interval 1 x 10^{-3} s^{-1}). (d) As in (c), but showing vertical vorticity stretching (contour interval 1 x 10^{-5} s^{-2}). Larger black dots show the (ground-relative) trajectory of a parcel starting near the flanking vertical vorticity stretching maximum. Smaller coloured circles in each panel are damage locations as surveyed by John Mason for TORRO. Noisy areas (where reflectivity was too low, in one or more of the scans, to retrieve Doppler wind fields) have been masked out manually. In panels (c) and (d), the flanking vertical vorticity and vertical vorticity stretching maximum of interest is circled.

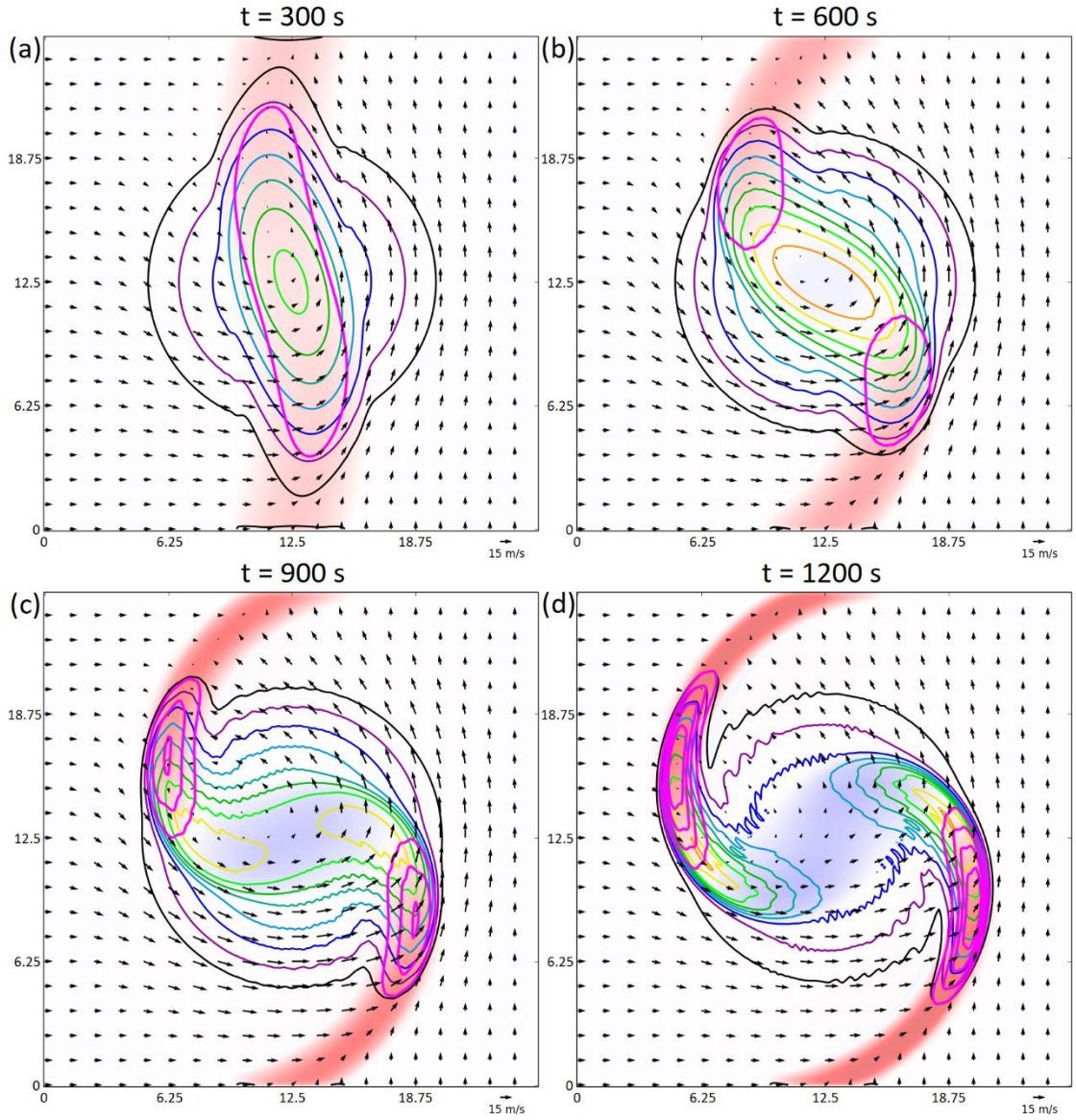

Figure 5.20: Output from simple model in which a circularly symmetric, vortical flow field of diameter 25 km, centred at the middle of the domain, advects an initially straight shear zone separating specified pre- and post-frontal wind fields, in which the wind speed is equal on both sides of the shear zone and veers by 90° across the shear zone. The initial shear zone width is 6.25 km. The vortical flow field varies with $cos\left[\pi\left(\left(\frac{t}{T}\right)-0.5\right)\right]$, where t is the time since the start of the run, in seconds, and T is the duration of the run. The vortical flow field is therefore zero at the start and end of the run and reaches a maximum at $t = 0.5T$, in order to simulate a vortex that develops, intensifies and then decays during the run. Convergence (divergence) is shown by red (blue) shading, with deeper shading indicating stronger magnitudes of each. Vertical vorticity is shown by coloured contours at intervals of 1 x 10^{-3} s^{-1}, starting at 0.5 x 10^{-3} s^{-1}. Vertical vorticity stretching is shown by bold magenta contours at intervals of 1 x 10^{-5} s^{-2}, starting at 0.5 x 10^{-5} s^{-2}.

5.8 Outstanding questions and directions for future research

Questions unanswered in the current work, additional questions posed, and possible avenues for future research have been alluded to throughout this chapter. A more complete listing of the various possibilities for future research now follows.

5.8.1 The composite NCFR tornado risk parameter, p[TN]

- In the current work, *p*[TN] was calculated using both ERAi and 1.5 km model fields. It would be useful to compare with parameter values derived from other data sources (such as global numerical weather prediction models), to test whether values are indeed independent of the resolution of the dataset, subject to the conditions listed in Section 5.4.2.
- The calculation of *p*[TN] could be fully automated if coupled with existing objective techniques for the identification of surface fronts (e.g., Hewson, 1997; 2009). These objective techniques employ kinematic parameters, such as vertical vorticity, and should therefore be well-suited to NCFR-bearing fronts (which tend to be kinematically well-marked). Although full automation is necessary for routine operational implementation of *p*[TN], the nomogram presented in Figure 2.3(a) also allows rough calculations to be made 'manually' at specified points, as already done for a small number of cases (Matthew Lehnert, Pers. Com.).
- Automated calculation of *p*[TN] using objective fronts would also pave the way for a global analysis of NCFR tornado-favourable environments. This could feasibly be extended to climate models, to investigate any future changes in the global and regional frequencies of NCFR tornado-favourable environments in a warmer world.

5.8.2 Conceptual models

- Analysis of a larger event set, drawn from a longer period, could eventually be conducted to see whether the relative frequency of tornadic event types found within the current study period applies more generally (such analysis requires longer archives of composite radar data than are currently available in the UK, for example).
- Objective classification techniques, such as principal component analysis (e.g., Graf *et al*., 2017; Spensberger and Sprenger, 2018), could be employed to derive

a more robust set of tornadic NCFR types; if applied to a larger set of events, this may lead to the discovery of additional event types not represented or identified in the current sample.

5.8.3 Observational studies

The results of the current work suggest that high-resolution observations, including those from dedicated research campaigns (e.g., mobile X-band radars, rapidly deployable automatic weather stations), could usefully be focussed on the following aspects:

- High-resolution observations of miso-scale vortices, with a focus on documentation of the vortex substructure, and comparing this with the results from high-resolution simulations and detailed ground surveys of the damage in tornadic cases. Observations of the vortex-genesis process, the possible cascade of vortices to smaller scales, and associated development of the core-and-gap NCFR morphology, would also be of interest in any non-tornadic cases exhibiting miso-scale vortices.
- Observations showing the cross-sectional structure of fronts and its evolution (e.g., a sequence of range–height radar scans) could provide additional insights into the role of evaporative cooling, and how this relates to the strength and evolution of the NCFR rear inflow.
- Higher-resolution observations of the pre-frontal environment could yield useful additional insights into aspects such as the static stability and its horizontal variability; proximity soundings from the operational network are unlikely to be representative in all cases, given the existence of small-scale variability in at least some of the parameters of interest (e.g., Apsley *et al*., 2016; King *et al*., 2017).
- Archived data from the current set of operational Doppler radars in the UK, coupled with TORRO tornado reports, could be analysed for a large set of tornadic and non-tornadic NCFR vortices, to investigate whether differences exist in terms of vortex intensity, longevity and evolution, as has been done for mesocyclones in tornadic and non-tornadic supercells in the US (e.g., Homeyer *et al*., 2020).

5.8.4 High-resolution modelling

- Analysis of more case studies would be a useful first step, using models of a similar resolution to those in the current study, to assess the generality or otherwise of the results obtained herein.
- Standard output files from the operational Met Office 1.5 km model (as used in Chapter 4) appear sufficient to elucidate the key physical mechanisms on the meso-β-scale and larger, but bespoke, higher resolution simulations (ideally with a grid spacing ≤ 50 m) will be required to investigate the sub-structure of miso-scale vortices and the tornado-genesis mechanisms. Such modelling capability has already been applied to supercell storms (e.g., Orf *et al*., 2017).

5.8.5 Idealised models (including analytical models)

- It would be useful to return to the work of Moore (1985), to further understand how the shear zone evolves under the two identified modes of HSI (i.e., the pure shear mode and the buoyancy–shear hybrid mode). For example, if characteristic differences can be found between the modes, in terms of the structure and evolution of the shear zone, this might allow the modes to be identified in real-data simulations or observations of NCFRs. This could, in turn, allow investigations into whether the mode has any impact upon the intensity of vortices and the likelihood of tornado-genesis. More generally, studies investigating the impact of static stability on the vortex- and tornado-genesis processes could provide additional insights into the environments most supportive of NCFR tornadoes.
- The Dritschel *et al*. (1991) model, which demonstrates that the release of HSI is prevented when the horizontal strain is greater than approximately one-quarter of the vertical vorticity within a vorticity strip, and other studies pertaining to the stability of vertical vortex strips (e.g., Bishop and Thorpe, 1994), are apparently of key relevance to the frontal wave case analysed herein. The setup in Dritschel *et al*. (1991) differs from that of a trailing cold front in several respects; in particular, the vorticity strip at a surface front also typically contains strong horizontal convergence. Bishop and Thorpe's (1994) model, on the other hand, which relates specifically to fronts, does include convergence in association with the front-transverse ageostrophic circulation. A deeper exploration of the current

results in comparison with those of Bishop and Thorpe (1994) would therefore be beneficial. More generally, a closer examination of the similarities and differences between vorticity strips in the various analytical models and in real fronts (for example, using high-resolution observations) would be useful, and could lead to refinement of the conceptual model presented herein for frontal wave tornadic NCFRs.

5.9 Concluding remarks

This thesis establishes a basis for the understanding and forecasting of tornadoes in NCFRs, which are the single largest source of substantially damaging tornadoes (≥T2 on the International Tornado Intensity Scale) in the UK. The work has described the large-scale situations most often associated with tornadic NCFRs, elucidated physical links between the large-scales and small-scales in these situations, identified environmental parameters capable of distinguishing between tornadic and non-tornadic NCFRs, derived practical tools for operational forecasting of NCFR tornado risk (*p*[TN] and the conceptual models) and made some progress in explaining the fluid-dynamical processes leading to the formation of NCFR tornado parent vortices. It is hoped that the work will stimulate and provide a solid foundation for further study in these areas, with a particular focus on the vortex- and tornado-genesis mechanisms, and detailed ground surveys of the damage in relation to high-resolution observations and model simulations. Such studies should, in time, lead to a more complete understanding of the phenomenon of tornadoes in NCFRs.

References

Apsley M, Mulder KJ, Schultz DM. 2016. Reexamining the United Kingdom's greatest tornado outbreak: forecasting the limited extent of tornadoes along a cold front. *Wea. Forecasting* **31**: 853–875.

Ayrault F, Lalaurette F, Joly A, Loo C. 1995. North Atlantic ultra high frequency variability. *Tellus A* **47**: 671–696.

Bishop CH, Thorpe AJ. 1994. Frontal wave stability during moist deformation frontogenesis. Part II: The suppression of nonlinear wave development. *J. Atmos. Sci*. **51**: 874–888.

Browning KA. 1990. Organization of clouds and precipitation in extratropical cyclones. In *Extratropical Cyclones, Erik Palmen Memorial Volume*, C. W. Newton and E. O. Holopainen, Eds., Amer. Meteor. Soc., 129–153.

Browning KA. 1997. The dry intrusion perspective of extra-tropical cyclone development. *Meteor. Appl.* **4**: 317–324.

Browning KA. 1999. Mesoscale aspects of extratropical cyclones: An observational perspective. In *The Life Cycles and Extratropical Cyclones,* M. A. Shapiro *et al*., Eds., Amer. Meteor. Soc., Boston, MA., 265–283.

Browning KA, Monk GA. 1982. A simple model for the synoptic analysis of cold fronts. *Q. J. Roy. Meteor. Soc.* **108**: 435–452.

Browning KA, Roberts NM. 1994. Structure of a frontal cyclone. *Q. J. Roy. Meteor. Soc.* **120**: 1535–1557.

Browning KA, Roberts NM. 1996. Variation of frontal and precipitation structure along a cold front. *Q. J. Roy. Meteor. Soc*. **122**: 1845–1872.

Buban MS, Ziegler CL. 2016. The formation of small-scale atmospheric vortices via horizontal shearing instability. *J. Atmos. Sci.* **73**: 2061–2084.

Buckingham TJ, Schultz DM. 2020. Synoptic-scale environments and precipitation morphologies of tornado outbreaks from quasi-linear convective systems in the United Kingdom. *Wea. Forecasting* **35**: 1733–1759.

Burt S. 2021. Two hundred years of thunderstorms in Oxford. *Weather* **76**: 212–222.

Clark M. 2010. A survey of damage caused by the Monkwood, Hampshire, UK tornado of 3 November 2009. *Int. J. Meteorol. (UK)* **35**: 291–297.

Clark MR. 2012. Doppler radar observations of non-occluding, cyclic vortex-genesis within a long-lived tornadic storm over southern England. *Q. J. Roy. Meteor. Soc.* **138**: 439–454.

Clark MR. 2013. A provisional climatology of cool-season convective lines in the UK. *Atmos. Res.* **123**: 180–196.

Clark MR, Parker DJ. 2014. On the mesoscale structure of surface wind and pressure fields near tornadic and nontornadic cold fronts. *Mon. Wea. Rev.* **142**: 3560–3585.

Clark MR, Webb JDC, Kirk PJ. 2018. Fine-scale analysis of a severe hailstorm using crowd-sourced and conventional data. *Meteor. Appl.* **25**: 472–492.

Dacre HF, Gray SL. 2006. Life-cycle simulations of shallow frontal waves and the impact of deformation strain. *Q. J. Roy. Meteor. Soc.* **132**: 2171–2190.

Davies HC, Schär C, Wernli H. 1991. The palette of fronts and cyclones within a baroclinic wave development. *J. Atmos. Sci.* **48**: 1666–1689.

Doswell CA III, Burgess DW. 1988. On some issues of the United States tornado climatology. *Mon. Wea. Rev.* **116**: 495–501.

Doswell CA III, Schultz DM. 2006. On the use of indices and parameters in forecasting severe storms. *Electronic J. Severe Storms Meteor.* **1**: 1–22.

Dritschel DG, Haynes PH, Juckes MN, Shepherd TG. 1991. The stability of a two-dimensional vorticity filament under uniform strain. *J. Fluid. Mech.* **230**: 647–665.

Feuerstein B, Dotzek N, Grieser J. 2005. Assessing a tornado climatology from global tornado intensity distributions. *J. Climate.* **18**: 585–596.

Garner JM. 2013. A study of synoptic-scale tornado regimes. *Electronic J. Severe Storms Meteor.* **8**: 1–25.

Graf MA, Wernli H, Sprenger M. 2017. Objective classification of extratropical cyclogenesis. *Q. J. Roy. Meteor. Soc.* **143**: 1047–1061.

Hart JA, Cohen AE. 2016. The challenge of forecasting significant tornadoes from June to October using convective parameters. *Wea. Forecasting* **31**: 2075–2084.

Hewson TD. 1997. Objective identification of frontal wave cyclones. *Meteor. Appl.* **4**: 311–315.

Hewson TD. 2009. Diminutive frontal waves—A link between fronts and cyclones. *J. Atmos. Sci.* **66**: 116–132.

Homeyer CR, Sandmæl TN, Potvin CK, Murphy AM. 2020. Distinguishing characteristics of tornadic and nontornadic supercell storms from composite mean analyses of radar observations. *Mon. Wea. Rev.* **148**: 5015–5040.

Hoskins BJ, Bretherton FP. 1972. Atmospheric frontogenesis models: mathematical formulation and solution. *J. Atmos. Sci.* **29**: 11–37.

Joly A, Thorpe AJ. 1990. Frontal instability generated by tropospheric potential vorticity anomalies. *Q. J. R. Meteor. Soc.* **116**: 525–560.

Juckes M. 1995. Instability of surface and upper-tropospheric shear lines. *J. Atmos. Sci.* **52**: 3247–3262.

Keyser D, Shapiro MA. 1986. A review of the structure and dynamics of upper-level frontal zones. *Mon. Wea. Rev.* **114**: 452–499.

King JR, Parker MD, Sherburn KD, Lackmann GM. 2017. Rapid evolution of cool season, low-CAPE severe thunderstorm environments. *Wea. Forecasting* **32**: 763–779.

Knightley P. 2006. Tornadogenesis across England on 28 July 2005. *Int. J. Meteorol. (UK)* **31**: 243–254.

Koch SE, Kocin PJ. 1991. Frontal contraction processes leading to the formation of an intense narrow rainband. *Meteorology and Atmospheric Physics* **46**: 123–154.

McGinnigle JB, Young MV, Bader MJ. 1988. The development of instant occlusions in the North Atlantic. *Meteorological Magazine (UK)* **117**: 325–341.

Meaden GT. 1991. Note regarding the Trowbridge tornado of Christmas Day 1990. *J. Meteor. (UK)* **16**: 46–50.

Moore GWK. 1985. The organization of convection in narrow cold-frontal rainbands. *J. Atmos. Sci.* **42**: 1777–1791.

Moore GWK, Peltier WR. 1987. Cyclogenesis in frontal zones. *J. Atmos. Sci.* **44**: 384–409.

Orf L, Wilhelmson R, Lee B, Finley C, Houston A. 2017. Evolution of a long-track violent tornado within a simulated supercell. *Bull. Amer. Meteor. Soc.* **98**: 45–68.

Parker DJ. 1998. Secondary frontal waves in the North Atlantic region: a dynamical perspective of current ideas. *Q. J. R. Meteor. Soc.* **124**: 829–856.

Parker DJ, Thorpe AJ. 1995. The role of snow sublimation in frontogenesis. *Q. J. R. Meteor. Soc.* **121**: 763–782.

Petterssen S, Smebye SJ. 1971. On the development of extratropical cyclones. *Q. J. R. Meteor. Soc.* **97**: 457–482.

Pike WS. 1992. The two East Anglian tornadoes of 12 November 1991 and their relationship to a fast-moving triple point of a frontal system. *J. Meteor. (UK)* **17**: 37–50.

Pike WS. 1993. The relationship between 'triple point' frontal passages and tornadoes over the southern United Kingdom and Ireland, including a historical synoptic reconstruction of the multiple outbreak on 19th October 1870. *J. Meteor. (UK)* **18**: 77–84.

Priestley MDK, Dacre HF, Shaffrey LC, Schemm S, Pinto JG. 2020. The role of secondary cyclones and cyclone families for the North Atlantic storm track and clustering over western Europe. *Q. J. R. Meteor. Soc.* **146**: 1184–1205.

Schär C, Davies HC. 1990. An instability of mature cold fronts. *J. Atmos. Sci.* **47**: 929–950.

Schemm S, Sprenger M. 2015. Frontal-wave cyclogenesis in the North Atlantic – a climatological characterisation. *Q. J. R. Meteor. Soc.* **141**: 2989–3005.

Schultz DM, Sanders F. Upper-level frontogenesis associated with the birth of mobile troughs in northwesterly flow. *Mon. Wea. Rev.* **130**: 2593–2610.

Scott RK, Dritschel DG. 2014. Numerical simulation of a self-similar cascade of filament instabilities in the surface quasigeostrophic system. *Physical Review Letters* **112**: 144505.

Shapiro MA. 1983. *Mesoscale weather systems of the central United States. The National STORM Program: Scientific and Technological Bases and Major Objectives*. RA Anthes, Ed., University Corporation for Atmospheric Research. Boulder, CO.

Shapiro MA, Keyser D. 1990. Fronts, jet streams and the tropopause. *Extratropical Cyclones, The Erik Palmen Memorial Volume*, C. W. Newton and E. O. Holopainen, Eds., Amer. Meteor. Soc. 167–191.

Spensberger C, Sprenger M. 2018. Beyond cold and warm: an objective classification for maritime midlatitude fronts. *Q. J. R. Meteor. Soc.* **144**: 261–277.

Tang B, Vaughan M, Lazear R, Corbosiero K, Bosart L, Wasula T, Lee I, Lipton K. 2016. Topographic and boundary influences on the 22 May 2014 Duanesburg, New York, tornadic supercell. *Wea. Forecasting* **31**: 107–127.

Thompson RL, Edwards R, Hart JA, Elmore KL, Markowski P. 2003. Close proximity soundings within supercell environments obtained from the Rapid Update Cycle. *Wea. Forecasting* **18**: 1243–1261.

Thorncroft CD, Hoskins BJ, McIntyre ME. Two paradigms of baroclinic-wave life-cycle behaviour. *Q. J. R. Meteor. Soc.* **119**: 17–55.

Uccellini LW, Keyser D, Brill KF, Wash CH. 1985. The Presidents' Day Cyclone of 18–19 February 1979: Influence of upstream trough amplification and associated tropopause folding on rapid cyclogenesis. *Mon. Wea. Rev.* **113**: 962–988.

Wakimoto RM, Bosart BL. 2000. Airborne radar observations of a cold front during FASTEX. *Mon. Wea. Rev.* **128**: 2447–2470.

Weckwerth TM, Murphey HV, Flamant C, Goldstein J, Pettet CR. 2008. An observational study of convection initiation on 12 June 2002 during IHOP_2002. *Mon. Wea. Rev.* **136**: 2283–2304.

Young MV. 1993. *Cyclogenesis: interpretation of satellite radar images for the forecaster.* Forecasting Research Division Tech. Report 73 (Bracknell, UK, Meteorological Office), unpublished.

Young MV. 1994. A classification scheme for cyclone life-cycles: applications in analysis and short-period forecasting. *The Life Cycles of Extratropical Cyclones*, Vol. III, Bergen Symposium, 27 June-I July 1994. 380–385.

Young MV, Hewson TD. 2012. The forecasting challenge of waving cold fronts: benefits of the ensemble approach. *Weather* **67**: 296–301.

Young MV, Monk GA, Browning KA. 1987. Interpretation of satellite imagery of a rapidly deepening cyclone. *Q. J. R. Meteor. Soc.* **113**: 1089–1115.

Young MV, Clark MR. 2018. Development of localized damaging wind gusts associated with a frontal wave and mesoscale vortex across south Wales on 18 May 2015. *Meteor. Appl.* **25**: 139–150.

Appendices

Appendix A: Full listing of events analysed in Chapter 2

Table S1: Details of the 114 events analysed in Chapter 2. The number of reported tornadoes, where applicable, is as shown in the TORRO tornado database (accessed 27 February 2015). 'N/A' indicates 'not applicable'. Events are listed in order of event class (high-tornadic, tornadic, non-tornadic) and then in chronological order within each event class. Tornado report times are to the nearest hour. This table was presented as supplementary material in Clark and Parker (2020).

Date	*Event class*	*Frontal type*	*Number of reported tornadoes*	*Tornado report time(s) (or tornadic period for outbreaks) (UTC)*	*Region(s) with tornado reports*
9 December 1979	High-tornadic	Cold	7	1800 – 2100	Midlands and southeast England
20 October 1981	High-tornadic	Cold	29	0500 – 0900	Southwest and southeast England
23 November 1981	High-tornadic	Cold	104	1000 – 1600	Wales, northwest England, northeast England, Midlands, East Anglia
21 September 1982	High-tornadic	Cold	24	0900 – 1200	Midlands, East Anglia, southeast England
9 December 1982	High-tornadic	Cold	7	2100 – 2300	Southwest and southeast England
21 March 1983	High-tornadic	Cold	8	0800 – 1200	Northwest England, Wales, Midlands
8 February 1984	High-tornadic	Cold	19	0200 – 0600	Wales, Midlands, southwest England, southeast England
21 February 1990	High-tornadic	Cold	7	0600 – 0900	Wales, Midlands, northeast England
25 December 1990	High-tornadic	Occluding cold	14	0900 – 1200	Southwest England, Wales, Midlands,

					northeast England
4 October 2004	High-tornadic	Cold	7	0500 – 0800	Southwest England, East Anglia, northwest England, northeast England, Scotland
27 – 28 December 2004	High-tornadic	Cold	8	2100 – 0100	Northwest England, Wales, southwest England
1 January 2005	High-tornadic	Cold	7	1100 – 1500	Republic of Ireland, Northern Ireland, northwest England, Scotland
24 November 2005	High-tornadic	Cold	7	1400 – 1600	Southeast England
30 December 2006	High-tornadic	Cold	11	1500 – 1800	Southeast England, East Anglia
24 September 2007	High-tornadic	Cold	13	0000 – 0700	Wales, Midlands, northeast England, southeast England, East Anglia
3 November 2009	High-tornadic	Cold	10	1100 – 1300	Southwest and southeast England
29 November 2011	High-tornadic	Cold	7	1200 – 1600	Wales, Midlands, northwest England, northeast England
25 January 2014	High-tornadic	Cold	7	1400 – 1700	Wales, Midlands, southeast England, northeast England, East Anglia
28 January 2004	Tornadic	Cold	2	1300, 1800	Northwest England, southwest England

4 April 2004	Tornadic	Cold	1	2100	Midlands
17 November 2006	Tornadic	Cold	1	1500	Southeast England
25 November 2006	Tornadic	Cold	1	1100	Southeast England
28 November 2006	Tornadic	Cold	1	0100	Wales
3 December 2006	Tornadic	Occlusion	1	0100	Republic of Ireland
11 December 2006	Tornadic	Cold	1	0700	Midlands
31 December 2006	Tornadic	Occluding cold	3	1300 – 1600	Northern Ireland, Scotland
29 December 2007	Tornadic	Cold	2	0000, 0200	East Anglia, southeast England
8 January 2008	Tornadic	Cold	1	2000	Northwest England
9 November 2008	Tornadic	Occluding cold	1	0000	East Anglia
10 November 2008	Tornadic	Cold	2	1400	East Anglia
12 November 2009	Tornadic	Occluding cold	1	1100	Republic of Ireland
6 December 2009	Tornadic	Cold	1	0700	Southeast England
29 August 2010	Tornadic	Cold	2	1300, 1400	East Anglia, southeast England
21 September 2011	Tornadic	Cold	1	1100	Scotland
17 October 2011	Tornadic	Cold	2	1500, 1600	Scotland, northwest England
23 December 2011	Tornadic	Cold	1	1400	Southwest England
3 January 2012	Tornadic	Cold	1	1200	Southeast England
15 August 2012	Tornadic	Cold	1	1500	Northwest England
29 August 2012	Tornadic	Cold	3	0600, 1100	Republic of Ireland, southeast England
12 September 2012	Tornadic	Cold	2	1800, 2000	Midlands, southeast England
31 January 2013	Tornadic	Occlusion	1	0500	Midlands
20 November 2013	Tornadic	Cold	5	0900 – 1200	Midlands, southeast England

18 December 2013	Tornadic	Cold	2	1500, 1600	Republic of Ireland
21 December 2013	Tornadic	Occlusion	2	1600	Wales
19 March 2004	Non-tornadic	Cold	0	N/A	N/A
13 September 2004	Non-tornadic	Cold	0	N/A	N/A
26 September 2005	Non-tornadic	Cold	0	N/A	N/A
8 November 2005	Non-tornadic	Cold	0	N/A	N/A
11 November 2005	Non-tornadic	Cold	0	N/A	N/A
1 December 2005	Non-tornadic	Cold	0	N/A	N/A
20 January 2006	Non-tornadic	Cold	0	N/A	N/A
6 October 2006	Non-tornadic	Cold	0	N/A	N/A
10 November 2006	Non-tornadic	Cold	0	N/A	N/A
16 November 2006	Non-tornadic	Cold	0	N/A	N/A
25 November 2006	Non-tornadic	Cold	0	N/A	N/A
5 December 2006	Non-tornadic	Cold	0	N/A	N/A
30 December 2006	Non-tornadic	Cold	0	N/A	N/A
10 January 2007	Non-tornadic	Cold	0	N/A	N/A
11 January 2007	Non-tornadic	Occluding cold	0	N/A	N/A
20 January 2007	Non-tornadic	Cold	0	N/A	N/A
28 October 2007	Non-tornadic	Cold	0	N/A	N/A
8 November 2007	Non-tornadic	Cold	0	N/A	N/A
30 November 2007	Non-tornadic	Cold	0	N/A	N/A
31 January 2008	Non-tornadic	Cold	0	N/A	N/A
9 September 2008	Non-tornadic	Cold	0	N/A	N/A
1 October 2008	Non-tornadic	Cold	0	N/A	N/A

10 November 2008	Non-tornadic	Cold	0	N/A	N/A
17 January 2009	Non-tornadic	Cold	0	N/A	N/A
20 October 2009	Non-tornadic	Occlusion	0	N/A	N/A
18 November 2009	Non-tornadic	Cold	0	N/A	N/A
24 November 2009	Non-tornadic	Cold	0	N/A	N/A
14 September 2010	Non-tornadic	Cold	0	N/A	N/A
2 November 2010	Non-tornadic	Cold	0	N/A	N/A
17 November 2010	Non-tornadic	Occlusion	0	N/A	N/A
21 May 2011	Non-tornadic	Cold	0	N/A	N/A
6 September 2011	Non-tornadic	Cold	0	N/A	N/A
5 October 2011	Non-tornadic	Cold	0	N/A	N/A
31 October 2011	Non-tornadic	Cold	0	N/A	N/A
24 November 2011	Non-tornadic	Cold	0	N/A	N/A
1 December 2011	Non-tornadic	Cold	0	N/A	N/A
8 December 2011	Non-tornadic	Cold	0	N/A	N/A
25 January 2012	Non-tornadic	Cold	0	N/A	N/A
4 March 2012	Non-tornadic	Occlusion	0	N/A	N/A
7 March 2012	Non-tornadic	Cold	0	N/A	N/A
9 April 2012	Non-tornadic	Cold	0	N/A	N/A
17 April 2012	Non-tornadic	Occluding cold	0	N/A	N/A
13 May 2012	Non-tornadic	Cold	0	N/A	N/A
10 September 2012	Non-tornadic	Cold	0	N/A	N/A
5 October 2012	Non-tornadic	Cold	0	N/A	N/A
31 October 2012	Non-tornadic	Cold	0	N/A	N/A

22 November 2012	Non-tornadic	Cold	0	N/A	N/A
25 November 2012	Non-tornadic	Cold	0	N/A	N/A
29 December 2012	Non-tornadic	Cold	0	N/A	N/A
31 December 2012	Non-tornadic	Cold	0	N/A	N/A
30 January 2013	Non-tornadic	Cold	0	N/A	N/A
15 September 2013	Non-tornadic	Cold	0	N/A	N/A
17 September 2013	Non-tornadic	Occlusion	0	N/A	N/A
26 October 2013	Non-tornadic	Occlusion	0	N/A	N/A
27 October 2013(a)	Non-tornadic	Cold	0	N/A	N/A
27 October 2013(b)	Non-tornadic	Cold	0	N/A	N/A
2 November 2013	Non-tornadic	Occluding cold	0	N/A	N/A
4 November 2013	Non-tornadic	Occlusion	0	N/A	N/A
5 December 2013	Non-tornadic	Cold	0	N/A	N/A
16 December 2013	Non-tornadic	Cold	0	N/A	N/A
24 December 2013	Non-tornadic	Cold	0	N/A	N/A
27 December 2013	Non-tornadic	Occluding cold	0	N/A	N/A
31 December 2013	Non-tornadic	Cold	0	N/A	N/A
7 April 2014	Non-tornadic	Cold	0	N/A	N/A
17 August 2014	Non-tornadic	Cold	0	N/A	N/A
3 October 2014	Non-tornadic	Cold	0	N/A	N/A
8 November 2014	Non-tornadic	Cold	0	N/A	N/A
9 December 2014	Non-tornadic	Cold	0	N/A	N/A
12 December 2014	Non-tornadic	Cold	0	N/A	N/A
22 December 2014	Non-tornadic	Cold	0	N/A	N/A

Appendix B: Formulae for the calculation of *p*[TN], given shear vorticity and $-v'_{cold}$

In Chapter 2, *p*[TN] was derived using linear discriminant analysis, as applied to a set of tornadic and non-tornadic analysis points within the two-dimensional parameter space defined by shear vorticity and $-v'_{cold}$ (see Figure 2.3(a)). In this appendix, we present formulae for the calculation of *p*[TN], given shear vorticity and $-v'_{cold}$. Details of the underlying methodology may be found in Hastie *et al*. (2009). The decision boundary, which is defined as the line of *p*[TN] = 0.5, is given by:

$$D_{db} = -(1.2865\ ShearVorticity) - (-v'_{cold}) + 23.7230$$

D_{db} describes the distance of the given point from the decision boundary. Negative values of D_{db} indicate *p*[TN] > 0.5, and positive values indicate *p*[TN] < 0.5. *p*[TN] may then be obtained from D_{db} using:

$$p[TN] = 1 - \left\{\left(EXP(0.2384D_{db})\right)/\left(1 + EXP(0.2384D_{db})\right)\right\}$$

Appendix C: Analysis of low *p*[TN] tornadic NCFRs (exceptions)

As demonstrated by Brooks *et al*. (1993), analysis of 'failure modes' for severe convection and related phenomena may be as instructive as analysis of supporting factors, and for this reason we analyse, in this appendix, exceptions to the rule that large $-v'_{cold}$ and large shear vorticity tend to favour tornadoes.

i) Tornadic points with low p[TN]

Manual inspection of surface analysis charts and 850 hPa geopotential height fields suggests that most tornadic points with *p*[TN] <0.3 arise as a result of limitations in the analysis methodology and datasets, rather than being indicative of events occurring in genuinely low shear vorticity and/or low $-v'_{cold}$ environments. Firstly, some points are explained by the occurrence of frontal waves that were too small to be resolved on the ERA-Interim reanalysis grid. An example is the cold front of 3 November 2009. Surface meso-analyses showed a frontal wave and collocated surface mesolow with a wavelength of only a few tens of kilometres along a trailing cold front (Clark, 2012). The wind field around the mesolow is suggestive of $-v'_{cold}$ and shear vorticity locally

much larger than in the reanalysis dataset. This event therefore appears to represent a special class of the frontal wave type, in which the horizontal scale of the secondary cyclone (and therefore the tornado-favourable section of the front) is unusually small. 4 points (8.3% of those with *p*[TN] <0.3) fit into this category.

A second explanation for low *p*[TN] points is large along-front gradients in *p*[TN], which sometimes resulted in values of $-v'_{cold}$ and/or shear vorticity at the analysis point being unrepresentative of those at the tornado location. This issue is suggested by the presence of adjacent analysis points with much larger *p*[TN]; for example, 25.0% of points with *p*[TN] < 0.3 were located within ±2 points (i.e., ± ~220 km) of a point with *p*[TN] ≥0.5. Some of these points occurred close to the apex of frontal waves. Filtering to remove points with trajectories orientated at a shallow angle to the front, where another point lay closer to the observed tornado location (as described in Section 2.2.6), reduces the number of points affected by this problem, but evidently some examples remain.

A third, and related, situation in which points with low *p*[TN] occurs is along fronts with large curvature, especially where the tornadic or near-tornadic point in question is situated on the down-front flank of a prominent bulge in the line (such as might occur down-front of a developing secondary cyclone). 25 (i.e., 52.1%) of the tornadic and near-tornadic points with *p*[TN] <0.3 were associated with sections of fronts exhibiting substantial curvature, of which 16 were located down-front of the centre of a prominent frontal bulge. Comparison of the actual tornado locations with the frontal bulges in these cases showed that tornadoes genuinely occurred on the trailing flanks of the frontal bulges in only five cases. Given the typically large along-front differences in key parameter values between the up-front and down-front flanks of frontal bulges, this suggests that, in the remaining 11 cases, conditions at the given point are unlikely to have been representative of those at the actual tornado location. This issue tends to arise when the along-front scale of the frontal wave and associated frontal bulge is relatively small, or where the frontal bulge was evolving rapidly.

The remaining points with *p*[TN] < 0.3 cannot be explained by limitations of the methodology, and therefore genuinely appear to be exceptions to the rule that tornadic fronts occur in high shear vorticity and high $-v'_{cold}$ environments; 21 points (43.8% of tornadic and near-tornadic points with *p*[TN] < 0.3, and 10.4% of all tornadic and near-

tornadic points) fall into this category. Most of these points were associated with events exhibiting anomalously weak wind fields, some of which occurred in the warm half of the year. For example, five of the 21 points were associated with the event of 29 August 2012. CP14, in their analysis of 15 events, found an anomalously unstable pre-frontal environment in the 29 August 2012 case ($N_S^2 < 0$), as estimated from pre-frontal proximity soundings. An analysis of pre-frontal N_S^2 in the current set of cases (see Section 2.4.2) reveals negative values for 10 of the 21 low-*p*[TN] tornadic and near-tornadic points not explained by limitations of the methodology, with a median N_S^2 over all 21 points of 0.00 x 10^{-4} s^{-1}. This is substantially lower than the all-tornado-cases median value of 0.70 x 10^{-4} s^{-1} (Table 2.1), with differences significant at the 95% level. These results suggest that tornadic points in low *p*[TN] environments that cannot be explained by limitations of the methodology represent a set of cases in which buoyant instability plays a greater role in NCFR formation and tornadogenesis, and in which kinematic parameters such as the vertical vorticity and $-v'_{cold}$ play a lesser role, than is typical for NCFR events.

ii) Non-tornadic points with high p[TN]

In the unfiltered set of non-tornadic points over UK and Ireland land areas (i.e., including analysis points where the front did not exhibit an NCFR), 63 points (7.9%) had *p*[TN] >0.6. Of these, 15 points exhibited frontolysis (i.e., total F < 0). An example of high *p*[TN] in a region of frontolysis is shown in Figure 2.8 for the case of 3 January 2012. In this case, the strong frontolysis is within the frontal fracture region of a primary cyclone, just off the west coast of Norway[39] (Figure 2.8(b)), where *p*[TN] is also very large (>0.95; Figure 2.8(a)). A secondary maximum in *p*[TN] is evident further down-front, near a subtle frontal wave over southeast England, where at least one tornado occurred. Since it is unlikely that an NCFR would be present in the frontal fracture region, *p*[TN] provides an unrealistic estimate of the true tornado probability in this region. Conversely, near the frontal wave over southeast England, large frontogenesis accompanies large *p*[TN], suggesting an NCFR is more likely within this

[39] In this case, these latter analysis points would not have appeared in the filtered dataset in e.g., Figure 2.3(a), since they are not located over UK and Ireland land areas. However, we choose to discuss the case here because it is a good illustration of the point in hand.

part of the front, and therefore that tornadoes are more likely in this region (as observed).

In order to address this issue, the probability of an NCFR being present, and its dependence on various environmental parameters, was assessed by comparison of the distribution of parameter values at UK and Ireland land points with and without NCFRs. For this purpose, an NCFR was deemed to be present if one could be discerned in composite radar rainfall fields within ~100 km of each along-front point, and within ~2 hours of the analysis time. The probability of an NCFR was found to be a strong function of total frontogenesis (consistent with the idea that collapse of the frontal zone to small cross-frontal scales, and associated development of an NCFR, requires substantial frontogenesis; e.g., Koch and Kocin, 1991). NCFR probabilities (hereafter *p*[NCFR]) were calculated by dividing the number of points with an NCFR by the total number of points within different frontogenesis classes. The dependence of *p*[NCFR] on the midpoint frontogenesis for each frontogenesis class may be approximated by the third-order polynomial equation:

$$p[NCFR] = 0.00004\,F^3 - 0.0021F^2 + 0.0467F + 0.4679$$

where *F* is the total frontogenesis. Negative values of *p*[NCFR] are set to zero. This equation was used to derive *p*[NCFR] for all points in the 3 January 2012 case (Figure 2.8(c)). As expected, *p*[NCFR] is at or close to zero in the frontal fracture region due to the strong frontolysis, but much larger (>0.7) near the frontal wave over southeast England. Weighting of *p*[TN] by *p*[NCFR], for example by calculating the product of the two parameters, provides a more realistic estimate of tornado risk in this case (Figure 2.8(d)), usefully highlighting the region over southern England whilst giving much lower probabilities within the frontal fracture region.

Other non-tornadic points with low *p*[TN], where an NCFR was present and frontogenesis was positive, represent situations apparently favourable for tornadoes, but in which no tornadoes were reported. One possible explanation is underreporting, which is known to be a universal problem with existing tornado databases, being particularly relevant in the case of weaker tornadoes (e.g., Feuerstein *et al.*, 2005). Alternatively, it is possible that the tornadic phase of the event in these cases occurred prior to arrival of the front into the UK and Ireland (recalling that the tornadic period tends to occur

relatively early in the lifecycle of frontal waves, and that high *p*[TN] may persist beyond the tornadic phase). A third possible explanation is provided by analysis of the trends in parameter values. In at least three cases, the wind field showed marked weakening by the next analysis time, suggesting that, where present, the frontal wave was weakening, that the front was moving into a region of weaker large-scale flow, or that the frontal trough was becoming shallower, such that shear vorticity and $-v'_{cold}$ trends were negative. This is consistent with the results presented in Appendix D i.e., that the presence of a frontal wave is not a sufficient condition for tornadogenesis; non-developmental or weakening waves tend not to favour tornadoes, since they do not exhibit the requisite temporal changes in key parameter values. A final possible explanation for such events was uncovered by operational trials of *p*[TN] during winter 2019-20 (Matthew Lehnert, Pers. Comm.). In one event, the frontal zone was found to comprise multiple shear zones separated by ~10 – 20 km in the cross-front direction. Although high-resolution operational models indicated collapse to a single shear zone as the front crossed the UK, in the event this did not occur until after the front had cleared the region. Therefore, although the bulk shear vorticity was large, it continued to be distributed across multiple, weaker shear zones. Such events are likely under-represented in the analysed dataset because they tend to exhibit rather weak and discontinuous NCFRs. The failure to collapse to a single shear zone suggests weak frontogenesis, again highlighting the likely importance of sufficient frontogenesis (and the operation of frontogenesis for sufficient length of time), in combination with high *p*[TN], in tornadic events.

Appendix D: Frontal waves in non-tornadic events

Although frontal waves are capable of creating an environment favourable for NCFR tornadoes, as discussed in Section 2.3.7, a substantial number of non-tornadic cases also exhibited frontal waves at the time of passage of the front across the UK and Ireland. Inspection of surface analysis charts shows that non-tornadic fronts exhibited a warm-front–cold-front pair or an inflection point over or close to the UK in 25 cases (i.e., 36.8% of non-tornadic events; *cf.* 42.3% of tornadic events and 72.2% of high-tornadic events). In other words, the presence of a frontal wave is not a sufficient condition for tornadogenesis. In order to assess whether tornadic waves can be distinguished from

non-tornadic waves, bulk parameters were compared for frontal wave cases in the high-tornadic, tornadic and non-tornadic event classes. Tornadic and high-tornadic events were treated as one combined class ('all-tornadic'), owing to the relatively small sample size in each individual class. Results show significant differences (at the 95% level) between all-tornadic and non-tornadic waves for several parameters including $-v'_{cold}$, front-normal forward motion, shear vorticity, total frontogenesis and overall mean wind speed, with tornadic waves having larger median values in each case. Crucially, the median $-v'_{cold}$ trend was negative for the non-tornadic waves (median value – 0.45 m s^{-1} / 6 hours) but positive for tornadic events (median value 1.28 m s^{-1} / 6 hours). Similarly, the shear vorticity trend was near zero in non-tornadic waves (median value 0.3 x 10^{-5} s^{-1} / 6 hours), but positive in tornadic waves (median value 1.39 x 10^{-5} s^{-1} / 6 hours). These results suggest that developing waves are more conducive to tornadogenesis than non-developmental waves, and further emphasise the importance of temporal trends in parameter values (i.e., increases in shear vorticity and $-v'_{cold}$) in tornadic cases.

Appendix E: Idealised wind and pressure fields near a frontal wave

As discussed in Section 2.4.1, the along-front variability in shear vorticity, $-v'_{cold}$ and *p*[TN] arising near to a frontal wave may be understood, in part, by consideration of an idealised "toy model" of the pressure and associated geostrophic wind field, comprising three components:

1. A large-scale background pressure field and associated geostrophic wind field, in which a uniform pressure gradient of 1.18 x 10^{-5} hPa m^{-1} and associated south-westerly geostrophic flow of 7.9 m s^{-1} are orientated at an angle of 45° to the trailing front, with lower pressure towards the northwest.
2. An S-shaped front and associated pressure trough, the trough having half width W = 300 km, with uniform (along the front) central pressure deficit p_{tr} = 2 hPa at the trough axis (collocated with the front), and in which the pressure deficit reduces with increasing distance, *w*, from the trough axis and front according to $p_{tr}\left\{1 - sin\left[0.5\,\pi\left(\frac{w}{W}\right)\right]\right\}$. Smoothing is applied near the trough axis to avoid very large wind gradients.

3. A circularly symmetric, negative pressure anomaly and associated non-divergent, cyclonic, flow field representing the wave depression pressure and associated geostrophic wind fields. The anomaly central pressure deficit, *M*, is equal to 4.15 hPa and the pressure deficit reduces with distance, *d*, from the centre according to $0.5\ M\left\{1 - sin\left[\pi\left(\frac{d}{R} - 0.5\right)\right]\right\}$, where *R* is the anomaly radius (600 km).

Superimposing these pressure and wind components yields an idealised depiction of the flow fields near a frontal wave in the early stages of development. The associated along-front variability in trough structure, shear vorticity, and $-v'_{cold}$ are shown in Figure 2.13, as described in the main text.

Appendix F: Calculations of primary vortex spacing relative to the unperturbed shear zone width

Shear zone width in the 1.5 km and 300 m simulations was estimated by analysis of the 75 m AGL vertical vorticity field in areas exhibiting a general absence of local perturbations in the shear zone. In the 1.5 km model, the shear zone width was estimated as 4.75 km along the highly two-dimensional part of the shear zone to the southwest of Ireland (Figure 3.7), using 1 x 10^{-3} s^{-1} as the lower vorticity limit with which to define the edges of the shear zone (peak values within the shear zone in this region being ~7 x 10^{-3} s^{-1}). According to linear theory (Miles and Howard, 1964), this yields an expected vortex spacing of 35.6 km following vortex sheet roll-up, which compares to a mean primary vortex spacing of 37.9 km (range 31.6 – 44.3 km) near to vortex C at 1400 UTC. In the 300 m model, estimates are more uncertain due to the presence of perturbations over most of the domain. However, over eastern parts of Eire at 1600 UTC, where the shear zone was relatively free of local perturbations, shear zone width was estimated as 1.8 ± 0.3 km, equating to an expected vortex spacing of 11.3 – 15.8 km. This compares to a mean spacing of primary vortices of 14.2 km just east of the Northern Ireland coast at 1500 UTC (Figure 3.11).

The shear zone width estimates also reveal that the shear zone is only marginally resolved by the 1.5 km model, being ~3 times the grid length, as compared to ~6 times

the grid length in the 300 m model. It is generally accepted that the effective resolution of a model is in the range 5 – 8 times the grid length (e.g., Lean & Clark, 2003).

Appendix G: Vertical variation of S_{HSI} and its along-front variability

Analysis of horizontal sections at various heights in the 1.5 km simulation shows that S_{HSI} exhibits large gradients in the vertical, with values increasing with decreasing height. Since we invoke the onset of $S_{HSI} < 0$ down-front of the wave centre (as analysed at 1390 m AGL) to explain the preferential genesis of vortices in this region, the height dependency of S_{HSI} requires further consideration. Within the boundary layer, the height dependency relates to the fact that friction acts to reduce vertical vorticity and increase horizontal convergence along the shear zone, such that the convergence (and therefore bulk cross-frontal confluence) becomes relatively larger than the vorticity with decreasing height. Down-front of the wave centre, a height of transition from positive to negative S_{HSI} can be defined by inspection of values at all model levels between the surface and ~3.5 km AGL. The height of this transition is lowest, at around 0.5 km AGL, immediately down-front of the wave centre i.e., where the values of S_{HSI} at 1390 m AGL were also lowest, and often negative (Figure 3.6(c)). This is also where the NCFR updrafts and shear zone tended to be deepest. If the height at which the shear zone becomes indistinguishable from the surrounding vertical vorticity field is taken as the depth of the shear zone, then this varies from ~1.0 – 1.5 km along the trailing front, well down-front of the wave centre, and in a separate region up-front of the wave centre, to ~2.5 km in vortex-prone region immediately down-front of the wave centre. The shear zone therefore extends well above the height of transition to negative S_{HSI} in the vortex-prone region (~80% of the depth of the shear zone being situated within $S_{HSI} < 0$). Conversely the majority, or all, of the shear zone is situated within positive S_{HSI} along the trailing part of the front far down-front of the wave centre, and up-front of the wave centre.

Moore (1985) showed that vortex growth due to pure shearing instability in statically stable environments (as distinct from a buoyancy–shear hybrid instability found in environments exhibiting horizontal wind shear *and* buoyant instability) occurs only in shear zones having aspect ratios greater than unity, where aspect ratio is defined

as shear zone depth divided by width. Although this was suggested to be unrealistic for real fronts, the 300 m simulation in the present case shows aspect ratios as high as 2.5 – 3.0 along the braid regions between primary vortices over the Irish Sea (e.g., as in Figures 3.15(a) and (b)). It is difficult to estimate aspect ratios prior to primary vortex-genesis because increasing shear zone depth apparently occurs in concert with the development of primary vortices. There is no evidence, however, that the shear zone was systematically wider in the vortex-prone region than elsewhere along the front, suggesting that the aspect ratio was probably largest where the shear zone was deepest. Given the estimated unperturbed shear zone width of 1.8 ± 0.3 km (Appendix F), and a typical shear zone depth of ~2.0 – 2.5 km immediately down-front of the wave centre, the aspect ratio of the line was likely close to unity in the vortex-prone region prior to primary vortex-genesis. Therefore, we conclude that both the reduced S_{HSI} (considering mean values over the depth of the shear zone), and the increased aspect ratio, would tend to favour vortex-genesis by the release of HSI in the same region, just down-front of the wave centre.